Structural performance of permanent post-tensioned CFRP ground anchors with strap ends

THÈSE N^O 7923 (2017)

PRÉSENTÉE LE 8 SEPTEMBRE 2017
À LA FACULTÉ DE L'ENVIRONNEMENT NATUREL, ARCHITECTURAL ET CONSTRUIT
LABORATOIRE DE CONSTRUCTION EN COMPOSITES
PROGRAMME DOCTORAL EN GÉNIE CIVIL ET ENVIRONNEMENT

ÉCOLE POLYTECHNIQUE FÉDÉRALE DE LAUSANNE

POUR L'OBTENTION DU GRADE DE DOCTEUR ÈS SCIENCES

PAR

Haifeng FAN

acceptée sur proposition du jury:

Prof. I. Smith, président du jury
Prof. T. Keller, Dr A. Vassilopoulos, directeurs de thèse
Prof. Z. Wu, rapporteur
Prof. B. Benmokrane, rapporteur
Prof. U. Meier, rapporteur

ÉCOLE POLYTECHNIQUE
FÉDÉRALE DE LAUSANNE

Suisse
2017

To all the people that I have met

Preface

Permanent post-tensioned ground anchors are normally composed of steel strand tendons. Since steel may be subject to corrosion and the condition of these anchors can no longer be easily and reliably assessed once installed, elaborate and costly measures have to be implemented in order to protect and electrically insulate the steel tendons. The approach adopted in this project is to replace the steel material by much more durable carbon fiber-reinforced polymer (CFRP) materials that do not require any further corrosion protection. However, CFRP tendons also present certain problems - the anchoring of the tendons is difficult due to the strong material anisotropy of CFRP. Simple mechanical wedge anchors as used in steel cannot be applied without significantly decreasing the anchor capacity. A much more material-tailored anchoring method for post-tensioned CFRP tendons is based on strap ends. Consequently, anchor heads with multiple strap ends for CFRP ground anchors were developed in this project. Furthermore, the mechanical behavior of non-laminated CFRP straps comprising up to 100 loops was investigated.

I would like to acknowledge the support for this research project by the Commission for Technology and Innovation CTI (Project-No. 14139.2 PFIW-IWF_IPR) and industry partner F. J. Aschwanden AG, Lyss, Switzerland.

Prof. Dr. Thomas Keller

Acknowledgements

During my Ph.D. study in CCLab at EPFL, I have been lucky enough to receive constant support and encouragement from many kindhearted people, without which I could hardly complete this work. I am thus sincerely grateful to all of them.

I would like to first express my sincere gratitude to Prof. Keller for having provided me this precious opportunity and interesting project and also his excellent guidance, insightful suggestions and constant support. Without his strong support, I could not have finished the thesis on time. I have learnt many skills and knowledge from him, including how to conduct a research project, how to analyze results and clearly present them and also how to well organize things. My sincere thanks also go to my co-supervisor Dr. Vassilopoulos for the fruitful discussions during the meeting, correction of my papers and constant support. Furthermore, my appreciation goes to Dr. Julia de Castro for her constant support, kind suggestions for my career and careful correction of my French CV and abstract.

I would like to sincerely thank the jury members of the thesis defense committee – Prof. Benmokrane (Université de Sherbrooke, Canada), Prof. Meier (EMPA, Switzerland), Prof. Smith (EPFL, Switzerland) and Prof. Wu (Southeast University, China) – for their time and effort that they have devoted to the evaluation of my thesis, coming so far away for my oral exam and their valuable comments.

I would also like to acknowledge the financial support of the Commission for Technology and Innovation (CTI) and the partners of this project: F. J. Aschwanden AG, Carbo-Link AG, Riostra and Sika Schweiz AG. Without their support and cooperation, the project could not have been successfully completed.

The experimental parts in this work can not be completed without the strong support of the technical collaborators in the Structural Engineering Institute. My sincere thanks go to Sylvain, Gérald, Gilles, Armin, Serge, François, Frédérique and Patrice for their professional collaborations and constant support to my experiments. Working and talking with them made the moments in the laboratory more interesting and memorable. My thanks also go to Lionel, Antonino and Jean in the Laboratory of Construction and Materials (LMC) where I fabricated some specimens.

The tremendous support and encouragement of all the CCLabians were indispensable for me to have overcome all the difficulties and enjoyed my work and life in Lausanne. I would like to sincerely thank all of them: Ehsan, Moslem, Carlos, Michael, Robert, Wei, Kyriaki, Alireza, Myrsini, Sonia, Maria, Vahid, Aida, Martin, Mário, João, Xinmiao, Chao, Xin and Zhengwen. They have made me feel like home at CCLab. I also appreciate the sound support from Mrs. Schauenberg and especially Mrs. Mohamed for their administrative coordination and Mrs. Howett for her meticulous English correction and strong support to help me meet my deadlines.

My former supervisor Prof. Liu and his wife Mrs. Gao at Tongji University have also been constantly supportive to me. Dr. Hu and his family have treated me as a family member, taught me valuable things and brought me into meaningful areas. All the teachers at the language center of EPFL and my language partners have enormously helped me in language learning. Furthermore, the Chinese community in Lausanne also provided me a friendly environment. I am sincerely grateful to all of them.

Last but not least, I would like to express my deepest gratitude to my parents for having brought me to this world and also for their tireless support, encouragement and love.

Life is a train journey. During the past five years of joyful journey, I have met many companions that are not listed here. I am grateful to all of them, no matter how long they have shared their life’s journey with me and no matter what they have brought.

Abstract

Permanent post-tensioned ground anchors made of steel are widely used for the stabilization of different structures in civil engineering. However, the steel components are generally vulnerable to galvanic corrosion. Instead of solving this durability problem with expensive and not always reliable protection systems, the replacement of steel by corrosion-resistant fiber-reinforced polymers (FRPs) – carbon-FRPs (CFRPs) in particular – has evolved as an alternative solution. Conceptually similar to steel tendons, mechanical or bonded anchors are commonly used for FRP tendons. However, carbon fibers are strongly anisotropic, exhibiting much lower strengths in the transverse fiber direction, which may lead to premature failure in the anchoring area due to high shear and through-thickness stress concentrations. A simpler and much more material-tailored anchoring method is based on strap ends, allowing the CFRP tendon to be anchored using simple steel pins. The objective of this research is to develop a new application of the strap anchorage method for permanent post-tensioned CFRP ground anchors with a capacity of at least 2500 kN.

The CFRP tendon comprises a multi-strap anchor head on the ground side, in which the CFRP strap end is prefabricated in a lightweight high-strength grout cylinder confined with CFRP rings. The confinement rings deviate the spreading forces – occurring at the strap ends and at the transition from the strap to the rod segment – into the cylinder's axial direction. The grout cylinder is stepwise axially loaded in compression by the axial components of the spreading forces.

The uniaxial compressive stress vs strain curves, including the softening branch, of four cement- and resin-based grout materials were obtained in compression experiments. The concrete compression model developed by Sargin was successfully applied to also describe the compressive grout behavior and subsequently used for finite element (FE) analyses of the CFRP ground anchors.

In a first stage, CFRP ground anchor heads with one-strap ends on the ground side were developed and investigated in pull-out experiments. The one-strap end was embedded in a high-strength grout cylinder confined with and without a steel tube, simulating anchor applications in rock and soil. In the rock application, the anchor can be used without additional confinement, while in the case of soil, an additional CFRP confinement ring with optimized length and position is needed to prevent premature grout failure in the strap region.

In a second stage, CFRP ground anchors with two-strap ends on the ground side were developed and investigated in pull-out experiments. The two-strap end was prefabricated in a lightweight conical anchor body of high-strength grout, inserted into a steel tube and anchored with normal-strength grout. Three specimens with different tube thicknesses were investigated to simulate anchor applications in different rock types. The anchors reached an average load-bearing capacity of 1384 kN with final failure occurring in the CFRP straps.

In a third stage, based on the pull-out experiments on the one- and two-strap anchors and the newly conducted FE analyses on the one-strap anchors, the load-transfer mechanism in multi-strap anchors was investigated. Different strap geometries influenced the load transfer but not the global pull-out behavior of the anchors. The anchors with similar strap geometries but different strap numbers exhibited similar pull-out and load-transfer behavior. An empirical model was developed for deriving the load-transfer diagram along the embedded straps for multi-strap anchors and subsequently applied to a new three-strap anchor with a targeted capacity of 2500 kN.

Furthermore, since strap rupture occurred in the one- and two-strap anchors, the tensile behavior of non-laminated and laminated straps, both applicable for strap anchors, was investigated using experimental, numerical and analytical methods. The non-laminated straps showed significantly higher load-bearing efficiency for layer numbers higher than 20 and exhibited lower sensitivity to tape anisotropy and friction at the strap/pin interface than the laminated straps. An empirical model for the non-laminated straps and an analytical model for the laminated straps were developed to predict the strap capacity; in the latter, the strap anisotropy and friction at the strap-pin interfaces were also taken into account.

The findings of this research therefore demonstrate that conventional steel anchors can be replaced by high-capacity CFRP strap anchors. This will lead to cost saving since the anchor can be easily handled and will no longer need to be monitored and replaced.

Keywords: Carbon fiber-reinforced polymer, Ground anchor, Strap end, Confinement, Pull-out behavior, Load-transfer mechanism, Non-laminated strap, Laminated strap.

Résumé

Les tirants d'ancrage précontraints permanents en acier sont couramment utilisés pour stabiliser différentes structures de génie civil. Cependant, les composants métalliques sont généralement vulnérables à la corrosion. Une alternative à l'utilisation de systèmes de protection coûteux et pas toujours fiables permettant de résoudre ce problème de durabilité consiste en remplacer l'acier par des polymères renforcés de fibres (PRF) résistants à la corrosion, des PRF de carbone (PRFC) en particulier. Des ancrages mécaniques et par adhérence similaires, du point de vue conceptuel, à ceux des tirants en acier sont souvent utilisés pour les tirants en PRF. En revanche, les fibres de carbone sont fortement anisotropes et présentent donc de plu faibles propriétés dans la direction transversale aux fibres ce qui entraînent une rupture prématurée dans la zone d'ancrage suite aux fortes concentrations de contraintes de cisaillement et dans le sens de l'épaisseur. Une méthode d'ancrage plus simple et plus adapté au matériau est basée sur des systèmes de boucles permettant d'ancrer simplement le tirant en PRFC avec des tiges en acier. L'objectif de cette thèse est de développer une nouvelle application de cette méthode d'ancrage de boucle pour des tirants d'ancrage précontraints permanents d'une capacité portante supérieure à 2500 kN.

Le tirant en PRFC a une tête d'ancrage à boucles multiples du côté terrain, dans laquelle la boucle est préfabriquée dans un cylindre de coulis léger, à haute résistance et confiné dans des anneaux en PRFC. Les anneaux de confinement dévient les forces de diffusion apparaissant à l'extrémité de la boucle et à la transition entre la boucle et la tige, dans la direction axiale du cylindre. Le cylindre de coulis est donc sollicité en compression axiale par les composantes axiales des forces de diffusion.

Une campagne expérimentale a permis d'obtenir les courbes contrainte-déformation de compression, y compris la branche décroissante, de quatre coulis de ciment et de résine. Le modèle développé par Sargin pour le béton comprimé a été appliqué avec succès pour caractériser le comportement en compression du coulis puis a été utilisé dans les analyses d'éléments finis des ancrages en PRFC.

Dans la première phase, les têtes d'ancrage en PRFC à une boucle du côté terrain ont été développées et étudiées à partir d'essais d'arrachement. La boucle a été scellée dans un cylindre de coulis à haute résistance et confiné avec ou sans un tube en acier simulant leur applications dans la roche ou le sol. Cet ancrage peut être utilisé sans confinement supplémentaire dans la roche, mais un anneau de confinement en PRFC a été exigé dans le sol afin d'empêcher la rupture prématurée de coulis dans la région de la boucle.

Dans la deuxième phase, les ancrages en PRFC à deux boucles du côté terrain ont été développés et étudiés lors d’essais d'arrachement. Les deux boucles ont été préfabriquées dans un corps d’ancrage léger, conique et de coulis à haute résistance. La partie préfabriquée a été introduite dans un tube en acier et finalement ancrée par du coulis de résistance normale. L’investigation de trois éprouvettes avec des tubes d’épaisseurs différentes a été réalisée simulant les applications d’ancrages dans différents types de roche. Une capacité portante moyenne de 1384 kN a été obtenue avec la rupture des boucles en PRFC.

Dans la troisième phase, le mécanisme de transfert de charge a été analysé en se basant sur la totalité des essais d'arrachement et sur les nouvelles analyses d’éléments finis des ancrages d’une boucle. Les différentes géométries de la boucle ont influencé le transfert de charge mais pas le comportement d’arrachement global. Les ancrages de géométries similaires mais avec différents nombres de boucles ont présenté un comportement à l’arrachement et de transfert de charge similaire. Un modèle empirique a été développé permettant de déduire le diagramme de transfert de charge le long des boucles scellées des ancrages à boucles multiples. Ce modèle a ensuite été appliqué pour un nouvel ancrage à trois boucles d’une capacité portante de 2500 kN.

En outre, puisque la rupture de la boucle est apparu dans les ancrages à une et à deux boucles, une campagne expérimentale, numérique et analytique a permis de caractériser le comportement en traction des boucles non-laminées et laminées, les deux étant applicables aux ancrages à boucles. Les boucles non-laminées ont présenté des capacités portantes plus élevées et une plus faible sensibilité à l’anisotropie du matériau et au frottement à l’interface entre l’axe et la boucle que les boucles laminées. Un modèle empirique pour les boucles non-laminées et un modèle analytique pour les boucles laminées ont été développés permettant d’estimer leurs capacités portantes. Ce dernier a aussi pris en considération l’anisotropie de la boucle et le frottement entre l’interface de l’axe et la boucle. D’après ces résultats, le remplacement des tirants d’ancrage conventionnels en acier par les tirants d’ancrages à boucles en PRFC de haute résistance serait envisageable dans le futur. Ceci permettrait de réduire les coûts de construction et de maintenance puisque l’ancrage proposé peut être facilement installé et pourrait potentiellement éviter les travaux de surveillance et de remplacement.

Mots-clés: polymères renforcés de fibres de carbone (PRFC), tirants d’ancrage, bouts de boucle, confinement, comportement à l’arrachement, mécanisme de transfert de charge, boucles non-laminées, boucles laminées

Table of contents

Preface i

Acknowledgements iii

Abstract/Résumé v

List of Tables xiv

List of Figures xv

1 Introduction 1

- 1.1 Context and motivations 3
- 1.2 Objectives 8
- 1.3 Methodology 8
- 1.4 Thesis organization 10
- 1.5 List of publications 13

2 Evaluation of grout materials for CFRP ground anchors with strap ends 17

- 2.1 Introduction 19
- 2.2 Materials and experimental setup 20
  - 2.2.1 Grout materials 20
  - 2.2.2 Cylinder specimens 21
  - 2.2.3 Curing conditions 24
  - 2.2.4 Experimental procedure and instrumentation 24
  - 2.2.5 Loading-control methods 25
  - 2.2.6 Boundary conditions 26
- 2.3 Experimental results and modeling 26
  - 2.3.1 Compressive strength, elastic modulus and Poisson’s ratio 26
  - 2.3.2 Compressive stress vs strain curves 27
  - 2.3.3 Compressive stress vs axial strain modeling 31
- 2.4 Experimental validation of compressive grout models 33
  - 2.4.1 Previous experiments on anchor heads 33
  - 2.4.2 High-strength grout material selection and models 33
  - 2.4.3 FE model description 34
  - 2.4.4 Model calibration based on anchor head C200 37
  - 2.4.5 FE model validation based on anchor heads C380 39
- 2.5 Conclusions 41

3 Pull-out behavior of CFRP one-strap ground anchors 45

3.1 Introduction..47

3.2 Experimental program 49

3.2.1 CFRP one-strap anchor specimens 49

3.2.2 Material description 51

3.2.3 Experimental set-up and instrumentation 52

3.3 Results and discussion 54

3.3.1 Load vs pull-out displacement responses and failure modes 54

3.3.2 Load vs tangential tensile strain responses of CFRP tendons 57

3.3.3 Tangential tensile strain distributions in steel and CFRP confinements 59

3.3.4 Longitudinal compressive strains in unconfined grout 60

3.3.5 Longitudinal compressive strain distributions in steel and CFRP confinements 62

3.3.6 Confinement efficiency 62

3.4 Conclusions..65

4 Pull-out behavior of CFRP ground anchors with two-strap ends 69

4.1 Introduction..71

4.2 Experimental program 73

4.2.1 CFRP tendon with strap ends 73

4.2.2 CFRP anchor 74

4.2.3 CFRP pull-out anchor specimens 75

4.2.4 Experimental set-up and instrumentation 77

4.3 Results and discussion 79

4.3.1 Load vs pull-out displacement responses and failure modes 79

4.3.2 Load vs tensile strains in CFRP tendons 81

4.3.3 CFRP tendons – grout load transfer...83

4.3.4 Tangential tensile strains in CFRP rings 84

4.3.5 Strain distributions in steel tubes 86

4.3.6 Failure sequence in embedded straps..88

4.3.7 Confined grout behavior 89

4.4 Conclusions..91

5 Load-transfer mechanisms in CFRP ground anchors with multi-strap ends 95

5.1 Introduction....97
5.2 CFRP strap anchor description....99
  5.2.1 One-strap anchor with curved strap geometry (1C7) 99
  5.2.2 One-strap anchor with straight strap geometry (1S7)....101
  5.2.3 Two-strap anchors with straight strap geometry (2S5/10) 101
  5.2.4 CFRP and grout material properties 102
5.3 Pull-out experiments and FE modeling 102
  5.3.1 Pull-out experiments on one- and two-strap anchors....102
  5.3.2 FE modeling of pull-out experiments on one-strap anchors....103
  5.3.3 FE model validation....105
5.4 Influence of strap geometry on load-transfer mechanism....107
5.5 Load-transfer mechanism in multi-strap anchors....110
  5.5.1 Influence of strap configuration on global pull-out behavior 110
  5.5.2 Empirical model of load-transfer diagram for multi-strap anchors....111
  5.5.3 Design of three-strap anchor 116
5.6 Conclusions....118

6 Experimental and numerical investigation of tensile behavior of non-laminated CFRP straps....121

6.1 Introduction....123
6.2 Experimental program 125
  6.2.1 Specimen description 125
  6.2.2 Experimental set-up and instrumentation 126
6.3 Experimental Results....128
  6.3.1 Load vs strap elongation responses and failure modes 128
  6.3.2 DIC displacements and longitudinal strains of individual layers 129
  6.3.3 Longitudinal strain distribution in fusion-bonding part....131
6.4 Finite element modeling and validation....132
  6.4.1 FE model description 132
  6.4.2 Influence of friction on vertical displacements and longitudinal strains 134
  6.4.3 FE model validation....135

6.5 Discussion 136
6.5.1 Longitudinal strains and stresses in curved strap segments 136
6.5.2 Vertical displacements and longitudinal strains in straight strap segments 139
6.5.3 Failure mechanism 139
6.6 Conclusions 141
7 Numerical and analytical investigation of tensile behavior of non-laminated and laminated CFRP straps 145
7.1 Introduction 147
7.2 FE modeling of non-laminated straps 148
7.2.1 Description of 2D FE model 148
7.2.2 Validation of 2D FE model 152
7.2.3 Discussion of modeling results 154
7.3 Analytical and FE modeling of laminated straps 158
7.3.1 Review of existing studies in literature 159
7.3.2 Analytical modeling 160
7.3.3 Description of 2D FE model 161
7.3.4 Validation of FE and analytical models 162
7.3.5 Modified analytical model 163
7.4 Comparison of non-laminated and laminated straps 164
7.4.1 Influence of interface friction and orthotropic material properties 164
7.4.2 Strain distribution in thickness direction at flank 165
7.4.3 Load-bearing efficiency 166
7.4.4 Practical application aspects 167
7.5 Conclusions 168
8 Conclusions and future work 171
8.1 Summary of conclusions 173
8.1.1 Evaluation of cement- and resin-based grout materials 173
8.1.2 Pull-out behavior of one-strap anchor 173
8.1.3 Pull-out behavior of two-strap anchor 174
8.1.4 Load-transfer mechanism in multi-strap anchor 174
8.1.5 Tensile behavior of non-laminated and laminated straps 175

8.2 Original contributions 176
8.3 Future work 177
8.3.1 Shear performance of multi-strap CFRP ground anchors 177
8.3.2 Creep and relaxation performance of multi-strap CFRP ground anchors 178
8.3.3 Fatigue performance of multi-strap CFRP ground anchors 178
8.3.4 Durability performance of multi-strap CFRP ground anchors 178
8.3.5 Optimization of tendon design for coil requirement 179
Annexes 181
A Evaluation of grout materials for CFRP ground anchors with strap ends 181
B Pull-out behavior of CFRP single-strap ground anchors 187
C Pull-out behavior of CFRP ground anchors with two-strap ends 195
D Design of CFRP tendons with three-strap ends 205
E Pull-out behavior of CFRP ground anchors using strand tendons 215
Curriculum Vitae 227

List of Tables

Table 1.1	Summary of commercially available FRP tendons	4
Table 2.1	Overview of experimental parameters and designations	21
Table 2.2	Overview of experimental matrix	22-23
Table 2.3	Elastic moduli and Poisson’s ratios	27
Table 3.1	Overview of experimental series and results	50
Table 3.2	Summary of uniaxial compression experiments on grout cylinders	52
Table 3.3	Deformation and stiffness calculation	55
Table 3.4	Calculation of confinement effectiveness coefficient k_1 in anchor C380-1	64
Table 3.5	Estimation of confined compressive grout strength	64
Table 4.1	Summary of experimental results	75
Table 4.2	Calculation of confinement effectiveness coefficient k_1 at 1389 kN in anchor ST5	90
Table 4.3	Estimation of confined compressive strength of grout in anchor ST5	90
Table 5.1	Overview of denominations and experimental matrix	99
Table 5.2	Calculated parameters for load-transfer diagrams for 2S5/10 anchors	115
Table 5.3	Calculated parameters for load-transfer diagrams for anchor 3S	118
Table 6.1	Summary of experimental results	128
Table 7.1	Comparison of non-laminated and laminated straps	166

List of Figures

Fig. 1.1	Ground anchor applications	3
Fig. 1.2	Typical ground anchor configuration	4
Fig. 1.3	FRP tendons: (a) Technora AFRP tendon; (b) CFCC CFRP tendon; (c) CFCC tendons in ground anchor applications	5
Fig. 1.4	NM system applied for slope stabilization: (a) in high-temperature environment; (b) in mountain areas with strongly acid environment	5
Fig. 1.5	FRP strap anchorage: (a) non-laminated straps with inner free end; (b) laminated straps in wedge shape	6
Fig. 1.6	Permanent post-tensioned CFRP ground anchor with multi-strap anchor head on ground side	7
Fig. 1.7	Thesis organization	12
Fig. 2.1	Experimental set-up and instrumentation in (a) Program I (specimen M2-10, cement-grout); (b) Program III (M4-1, epoxy-grout)	24
Fig. 2.2	Compressive stress vs strain curves of M1 specimens	28
Fig. 2.3	Compressive stress vs strain curves of M2 specimens	28
Fig. 2.4	Compressive stress vs strain curves of M3 and M4 specimens	28
Fig. 2.5	Comparison of compressive stress vs axial strain curves of all materials	29
Fig. 2.6	Normalized compressive stress vs axial strain curves of all specimens	30
Fig. 2.7	Compressive stress vs volumetric strain of selected specimens	31
Fig. 2.8	Calibration of compressive stress vs axial strain model for M1 specimens	32
Fig. 2.9	Calibration of compressive stress vs axial strain model for M2 specimens	32
Fig. 2.10	Calibration of compressive stress vs axial strain model for M3 and M4 specimens	32
Fig. 2.11	CFRP ground anchor experiments: (a) anchor specimen C200; (b) anchor heads of C380 and C200 with different CFRP confinement ring arrangements	33
Fig. 2.12	Compressive stress vs strain curves for selected grout (M2) of anchor heads	34
Fig. 2.13	FE model of C380 CFRP anchor head	35
Fig. 2.14	Tensile stress vs crack opening model	36
Fig. 2.15	Bilinear bond-slip law for CFRP/grout interface	37

Fig. 2.16	Comparison of experimental and calibrated numerical load vs tangential tensile strain responses of strap end (C4) in anchor head C200	38
Fig. 2.17	Comparison of experimental and numerical load vs pull-out displacement responses in anchor head C200	38
Fig. 2.18	Progressive debonding along CFRP tendon and grout interface in anchor head C200	39
Fig. 2.19	Failure analysis of unconfined grout at peak load (250 kN): (a) crack pattern in experiment; (b) distribution of equivalent plastic tensile strain (PEEQT, for *D*=0.1)	39
Fig. 2.20	Comparison of experimental and numerical load vs pull-out displacement responses in anchor heads C380-1/2	40
Fig. 2.21	Comparison of experimental and numerical load vs tangential tensile strain responses of strap end (C4) in anchor head C380-1	40
Fig. 2.22	Comparison of experimental and numerical load vs compressive strain responses on unconfined grout (G3) in anchor heads C380-1/2	41
Fig. 2.23	Comparison of failure mode in anchor head C380-2: (a) experiment; (b) distribution of PEEQT at peak load in FE model (*D*=1.0)	41
Fig. 3.1	Permanent prestressed CFRP ground anchor with multi-strap anchor head on ground side	48
Fig. 3.2	CFRP one-strap tendon specimen (without high-strength grout cylinder on left ground side), (a) dimensions in [mm] (not to scale), (b) photo	49
Fig. 3.3	Configurations of CFRP anchor heads on ground side	50
Fig. 3.4	One-strap anchor specimens	51
Fig. 3.5	Experimental set-up and instrumentation layout	53
Fig. 3.6	Load vs pull-out displacement responses (failure cycle)	55
Fig. 3.7	Failure mode of anchor S605: (a) cut view of ground-side anchor head; (b) rupture of embedded strap at gage location; (c) strap delamination at gage location	56
Fig. 3.8	Failure mode of anchor C380-2: (a) double-cone failure of unconfined grout; (b) similar failure mode in uniaxial compression experiment G1; (c) undamaged strap in confined part	56
Fig. 3.9	Failure mode of anchor C200: (a) vertical grout crack at around 250 kN; (b) splitting failure of unconfined grout around embedded strap	56
Fig. 3.10	Load vs tangential tensile strain responses of air-side straps	58
Fig. 3.11	Load vs tangential tensile strain responses of embedded straps	58

Fig. 3.12	Tangential tensile strain distributions along steel tube in S605 at different load levels, parallel to strap plane	59
Fig. 3.13	Tangential tensile strain distributions along steel tube in C380-1 at different load levels: (a) parallel to strap plan; (a) perpendicular to strap plane	60
Fig. 3.14	Tangential tensile strain distributions along CFRP ring in C200 at different load levels: (a) parallel to strap plan; (a) perpendicular to strap plane	60
Fig. 3.15	Load vs compressive strain responses of unconfined grout	61
Fig. 3.16	Compressive strain distribution along length of unconfined grout in C380-1 at different load levels	61
Fig. 3.17	Load vs longitudinal compressive strain responses in steel tube and CFRP rings	62
Fig. 3.18	Activation sequence of confinement along CFRP ring in C380-2 derived from tangential tensile strains	63
Fig. 4.1	Prestressed and permanent CFRP ground anchor with multi-strap ends	72
Fig. 4.2	CFRP two-strap tendon: (a) schematic (dimensions in [mm]); (b) photo	73
Fig. 4.3	CFRP two-strap anchor head: (a) schematic (dimensions in [mm]); (b) photo	74
Fig. 4.4	CFRP two-strap anchor specimen: (a) schematic (dimensions in [mm]); (b) photo	75
Fig. 4.5	Fabrication of two-strap anchor specimens (only anchor body is shown): (a) mold with corrugated surface; (b) installation of CFRP tendon and rings; (c) anchor head after casting of high-strength mortar	76
Fig. 4.6	Experimental set-up (dimensions in [mm], DIC random speckle pattern on tube)	77
Fig. 4.7	Instrumentation layout (dimensions in [mm])	78
Fig. 4.8	Load vs pull-out displacement responses	79
Fig. 4.9	Failure modes: (a) cut view of anchor ST10-1; details in (b) ST10-1, (c) ST10-2, (d) ST5	80
Fig. 4.10	Load vs tensile strain responses of air-side strap: (a) anchor ST10-2; (b) anchor ST5	81
Fig. 4.11	Load vs tensile strain responses of ground-side large strap: (a) along straight segment; (b) at strap end	82
Fig. 4.12	Load vs strain responses of ground-side small strap: (a) along straight segment; (b) at strap end	82
Fig. 4.13	Load transfer along embedded straps at 500 and 1389 kN in anchor ST5	84

Fig. 4.14 Load vs tangential strain responses in CFRP rings at: (a) division point; (b) small strap location; (c) large strap location 85

Fig. 4.15 Longitudinal strain distributions along steel tube in plane perpendicular to strap plane, in anchor ST5 at different load levels 86

Fig. 4.16 Longitudinal strain distribution along 700-mm-long upper part of steel tube at 1300 kN measured by DIC in anchor ST5 87

Fig. 4.17 Tangential strain distributions along steel tube in ST5 at different load levels: (a) perpendicular to strap plane; (b) parallel to strap plane 88

Fig. 5.1 CFRP tendons: (a) 1C7 (b) 1S7, (c) 2S5/10 (dimensions in [mm]) 100

Fig. 5.2 CFRP anchor specimens: (a) 1C7 (b) 1S7, (c) 2S5/10 (dimensions in [mm]) 100

Fig. 5.3 FE models of 1S7 and 1C7 anchors 103

Fig. 5.4 Experimental and numerical load vs tangential tensile strain responses of embedded strap end (C4/13) in 1S7 and 1C7 anchors 105

Fig. 5.5 Calibrated cohesive laws for tendon/grout and strap/cross-beam interfaces in FE models of 1S7 and 1C7 anchors 105

Fig. 5.6 Experimental and numerical load vs pull-out displacement responses of 1S7 and 1C7 anchors 106

Fig. 5.7 Tangential strain distribution along length of steel tube at 500 kN in 1S7 and 1C7 anchors 106

Fig. 5.8 Failure modes: (a) 1S7 (experiment); (b) 1S7 (FE model results at $F_{ult,2}$); (c) 2S10 (experiment) 107

Fig. 5.9 Load vs tensile strain responses of air-side strap of 1S7 and 1C7 anchors 108

Fig. 5.10 Comparison of load-transfer diagrams along embedded strap at 497 kN obtained from FE models of 1S7 and 1C7 anchors 109

Fig. 5.11 Load transfer along embedded strap in anchor 1S7 at different load levels 110

Fig. 5.12 Normalized load vs normalized pull-out displacement responses of 1S7 and 2S5/10 anchors 111

Fig. 5.13 Normalized load vs tensile strains of air-side strap of 1S7 and 2S5/10 anchors 111

Fig. 5.14 Frictional transfer rate vs applied strap load in 1S7 and 2S5/10 anchors 112

Fig. 5.15 Division load drop ratio vs strap load in 1S7 and 2S5/10 anchors at confinement level of $E_{rock,4}$ 114

Fig. 5.16 Derived load-transfer diagrams for 2S5/10 anchors 116

Fig. 5.17 Anchor 3S: (a) CFRP tendon; (b) anchor head 117

Fig. 5.18 Calculated load-transfer diagrams at 1250 and 2500 kN for anchor 3S 118

Fig. 6.1 Schematic of: (a) laminated strap; (b) non-laminated strap 123

Fig. 6.2 Application of non-laminated CFRP straps for punching shear strengthening of concrete slabs: a) flexible strap component; b) installed and prestressed strap 124

Fig. 6.3 Non-laminated strap: (a) schematic (dimensions in [mm]); (b) slack strap 125

Fig. 6.4 Experimental set-up and instrumentation layout (dimensions in [mm]) 126

Fig. 6.5 Lateral strap movement in DIC images taken at 0.0, 2.5, 6.4 and 29.2 kN on strap S4 128

Fig. 6.6 Load vs strap elongation responses (a) and failure modes: (b) tape rupture (S6); (c) fusion-bond (S5) 129

Fig. 6.7 Load vs DIC displacement responses of strap S5 layers on (a) free-end side (loaded to 50 kN) and (b) bond-end side (loaded to failure), experimental and numerical results 130

Fig. 6.8 Relative displacements between strap S5 layers on (a) free-end side and (b) bond-end side 130

Fig. 6.9 Load vs longitudinal strain responses of strap S5 layers on (a) free-end side (loaded to 50 kN) and (b) bond-end side (loaded to failure), experimental and numerical results 131

Fig. 6.10 Experimental set-up and instrumentation layout of fusion-bonding area of strap S6 (dimensions in [mm]) 132

Fig. 6.11 Strain distribution along fusion-bonding length of strap S6 (P1-P11 refer to Fig. 6.10) 132

Fig. 6.12 FE model of tensile experiments (dimensions in [mm]) 133

Fig. 6.13 Influence of μ on vertical layer displacements of straight strap segments from 5.2 to 48.8 kN (a) on free-end side, (b) on bond-end side ($\mu=\mu_{steel/CFRP}=\mu_{CFRP/CFRP}$, γ_i=0.25 mm) 134

Fig. 6.14 Influence of μ on layer longitudinal strains of straight strap segments from 5.2 to 48.8 kN, (a) on free-end side, (b) on bond-end side ($\mu=\mu_{steel/CFRP}=\mu_{CFRP/CFRP}$, γ_i=0.25mm) 135

Fig. 6.15 Comparison of layer displacements and longitudinal strains of strap S5 at 48.8 kN, experimental and numerical results 136

Fig. 6.16 Longitudinal strain distribution in layer L_1 around bottom pin at different loads ($\mu_{CFRP/CFRP}=\mu_{steel/CFRP}$=0.2 and γ_i=0.25) 137

Fig. 6.17 Longitudinal strain distribution in layer L_1 around bottom pin at 99.3 kN obtained from FE models using different μ and γ_i values 137

Fig. 6.18 Longitudinal stress distribution in two curved segments at 99.3 kN obtained from FE models using different μ and γ_i values 138

Fig. 6.19 Load vs longitudinal strain responses of strap S4 on bond-end side 140

Fig. 6.20 Status of DIC measuring areas at different load levels in strap S4 140

Fig. 6.21 Transversal strain concentrations in middle along tape length at 60.2 kN 141

Fig. 7.1 FE model of non-laminated straps (dimensions in [mm]) 150

Fig. 7.2 Load vs longitudinal strain responses of three layers on bond-end side in strap N7: experimental, previous 3D and new 2D FE results 152

Fig. 7.3 Load vs longitudinal strain responses at flank of L_1 and L_{20} layers on bond-end side in strap N20 using contact and horizontal constraint methods in straight segments 153

Fig. 7.4 Load vs strap elongation responses between two pins in N7–N70 straps 154

Fig. 7.5 First peak (F_{1P}) and ultimate (F_{ult}) loads and ratio ($\Delta F/F_{1P}$) vs layer number 154

Fig. 7.6 Load vs tensile stress responses at flank in L_1–L_5 layers on bond-end side in strap N70 155

Fig. 7.7 Stress distribution among layers on (a) free-end and (b) bond-end sides at first peak load 156

Fig. 7.8 Load-bearing efficiency vs radius ratio in non-laminated straps, experimental and numerical results 157

Fig. 7.9 Load-bearing efficiency vs radius ratio in laminated straps: experimental, analytical and numerical results 158

Fig. 7.10 FE model of laminated straps (dimensions in [mm]) 161

Fig. 7.11 Tangential strain distributions in thickness direction at flank in M7–M70 straps with μ=0.2 at estimated ultimate loads 162

Fig. 7.12 Comparison of modified analytical model with numerical and experimental results 163

Fig. 7.13 Longitudinal strain distribution at flank in N70 and M70 straps at 650 kN (μ=0.2) 165

Fig. 7.14 Load-bearing efficiency vs radius ratio for non-laminated and laminated straps (μ=0.2) 165

Fig. 8.1 Shear deformation due to unstable block sliding 177

1.

Introduction

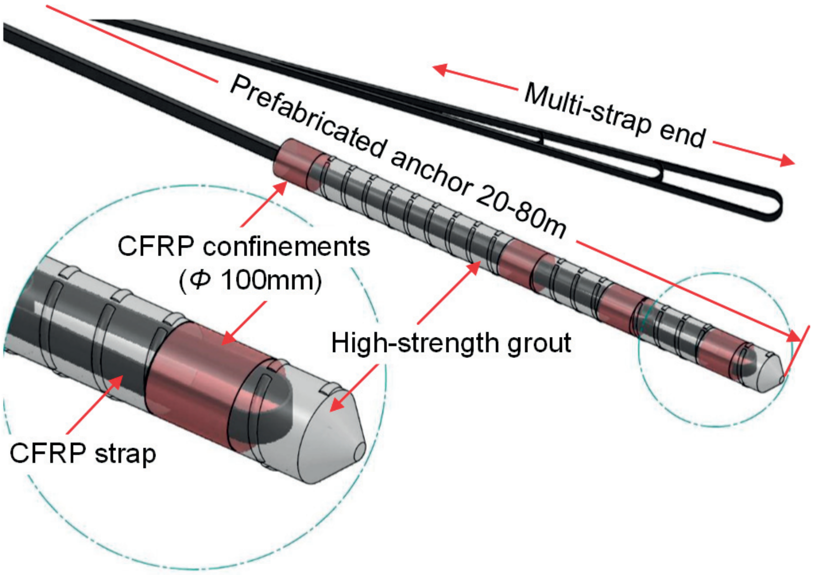
Multi-strap end
Prefabricated anchor 20-80m
CFRP confinements
(Φ 100mm)
High-strength grout
CFRP strap

1.1 Context and motivations

Ground anchors have been widely used for the stabilization of different structures such as retaining walls, towers, dams, underground structures and slopes, as shown in Fig. 1.1 [1]. The strengthening of dams using prestressed rock anchors has in particular received great attention since its first application in the Cheurfas dam in Algeria in 1934 [2, 3]. A total of approximately 470 dam anchoring projects in North America have been recorded during the period 1962–2012 [4].

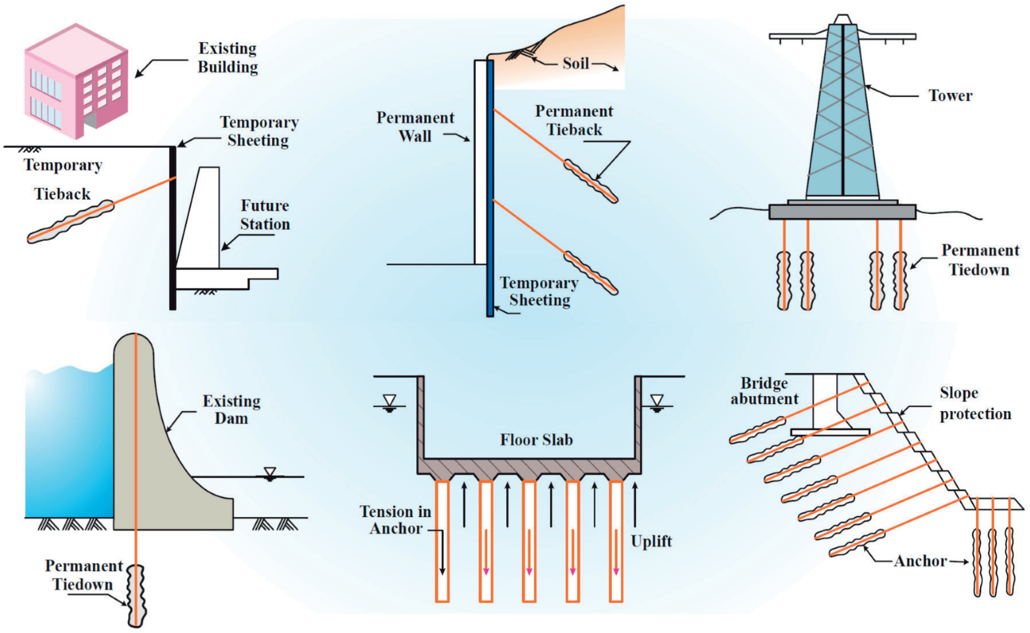
Existing Building
Temporary Sheeting
Temporary Tieback
Future Station
Soil
Permanent Wall
Permanent Tieback
Temporary Sheeting
Tower
Permanent Tiedown
Existing Dam
Permanent Tiedown
Floor Slab
Tension in Anchor
Uplift
Bridge abutment
Slope protection
Anchor

Fig. 1.1: Ground anchor applications [1]

A typical ground anchor usually consists of an air-side anchor head and a tendon which – after the free length part – is anchored into the soil or rock medium in a 3–10-m-long grouted anchoring length, as shown in Fig. 1.2. In conventional steel ground anchors, the tendons are generally vulnerable to galvanic corrosion. In order to prevent catastrophic failure caused by the corrosion problem as presented in [5, 6], different protection systems for the steel components, depending on environmental conditions, are generally prescribed in standards such as EN1537 [7] and periodical inspections are required. However, even the application of double protection systems with integrated electrical resistance measurement cannot always guarantee the intactness of an installed anchor since the interpretation of the measurement results is not always clear.

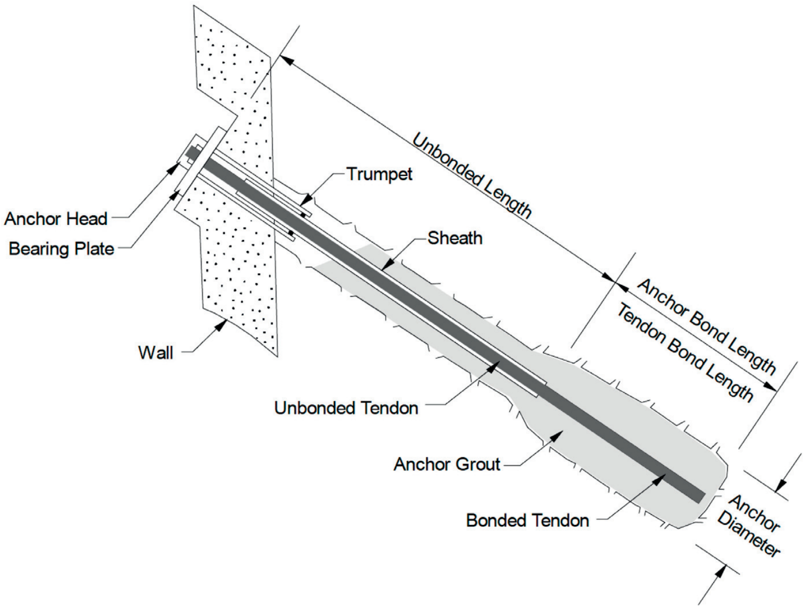
Unbonded Length
Trumpet
Anchor Head
Bearing Plate
Sheath
Anchor Bond Length
Tendon Bond Length
Wall
Unbonded Tendon
Anchor Grout
Bonded Tendon
Anchor Diameter

Fig. 1.2: Typical ground anchor configuration [8]

Instead of solving the durability problem with expensive and not always reliable protection systems, the replacement of steel by corrosion-resistant fiber-reinforced polymers (FRPs) has evolved as an alternative solution [9]. Different types of aramid (Arapree, FiBRA and Technora) and carbon (CFCC, Leadline and NACC) FRP tendons have been developed and commercialized, as shown in Table 1.1 [5, 10, 11]; the tendons can be in rod and flat-plate shapes like Technora (see Fig. 1.3 (a)) or twisted in strands like CFCC (see Fig. 1.3 (b)). However, these tendons, except CFCC, were primarily designed for the pre- and post-tensioning of concrete structures [11-13] and no frequent applications in ground anchors have been reported.

Table 1.1: Summary of commercially available FRP tendons [5, 10, 11]

Product	Material	Diameter (mm)	Anchorage methods	Country
Arapree	AFRP	5, 7.5	Wedge anchor / bonded anchor using cement mortar	Netherlands
FiBRA	AFRP	10.4, 12.7, 14.7	Wedge anchor / resin-cone anchor	Japan
Technora	AFRP	3, 4, 6, 7.4, 8	Wedge anchor / bonded anchor	Japan
CFCC	CFRP	1.5, 5, 5–40 (7–37 wire strands)	Five different types of anchors	Japan
Leadline	CFRP	3, 5, 8, 10, 12, 17	Wedge anchor / bonded anchor using cement grout	Japan
NACC	CFRP	15–35 (7–37 wire strands)	Wedge anchor / bonded anchor using cement grout	Japan

The CFCC tendons, developed by Tokyo Rope in Japan, have been integrated into the NM (New Material) ground anchor system and applied in around 80 projects in Japan between 1993–2015 [12], representing a total length of 336 km tendons, as shown in Fig. 1.3 (c). In the NM system, the CFCC tendons, composed of two to six Φ12.5-mm strands consisting of seven twisted wires each, can be post-tensioned to maximum 60% of the ultimate load (350–1000 kN) [12]. Because of the excellent corrosion resistance and high strength-to-weight ratio, the NM system exhibited considerable advantages over conventional steel anchors, particularly in a high-temperature (60–100°C) or strong-acid (pH 3–4) environment and in mountain or remote areas where accessibility is limited; two corresponding application examples are shown in Fig. 1.4 (a) and (b) respectively. Another application of CFRP ground anchors for the Aizhai suspension bridge in China was reported in [14], where two CFRP cables, assembled from 9/20 tendons of 12-mm diameter with load-bearing capacities of 1670 and 4100 kN respectively, were developed.

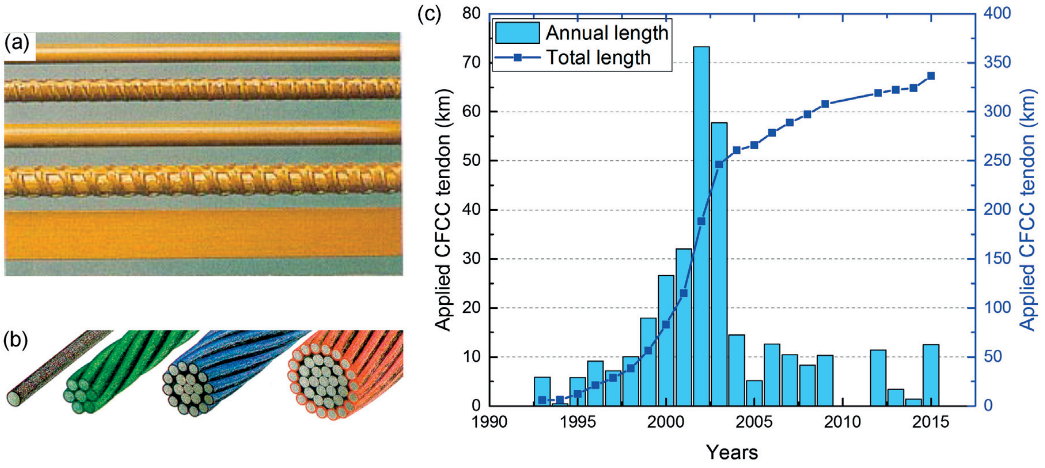

Fig. 1.3: FRP tendons: (a) Technora AFRP tendon; (b) CFCC CFRP tendon; (c) CFCC tendons in ground anchor applications (data from [12], no data available for 2010–2011)

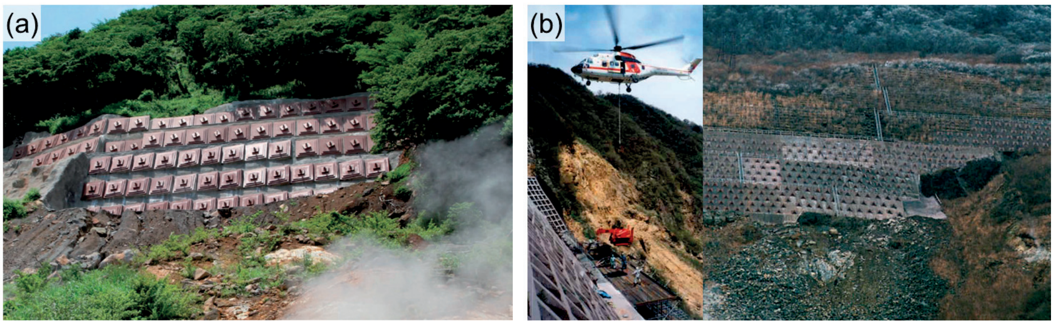

Fig. 1.4: NM system applied for slope stabilization: (a) in high-temperature environment; (b) in mountain areas with strongly acid environment [12]

For the above-mentioned FRP tendons, mechanical or bonded anchors, conceptually similar to steel tendons [15], are commonly used (see Table 1.1). However, the anisotropic material properties of FRP, and CFRP in particular, may cause premature failure in the anchorage zone due to high shear and through-thickness stress concentrations. One possible solution to avoid such concentrations was provided in [16] by using a gradient load-transfer medium with varying elastic modulus; this has already been applied in a 124-m-span cable-stayed bridge in Switzerland. Another approach with a similar concept was developed by continuously winding fibers into a conical-shaped medium, where the gradient load transfer was realized by varying the fiber directions from 45 to 90° in three different parts [17]. However, the fabrication of these anchors is not simple and they are expensive.

A simpler and much more material-tailored anchoring method, different from the above-mentioned technique for steel tendons, is based on strap ends, where CFRP tendons can be simply anchored using steel pins [18, 19], as shown in Fig. 1.5. Two concepts exist depending on the possibility of relative displacements between the constituent tape layers: (1) non-laminated [18, 20] and laminated [21] straps. Both straps are manufactured by winding continuous CFRP tapes around two steel pins. However, in the former, only the outermost layer is fusion bonded to the next outermost layer, while the innermost layer with a free end is anchored only by friction at the pin/strap interface (see Fig. 1.5(a)); the remaining layers are non-laminated and relative displacements between individual layers can thus occur. This anchorage method has already been used for the strengthening of concrete flat slabs [22], box girders [23], timber roofs [24] and masonry structures [25]. In contrast, in laminated straps, the layers are fully laminated and no relative displacements can thus occur; the straps are usually manufactured into a wedge shape, as shown in Fig. 1.5(b). This anchorage method has also been used in different applications such as prestressed tendons in concrete structures [26] and rigging systems for yachts [27].

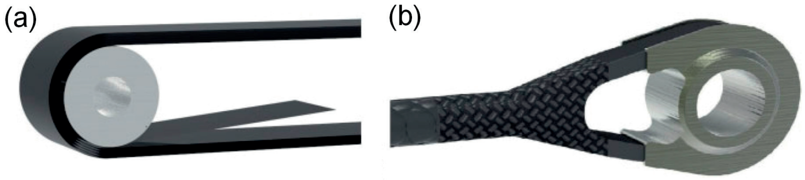

Fig. 1.5: FRP strap anchorage: (a) non-laminated straps with inner free end; (b) laminated straps in wedge shape [19]

Research has been conducted to investigate the tensile behavior of both non-laminated [18, 20] and laminated [18, 28] straps. In non-laminated straps, the influence of different parameters – including the constituent materials, interface friction, layer number and outer to inner radius ratio – on their tensile behavior was first investigated on straps composed of 1–10 layers [18]. A subsequent series of experiments on straps with up to 70 layers was conducted to further investigate the influence of the layer number and radius ratio [20]. However, no numerical or analytical model, particularly for straps with a high layer number, has been developed and the load-bearing mechanism is thus not yet clearly understood. For laminated straps, tensile experiments were conducted on 45 CFRP straps with 5–15 layers, based on which existing analytical models, developed in [29, 30], were used to predict the load-bearing capacity of the straps [18]; however, no good agreement with experimental results has been achieved. Furthermore, the stress distribution in the semicircular parts of the straps was investigated in [28, 31]; however, no analytical model has been developed that is able to predict the load-bearing capacity of CFRP straps well.

The purpose of this research is to develop a new application of the strap anchorage method for permanent post-tensioned CFRP ground anchors with a capacity of at least 2500 kN. The CFRP tendon comprises a multi-strap anchor head on the ground side, in which the CFRP strap end is prefabricated in a lightweight high-strength grout cylinder confined with CFRP rings, as shown in Fig. 1.6; on the air side, a pin-loaded anchorage system as presented in [22] is used, replacing the conventional anchor head shown in Fig. 1.2. The ground anchor with the prefabricated anchor head can be 20–80 m long, coiled and transported to the construction site, inserted into the borehole and anchored by injecting fresh standard (normal-strength) grout; the anchor can be post-tensioned to 60% of the design load.

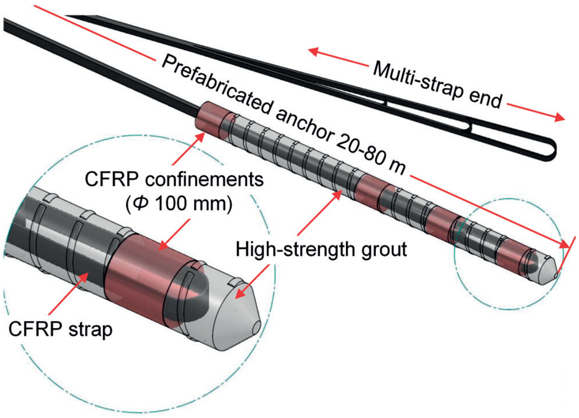

Fig. 1.6: Permanent post-tensioned CFRP ground anchor with multi-strap anchor head on ground side

In the multi-strap CFRP ground anchor, potential failure could occur in (1) the grout parts and (2) the CFRP strap ends, not taking into account the possible bond failure at the grout/ground interface. The CFRP confinement rings deviate the spreading forces – occurring at the strap ends and at the transition from the strap to the rod segment – into the cylinder's axial direction; thus, the grout cylinder is stepwise axially loaded by the axial components of the spreading forces. In order to conduct failure analyses of CFRP ground anchors with integrated grout failure criteria, the complete stress vs strain responses of the grouts, including the softening branch, were required. However, despite a large amount of existing research on the strain softening behavior of concrete [32, 33] and rock [34, 35], similar work on grout materials, including cement- and resin-based grouts, is rare. Furthermore, failure analyses were also needed for the CFRP strap ends. The laminated strap anchorage method was applied in the multi-strap CFRP ground anchor; the application of the non-laminated method was however also taken into account, since no explicit comparison between non-laminated and laminated straps, from both the mechanical and practical points of view, has been made.

1.2 Objectives

The aim of this research is to develop a permanent post-tensioned CFRP ground anchor with strap ends. In order to achieve this, the following objectives have been defined:

1. Evaluate cement- and resin-based grout materials for applications in CFRP ground anchors with strap ends;
2. Characterize the pull-out behavior of CFRP ground anchor heads with one-strap ends in rock and soil applications;
3. Characterize the pull-out behavior of CFRP ground anchors with two-strap ends in different rock applications;
4. Develop models to derive the load-transfer diagram along the embedded straps for CFRP ground anchors with multi-strap ends;
5. Develop models to predict the load-bearing capacity of non-laminated and laminated straps.

1.3 Methodology

To achieve these objectives, the following methodology was adopted:

For objective 1,

1) Uniaxial compression experiments on cement- and resin-based grout materials to obtain complete stress vs strain curves including the softening branch;
2) Analytical and numerical modeling of the compressive stress vs strain behavior of the grouts using existing concrete models.

For objective 2,

1) Experimental investigation of the pull-out behavior of CFRP one-strap ground anchor heads with different confinements, simulating their applications in rock and soil.

For objective 3,

1) Experimental investigation of the pull-out behavior of two-strap CFRP ground anchors with different confinement levels, simulating their applications in different rock types.

For objective 4,

1) Numerical modeling of the pull-out behavior of CFRP one-strap ground anchors with different strap geometries;
2) Development of an empirical model for deriving the load-transfer diagram along embedded straps for multi-strap CFRP anchors.

For objective 5,

1) Experimental and numerical investigations of the tensile behavior of non-laminated CFRP straps with seven layers;
2) Numerical investigation of non-laminated CFRP straps with up to 70 layers and development of empirical models to predict the load-bearing capacity of straps with up to 100 layers;
3) Numerical and analytical investigations of the tensile behavior of laminated CFRP straps with up to 100 layers and development of new analytical models for predicting the load-bearing capacity of these straps.

1.4 Thesis organization

The research work presented in this thesis is divided into three parts: (1) evaluation of cement- and resin-based grout materials, presented in Chapter 2, (2) investigation of the pull-out behavior of CFRP ground anchors with strap ends, presented in Chapters 3–5, and (3) investigation of the tensile behavior of non-laminated and laminated CFRP straps, presented in Chapters 6–7. A summary of each part and the associated chapters is as follows:

In part (1), i.e. Chapter 2, an evaluation of four cement- and resin-based grout materials for applications in CFRP ground anchors with strap ends is presented. The evaluation focused on their uniaxial compressive stress vs strain behavior, since grout in CFRP strap ground anchors is mainly subjected to axial loads. Appropriate loading-control methods and boundary conditions were first investigated to obtain the softening responses of the grouts. The Sargin concrete model was applied to model the compressive stress vs strain behavior of the investigated grouts; a validation concerning this applicability is presented by comparing the FE results of the CFRP ground anchor head and implemented grout model with the experimental results presented in Chapter 3. This chapter corresponds to **Paper 1** in the list of publications in Section 1.5 below.

In part (2), experimental and numerical investigations of the pull-out behavior of CFRP ground anchors with one- and two-strap ends are presented, based on which an empirical model for deriving the load-transfer diagram along the embedded straps in multi-strap anchors was developed.

In Chapter 3, an extensive experimental investigation of the pull-out behavior of CFRP ground anchors with one-strap ends on the ground side is presented. The ground-side one-strap end was embedded in a high-strength grout cylinder, i.e. an anchor head. The anchor heads were confined with different confinements, i.e. with and without a steel tube, simulating their direct applications in rock and soil. In the soil application, additional CFRP confinement rings, with different lengths and positions, were applied to prevent premature grout failure in the strap region. The influence of the confinement level and the length and position of the CFRP rings on the failure mode of the anchor heads and the load transfer from the strap to the high-strength grout cylinder was investigated. This chapter corresponds to **Paper 2** in the list of publications in Section 1.5 below.

In Chapter 4, an extensive experimental investigation of the pull-out behavior of CFRP ground anchors with two-strap ends on the ground side is presented. The ground-side two-strap end was prefabricated in a lightweight conical anchor body of high-strength grout, inserted into a steel tube and anchored with normal-strength grout. Steel tubes with different thicknesses were applied to simulate the anchor applications in different rock types. An evaluation of the two-strap anchor design, particularly the desired anchor capacity and failure mode, is presented. The influence of the confinement level on the load transfer from the embedded straps to the surrounding grouts was investigated, based on which a first load-transfer diagram derived along the embedded straps is presented. This chapter corresponds to **Paper 3** in the list of publications in Section 1.5 below.

In Chapter 5, the experimental results on the one- and two-strap anchors presented in Chapters 3 and 4, as well as new results obtained for a one-strap anchor with different strap geometry, were systematically analyzed. FE models were also developed to simulate the pull-out behavior of the one-strap anchors. Based on these experimental and numerical results, the influence of the strap geometry and strap number on the global pull-out and local load-transfer behavior of multi-strap anchors was investigated. For multi-strap anchors in rock applications, an empirical model to derive the load-transfer diagram along the embedded straps is presented. A subsequent application of this model to a new three-strap anchor with a targeted capacity of 2500 kN is also presented. This chapter corresponds to **Paper 4** in the list of publications in Section 1.5 below.

Part (3) deals with the tensile behavior of straps since strap rupture, resulting in the final anchor failure, was observed in the one- and two-strap anchors. Both non-laminated and laminated straps were investigated in order to make an explicit comparison concerning their mechanical behavior and practical applications.

In Chapter 6, experimental and numerical investigations of the tensile behavior of seven-layer non-laminated CFRP straps are presented. The failure mechanism of the straps and vertical displacement and longitudinal strain distributions among the constituent tape layers were investigated. The influence of the frictional parameters in the FE model on the simulated tensile behavior of the straps was also studied. This chapter corresponds to **Paper 5** in the list of publications in Section 1.5 below.

In Chapter 7, extensive numerical and analytical investigations of the tensile behavior of non-laminated and laminated straps with up to 100 layers are presented. The influence of layer number on (1) the failure mode of the non-laminated straps and (2) the strain distributions among the constituent tape layers of both non-laminated and laminated straps were investigated. For the non-laminated straps, an empirical model for predicting the load-bearing capacity of straps with up to 100 layers is presented. For the laminated straps, an analytical model, taking into account the strap anisotropy and friction at the strap-pin interfaces, was developed to model the relationship between the load-bearing efficiency and the strap radius ratio. An explicit comparison between the non-laminated and laminated straps, from both the mechanical and practical points of view, is presented. This chapter corresponds to **Paper 6** in the list of publications in Section 1.5 below.

In Chapter 8, general conclusions concerning this research are presented with emphasis on the contributions made to the scientific and industrial communities. Furthermore, suggestions for future research areas in this field are given. The organization of the thesis is shown in Fig. 1.7.

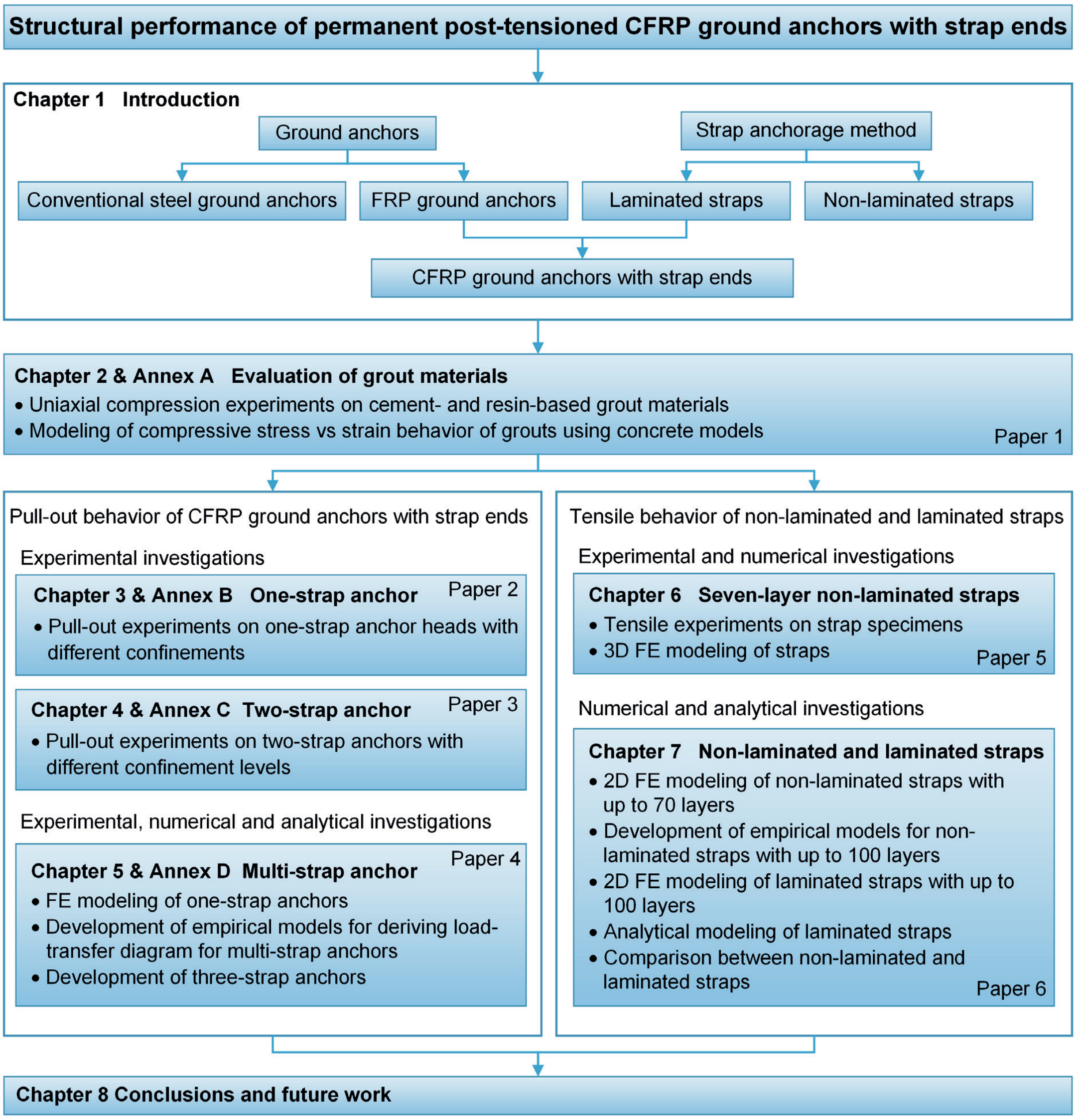
Structural performance of permanent post-tensioned CFRP ground anchors with strap ends
Chapter 1 Introduction
Ground anchors
Strap anchorage method
Conventional steel ground anchors
FRP ground anchors
Laminated straps
Non-laminated straps
CFRP ground anchors with strap ends
Chapter 2 & Annex A Evaluation of grout materials
• Uniaxial compression experiments on cement- and resin-based grout materials
• Modeling of compressive stress vs strain behavior of grouts using concrete models
Paper 1
Pull-out behavior of CFRP ground anchors with strap ends
Experimental investigations
Chapter 3 & Annex B One-strap anchor
Paper 2
• Pull-out experiments on one-strap anchor heads with different confinements
Chapter 4 & Annex C Two-strap anchor
Paper 3
• Pull-out experiments on two-strap anchors with different confinement levels
Experimental, numerical and analytical investigations
Chapter 5 & Annex D Multi-strap anchor
Paper 4
• FE modeling of one-strap anchors
• Development of empirical models for deriving load-transfer diagram for multi-strap anchors
• Development of three-strap anchors
Tensile behavior of non-laminated and laminated straps
Experimental and numerical investigations
Chapter 6 Seven-layer non-laminated straps
• Tensile experiments on strap specimens
• 3D FE modeling of straps
Paper 5
Numerical and analytical investigations
Chapter 7 Non-laminated and laminated straps
• 2D FE modeling of non-laminated straps with up to 70 layers
• Development of empirical models for non-laminated straps with up to 100 layers
• 2D FE modeling of laminated straps with up to 100 layers
• Analytical modeling of laminated straps
• Comparison between non-laminated and laminated straps
Paper 6
Chapter 8 Conclusions and future work

Fig. 1.7: Thesis organization

1.5 List of publications

Paper 1. Fan H, Vassilopoulos AP, Keller T. Evaluation of grout materials for CFRP ground anchors with strap ends, Constr Build Mater 2017;145:196-206.

Paper 2. Fan H, Vassilopoulos AP, Keller T. Pull-out behavior of CFRP single-strap ground anchors, J Compos Constr, 10.1061/(ASCE)CC.1943-5614.0000760 , 04016102.

Paper 3. Fan H, Vassilopoulos AP, Keller T. Pull-out behavior of CFRP ground anchors with two-strap ends, Compos Struct 2017;160:1258–1267.

Paper 4. Fan H, Vassilopoulos AP, Keller T. Load-transfer mechanisms in CFRP ground anchors with multi-strap ends. Submitted to Compos Struct, 2017.

Paper 5. Fan H, Vassilopoulos AP, Keller T. Experimental and numerical investigation of tensile behavior of non-laminated CFRP straps. Compos B Eng 2016;91:327-36.

Paper 6. Fan H, Vassilopoulos AP, Keller T. Numerical and analytical investigation of tensile behavior of non-laminated and laminated CFRP straps. Submitted to Compos B Eng, 2017.

References

[1] SAMWOO. Anchor technology. < http://www.groutingservices.co.nz/assets/Uploads/ Ground-Anchors-Removable-Anchors-Load-Distributive-Anchors-English-catalog-123010.pdf> (May 02 2017).

[2] Xu H, Benmokrane B. Strengthening of existing concrete dams using post-tensioned anchors: a state-of-the-art review. Can J Civil Eng 1996;23:1151-71.

[3] Xanthakos PP. Ground anchors and anchored structures. Washington, U.S.A.: John Wiley & Sons, 1991.

[4] Bruce DA, Wolfhope J, Wullenwaber J. Rock Anchors for Dams: A Five-Year Update. In: 33rd USSD Annual Meeting and Conference, Glendale, US, February 2013. 11-5.

[5] Sentry M, Bouazza A, Al-Mahaidi R, Loidl D, Bluff C, Carrigan L. Advancements in Ground Anchors: Carbon Fibre Reinforced Polymer (CFRP) Strands. In: International conference on ground anchorages and anchored structures in service, London, UK, 26-27 November, 2007.

[6] Weerasinghe R, Adams D. A technical review of rock anchorage practice 1976-1996. In: International conference on ground anchorages and anchored structures, London, UK, 20-21 March, 1997.

[7] European Committee for standardization (CEN). Execution of special geotechnical work– ground anchor. BS EN 1537, Brussels, Belgium, 2000.

[8] Sabatini P, Pass D, Bachus RC. Geotechnical engineering circular no. 4: Ground anchors and anchored systems. US DOT Federal Highway Administration, 1999.

[9] Aoyagi K, Yoshida T, Yamazai Y, Maruyama K. NM (new material) ground anchor system. In: Proceedings of the 2nd international conference on advanced composite materials in bridges and structures, Montreal, Canada, 11-14 August 1996. 727-34.

[10] Benmokrane B, Zhang B, Chennouf A. Tensile properties and pullout behaviour of AFRP and CFRP rods for grouted anchor applications. Constr Build Mater 2000;14:157-70.

[11] Benmokrane B, Xu H, Nishizaki I. Aramid and carbon fibre-reinforced plastic prestressed ground anchors and their field applications. Can J Civ Eng 1997;24:968-85.

[12] Tokyo Rope Co. Ltd. Summary of application projects. <https://isabou.net/sponsor/nm-anchor/sekou.asp> (May 02, 2016).

[13] Karbhari VM. Use of composite materials in civil infrastructure in Japan. International Technology Research Institute, World Technology (WTEC) Division, 1998.

[14] Fang Z, Zhang K, Tu B. Experimental investigation of a bond-type anchorage system for multiple FRP tendons. Eng Struct 2013;57:364-73.

[15] Schmidt JW, Bennitz A, Täljsten B, Goltermann P, Pedersen H. Mechanical anchorage of FRP tendons–A literature review. Constr Build Mater 2012;32:110-21.

[16] Meier U, Farshad M. Connecting high-performance carbon-fiber-reinforced polymer cables of suspension and cable-stayed bridges through the use of gradient materials. J Comput Aided Mater 1996;3:379-84.

[17] Wang X, Xu P, Wu Z, Shi J. A novel anchor method for multitendon FRP cable: manufacturing and experimental study. J Compos Constr 2015;19:04015010.

[18] Winistöerfer AU. Development of non-laminated advanced composite straps for civil engineering applications. Coventry, UK: Department of Engineering, University of Warwick; 1999.

[19] Schlaich M, Zwingmann B, Liu Y, Goller R. Zugelemente aus CFK und ihre Verankerungen. Bautechnik 2012;89:841-50.

[20] Winistöerfer A, Meier U. CARBOSTRAP-An advanced composite tendon system. In: 6th International Symposium on FRP Reinforcement for Concrete Structures (FRPRCS-5), Cambridge, UK, July 231-8; 2001.

[21] Bauersfeld D. Composite graphite/epoxy tensile element. Report 2404. United States Army, Belvoir Research & Development Center, Fort Belvoir, Virginia; 1984.p.1-62.

[22] Keller T, Kenel A, Koppitz R. Carbon Fiber-Reinforced Polymer Punching Reinforcement and Strengthening of Concrete Flat Slabs. ACI Struct 2013;110.

[23] Czaderski C, Motavalli M, Winistörfer A, Motavalli M. Prestressed shear strengthening of a box girder bridge with non-laminated CFRP straps. In: Proceedings of the 4th International Conference on FRP Composites in Civil Engineering (CICE2008), Zurich, Switzerland, July 7.B.6; 2008.

[24] Huster U, Broennimann R, Winistörfer A. Strengthening of a historical roof structure with CFRP-straps. In: Proceedings of the 4th International Conference on FRP Composites in Civil Engineering (CICE2008), Zurich, Switzerland, July 8.B.4; 2008.

[25] Triantafillou TC, Fardis MN. Strengthening of historic masonry structures with composite materials. Mater Struct 1997;30:486-96.

[26] Djamaluddin R, Yamaguchi K, Hino S. Mechanical behavior of the U-anchor of super-CFRP rod under tensile loading. J Compos Mater 2014;48:1875-85.

[27] Gardner Business Media Inc. CompositesWorld, March 2015. <http://cw.epubxp.com/i/467593-mar-2015> (May 02 2017).

[28] Schürmann H. Konstruieren mit Faser-Kunststoff-Verbunden: Springer, 2005.

[29] Mansfield E. Load transfer from a pin to a wound fibre composite strip. J Compos Mater 1983;17:414-9.

[30] Conen H. Deformation und versagen von GFK-strangschlaufen. Kunststoffe. 1966;56:629-31.

[31] Havar T. Beitrag zur Gestaltung und Auslegung von 3D-verstärkten Faserverbundschlaufen. Stuttgart, Germany: University of Stuttgart; 2007.

[32] RILEM TC 148-SSC. Test method for measurement of the strain-softening behaviour of concrete under uniaxial compression. Mater Struct 2000;33:347-51.

[33] RILEM TC 148-SSC. Strain-softening of concrete in uniaxial compression. Mater Struct 1997;30:195-209.

[34] Read HE, Hegemier G. Strain softening of rock, soil and concrete—a review article. Mech Mater 1984;3:271-94.

[35] Okubo S, Nishimatsu Y. Uniaxial compression testing using a linear combination of stress and strain as the control variable. Int J Rock Mech Min 1985;323-330.

2.

Evaluation of grout materials for CFRP ground anchors with strap ends

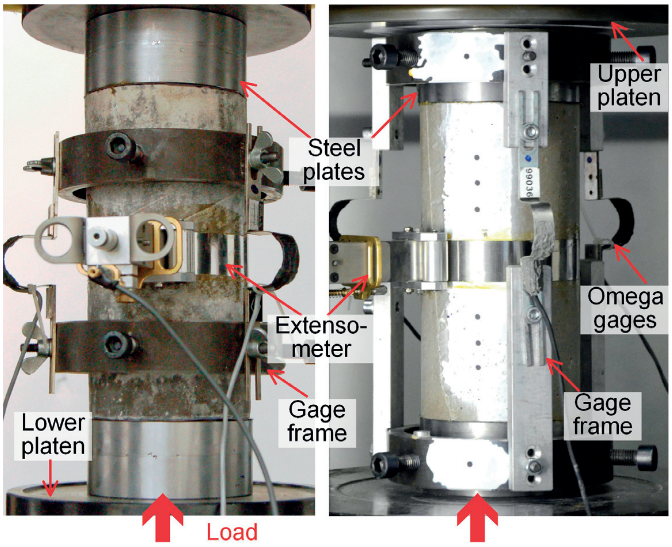
Steel plates
Upper platen
Extenso-meter
Omega gages
Gage frame
Lower platen
Gage frame
Load

Reference detail:

Fan H, Vassilopoulos AP, Keller T. Evaluation of grout materials for CFRP ground anchors with strap ends, Constr Build Mater 2017;145:196-206.

2.1 Introduction

In ground anchor systems, the evaluation of appropriate grout materials is significant since they transfer the anchor force in the borehole from the tension member to the surrounding ground. In conventional steel strand ground anchors, cement-based grouts or mortars are commonly used, while resin-based grouts are considered as an alternative [1, 2]. In more recent ground anchor systems composed of carbon fiber-reinforced polymer (CFRP) strands, the use of cement-based grouts to anchor CFRP tendons was also proved to be possible [3, 4]. In the NM (New Material, CFRP) ground anchor system [5], which has been widely used in Japan for the past 20 years, both cement- and resin-based grouts are used; however, long-term exposure experiments in a high-temperature (60–100°C) and strong-acid (pH 3–4) environment showed that resin-based grouts provided a better performance in aggressive conditions [5]. Combinations of these two grout matrix materials, i.e. epoxy resin-modified cement-grouts, enable the grout strength and elastic modulus [6] to be improved. Grout materials, however, are not only used in the borehole load transfer, but also integrated into the anchor heads in some CFRP systems. Special grouting materials were developed in such cases, e.g. cement-based Reactive Powder Concrete (RPC) with a high compressive strength of 130 MPa [7].

A new permanent post-tensioned CFRP ground anchor was recently developed, consisting of a CFRP tendon with a strap end integrated into an anchor head on the ground side [8, 9], i.e. the CFRP strap end is embedded in a prefabricated high-strength grout cylinder, which is confined with CFRP rings. This anchor head is then inserted into the borehole, where it is anchored in standard (normal-strength) grout and then post-tensioned to 60% of the design load. For the evaluation and subsequent selection of an appropriate high-strength grout material in the anchor head, the required basic mechanical properties, i.e. compressive [10, 11] and tensile strengths [11, 12], elastic modulus and Poisson's ratio [12, 13], can be obtained based on existing standards for grout materials. Factors that influence the grout mechanical behavior, e.g. constituent components and curing conditions, are also well documented [14, 15]. However, since the anchor head is designed to fail in the high-strength grout, the complete stress-strain response of the grout, including the softening branch, is needed to conduct a detailed failure analysis.

A considerable number of works about strain softening is available for concretes [16-18] and other brittle materials like rocks [19, 20]. For concretes, a round robin program to investigate the parameters that influence the strain-softening behavior, i.e. specimen geometry, loading-control method and boundary condition, was organized by RILEM [21], based on which a corresponding test method was established [22]. Furthermore, various concrete models were proposed, e.g. [23, 24], which facilitate the failure analysis of concrete structures. On the contrary, such information for cement- and resin-based grout materials is rare. Complete stress-strain curves were obtained from cement mortar specimens in [25]; however, 120×60×20 mm^3 prismatic shapes were used instead of standard ones. In most cases, stress-strain curves stop shortly after the peak stress, e.g. before 75% of the peak stress in the softening part in [26, 27]. No systematic experiments on obtaining complete stress-strain curves of grouts could be found and no analytical model has been developed. A common approach to overcome this problem would be directly using concrete models [28, 29]. However, the applicability of concrete models to grout materials has not yet been validated.

In this chapter, the axial compressive stress vs strain behaviors of four grout materials, including the softening branches, were investigated according to [21, 22]. Loading-control methods and boundary conditions were varied in order to evaluate their influence, particularly on the compressive strain softening. The Sargin concrete model [24] was applied to model the obtained stress vs strain curves of the grouts. The models were implemented in an FE analysis of previously performed pull-out experiments on the CFRP strap-end anchor heads [8] in order to validate the applicability of the concrete model to grout materials. Furthermore, the influence of the grout strain-softening behavior on the pull-out response of the anchors was investigated.

2.2 Materials and experimental setup

2.2.1 Grout materials

Four grout materials were investigated, i.e. one sand/cement-based normal-strength borehole grout and one sand/cement- and two epoxy resin-based high-strength grouts for the above-mentioned CFRP strap-end anchor head, as shown in Table 2.1, with the following denominations and mixtures:

1) Sika Rock Mortar (designated M1) [30], which is a normal-set cement mortar made from Portland cement, commonly used as borehole filling grout material in ground anchor applications. Its maximum aggregate size is 0.8 mm and the water/powder ratio 1.0 L/5.7 kg.

2) SikaGrout 212 (M2) [31], which is a high-strength, high-workability and non-shrink anchoring material made from Portland cement with a maximum aggregate size of 4.0 mm and a water/powder ratio of 1.0 L/8.3 kg.
3) Sikadur 42 HE (M3) [32], which is a synthetic mortar composed of an epoxy resin and aggregates of 3.2-mm size.
4) Sikadur 42 LE Plus (M4), which is a modified version of Sikadur 42 HE with low exothermic behavior.

Table 2.1: Overview of experimental parameters and designations

x	Material type (Mx)	Loading-control method (Lx)	Friction-reducing method (Fx)
1	Sika Rock Mortar	Circumferential 0.5 µm/s	Teflon 0.1 mm
2	SikaGrout 212	Circumferential 1.0 µm/s	Teflon 0.5 mm with one-side adhesive
3	Sikadur-42 HE	Axial 1.0 µm/s	2 Teflon 0.1 mm with grease in between
4	Sikadur-42 LE Plus	Axial 5.0 µm/s	

2.2.2 Cylinder specimens

Twenty seven cylinder specimens, i.e. 10 Sika Rock Mortar (M1), 11 SikaGrout 212 (M2), 3 Sikadur-42 HE (M3) and 3 Sikadur-42 LE Plus (M4) specimens, were fabricated from six batches of mixed fresh grout. The cylinders' slenderness ratio, h/d (height/diameter), was 2.00±0.03, except in specimens M1-1 to M1-4 and M3-2/3, as shown in Table 2.2. In specimens M1-1 to M1-4, cylindrical cardboard molds of 114×216 mm (4.5×8.5 in.) were used instead the 100×200-mm molds used for the remaining specimens. Furthermore, specimen M3-1 exhibited an unusual initially nonlinear stress vs strain response, which was attributed to a lack of aggregates in the top 10-mm-thick layer, observed when the failed specimen was cut into two halves along the height direction. A uniform distribution of aggregates existed however in the remaining part. Therefore, a top 15-mm-thick part was cut off in specimens M3-2/3, leading to a slightly lower slenderness ratio.

Table 2.2: Overview of experimental matrix

Batch group	Specimen	h/d	Time to experiment (day)	Loading-control method < 0.8/0.4 f_c	Loading-control method > 0.8/0.4 f_c	Friction-reducing method	Program	f_c (MPa)	ε_c (%)	E_0/Es
1	M1-1	1.80	28	L3	L3	F2	II	39.0	0.36	2.09
	M1-2	1.87	28	L3	L3	F2	II	38.7	0.33	1.88
	M1-3	1.80	28	L1	L1	F2	II	41.1	0.34	1.92
	M1-4	1.80	28	L2	L2	F2	II	42.9	0.32	1.82
2	M1-5	2.02	29	L2	L2	F2	II	48.8	0.35	1.70
	M1-6	2.03	29	L3	L1	F1	II	43.1	0.40	1.59
	M1-7	2.00	29	L3	L1	F1	II	43.3	0.37	1.75
	M1-8	2.02	34	L3	L1	F1	I	47.5	0.37	2.12
	M1-9	2.01	34	L3	L1	F3	I	47.2	0.38	2.17
	M1-10	2.02	34	L1	L1	F3	I	47.2	0.40	2.32
	Avg. M1							43.9±3.6	0.36±0.02	1.94±0.23
3	M2-1	1.95	28	L4	L4	F3	II	67.2	0.34	1.66
	M2-2	1.91	28	L4	L1	F3	II	54.3	0.32	1.49
	M2-3	1.96	28	L3	L1	F3	II	58.0	0.29	1.41
	M2-4	1.95	28	L3	L1	F3	II	61.6	0.29	1.34
4	M2-5	1.99	29	L1	L1	F1	II	60.0	0.33	1.71
	M2-6	1.96	29	L3	L1	F1	II	63.6	0.35	1.58
	M2-7	2.00	29	L3	L1	F1	II	63.8	0.36	1.58
	M2-8	1.99	30	L3	L1	F3	II	62.0	0.29	1.50
	M2-9	1.99	30	L3	L1	F3	II	62.3	0.29	1.63
	M2-10	1.96	33	L1	L1	F3	I	71.7	0.33	1.93
	M2-11	1.98	33	L3	L1	F3	I	70.2	0.30	1.75
	Avg. M2							63.1±5.1	0.32±0.03	1.60±0.17

Table 2.2: (continued) Overview of experimental matrix

Batch group	Specimen	h/d	Time to experiment (day)	Loading-control method		Friction-reducing method	Program	f_c (MPa)	ε_c (%)	E_0/Es
				$< 0.8/0.4\, f_c$	$> 0.8/0.4\, f_c$					
5	M3-1	1.99	7	L3	L2	F3	III	96.0	-	-
	M3-2	1.77	14	L3	L2	F3	III	107.6	1.23	2.41
	M3-3	1.78	14	L3	L2	F3	III	98.2	0.98	2.19
	Avg. M3-2/3							102.9±6.6	1.11±0.18	2.30±0.16
6	M4-1	1.94	7	L3	L2	F3	III	79.2	0.60	1.77
	M4-2	1.96	7	L3	L2	F3	III	70.2	0.54	1.70
	M4-3	1.97	7	L3	L2	F3	III	69.8	0.63	1.90
	Avg. M4							73.1±5.3	0.59±0.05	1.79±0.10

2.2.3 Curing conditions

Cement-grout specimens (M1 and M2) were fabricated and cured according to EN 196-1 [11], i.e. the cylinders were cured inside the cardboard molds in a conditioning room (99% RH and 20.0±1.0°C) for 24 hours and then stored in water at 20.0±1.0°C after demolding, except specimens M2-1 to M2-4 which were cast and cured together with two CFRP strap-end anchor head specimens (as mentioned above) at a room temperature of 23±2°C [8]. After 28 days, the specimens were taken out of the water, ground, covered with wet cloths and stored at room temperature until the experiments (which took place up to six days later, see Table 2.2). Epoxy-grout specimens (M3 and M4) were fabricated using the same cardboard molds as for the M1/M2 specimens and Sika Trennmittel-810 as a demolding agent. They were cured in air at a room temperature of 23.0±2.0°C and investigated seven or 14 days after casting. During fabrication of the M3 specimens, a strong exothermic reaction, i.e. a temperature increase up to 90°C, was observed at the cylinder top surface, 70–90 minutes after casting. In contrast, the maximum measured temperature was only 28°C in the M4 specimens.

2.2.4 Experimental procedure and instrumentation

Uniaxial compression experiments were conducted on a 2000-kN Schenck machine, as shown in Fig. 2.1, at a temperature of 23±2°C and a relative humidity of 50±5%; the specimens, together with two steel plates, were placed between the two platens of the machine; the load was applied from the lower one.

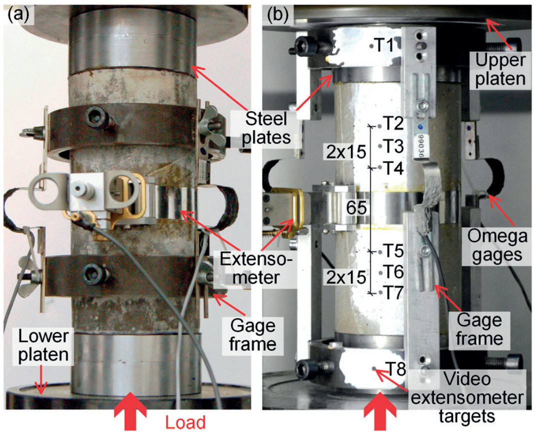

Fig. 2.1: Experimental set-up and instrumentation in (a) Program I (specimen M2-10, cement-grout); (b) Program III (M4-1, epoxy-grout) (dimensions in [mm])

Three experimental programs (I–III), using different loading procedures and instrumentations, were applied, see Table 2.2. From Program I the elastic modulus, E, and Poisson's ratio, v, were obtained according to ASTM C469 [13]. The axial deformation was measured by three surface-mounted Omega gages (PI-2-100 from Tokyo Sokki Kenkyujo, Japan). These were located at mid-height of the cylinder at 120° intervals with a gage length of 110 mm, as shown in Fig. 2.1 (a). Three load cycles up to 40% of the expected ultimate load were first applied in load-control mode at a rate of 0.25 MPa/s, preceding the fourth cycle up to failure.

Program II served to measure the complete compressive stress vs strain curves, using the RILEM methods specified for concrete [21, 22]. The axial deformation was obtained from the same type of Omega gages as in Program I, but installed between the steel plates with a gage length of 245 mm and not surface mounted. Surface-mounted gages may record invalid responses in the post-peak part because of cracks on the specimen surface [22, 33]. Specimens were directly loaded to failure in one cycle. Program III was performed to measure not only E and v but also the complete compressive stress vs strain curves. The former was achieved by using a video extensometer, while the latter were obtained from Omega gages installed as in Program II, see Fig. 2.1 (b).

In all three programs, the circumferential deformation was measured at mid-height of the specimens using an extensometer, consisting of a thin flexural steel strip, a steel head and an inductive displacement transducer (1-WI/2 mm-T for M1/M2 specimens and 1-WI/5 mm-T for M3/M4 from HBM AG, Switzerland), as shown in Fig. 2.1. The deformation was determined by measuring the elongation of the steel strip. The cylinder surface, where the extensometer was located, was sanded, cleaned and greased before the installation of the instrument.

2.2.5 Loading-control methods

The selection of an appropriate loading-control method is essential for avoiding sudden failure at the peak stress in brittle materials like concretes [21]. In this work, two control methods were used, i.e. circumferential-deformation control at rates of 0.5/1.0 μm/s (designated L1/L2) and axial-deformation control at 1.0/5.0 μm/s (L3/L4), as indicated in Tables 2.1 and 2.2.

The axial-deformation control at a rate of 1.0 μm/s (L3), recommended by RILEM for concrete with a uniaxial compressive strength of 60–70 MPa [22], was first used in specimens

M1-1/2. A sudden failure occurred however at the peak stress and the strain-softening behavior could thus not be measured. Specimen M2-1 was also investigated using this control method but at a rate of 5.0 µm/s (L4), which corresponded to the loading rate in the pull-out experiments on the CFRP anchor heads (mentioned above, see [8]); however, sudden failure at the peak stress occurred again.

Circumferential-deformation control (L1 or L2) was subsequently used in the specimens indicated in Table 2.2. The strain-softening behavior could be recorded; however, the axial deformation rate in the pre-peak part was significantly higher if L1 or L2 was used there instead of L3 or L4 due to the low Poisson’s ratio of the cement-grouts. A combined control method was thus applied with the remaining specimens, i.e. axial-deformation control in the pre-peak and circumferential control in the post-peak part, see Table 2.2. The switch from L3/L4 to L1/L2 was performed at 0.2% of axial strain, i.e. at around 80% of the compressive strength ($0.8 \cdot f_c$) in M1/M2 and $0.4 \cdot f_c$ in the M3/M4 specimens.

2.2.6 Boundary conditions

From concretes it is known that the peak stress and the strain-softening behavior also depend on the boundary conditions [22]. Three different friction-reducing methods (designated F1–F3) were thus applied, i.e. F1 using a single 0.1-mm-thick standard Teflon sheet on both specimen sides; F2 with a much thicker 0.5-mm Teflon sheet adhesively bonded to both specimen sides; and F3 using two 0.1-mm-thick Teflon sheets with grease in between on both specimen sides, see Tables 2.1 and 2.2. The Teflon sheets, which had an elastic modulus of 0.6 GPa according to the manufacturer, were provided by Guarniflon SpA, Italy. The simplest solution with a single Teflon sheet on both sides, which was also used in some experiments in [21], was first applied in specimens M1-1 to M1-5 with a thickness of 0.5 mm (F2) and M1-6 to M1-8 and M2-5 to M2-7 with a thickness of 0.1 mm (F1). However, snapback and oscillating responses were observed in the post-peak part. The F3 method, also recommended in [22], was thus used for the remaining specimens.

2.3 Experimental results and modeling

2.3.1 Compressive strength, elastic modulus and Poisson’s ratio

The compressive strengths, f_c, of all specimens are shown in Table 2.2. Cement-grouts (M1/M2) exhibited lower compressive strengths than epoxy-grouts (M3/M4). In the former, M1 specimens (43.9±3.6 MPa) had 30.5% lower average strength than M2 (63.1±5.1 MPa);

in the latter, M3 (102.9±6.6 MPa) showed a 40.8% higher average strength than M4 (73.1±5.3 MPa). This difference in the epoxy-grouts was attributed to a higher curing degree in M3 due to the much stronger exothermic reaction. Furthermore, the higher pre-peak axial deformation rate of specimens subjected to L1/L2 control than those under L3/L4 (as explained above) led to a higher compressive strength in the former, except in M2-2 and M2-5, see Table 2.2. This displacement-rate-dependent behavior was also observed in cement-mortars [34]. In contrast, no obvious influence of the boundary conditions on the compressive strength was observed.

The measured axial stress, axial and circumferential strains in the second and third cycles of the Program I and III specimens were used to calculate the elastic modulus, E, and Poisson's ratio, v, according to ASTM C469 [13], see Table 2.3. As mentioned above, in M1 and M2 specimens, the axial deformation was obtained from three Omega gages (see Fig. 2.1(a)), while in M3 and M4, the deformation of the area between targets T4/5 was measured by the video extensometer (see Fig. 2.1(b)).

Table 2.3: Elastic moduli and Poisson's ratios

	M1	M2	M3	M4
E (GPa)	25.9 ± 0.3	39.0 ± 1.9	21.4 ± 0.5	23.6 ± 1.1
v	0.094 ± 0.051	0.086 ± 0.025	0.220 ± 0.010	0.190 ± 0.010

2.3.2 Compressive stress vs strain curves

The compressive stress vs circumferential and axial strain curves of specimens M1–M4 are shown in Figs. 2.2–2.4 respectively and the comparison of all stress vs axial strain curves is shown in Fig. 2.5; positive and negative signs were attributed to axial compression and circumferential expansion respectively. The axial deformation measured by the three omega gages was first averaged and then corrected by eliminating the deformations of the steel plates located inside the measuring range (45 mm) and those of the Teflon sheets. The correction due to the Teflon sheet deformations was significant in the initial linear elastic part of the ascending curves; they contributed 4% (F1) to 18% (F2) to the total axial deformation in this range. In Program I specimens, the axial strain is only shown up to the peak stress due to subsequent unstable measurements from the surface-mounted omega gages (as explained above).

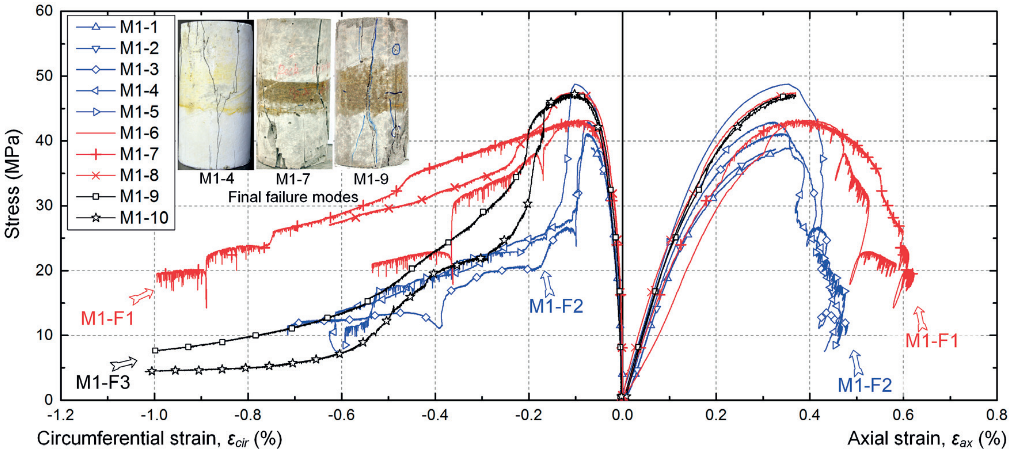

Fig. 2.2: Compressive stress vs strain curves of M1 specimens

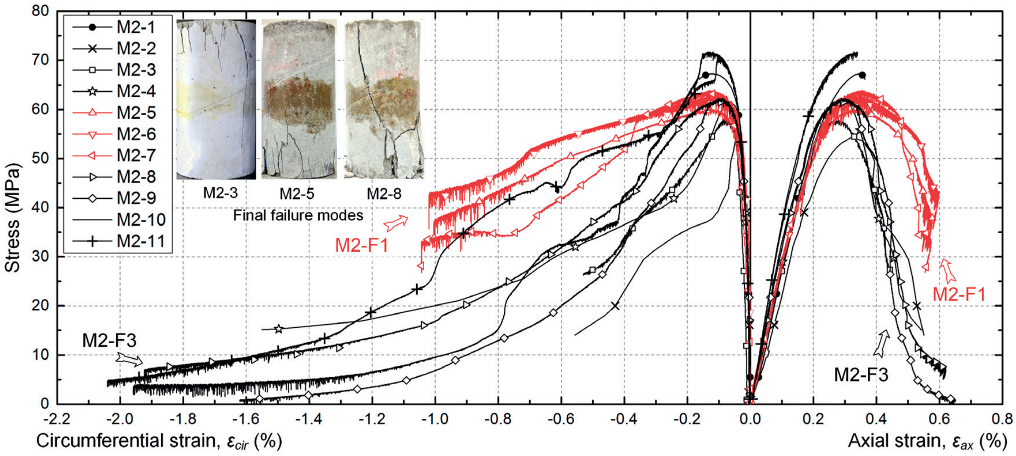

Fig. 2.3: Compressive stress vs strain curves of M2 specimens

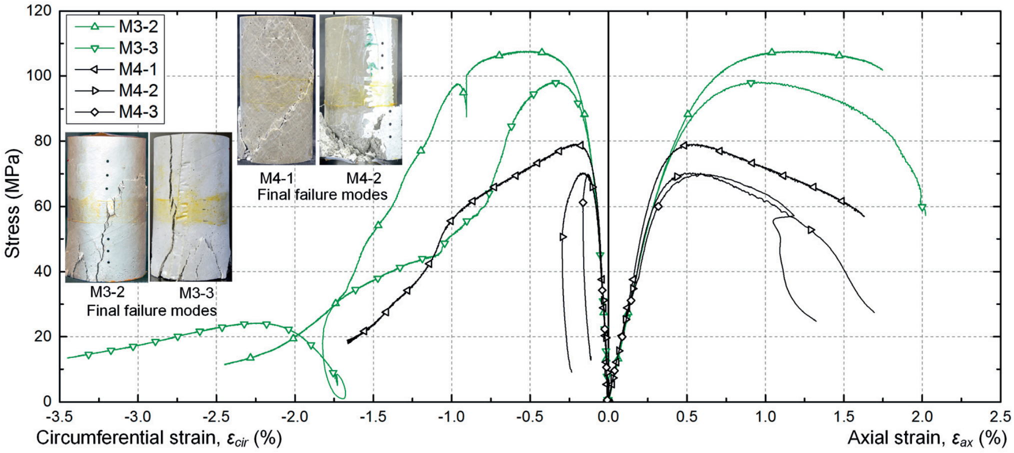

Fig. 2.4: Compressive stress vs strain curves of M3 and M4 specimens

In the pre-peak part, higher displacement rates resulted in steeper slopes of the compressive stress vs strain curves in M1 and M2 specimens (see Figs. 2.2 and 2.3). However, no obvious influence of the boundary conditions on the curve slope was observed. In M3 and M4 specimens (see Fig. 2.4) where the same loading-control method and boundary conditions were applied, the stress vs strain curves exhibited almost identical slopes in the linear elastic part. Furthermore, the four different materials exhibited different slopes in the pre-peak part, as shown in Fig. 2.5, i.e. slope of M2>M3>M4>M1.

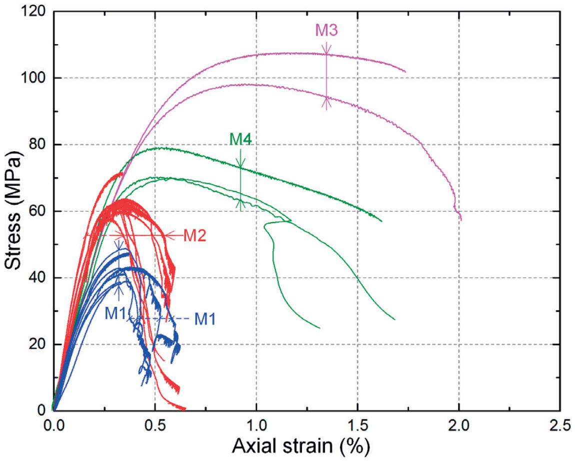

Fig. 2.5: Comparison of compressive stress vs axial strain curves of all materials

In the post-peak part, displacement rates and boundary conditions had an opposite effect on the response to that observed in the pre-peak part, i.e. only the latter had an obvious influence on the slope of the softening curve. The responses of M1 and M2 specimens could be divided into different groups according to the boundary conditions, i.e. M1-F1 and M1-F2 (see Fig. 2.2), and M2-F1 and M2-F3 (see Fig. 2.3). To better compare these groups, the compressive stress vs axial strain curves were further normalized by the peak stress and the corresponding axial strain, as shown in Fig. 2.6. Comparison of the normalized curves showed that the slope of the softening curves was determined by 1) the extent of friction at the grout cylinder and steel plate interface and 2) the material type. The greater the friction, i.e. F1>F3>F2, the more gradual the slope. The F2 condition therefore produced less lateral constraint at the cylinder ends than F1 due to the much thicker Teflon sheet and consequently larger in-plane deformations. In F1/F3, local penetration in the thin sheets was observed after the experiments, which may have restricted deformations despite the grease layer.

Furthermore, the resin-based grout curves showed more gradual slopes than the cement-based ones.

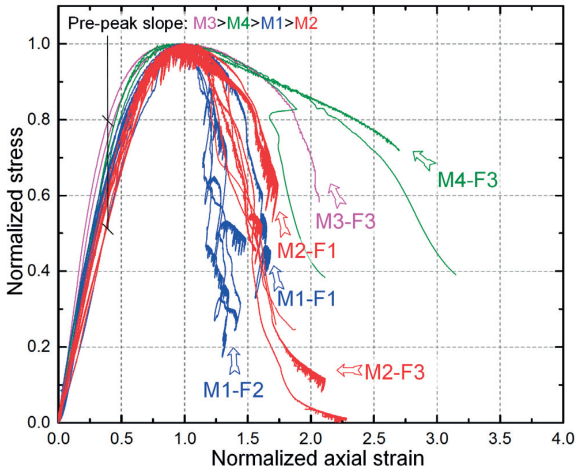

Fig. 2.6: Normalized compressive stress vs axial strain curves of all specimens

The differences observed in the softening curve could be correlated to the crack initiation, which – as in concretes – is indicated by the minimum volume, i.e. the state at which the volumetric strain, ε_{vol}, which is the difference between the circumferential and axial strains, $\varepsilon_{vol}=|\varepsilon_{cir}|-|\varepsilon_{ax}|$, reaches its minimum, $\varepsilon_{vol,min}$ [33]. The stress vs volumetric strain curves of representative M1–M4 specimens, from each boundary condition, are shown in Fig. 2.7. All specimens exhibited a continuously decreasing ε_{vol} in the pre-peak part. After the peak, however, lower friction in M1-4(F2) and M2-3/8(F3), compared to M1-7 (F1) and M2-5 (F1) respectively, resulted in smaller circumferential strains at mid-height (see Figs. 2.2 and 2.3), which consequently led to the later occurrence of $\varepsilon_{vol,min}$ and thus crack initiation. Subsequently, the increase of the volumetric strain was lower, i.e. the curves corresponding to lower friction exhibited a downward shift, as shown in Fig. 2.7. In specimens M3 and M4, $\varepsilon_{vol,min}$ could only be obtained in M3-3, because the measurement of the axial strain stopped early in M3-2 and M4-1, while in M4-2/3 cracks were located below the extensometer, see Fig. 2.4, and their effect was thus not captured. In all the specimens where $\varepsilon_{vol,min}$ was reached, complete through-height cracks developed subsequently until the experiments were stopped, see Figs. 2.2–2.4, except in M2-5 to M2-7 where the experiments stopped at high stress levels (30–40 MPa).

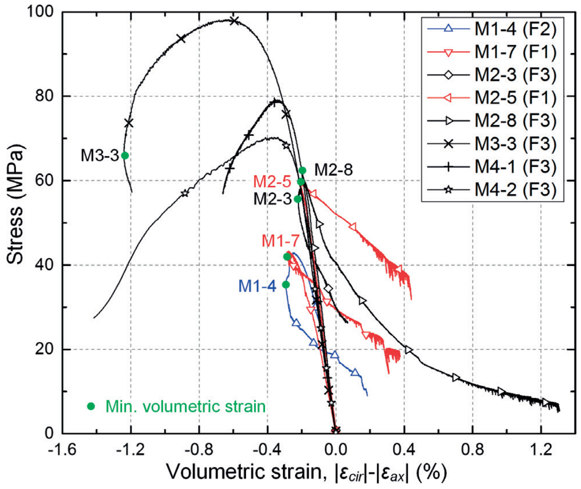

Fig. 2.7: Compressive stress vs volumetric strain of selected specimens

2.3.3 Compressive stress vs axial strain modeling

Due to the lack of existing stress vs strain models for grouts, the widely used Sargin model for concretes under compression was applied in this work [24]:

$$y = \frac{E_0 / E_s \cdot x + (D-1)x^2}{1 + (E_0 / E_s - 2) \cdot x + D \cdot x^2} \tag{2.1}$$

where y is the normalized stress ($=\sigma/f_c$), x is the normalized strain ($=\varepsilon/\varepsilon_c$), σ and ε are the axial stress and strain, f_c and ε_c are the peak stress and corresponding strain (see Table 2.2), E_0 and E_s are the initial and secant moduli at the peak obtained from Figs. 2.2–2.4, and D is a constant based on the curve shape. Higher values of D lead to a more gradual slope of the softening curve, i.e. correspond to higher friction at the grout-steel interface in the cylinder experiments, which could benefit the stress redistribution after crack initiation in redundant systems and consequently increase their ultimate load [35, 36]. For D=0.0, this model is equivalent to that of the FIB model code [37] and it changes to the Saenz model [38] with D=1.0.

The average E_0/Es was used for each type of grout, as shown in Table 2.2, while D was calibrated by fitting Eq.(2.1) to the normalized experimental curves, as shown in Figs. 2.8–2.10 for M1–M4 specimens respectively. In M1 and M2, the two groups were calibrated separately. Group M4-F3 exhibited the highest D value (1.3) and M1-F2 the lowest one (-0.5).

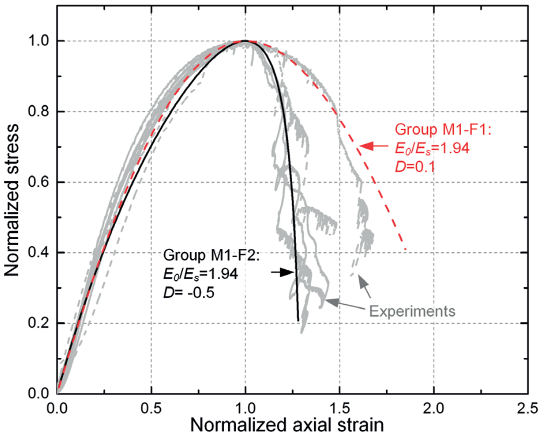

Fig. 2.8: Calibration of compressive stress vs axial strain model for M1 specimens

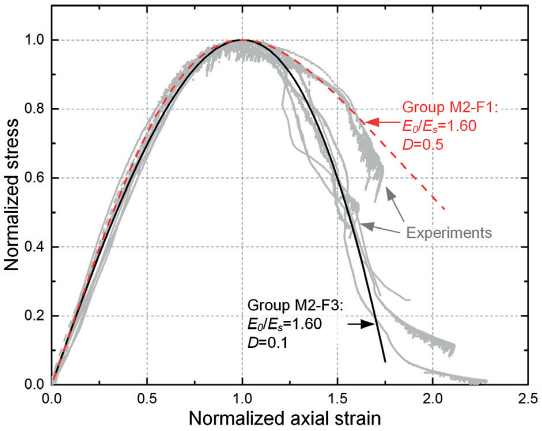

Fig. 2.9: Calibration of compressive stress vs axial strain model for M2 specimens

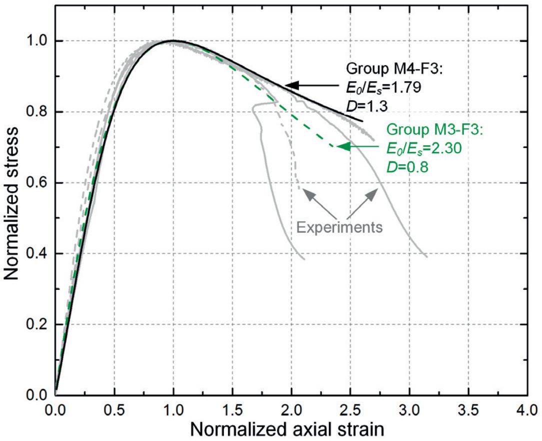

Fig. 2.10: Calibration of compressive stress vs axial strain model for M3 and M4 specimens

2.4 Experimental validation of compressive grout models

2.4.1 Previous experiments on anchor heads

Two anchor-head configurations, C380-1/2 (examined twice) and C200, were investigated; the dimensions and the experimental loading conditions are shown in Fig. 2.11. The top surface of the high-strength grout was supported and this zone was confined by a 70-mm-long steel ring to prevent local failure; the load was applied on the air-side strap. In anchor heads C380, the spreading forces at the embedded strap end and the transition from the strap to the tendon were balanced by a 380-mm-long and 2-mm-thick CFRP confinement ring. The unconfined 200-mm-long grout part was thus loaded in axial compression. In contrast, in anchor head C200, the shorter 200-mm-long confinement ring only covered the transition zone; the spreading forces at the strap end remained thus unbalanced.

The pull-out displacement of the CFRP tendon was measured by LVDTs located at a 200-mm distance from the support surface and the strains in the embedded CFRP strap, CFRP confinement ring and unconfined grout part were measured by strain gages. Details concerning the experimental set-up and results are presented in [8].

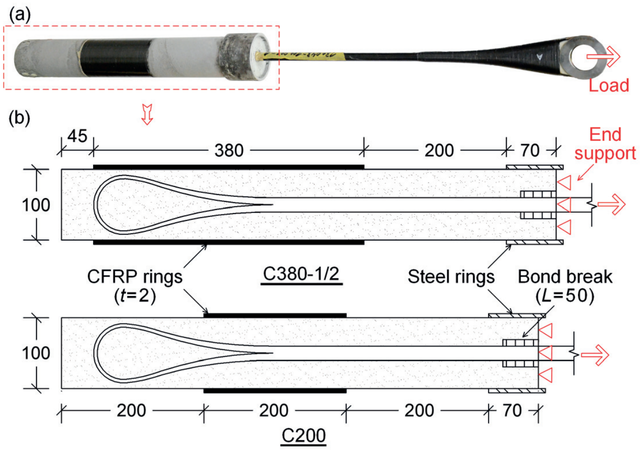

Fig. 2.11: CFRP ground anchor experiments: (a) anchor specimen C200; (b) anchor heads of C380 and C200 with different CFRP confinement ring arrangements (dimensions in [mm])

2.4.2 High-strength grout material selection and models

The main differences in the sand/cement-based grouts were the higher aggregate size and lower water/powder ratio of grout M2, which may be the main reasons for the much higher strength. The latter was further improved by changing to the epoxy-based material in M3 and

M4. The nominal breaking load of the CFRP tendon was 335 kN [8], which corresponded to a compressive stress of 42.7 MPa in the unconfined grout part. Considering a post-tensioning level of 60%, the long-term compressive stress was 25.6 MPa, i.e. 24.9/35.0% of the compressive strength of the M3/M4 specimens and thus at the limit of or higher than the admissible 20–25% allowed by the manufacturer to prevent creep rupture. Considering the high strength and better creep performance, SikaGrout 212 (M2) was selected as the grout material for the CFRP anchor heads.

The compressive stress vs strain curves of the anchor head grout were obtained by scaling the two normalized M2-models in Fig. 2.9 by the average f_c (60.3 MPa) and ε_c (0.31%) of the cylinder specimens M2-1 to M2-4 (see Table 2.2), which were fabricated together with anchor heads C380-2 and C200. The resulting models for D=0.1 and D=0.5, shown in Fig. 2.12, were implemented into FE models established to simulate the pull-out experiments. Experimental and numerical results were compared in order to validate these compressive grout models, as described in the following.

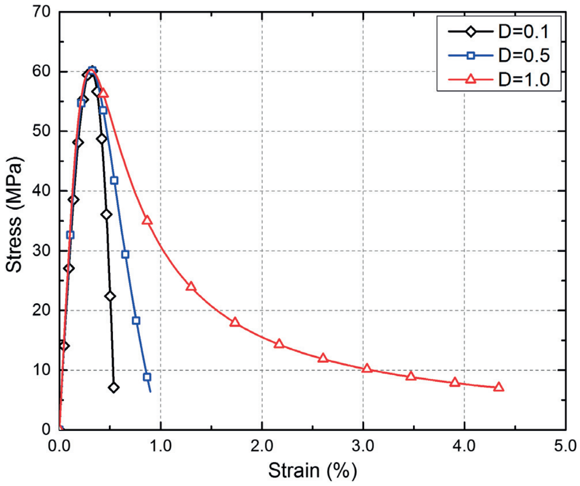

Fig. 2.12: Compressive stress vs strain curves for selected grout (M2) of anchor heads

2.4.3 FE model description

FE models of the two anchor-head configurations were developed using the commercial Finite Element Analysis (FEA) software ABAQUS 6.11. Taking advantage of double symmetry in the transversal directions, only a quarter of the model was built with a symmetric boundary condition on the x-y and x-z planes, as shown in Fig. 2.13. The grout parts, CFRP tendon with strap end and steel ring were modeled using solid elements (C3D8R, eight-node linear brick elements with reduced integration) and the CFRP confinement rings using shell elements (S4R, four-node quadrilateral elements with reduced integration). A general mesh size of 2.5 mm was selected for the grout around the embedded strap, while a 4.5-mm size was used for the rest of the grout part. The same mesh size was applied for the CFRP tendon and CFRP and steel rings as for the grout part and the tendon was meshed into four elements in the thickness direction to reduce hourglass effects [39]; the total element number was 28096. The input material properties for the CFRP tendon were E_1=143.4 GPa (in the fiber direction), E_2=E_3=5.7 GPa, ν_{12}=ν_{13}=0.27, and ν_{23}=0.4, while E_1=170 GPa (in the fiber direction), E_2=5.7 GPa, and ν_{12}=0.27 were selected for the CFRP ring [8]. The elastic modulus and yield stress of the steel ring were 210 GPa and 355 MPa respectively.

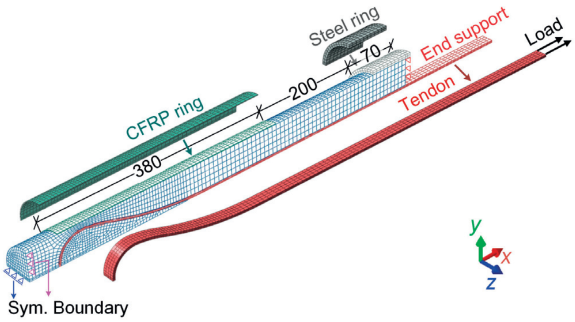

Fig. 2.13: FE model of C380 CFRP anchor head

The grout properties were simulated using the Concrete Damaged Plasticity (CDP) model in ABAQUS, which is applicable for compressive crushing and tensile cracking [39]; the degradation of the elastic modulus during unloading was not taken into account. In this model, the compressive stress vs inelastic strain and tensile stress vs crack opening have to be implemented in tabular form.

The implemented compressive stress vs inelastic strain curves were derived from the complete stress vs strain grout model curves, as obtained in Fig. 2.12, by removing the elastic strain. The boundary conditions of the unconfined grout parts in the two anchor-head configurations were different from those of the grout cylinder specimens. A fixed end-constraint, i.e. an infinite frictional boundary condition, existed on both sides in C380 while in C200 only one side was fully restrained and the other one was totally free. In addition to the D-values of 0.1 and 0.5 obtained for the compression grout models, a higher value of D=1.0

was thus also considered, to take an even higher restraint than in boundary condition F1 into account. The corresponding compressive stress vs strain curve was added in Fig. 2.12.

In tension, the bilinear stress vs crack opening model of the FIB model code for concrete [37] was used, as shown in Fig. 2.14; the tensile strength, f_t, was 3.1 MPa (which was converted from the flexural strength 7.0 MPa (manufacturer data) according to the FIB model code), the fracture energy, G_F=153 N/m and the average compressive strength, f_c=60.3 MPa. Furthermore, the average elastic modulus obtained from the experiments (39.0 GPa) was used for both tension and compression and other parameters in the CDP model were: the dilation angle=30°, flow potential eccentricity=0.1 and viscosity parameter=0.0005.

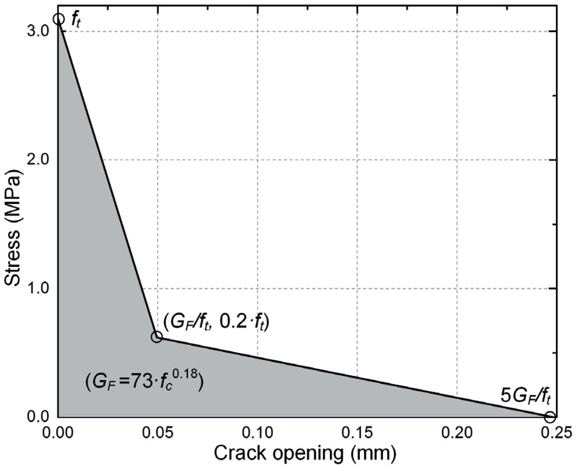

Fig. 2.14: Tensile stress vs crack opening model

The CFRP tendon and grout interface was simulated using a combination of cohesive and contact models. A bilinear surface-based cohesive model was used up to complete bond failure [39], as shown in Fig. 2.15. After bond failure, a “hard contact” model with the augmented Lagrange method was applied in the out-of-plane direction, while in the in-plane direction, the isotropic Coulomb friction model with the “penalty method” was applied. The parameters of the cohesive model and the coefficient of friction, μ, in the contact model were calibrated using the experimental results obtained for anchor head C200, see next section. Furthermore, the interface between the grout and CFRP and steel ring were simulated using the same friction model with a constant μ of 0.2.

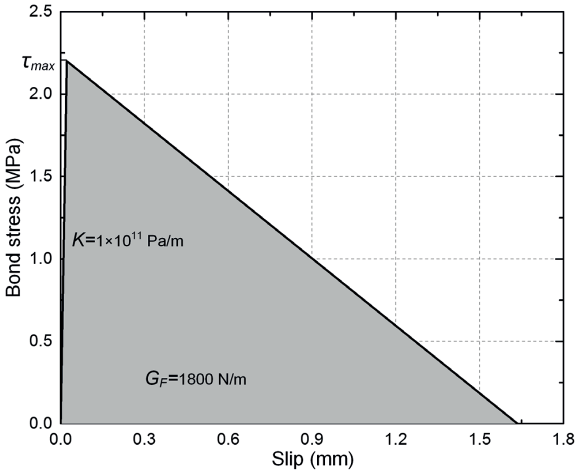

Fig. 2.15: Bilinear bond-slip law for CFRP/grout interface

2.4.4 Model calibration based on anchor head C200

The experimental load vs tangential tensile strain response of the embedded strap in anchor head C200 was first used to calibrate the parameters of the cohesive and contact interface models, as shown in Fig. 2.16. The same parameters were used for all the following FE models. The calibrated cohesive model is shown in Fig. 2.15; it is characterized by an identical stiffness in two tangential directions, $K=1\times10^{11}$ Pa/m; a maximum bond stress, $\tau_{max}=2.2$ MPa; and a fracture energy for linear damage evolution, $G_F=1800$ N/m. The coefficients of friction in the contact model were 0.4 and 0.2 for below and above 200 kN respectively, which approximately corresponded to the load at which a change of slope was observed in the experiment (see Fig. 2.16). By using these cohesive and contact methods, the bond- and friction-caused delay of the load transfer to the end of the embedded strap (no load transfer occurred up to 100 kN, see [8]) was well simulated by the three FE models.

Following the calibration of the interface parameters using only one measurement, the three FE models were applied to simulate the remaining experimental results obtained for anchor head C200. The comparison of experimental and numerical load vs pull-out displacement responses is shown in Fig. 2.17. The initially nonlinear response was well simulated by all three FE models and could be attributed to the progressive debonding along the CFRP tendon and grout interface, as shown in Fig. 2.18, where CSDMG=1.0 (cohesive surface damage index [39], varying between 0.0 and 1.0) indicated a complete bond failure. A good agreement regarding the peak load was achieved for the FE model with $D=0.1$, while the remaining two models overestimated the peak load. This suggested that the stress redistribution was low and that the large softening branch of the D=1.0 model could thus not be exploited. The crack development observed in the experiment was also simulated by the FE model, as shown in the distribution of the equivalent plastic tensile strain (PEEQT [39]) in Fig. 2.19. This crack initiated at around 180 kN and finally developed into a complete longitudinal tensile crack at 250 kN, which was caused by the unbalanced spreading forces.

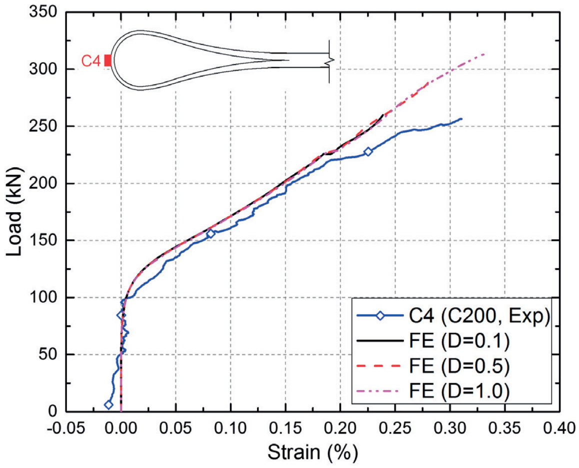

Fig. 2.16: Comparison of experimental and calibrated numerical load vs tangential tensile strain responses of strap end (C4) in anchor head C200

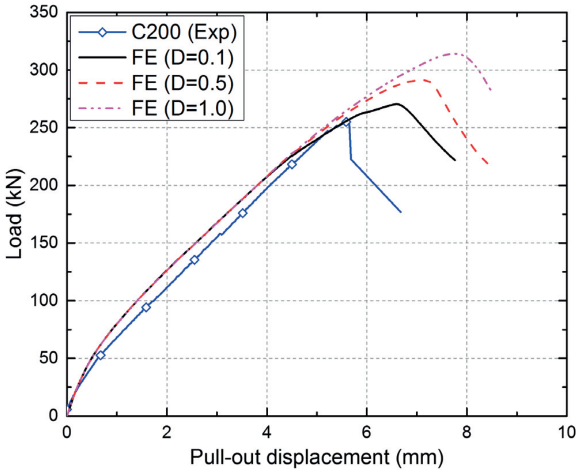

Fig. 2.17: Comparison of experimental and numerical load vs pull-out displacement responses in anchor head C200

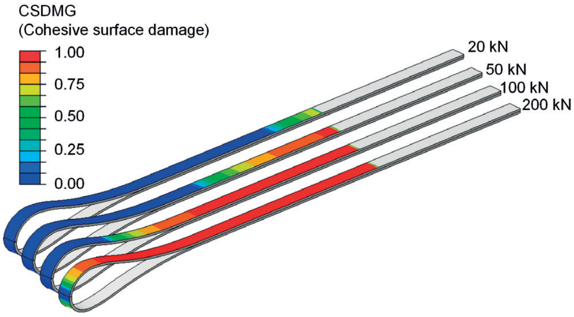
CSDMG
(Cohesive surface damage)
1.00
0.75
0.50
0.25
0.00
20 kN
50 kN
100 kN
200 kN

Fig. 2.18: Progressive debonding along CFRP tendon and grout interface in anchor head C200

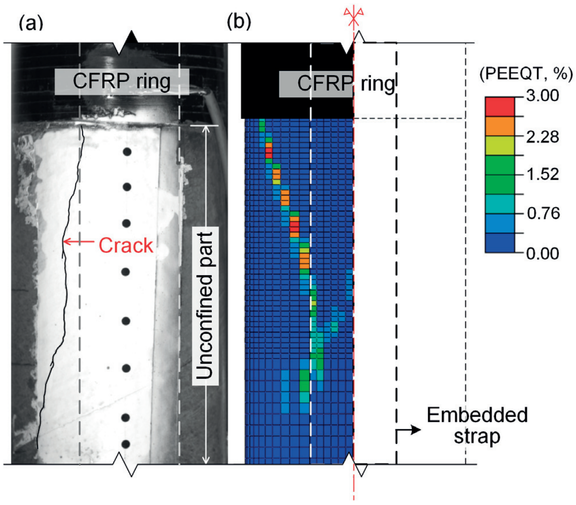
(a)
(b)
CFRP ring
Crack
Unconfined part
CFRP ring
(PEEQT, %)
3.00
2.28
1.52
0.76
0.00
Embedded strap

Fig. 2.19: Failure analysis of unconfined grout at peak load (250 kN): (a) crack pattern in experiment; (b) distribution of equivalent plastic tensile strain (PEEQT, for D=0.1)

2.4.5 FE model validation based on anchor heads C380

To further validate the FE models calibrated on anchor head C200 and particularly the compressive grout model, they were applied to simulate the C380 anchor experiments, where only the length and position of the CFRP confinement ring were adjusted. The comparisons of the experimental and numerical load vs pull-out displacement, load vs tangential tensile strain at the strap end and load vs compressive strain responses of the unconfined grout are shown in Figs. 2.20–2.22 respectively. A good agreement between the numerical and experimental results was achieved. The model with D=1.0 exhibited the best prediction of the ultimate load (455 kN), i.e. only 4.0% lower than in anchor C380-2 (474 kN), which was manufactured from the same grout batch as the cylinders used to obtain the stress vs strain model (M2-1 to M2-4). The compressive strength of the grout used in anchor C380-1 was not measured, but the higher ultimate load (526 kN) corresponded to a back-calculated value of 71.7 MPa, which was in the range of the strength values obtained for the cylinder specimens (M2-10/11, see Table 2.2). The compressive crushing of the unconfined grout part and the corresponding typical double-cone failure mode were also simulated by the FE model, i.e. by the X-shaped path of PEEQT formed at the ultimate load, as shown in Fig. 2.23. The PEEQT values in C380 were much lower than in C200 (see Fig. 2.19), which was confirmed by the shorter crack length and width observed in C380 (see [8]). Furthermore, varying *D* from 0.0 to 1.0 only resulted in a 1.9% increase in the ultimate load and had no influence on the strain development in the tendon and grout (see Figs. 2.21 and 2.22), suggesting that only limited stress redistribution occurred in the unconfined grout part.

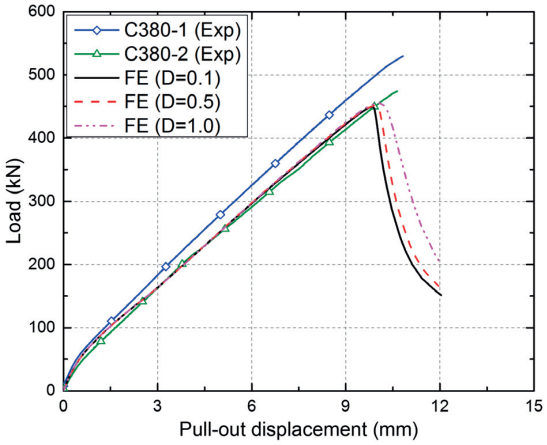

Fig. 2.20: Comparison of experimental and numerical load vs pull-out displacement responses in anchor heads C380-1/2

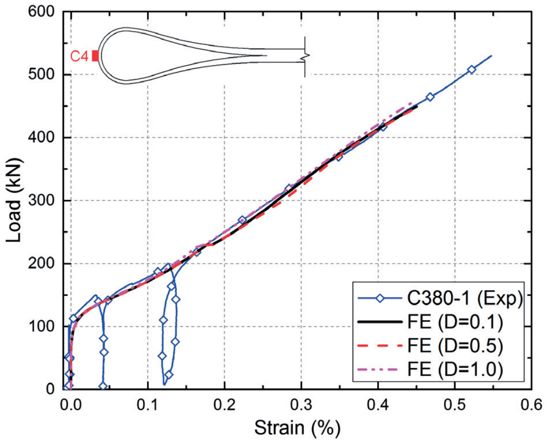

Fig. 2.21: Comparison of experimental and numerical load vs tangential tensile strain responses of strap end (C4) in anchor head C380-1

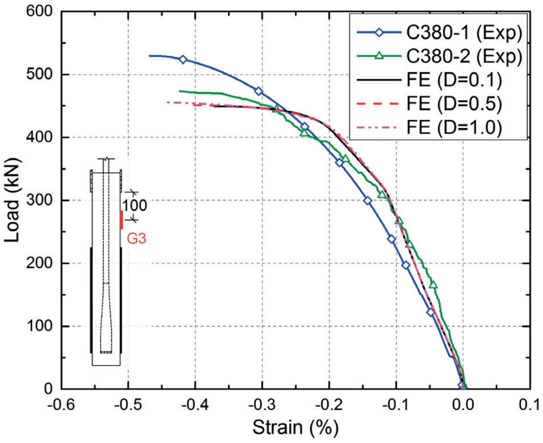

Fig. 2.22: Comparison of experimental and numerical load vs compressive strain responses on unconfined grout (G3) in anchor heads C380-1/2

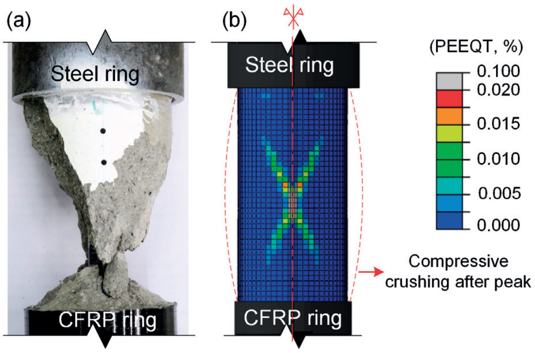

Fig. 2.23: Comparison of failure mode in anchor head C380-2: (a) experiment; (b) distribution of PEEQT at peak load in FE model (D=1.0)

2.5 Conclusions

The uniaxial compressive stress vs strain behavior of cylinder specimens of four cement- and resin-based grout materials was investigated, with a view to their application in anchor heads and boreholes of CFRP ground anchors. The influence of different loading-control methods and boundary conditions on the softening behavior particularly was studied. The Sargin concrete model was applied to model the complete compressive stress vs strain behavior of the grouts. The modeling results were implemented in FE models of CFRP strap-end anchor heads and validated by comparing the numerical and experimental results. The following conclusions were drawn:

1. To obtain the softening responses for grout materials like those used in this work, a combined axial and circumferential deformation control and two 0.1-mm-thick Teflon

sheets with grease in between should be used. However, since the deformation of the Teflon sheets was significant in the linear elastic range, the axial specimen deformations should be corrected accordingly.

2. The pre-peak branch of the compressive stress vs strain curves was mainly influenced by the loading-control method, while the softening behavior in the post-peak branch was determined by the boundary conditions of the cylinder specimens.
3. The Sargin compression model developed for concrete proved to also be applicable to the investigated cement- and resin-based grout materials.
4. A parametric study based on different softening behaviors of the grouts showed that only limited stress redistribution occurred after crack initiation in the high-strength gout anchor heads of the CFRP ground anchors.

References

[1] European Committee for Standardization (CEN). Execution of special geotechnical work – ground anchor BS EN 1537. Brussels, Belgium, 2013.

[2] British Standards Institution (BSI). Code of practice for grouted anchors BS 8081. London, UK, 2015.

[3] Benmokrane B, Zhang B, Chennouf A. Tensile properties and pullout behaviour of AFRP and CFRP rods for grouted anchor applications. Constr Build Mater 2000;14: 157–70.

[4] B. Benmokrane, H. Xu, I. Nishizaki, Aramid and carbon fibre-reinforced plastic prestressed ground anchors and their field applications. Can J Civ Eng 1997;24:968-85.

[5] Littlejohn S, Enomoto T, Sugisaki T, Suga K, Sueyoshi T. Ground Anchor Made of New Materials Applicable for Highly Corrosive Environments. In: Proceedings of the two day international conference organised by the Institution of Civil Engineers and held in London, November 26-27 2007: 341-350.

[6] Anagnostopoulos CA, Sapidis G, Papastergiadis E. Fundamental properties of epoxy resin-modified cement grouts. Constr Build Mater 2016;125:184-195.

[7] Fang Z, Zhang K, Tu B. Experimental investigation of a bond-type anchorage system for multiple FRP tendons. Eng Struct 2013;57:364-373.

[8] Fan H, Vassilopoulos AP, Keller T. Pull-out behavior of CFRP single-strap ground anchors. J Compos Constr, 10.1061/(ASCE)CC.1943-5614.0000760 , 04016102.

[9] Fan H, Vassilopoulos AP, Keller T. Pull-out behavior of CFRP ground anchors with two-strap ends. Compos Struct 2017;160:1258–1267.

[10] American Society for Testing and Materials (ASTM). Standard Test Methods for Compressive Strength of Chemical-Resistant Mortars ASTM C579. West Conshohocken (PA), 2001.

[11] European Committee for standardization (CEN). Methods of testing cement–Part 1: Determination of strength EN 196-1. Brussels, Belgium, 2005.

[12] American Society for Testing and Materials (ASTM). Standard Test Method for Flexural Strength and Modulus of Elasticity of Chemical-Resistant Mortars, Grouts, Monolithic Surfacings, and Polymer Concretes ASTM 580. West Conshohocken (PA), 2012.

[13] American Society for Testing and Materials (ASTM). Standard test method for Static Modulus of Elasticity and Poisson's Ratio of Concrete in Compression ASTM C469M. West Conshohocken (PA), 2014.

[14] Lim SK, Tan CS, Chen KP, Lee ML, Lee WP. Effect of different sand grading on strength properties of cement grout. Constr Build Mater 2013;38:348-355.

[15] Sajedi F, Razak HA. Effects of curing regimes and cement fineness on the compressive strength of ordinary Portland cement mortars. Constr Build Mater 2011;25(4): 2036-2045.

[16] Jansen DC, Shah SP. Effect of length on compressive strain softening of concrete. J Eng Mech 1997;123(1):25-35.

[17] Shah S, Gokoz U, Ansari F. An experimental technique for obtaining complete stress-strain curves for high strength concrete. Cem Concr Aggreg 1981;3(1):21-27.

[18] Wee T, Chin M, Mansur M. Stress-strain relationship of high-strength concrete in compression. J Mater Civ Eng 1996;8(2):70-76.

[19] Read HE, Hegemier G. Strain softening of rock, soil and concrete—a review article. Mech Mater 1984;3(4):271-294.

[20] Okubo S, Nishimatsu Y. Uniaxial compression testing using a linear combination of stress and strain as the control variable. Int J Rock Mech Min 1985;22 (5):323-330.

[21] RILEM TC 148-SSC. Strain-softening of concrete in uniaxial compression. Mater Struct 1997;30(4):195-209.

[22] RILEM TC 148-SSC. Test method for measurement of the strain-softening behaviour of concrete under uniaxial compression. Mater Struct 2000;33(230):347-351.

[23] E. Hognestad, Study of combined bending and axial load in reinforced concrete members. University of Illinois. Eng Exp Station Bulletin (1951) no. 399.

[24] Sargin M. Stress-strain relationships for concrete and the analysis of structural concrete sections. Solid Mechanics Division, University of Waterloo, Ontario, Canada, 1971.

[25] Torrenti J, Benaija E, Boulay C. Influence of boundary conditions on strain softening in concrete compression test. J Eng Mech 1993;119(12):2369-2384.

[26] Vipulanandan C, Weng Y, Zhang C. Designing flowable grout mixes using foundry sand, clay and fly ash. In: Advances in Grouting Modification. Geotechnical Special Publications, ASCE, 2000: 215-233.

[27] Kaushik HB, Rai DC, Jain SK. Stress-strain characteristics of clay brick masonry under uniaxial compression. J Mater Civ Eng 2007;19(9):728-739.

[28] Zhang B, Benmokrane B, Ebead UA. Design and evaluation of fiber-reinforced polymer bond-type anchorages and ground anchors. Int J Geomech 2006;6(3):166-175.

[29] Dhanasekar M, Haider W. Explicit finite element analysis of lightly reinforced masonry shear walls. Comp & Struct 2008;86(1):15-26.

[30] Sika Schweiz AG. Sika Rock Ankermörtel Normal. <http://che.sika.com/dms/getdocument.get/c886d0c9-e538-3a71-8f20-730c5285ce4b/PDS_Sika_Rock_Ankermoertel_Normal_DECH.pdf >, (March 21, 2017).

[31] Sika Schweiz AG. SikaGrout-212. <http://che.sika.com/dms/getredirect.get/chproducts.webdms.sika.com/6034 >, (March 21, 2017).

[32] Sika Schweiz AG. Sikadur-42 HE. <http://che.sika.com/dms/getdocument.get/abd8883e-5e83-3802-b257-d170cc5e59ef/PDS_Sikadur-42_HE_FRCH.pdf >, (March 21, 2017).

[33] van Mier JG. Fracture process of concrete: Assessment of material parameters for fracture models. CRC Press, Boca Raton, FL, 1997.

[34] Harsh S, Shen Z, Darwin D. Strain-rate sensitive behavior of cement paste and mortar in compression. ACI Mater J 1990;87(5):508-516.

[35] Bažant ZP. Instability, ductility, and size effect in strain-softening concrete. J Eng Mech Div 1976;102(2):331-344.

[36] Ottosen NS. Nonlinear finite element analysis of concrete structures. Riso National Laboratory Roskilde, Denmark, 1980.

[37] Fédération Internationale du Béton (FIB). Model Code 2010 final completed draft. Bulletins 66, Lusanne, Switzerland, 2012.

[38] Saenz LP. Discussion of equation for the stress-strain curve of concrete by Desayi and Krishnan. ACI J 1964;61(9):1229-1235.

[39] Abaqus Inc. Abaqus analysis user's manual, version 6.11. Providence, RI, USA; 2011.

3.

Pull-out behavior of CFRP one-strap ground anchors

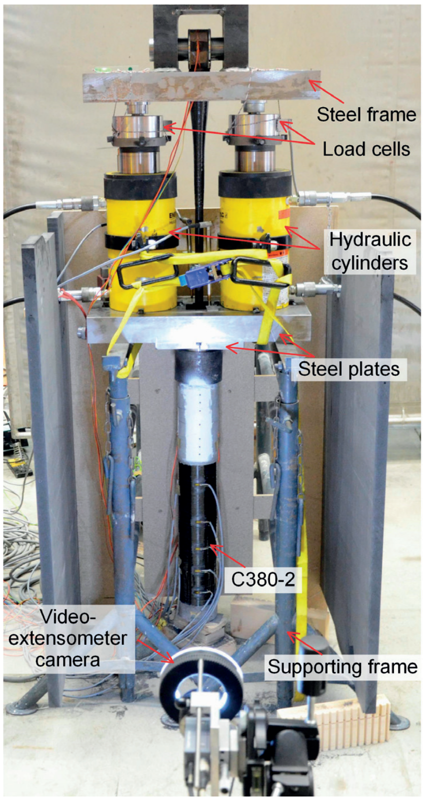
Steel frame
Load cells
Hydraulic cylinders
Steel plates
C380-2
Video-extensometer camera
Supporting frame

Reference detail:

Fan H, Vassilopoulos AP, Keller T. Pull-out behavior of CFRP single-strap ground anchors, J Compos Constr, 10.1061/(ASCE)CC.1943-5614.0000760 , 04016102.

3.1 Introduction

Permanent prestressed ground anchors made of steel are widely used for the stabilization of structures in civil engineering, such as slopes, dams, tunnels and bridge foundations. Ground anchors usually consist of an air-side anchor head and a tendon which – after the free length part – is anchored into the soil or rock medium in a 3–10-m-long grouted anchoring length. One of their earliest applications was the strengthening of the Cheurfas dam in Algeria in 1934 [1]. However, the components of conventional steel anchors are generally vulnerable to galvanic corrosion. Thus different corrosion protection systems for the steel components, depending on environmental conditions, are generally prescribed in standards such as EN1537:2013 [2] and periodical inspections are required. However, even the application of double protection systems with integrated electrical resistance measurement cannot always guarantee the intactness of an installed anchor since the interpretation of the measurement results is not always clear.

Instead of solving the durability problem with expensive and not always reliable protection systems, replacing steel by corrosion-resistant fiber-reinforced polymers (FRPs) has evolved as an alternative solution [3]. The use of commercially available aramid- and carbon-FRP (AFRP and CFRP) tendons in ground anchor applications, between 1990 and 1996, has been reported [4]. Because of their excellent mechanical properties and resistance to various environmental conditions, prestressed permanent CFRP ground anchors were further used in around 80 applications in Japan between 1993 and 2015 [5]. A CFRP ground anchor system was recently designed for the Aizhai suspension bridge in China; two CFRP cables, assembled from nine or 20 tendons of 12-mm diameter, were developed to achieve load-bearing capacities of 1670 and 4100 kN respectively [6].

Conceptually similar to steel tendons, mechanical or bonded anchors are commonly used for FRP materials [7]. However, carbon fibers are strongly anisotropic, exhibiting much lower properties in the transverse fiber direction, which may lead to premature failure in the anchoring area due to high shear and through-thickness stress concentrations. In order to avoid such stress peaks, a gradient load transfer medium with varying elastic modulus was developed and the method was applied in a 124-m-span cable-stayed bridge in Switzerland [8]. Another design to achieve a gradient load transfer medium was recently developed by continuously winding fibers into a conical shape and varying the fiber directions from 45 to 90° in three different parts [9]. However, the fabrication of these anchors is not simple and they are expensive.

A simpler and much more material-tailored anchoring method, which does not mimic the anchorage technique of steel anchors, is based on strap ends, allowing the CFRP tendon to be anchored using simple steel pins [10,11]. This anchorage method has already been used to strengthen existing reinforced concrete flat slabs against punching [12], timber roof structures [13] and masonry structures [14]. Recently, a CFRP rod with a one-strap end was developed for anchoring in concrete; a load-bearing capacity of 140 kN was obtained in one pull-out experiment on a rod specimen anchored in a concrete block [15]. However, no research has yet been conducted on the anchoring of strap ends of ground anchors in a soil or rock medium.

In this work, a new application of the strap anchorage method for permanent prestressed CFRP ground anchors with a capacity of more than 1000 kN is presented. The CFRP tendon comprises a multi-strap end on the ground side and a one-strap end on the air side, see Fig. 3.1. The multi-strap end is embedded in a prefabricated high-strength grout cylinder, i.e. a ground-side anchor head, which is then anchored in the borehole. The cylinder is confined by CFRP rings which deviate the spreading forces – occurring at the strap ends and at the transition from the straps to the straight-tendon segment – into the cylinder's axial direction; their purpose is therefore not to increase the strength of the (already) high-strength grout in the axial direction. The grout cylinder is thus stepwise axially loaded by the axial components of the spreading forces. The prefabricated ground anchors can be 20–80 m long and coiled, then transported to the construction site, inserted into the borehole, anchored by injecting fresh grout and finally prestressed to 60% of the design load.

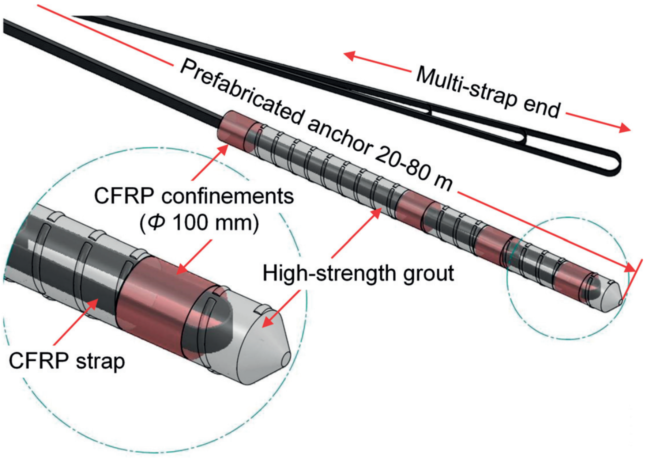

Fig. 3.1: Permanent prestressed CFRP ground anchor with multi-strap anchor head on ground side

This chapter presents a first stage of development of the multi-strap concept, i.e. a CFRP ground-side anchor head with a one-strap end, which can however already be used where only smaller loads need to be transmitted. The anchor capacity was determined in pull-out experiments of the CFRP tendon from the prefabricated high-strength grout cylinder. The influence of different confinement levels and CFRP ring arrangements on the load-bearing behavior of the anchor was investigated. Furthermore, the load-transfer mechanisms and failure modes were investigated.

3.2 Experimental program

3.2.1 CFRP one-strap anchor specimens

The CFRP one-strap tendons used in this study were produced by Carbo-Link, Fehraltorf, Switzerland. They were fabricated by winding continuous unidirectional carbon fibers around two identical steel pins at a 1.30-m center-to-center distance to form strap ends and then transversely wrapping the 780-mm-long middle part to form a rod shape of 20-mm diameter, see Fig. 3.2. The 252-mm-long strap on the ground side was embedded in a grout cylinder (see below), while a steel ring and pin of 50-mm diameter was used on the air side to apply the load. The inner diameter, width and thickness of the circular part of the strap ends on both sides were 74, 40 and 4 mm respectively. The geometry was designed to fit in boreholes larger than 100 mm in diameter.

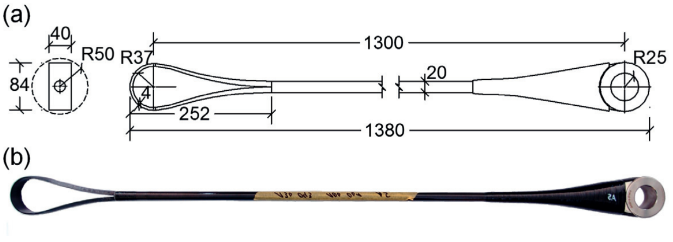

Fig. 3.2: CFRP one-strap tendon specimen (without high-strength grout cylinder on left ground side), (a) dimensions in [mm] (not to scale), (b) photo

Four anchor specimens with different configurations of the high-strength grout cylinder on the ground side, simulating applications in both rock and soil, were investigated; an overview of the experimental series is shown in Table 3.1 and of the anchor configurations in Fig. 3.3. In experiment S605, a 7- mm-thick and 605-mm-long steel tube with an inner diameter of 100 mm was used to simulate the stiffness and confining pressure of a surrounding rock mass, as shown in Fig. 3.3 (a). Based on the thick-wall cylinder theory, the elastic modulus of the equivalent rock medium, with a Poisson's ratio of 0.25, was 35.6 GPa. No further CFRP confinement ring was applied to the grout cylinder in this case. For applications in soil, the weak confinement provided by the surrounding soil mass is negligible and thus no steel tube was used. In this case, a 2-mm-thick CFRP confinement ring with an inner diameter of 100 mm was installed around the grout-embedded strap end to deviate the spreading forces, as shown in Fig. 3.3 (b) and (c). The elastic modulus of a surrounding soil medium, equivalent to the CFRP ring, was 8.8 GPa, assuming a Poisson's ratio of 0.25. The length and position of the CFRP ring were varied between anchors C380 and C200, while the unconfined grout part remained 200 mm long in both cases. The 380-mm length covered both regions where spreading forces arose, i.e. the strap end and strap-rod transition, while the 200 mm covered only the latter region and thus failure was expected in the former one. Furthermore, an 80-mm-long steel ring was installed at the bearing end to prevent local boundary failure during the pull-out experiments and a 50-mm-long bond break was inserted, in all specimens, by installing a plastic tube of 23 mm diameter around the CFRP tendon.

Table 3.1: Overview of experimental series and results

Specimen	Confinement	Confinement length (mm)	Confinement thickness (mm)	Ultimate load (kN)	Failure mode
S605	Steel tube	605	7	497	Strap rupture
C380-1	CFRP ring	380	2	529	Grout compression
C380-2	CFRP ring	380	2	474	Grout compression
C200	CFRP ring	200	2	256	Grout splitting

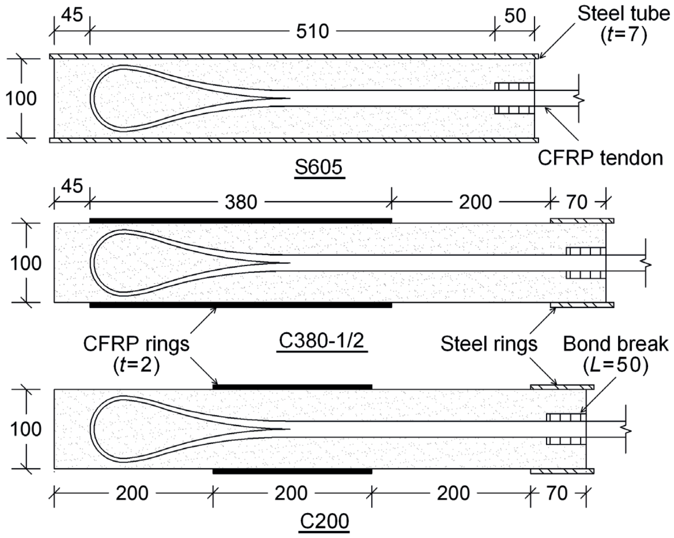

Fig. 3.3: Configurations of CFRP anchor heads on ground side (dimensions in [mm])

The anchors heads were poured in vertical position, using the steel tube (S605) or the CFRP rings, extended by carton tubes, as molds (C200/380). The three configurations of the anchor specimens are shown in Fig. 3.4. Configuration C380 was investigated twice to evaluate the repeatability of the results. After casting, the specimens were stored for 28 days at room temperature for grout curing.

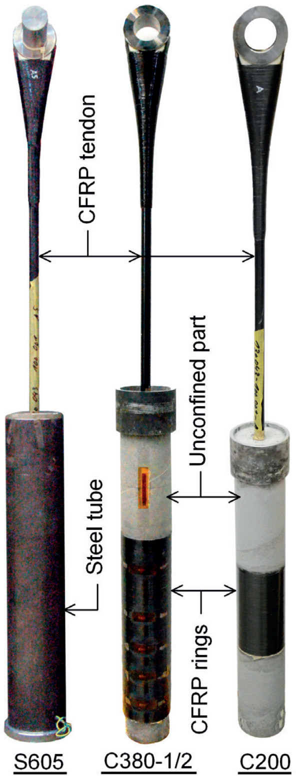

Fig. 3.4: One-strap anchor specimens

3.2.2 Material description

The CFRP tendons were composed of unidirectional UTS50 F24 24k 1600tex D carbon fibers impregnated with XB 3515 epoxy resin; the fiber volume fraction was 60 ± 2%. The nominal breaking load (NBL) was 335 kN according to the supplier. In order to investigate the tendon stiffness (*EA* = elastic modulus × cross-section area), a 300-mm-long rod segment, with an average diameter of 19.32±0.05 mm, was cut from the undamaged part of one tendon after the pull-out experiment and then investigated in a tensile experiment using a Walter+Bai LFV200 machine. Three load cycles up to 20 kN with a loading rate of 5 mm/min were applied. An extensometer with a gage length of 61 mm was installed in the middle of the rod specimen to measure the elongation. The average stiffness, calculated based on the load-elongation responses obtained in the last two cycles, was 42.0 MN and the corresponding average elastic modulus of the CFRP material was thus calculated as 143.4 GPa. The CFRP confinement rings were fabricated by filament winding, with an elastic modulus of 170 GPa (manufacturer data).

A non-shrink high-strength sand/cement grout SikaGrout-212 (provided by Sika Schweiz AG, Switzerland) with a maximum aggregate size of 4 mm was used; the water/cement ratio was 0.12. According to the product manual, the elastic modulus and 28-day uniaxial compressive strength were 36.7 GPa and 70 MPa respectively. Three cylinder specimens were cast from the same batch of grout as used for the anchor specimens and cured under the same conditions. They were investigated in compression according to the recommendations of RILEM [16]. Cylinder G1 was loaded in axial-deformation-control mode at a rate of 0.3 mm/min, while the other two specimens were controlled via a combination of axial (0.06 mm/min) and lateral (0.03 mm/min) deformations to obtain a complete stress-strain curve. Three Omega gages were installed at 120-degree intervals between the upper and lower loading platens to measure the axial deformation. Furthermore, friction-reducing pads, consisting of two 0.1-mm-thick Teflon sheets with a layer of bearing grease in between, were used. A summary of the experimental results is shown in Table 3.2. The average compressive strength was 62.2 MPa and thus 9% lower than the supplier value.

Table 3.2: Summary of uniaxial compression experiments on grout cylinders

Specimen	Diameter (mm)	Length (mm)	Load rate (mm/min)	Ultimate load (kN)	Compressive strength (MPa)	Peak strain (%)
G1	99.3	199.5	0.30/-	520	66.9	0.265
G2	99.3	198.2	0.06/0.03	440	57.8	0.263
G3	99.0	199.9	0.06/0.03	475	61.8	0.271
Avg.				478	62.2	0.266

3.2.3 Experimental set-up and instrumentation

A self-balanced experimental set-up was designed for the pull-out experiments, as shown in Fig. 3.5 (a). The load was transferred from two identical hollow-plunger hydraulic cylinders of 576-kN capacity to the upper strap end through a steel frame, while the vertical movement of the anchor head was blocked by steel plates under the cylinders. The steel plate support of the anchor head simulated the support provided by the grout cylinder of the normally 3–10-m-long grouted anchoring length, in which the anchoring force is transmitted from the ground-side anchor head to the surrounding rock or soil. In experiment S605, the loading was manually applied in load-control mode at a rate of 15 kN/min. In the other experiments, the loading was controlled by a digital multi-channel control system Walter+Bai PCS 8000; one of the hydraulic cylinders was in displacement-control mode at a rate of 0.3 mm/min, while an identical load pressure was applied to the other cylinder. Five load cycles up to 25, 50, 100, 150 and 200 kN respectively were applied to anchors C380-1/2 before the failure cycle. Only the first three were applied in S605 and the first two in C200 due to the lower expected capacity.

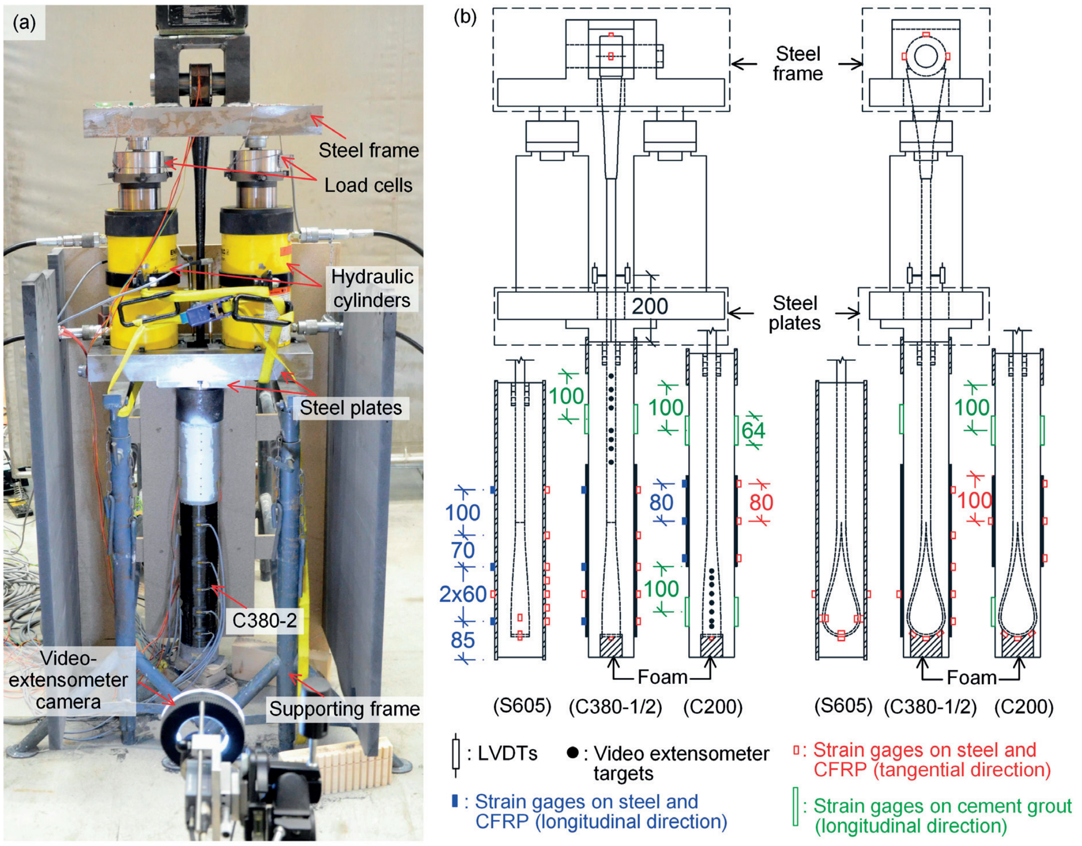
(a)
Steel frame
Load cells
Hydraulic cylinders
Steel plates
C380-2
Video-extensometer camera
Supporting frame
(b)
Steel frame
200
Steel plates
100
100
64
100
100
80
80
100
100
70
2x60
85
100
Foam
Foam
(S605)
(C380-1/2)
(C200)
(S605)
(C380-1/2)
(C200)
: LVDTs
●: Video extensometer targets
: Strain gages on steel and CFRP (tangential direction)
: Strain gages on steel and CFRP (longitudinal direction)
: Strain gages on cement grout (longitudinal direction)

Fig. 3.5: Experimental set-up and instrumentation layout (dimensions in [mm])

The instrumentation layout is shown in Fig. 3.5 (b). The loads in the two hydraulic cylinders were measured by two load cells located between the cylinders and the steel frame. Three types of instruments were used: Linear Variable Differential Transformer (LVDT) transducers, strain gages and video extensometers. The LVDTs were installed at a distance of

200 mm from the top surface of the anchor head to measure the pull-out displacement. Strain gages (1-LY61-6/120 from HBM AG, Switzerland) were used for the CFRP tendons (in the fiber direction, see Fig. 3.5 (b)), steel tube and CFRP rings (in the longitudinal or tangential directions), while gages with a 50-mm-long measuring grid (1-LY41-50/120 from HBM AG, Switzerland) were installed on the unconfined grout cylinders (in the longitudinal direction). Furthermore, video extensometers were used in experiments C380-1, C380-2 and C200 to derive the strain distributions in the longitudinal direction on the unconfined grout cylinder.

In the first experiment (S605), three axial gages were installed on both the inner and outer sides of the embedded strap (see Fig. 3.5 (b)). In order to protect these gages during grout casting and curing, a combined layer of 2-mm-thick silicon and 3.05-mm-thick ABM 75 (0.05-mm-thick aluminum foil coated with 3-mm-thick kneading compound) was applied on the gage surfaces. These thick layers interrupted the contact between the strap and grout on the inner side, leading to local bending of the strap. In the experimental results shown later, this local bending effect was eliminated by averaging the measurements of the gages installed on opposite sides at the same location. In the other experiments, only three gages on the outer surface of the strap were installed. A foam block of 90×60×45 mm^3 was placed under the embedded strap end during the grout casting (see Fig. 3.5 (b)). This block was removed after 21 days and the gages were then connected to the data acquisition system.

3.3 Results and discussion

3.3.1 Load vs pull-out displacement responses and failure modes

All anchors exhibited similar load vs pull-out displacement responses in the failure cycle, as shown in Fig. 3.6; the load cycles of anchor C380-1 are shown in the window of Fig. 3.6. A linear response was mainly observed, except the minor nonlinear behaviors at the beginning in all the specimens and at the end close to the ultimate load in the partially confined anchors. No stiffness degradation was observed between the cycles, but slight residual displacements were seen after unloading to 5 kN, resulting from the friction at the CFRP/grout interface.

The pull-out displacement was composed of two parts: the elongation of the CFRP tendon (d_C) and the compressive deformation of the grout (d_G). Assuming a linear stress-strain response for the grout and a uniform load distribution along the length after strap activation, $d_{C,cal}$ and $d_{G,cal}$ can be calculated, between 100 and 400 kN (ΔF), as $\Delta F \cdot L_C/(E \cdot A)$ and $\Delta F \cdot L_G/(E \cdot A)$, where L_C is the distance between the LVDT and strap end and L_G is the embedded length of the tendon, see Table 3.3; and E and A are the elastic modulus and cross-section area of the CFRP tendon and grout (see above). The resulting pull-out displacements, $d_{C+G,cal}$ (= $d_{C,cal}$ + $d_{G,cal}$), are in good agreement with the experimental ones, $d_{C+G,exp}$, as shown in Table 3.3. The tendons exhibited much higher deformations than the grout. Furthermore, anchor S605 showed a slightly higher stiffness (k_{exp}), assumed as being the slope of the load vs pull-out displacement curves ($\Delta F/d_{C+G,exp}$), than the others due to the smaller embedded length.

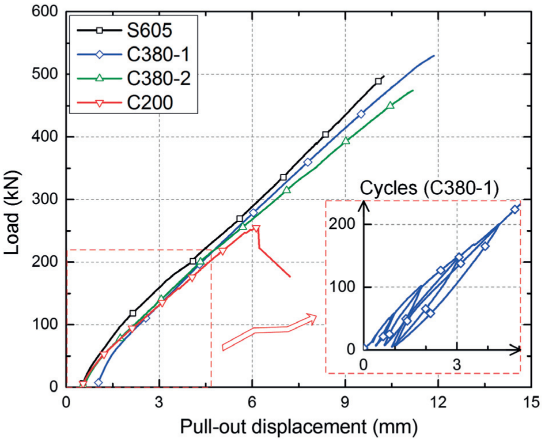

Fig. 3.6: Load vs pull-out displacement responses (failure cycle)

Table 3.3: Deformation and stiffness calculation

	ΔF (kN)	L_C (mm)	$d_{C,cal}$ (mm)	L_G (mm)	$d_{G,cal}$ (mm)	$d_{C+G,cal}$ (mm)	$d_{C+G,exp}$ (mm)	$d_{C+G,cal}$ $/d_{C+G,exp}$	k_{exp} (kN/mm)
S605	100-400	760	5.44	560	0.61	6.05	6.57	0.92	45.8
C380-1	100-400	850	6.07	650	0.70	6.77	6.88	0.98	43.6
C380-2	100-400	850	6.07	650	0.71	6.78	7.02	0.97	42.8
C200	100-200	825	1.95	625	0.22	2.17	2.31	0.94	43.0

The obtained ultimate loads, F_u, and observed failure modes are listed in Table 3.1. Anchor S605 exhibited strap rupture, as shown in Fig. 3.7, while compression failure (C380-1/2, see Fig. 3.8) and splitting failure (C200, see Fig. 3.9) of the unconfined grout occurred in the partially confined cases. In the strap rupture case, the failure was located at the position of one inner strain gage, where the CFRP/grout interface was interrupted by the thick protection layer, as mentioned before (see Fig. 3.7 (b)). This premature failure reduced the ultimate load of anchor S605 (497 kN) by at least 6.0% compared to C380-1 (529 kN) where no strap rupture occurred. Furthermore, delamination in the strap was observed at the locations where the other inner gages were installed (see Fig. 3.7 (c)), while no failure was observed in the grout, except minor inclined cracks (see Fig. 3.7 (a)).

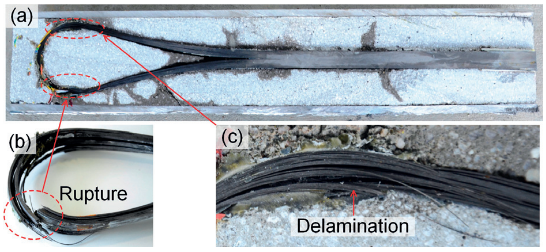
(a)
(b)
Rupture
(c)
Delamination

Fig. 3.7: Failure mode of anchor S605: (a) cut view of ground-side anchor head; (b) rupture of embedded strap at gage location; (c) strap delamination at gage location

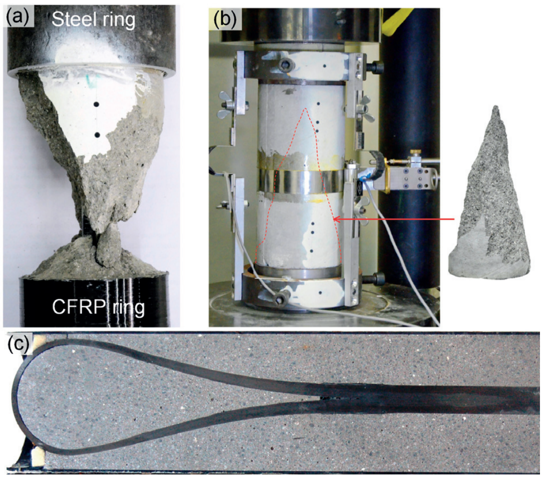
(a)
Steel ring
CFRP ring
(b)
(c)

Fig. 3.8: Failure mode of anchor C380-2: (a) double-cone failure of unconfined grout; (b) similar failure mode in uniaxial compression experiment G1; (c) undamaged strap in confined part

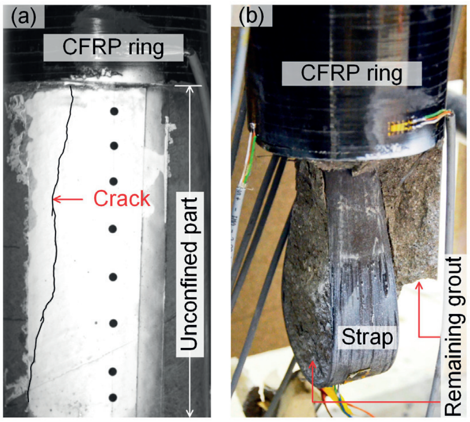
(a)
CFRP ring
Crack
Unconfined part
(b)
CFRP ring
Strap
Remaining grout

Fig. 3.9: Failure mode of anchor C200: (a) vertical grout crack at around 250 kN; (b) splitting failure of unconfined grout around embedded strap

In the grout failure cases (anchors C380-1/2), a double-cone failure mode was observed in the unconfined part, as shown in Fig. 3.8(a), which resembled the one in the uniaxial compression experiments on cylinder G1 (see Fig. 3.8(b)); similar ultimate loads were also obtained (see Table 3.2). The embedded straps remained undamaged. In contrast, anchor C200, where the strap was only partially confined, exhibited a 51.6 and 46.0% lower ultimate load compared to C380-1 and C380-2 respectively. A vertical crack in the unconfined grout around the strap was observed at around 250 kN due to tensile stresses in the radial direction (which could not be balanced by a confinement ring at this location), leading to a final splitting failure, while the grout inside the strap remained undamaged, as shown in Fig. 3.9. It could be concluded that the length and position of the CFRP ring had a significant influence on the load-bearing capacity of the partially confined anchors. The load-bearing capacity of these anchors mainly depended on the uniaxial compressive strength of the unconfined grout outside the strap region, if the CFRP confinement ring was installed at an optimized position to balance the spreading forces from the strap.

3.3.2 Load vs tangential tensile strain responses of CFRP tendons

The load vs tangential tensile strain responses of the upper (air-side) straps are shown in Fig. 3.10. The straps exhibited linear behavior until failure and no stiffness loss was observed during the cycles. The maximum strain location varied, i.e. it was at position C1 in anchor S605 and at C2 in C380-1 and C200. The strain differences between these two positions, however, were small (less than 10%) and could be traced back to a slight deviation of the gage axis from the fiber direction, minor variations of the strap thickness in the width direction and friction effects between the two positions. The maximum measured strain (1.10% at position C2 in anchor C380-1 at 529 kN) was 6.8% lower than the calculated average strain in the cross section (1.18%, from the load divided by the cross-section area and elastic modulus), which could be attributed to the local bending at position C2. The calculated load vs average strain curve is also shown in Fig. 3.10.

The load vs tangential tensile strain responses of the embedded straps are shown in Fig. 3.11; in anchor S605, the average strain values on the two opposite sides, at the same location on the strap, were used (as mentioned above). In all the anchors, the load transfer to the embedded strap was delayed and occurred between 100–200 kN, due to the bond and friction at the CFRP/grout interface, and also the transition from the rod to the flat and curved strap geometry, which already transferred part of the load to the grout through transverse compression (i.e. the spreading forces). The friction also depended on the confinement level, i.e. the higher the confinement, the later the strap was activated due to the higher friction. These mechanisms decreased the maximum strains at the ultimate loads at the embedded strap ends compared to the air-side ones. The loads transferred to the strap ends in anchors S605 and C380-1 at failure, calculated based on the measured strains (0.54 and 0.56% respectively), were 247 and 255 kN, corresponding to only 49.6 and 48.2% of their ultimate loads respectively. Furthermore, recovery of the strap strains during unloading was also prevented by the friction behavior. The strains thus remained at the same level during the unloading and reloading cycles (see Fig. 3.11).

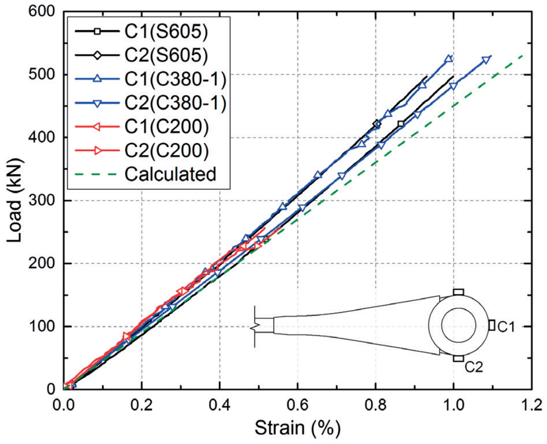

Fig. 3.10: Load vs tangential tensile strain responses of air-side straps

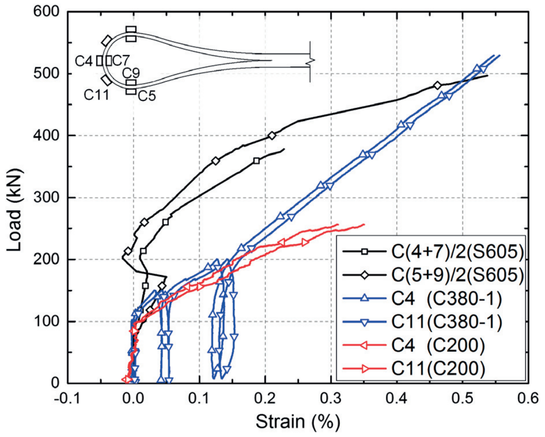

Fig. 3.11: Load vs tangential tensile strain responses of embedded straps

3.3.3 Tangential tensile strain distributions in steel and CFRP confinements

According to the multi-strap concept described in the introduction, the tangential tensile strains that occurred in the one-strap version can primarily be attributed to the deviation of the spreading forces into the cylinder's axial direction and secondly to the radial pressure of the axially compressed grout. The spreading forces occur mainly at two locations: the semicircular strap end and the curved transition from the flat strap to the rod geometry. At both locations the spreading forces arise 1) in the strap plane and 2) perpendicular to the strap plane, and thus cause tangential tensile strains 1) perpendicular and 2) parallel to the strap plane at these locations.

The tangential tensile strain distributions along the confinement elements in anchors S605, C380-1 and C200, parallel and perpendicular to the strap plane, are shown in Figs. 3.12–14 respectively. In all the anchors the strains were insignificant below 100 kN, i.e. before the strap was activated. During the subsequent load increase, strain peaks formed at the two above-mentioned locations of spreading force deviation: 1) positions R1 in anchor S605 and R3 in C380-1; and 2) positions R6 in S605, R6 and R11 in C380-1, and R2 and R5 in C200. However, the maximum strains at the ultimate loads were still low compared to the material ultimate strains. Furthermore, a sudden strain increase at 245 kN was observed in anchor C200 (at positions R1 and R4 in Fig. 3.14), caused by the load redistribution after cracking of the unconfined grout around the embedded strap. The strains along the cylinder length that generally increased with increasing load (i.e. not taking into account the peak effects) were caused by the increasing radial pressure of the grout.

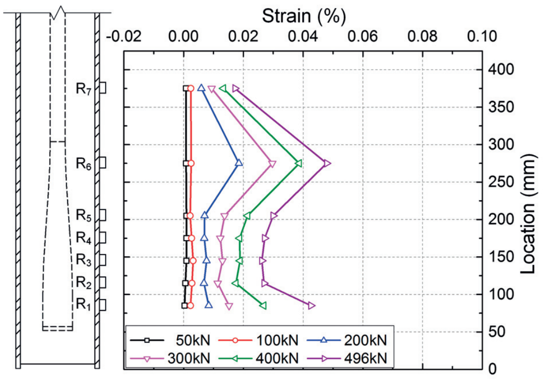

Fig. 3.12: Tangential tensile strain distributions along steel tube in S605 at different load levels, parallel to strap plane

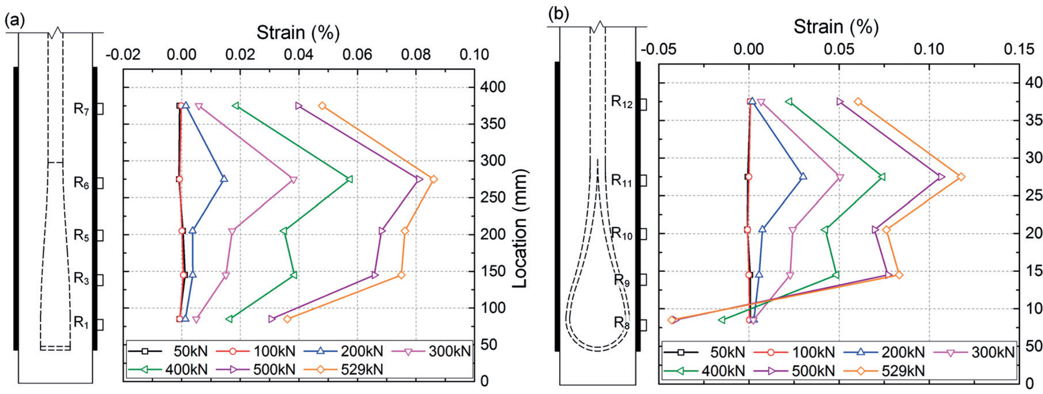

Fig. 3.13: Tangential tensile strain distributions along steel tube in C380-1 at different load levels: (a) parallel to strap plan; (a) perpendicular to strap plane

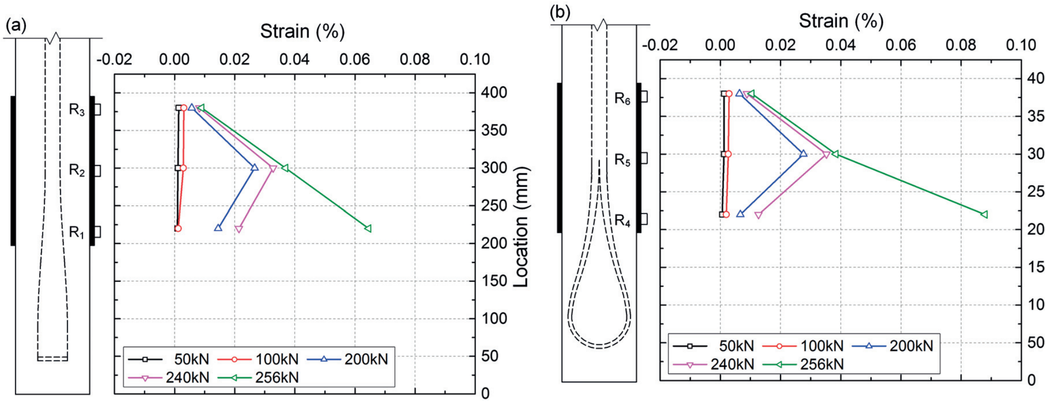

Fig. 3.14: Tangential tensile strain distributions along CFRP ring in C200 at different load levels: (a) parallel to strap plan; (a) perpendicular to strap plane

3.3.4 Longitudinal compressive strains in unconfined grout

The load vs longitudinal compressive strain responses in the unconfined grout, between the CFRP and 80-mm steel rings in anchors C380-1 (position G3) and C200 (G1) are shown in Fig. 3.15. In both anchors, the compressive strains increased almost linearly up to around 200 kN, and nonlinear behavior was then observed during the subsequent loading. In contrast, the unconfined grout located around the strap end in anchor C200 (position G7) exhibited significantly lower strains caused by the force spreading and delay in activation.

The ultimate strain at the peak load in anchor C380-1 (-0.47%, position G3 in Fig. 3.15) was significantly higher than the values obtained from the cylinder experiments (-0.27% in Table 3.2). The former was measured at the mid-height of the unconfined grout cylinder over a gage length of 50 mm, while the latter was an average estimated based on the axial deformation of the cylinders. The higher value in the former case resulted from a compressive strain localization at mid-height of the unconfined cylinder, between positions T3 and T5 as shown in Fig. 3.16 (video extensometer results), which could be attributed to the initiation of grout cracking in this zone. A similar compressive strain localization was also observed in compression experiments on concrete cylinders [17]. Furthermore, a strain decrease from T1 to T8 was observed below 300 kN, which may be attributed to the decreasing load along the tendon due to friction.

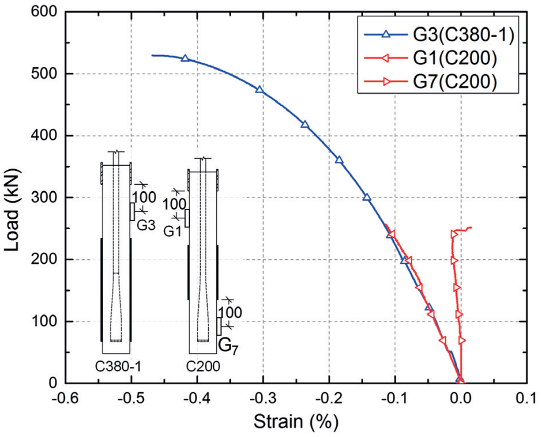

Fig. 3.15: Load vs compressive strain responses of unconfined grout

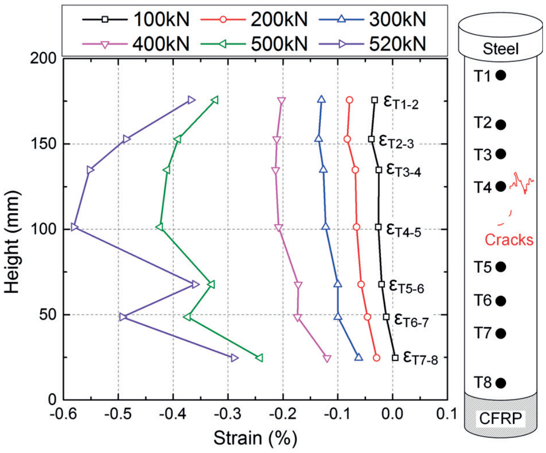

Fig. 3.16: Compressive strain distribution along length of unconfined grout in C380-1 at different load levels

3.3.5 Longitudinal compressive strain distributions in steel and CFRP confinements

The load vs longitudinal compressive strain responses along the confinement elements at two selected locations are shown in Fig. 3.17. Anchor C380-1 (position L2) and C200 (L1 and L2) exhibited almost identical responses up to 240 kN, which could be attributed to the similar measurement locations in the transition zone from the strap to the rod geometry and the identical CFRP/grout interfaces. In contrast, the strain at L2 in anchor S605 was 85.3% lower than in C380-1 due to the higher stiffness of the steel tube. Furthermore, only small strains were observed at L1, close to the strap end in both anchors S605 and C380-1; a decreasing behavior even occurred above around 150 kN in C380-1. Both observations concerning anchor C380-1 may indicate a possible slippage between the CFRP ring and grout close to the ring edge.

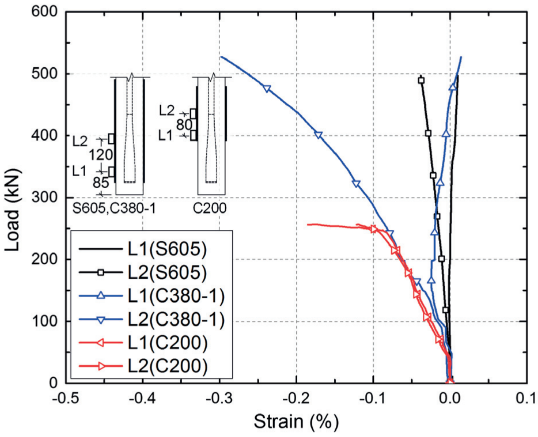

Fig. 3.17: Load vs longitudinal compressive strain responses in steel tube and CFRP rings

3.3.6 Confinement efficiency

According to the anchor concept, as explained above, the primary purpose of the CFRP ring is to balance the spreading forces and deviate them into the axial direction. Nevertheless, the axial compression in the grout cylinder also exerts a radial pressure on the CFRP ring and both effects increase the tangential strains in the ring. Based on the measurements of these strains along the anchor length, in the following an analysis is made of how these two mechanisms were activated and to what extent the compressive strength of the grout was also increased by the confining pressure. The confinement exerted by the embedded strap on the enclosed grout is also analyzed.

In anchor C380-2 for example, the confinement was progressively activated from the loading side (R12) to the strap end (R8) between 40 and 100 kN, as shown in Fig. 3.18. Gages R12 and R11 must have been activated by an initiation of slippage between the grout and CFRP rod at the end of the straight part; no relative movement had yet occurred in the R10 zone due to the additional friction caused by the curved geometry. A corresponding average bond stress, τ, between the CFRP rod segment and the grout could be estimated by dividing the activation load, F_{act}, by the rod surface in contact with the grout ($A_R=d_R\cdot l_b$, where d_R = rod diameter and l_b = bond length), assuming a uniform distribution of bond stress at the interface. For R12 and R11, F_{act}=37.5 and 57.5 kN, and l_b=230 and 330 mm (distance between the gage locations and bond break), which results in τ=2.7 and 2.9 MPa respectively. With increasing load, the slippage propagated into the curved zone and part of the load in the tendon started to be transferred to the grout by transverse pressure, i.e. the emerging spreading forces, which also locally initiated the tangential strains, as described above. In the last step, R9 and R8 were activated by the same mechanisms.

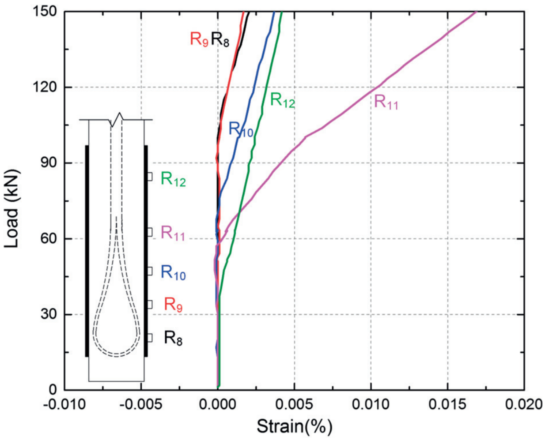

Fig. 3.18: Activation sequence of confinement along CFRP ring in C380-2 derived from tangential tensile strains

Based on the tangential strains in the CFRP rings and in the semicircle of the strap, ε_t, the radial confining pressure, f_r, at the inner surface of these elements, assuming a uniform pressure distribution, can be calculated as:

$$f_r = \frac{2 \cdot t \cdot E \cdot \varepsilon_t}{d} \tag{3.1}$$

where E, d and t are the elastic modulus, inner diameter and thickness of the confinement elements. At positions R5/R10 (similar values at R3/R9) and R6/R11 of the CFRP ring and at

C4/C11 of the strap, in anchor C380-1 that exhibited the maximum ultimate load, f_r was calculated, as shown in Table 3.4. A high confining pressure of 85.3 MPa resulted at the inner surface of the strap, while the values in the CFRP ring were small. Under these confining pressures, the confined compressive strength of the grout, f'_{cc}, assuming that the grout exhibited a confined behavior comparable to concrete, could be estimated as [18]:

$$f'_{cc} = (1 + k_1 \frac{f_r}{f'_{c0}}) f'_{c0} \tag{3.2}$$

where k_1 is the confinement effectiveness coefficient, which can be obtained from formulations derived from experiments with FRP confinements (see Table 3.4), and f'_{c0} is the unconfined compressive strength of the grout (62.2 MPa). The resulting f'_{cc} values, shown in Table 3.5, indicated that the compressive strength improvement was significant in the grout inside the strap (3.2–3.9 times f'_{c0}). At this location, f'_{cc} (197.0–240.5 MPa) was significantly higher than the compressive stress, 86.1 MPa, estimated by dividing the load transferred to the strap end (255 kN, see above) by the inner diameter (74 mm) and width (40 mm) of the strap. This comparison also confirmed that no failure occurred in the grout (see Fig. 3.8 (c)). In contrast, the compressive strength improvement caused by the CFRP ring confinement was small (1.2–1.4 times f'_{c0}). Compared to the results obtained from anchor C200, it was thus confirmed that the CFRP rings mainly served to deviate the spreading forces in the strap zone and prevented premature failure in those regions.

Table 3.4: Calculation of confinement effectiveness coefficient k_1 in anchor C380-1

	f_r (MPa)	$k_1 = 6.0 f_r^{-0.3}$ [19]	$k_1 = 2.2(f_r / f'_{c0})^{-0.16}$ [20]	k_1 [18]
$\varepsilon_{R6/R11} = 0.102\%$	6.9	3.36	3.13	2
$\varepsilon_{R5/R10} = 0.076\%$	5.2	3.66	3.27	2
$\varepsilon_{C4/C11} = 0.552\%$	85.3	1.58	2.09	2

Table 3.5: Estimation of confined compressive grout strength

Location	k_1	f'_{cc} (MPa)	f'_{cc} / f'_{c0}
R6/R11	[2, 3.36]	[76.1, 85.5]	[1.2, 1.4]
R5/R10	[2, 3.66]	[72.6, 81.2]	[1.2, 1.3]
C4/C11	[1.58, 2.09]	[197.0, 240.5]	[3.2, 3.9]

3.4 Conclusions

Pull-out experiments were performed on four CFRP ground anchors with one-strap ends. To simulate applications in a rock mass, a steel tube was used to exert the confining pressure of the rock mass on the prefabricated high-strength grout cylinder of the anchor. In a soil mass, however, where significant confinement cannot be expected, the anchors were confined with CFRP rings that were installed around the grout-embedded strap ends at different positions and lengths. The following conclusions were drawn:

1. In rock applications, the anchor can be applied directly without additional confinement, while in the case of soil, an additional CFRP confinement ring is needed to prevent premature grout failure in the strap region.
2. With optimized location and length of the CFRP ring, i.e. assured deviation of the spreading forces, the anchor capacity is only limited by the uniaxial compressive strength of the unconfined grout cylinder at the transition to the free anchor length.
3. The load is transferred progressively from the strap to the grout cylinder: approximately 50% of the load is transferred at the semicircular strap end while the remaining 50% is transferred at the CFRP/grout interface and curved transition part from the flat strap to the circular rod geometry. The embedded strap is thus much less loaded than the air-side strap.
4. The load transfer at the strap end and strap-rod transition occurs through spreading forces that are balanced and deviated in the cylinder direction by the confinement rings, leading to tangential strain concentrations at these locations.

References

[1] Xanthakos PP. Ground anchors and anchored structures. Washington, U.S.A.: John Wiley & Sons, 1991.

[2] European Committee for standardization (CEN). Execution of special geotechnical work–ground anchor. BS EN 1537, Brussels, Belgium, 2000.

[3] Aoyagi K, Yoshida T, Yamazai Y, Maruyama K. NM (new material) ground anchor system. In: Proceedings of the 2nd international conference on advanced composite materials in bridges and structures, Montreal, Canada, 11-14 August 1996. 727-34.

[4] Benmokrane B, Xu H, Nishizaki I. Aramid and carbon fibre-reinforced plastic prestressed ground anchors and their field applications. Can J Civ Eng 1997;24:968-85.

[5] Tokyo Rope Co. Ltd. Summary of application projects. <https://isabou.net/sponsor/nm-anchor/sekou.asp> (May 02, 2016).

[6] Zhang K, Fang Z, Nanni A, Hu J, Chen G. Experimental Study of a Large-Scale Ground Anchor System with FRP Tendon and RPC Grout Medium. J Compos Constr 2014;19:04014073.

[7] Schmidt JW, Bennitz A, Täljsten B, Goltermann P, Pedersen H. Mechanical anchorage of FRP tendons–A literature review. Constr Build Mater 2012;32:110-21.

[8] Meier U, Farshad M. Connecting high-performance carbon-fiber-reinforced polymer cables of suspension and cable-stayed bridges through the use of gradient materials. J Comput Aided Mater 1996;3:379-84.

[9] Wang X, Xu P, Wu Z, Shi J. A novel anchor method for multitendon FRP cable: manufacturing and experimental study. J Compos Constr 2015;19:04015010.

[10] Winistöerfer AU. Development of non-laminated advanced composite straps for civil engineering applications. Coventry, UK: Department of Engineering, University of Warwick; 1999.

[11] Fan H, Vassilopoulos AP, Keller T. Experimental and numerical investigation of tensile behavior of non-laminated CFRP straps. Compos B Eng 2016;91:327-36.

[12] Keller T, Kenel A, Koppitz R. Carbon Fiber-Reinforced Polymer Punching Reinforcement and Strengthening of Concrete Flat Slabs. ACI Struct 2013;110.

[13] Huster U, Broennimann R, Winistörfer A. Strengthening of a historical roof structure with CFRP-straps. In: Proceedings of the 4th International Conference on FRP Composites in Civil Engineering (CICE2008), Zurich, Switzerland, July 8.B.4; 2008.

[14] Triantafillou TC, Fardis MN. Strengthening of historic masonry structures with composite materials. Mater Struct 1997;30:486-96.

[15] Djamaluddin R, Yamaguchi K, Hino S. Mechanical behavior of the U-anchor of super-CFRP rod under tensile loading. J Compos Mater 2014;48:1875-85.

[16] RILEM TC 148-SSC. Test method for measurement of the strain-softening behaviour of concrete under uniaxial compression. Mater Struct 2000;33:347-51.

[17] Jansen DC, Shah S P. Effect of length on compressive strain softening of concrete. J Eng Mech, 10.1061/(ASCE)0733-9399(1997)123:1(25), 25-35.

[18] Lam L, Teng J. Strength models for fiber-reinforced plastic-confined concrete. J Struct Eng, 10.1061/(ASCE)0733-9445(2002)128:5(612), 612-623.

[19] Samaan M, Mirmiran A, Shahawy M. Model of concrete confined by fiber composites. J Struct Eng, 10.1061/(ASCE)0733-9445(1998)124:9(1025), 1025-1031.

[20] Saafi M, Toutanji H, Li Z. Behavior of concrete columns confined with fiber reinforced polymer tubes. ACI Mater J 1999;96(4):500-509.

4.

Pull-out behavior of CFRP ground anchors with two-strap ends

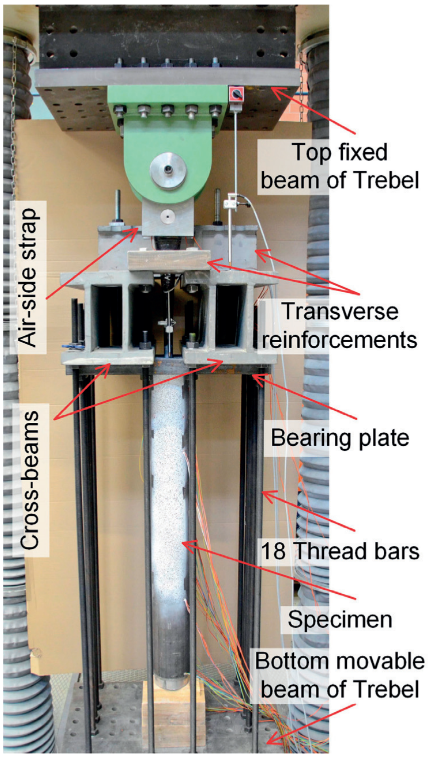
Top fixed beam of Trebel
Air-side strap
Transverse reinforcements
Cross-beams
Bearing plate
18 Thread bars
Specimen
Bottom movable beam of Trebel

Reference detail:

Fan H, Vassilopoulos AP, Keller T. Pull-out behavior of CFRP ground anchors with two-strap ends, Compos Struct 2017;160:1258–1267.

4.1 Introduction

Fiber-reinforced polymer (FRP) tendons are increasingly used to replace conventional steel tendons in ground anchors, taking advantage of their high strength-to-weight ratio and good corrosion resistance. Glass-FRP (GFRP) bars and cables are mainly used in temporary anchors for mining applications, due to their inferior durability and mechanical properties compared to aramid- and carbon-FRPs (AFRPs and CFRPs) [1]. Prestressed AFRP and CFRP tendons are used in permanent ground anchors since 1990 [2].

Conceptually similar to steel strands, FRP strands were also developed by twisting together a certain number of small-diameter wires. A high load-bearing capacity could be achieved by forming an FRP cable assembled from several strands, for example in the Carbon Fiber Composite (CFCC) system commercialized by Tokyo Rope in Japan. CFCC products are composed of two to six Φ12.5-mm strands consisting of seven twisted wires each, which can achieve ultimate loads of 350–1000 kN; the tendons are usually prestressed to 60% of the ultimate load. Because of their excellent mechanical properties and resistance to various environmental conditions, permanent prestressed CFCC tendons were reported as being used in around 80 ground anchor applications in Japan between 1993–2015 [2, 3]. FRP Cables based on a similar concept, assembled from rods with nominal diameters of 4.0 mm [4] or 12.6 mm [5], were also developed and studied.

To anchor the CFRP tendon on the air and ground sides, mechanical or bonded anchors are commonly used [6]. These types of CFRP anchors present two problems however, which could lead to premature failure in the anchor and thus prevent the full tendon capacity from being exploited: 1) high shear and through-thickness stress concentrations at the anchorage are more critical than in steel anchors due to the anisotropic properties of CFRP fibers; 2) uneven load distributions occur among the assembled strands or rods, i.e. some may be less loaded than others [4].

A simpler and much more material-tailored anchorage method, based on strap ends, was thus developed [7] and already used in different strengthening applications, e.g. against punching of concrete flat slabs [8], and for timber roof structures [9] and masonry structures [10]. A new application of this strap anchorage method for permanent prestressed CFRP ground anchors was recently proposed [11], consisting of a CFRP tendon with a multi-strap end on the ground side, embedded in a prefabricated high-strength grout cylinder confined with CFRP rings, as shown in Fig. 4.1. The main purpose of the CFRP rings is to deviate the spreading forces at the embedded strap ends into the cylinder's axial direction and not to increase the grout strength. The grout cylinder is thus axially loaded stepwise by the axial components of the spreading forces. The ground anchor with the prefabricated anchor body can be 20–80 m long and coiled for transportation to the construction site; it is then inserted into the borehole, anchored by injecting fresh standard (normal-strength) grout and finally prestressed to 60% of the design load. The normal-strength grout transfers the load from the high-strength grout to the surrounding ground material.

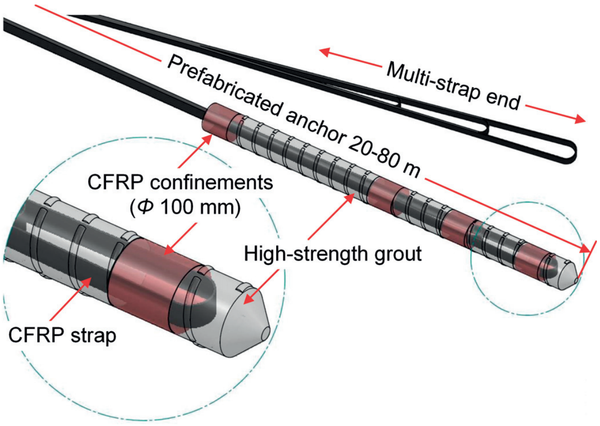

Fig. 4.1: Prestressed and permanent CFRP ground anchor with multi-strap ends

In a first stage, a CFRP ground anchor with a single-strap end on the ground side was developed [11]. A CFRP confinement ring (see Fig. 4.1) was installed at the strap end to deviate the spreading forces according to the anchor concept. A load-bearing capacity of around 500 kN was achieved in pull-out experiments, which is appropriate for soil applications. The load transfer from the strap to the grout cylinder occurred progressively; approximately 50% of the load was transferred at the semicircular strap end, while the remaining 50% was transferred at the curved transition from the strap to the rod segment of the free length.

This chapter presents the second development stage, where a two-strap end was conceived on the ground side to increase the load-bearing capacity to a load of more than 1000 kN, which normally needs a rock media to be anchored. Anchor specimens were pulled out from mortar cylinders confined by steel tubes of different thicknesses, which simulated different confinement levels of the rock mass. The load-transfer mechanisms within the anchor body components and from the anchor body to the steel tube are analyzed and discussed.

4.2 Experimental program

The anchor pull-out specimens were composed of different components and materials with different functions and fabricated by following a stepwise process. Therefore, their description will be subdivided in the following into the description of the pure CFRP tendon, the CFRP anchor head (tendon with confined high-strength grout anchor body), and the complete pull-out specimen (anchor head embedded in steel tube), including for each step the description of geometry, materials and fabrication.

4.2.1 CFRP tendon with strap ends

The CFRP tendons used in this study were produced by Carbo-Link, Fehraltorf, Switzerland. The tendons were 1.8 m long with a 32-mm-diameter rod segment between the ground-side two-strap and air-side one-strap ends, as shown in Fig. 4.2. On the ground side, the lengths, L, thicknesses, t, and inner diameters, d_{in}, of the semicircles of the large and small straps were 950 and 630 mm, 7 and 3 mm, and 66 and 44 mm respectively. On the air side, the thickness and inner diameter of the strap were 10 and 110 mm respectively; the strap was anchored by a steel ring and a pin of 50-mm diameter. The widths at all strap ends were 40 mm; the widths and thicknesses continuously varied in the segments located between the small-strap end and the division point, where the tendon geometry changed from the strap to the rod geometry; however, the total cross-section area, A, remained the same.

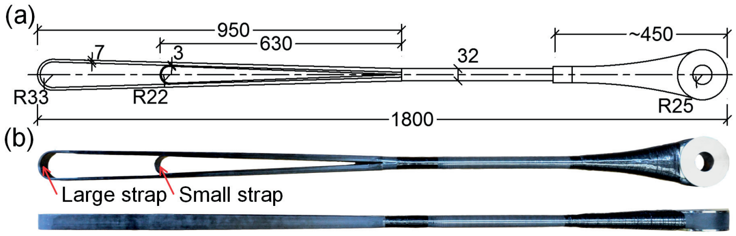

Fig. 4.2: CFRP two-strap tendon: (a) schematic (dimensions in [mm]); (b) photo

The CFRP tendons were composed of unidirectional UTS50 F24 24k 1600tex D carbon fibers impregnated with XB 3515 AD1571 ACC1573 epoxy resin; the fiber volume fraction was 60±2%; the same material constitution was used as in the single-strap anchors [11]. The nominal breaking load (NBL) was 1000 kN (manufacturer data), the elastic modulus 143.4 GPa and the ultimate strain 1.3–1.5%. The stiffness ratio between the large and small straps was 6:4 (stiffness defined as $2 \cdot E \cdot A / L$, where E is the Elastic modulus), which allowed a corresponding load distribution of approximately 60 and 40% between them (without considering the grout deformation). To achieve this load distribution, the two straps were separated by a Teflon sheet.

The tendons were fabricated in three steps: 1) winding the continuous unidirectional carbon fibers around a steel pin (ground side) and a steel ring (air side) at a 1390-mm center-to-center distance to form the small ground-side and inner part of the air-side strap end; 2) adding the Teflon sheet at the outer surface of the small strap and continuing winding the fibers around a second steel pin (ground side) and the steel ring (air side) at a 1695-mm center-to-center distance to form the large ground-side and complete the air-side strap end; 3) transversely wrapping the middle part to form the circular rod segment.

4.2.2 CFRP anchor heads

The two-strap end of the CFRP tendon was embedded in a 1060-mm-long high-strength grout body with an inclined and corrugated surface on the ground side, as shown in Fig. 4.3; the inclination angles of the 180-mm- and 430-mm-long corrugated surfaces were 2.2 and 2.6° respectively to improve the load transfer from the high- to normal-strength grout; the angles were optimized based on finite element analyses. Three 150-mm-long and 2-mm-thick identical CFRP confinement rings were installed around the two strap ends and the division point. These were all inserted from the large-strap end, and thus their inner diameters were all 100 mm. The anchor body geometry was designed to fit in boreholes with a minimum diameter of 130 mm.

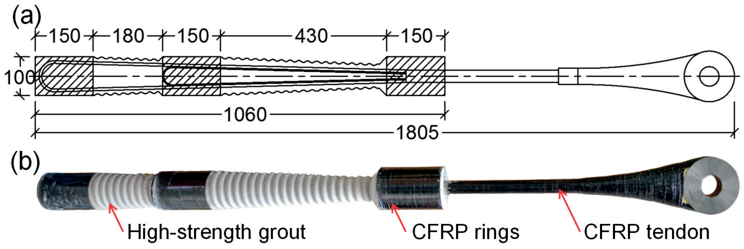

Fig. 4.3: CFRP two-strap anchor head: (a) schematic (dimensions in [mm]); (b) photo

A non-shrink sand/cement high-strength grout (SikaGrout-212 provided by Sika Schweiz AG, Switzerland) with a maximum aggregate size of 4 mm was used; the water/cement ratio was 0.12. The 28-day uniaxial compressive strength was 62.2 MPa [11].

The CFRP confinement rings, consisting of the same materials as the tendon, were fabricated by filament winding, thus achieving a higher fiber volume fraction than in the tendon and an elastic tangential modulus of 170 GPa (manufacturer data).

4.2.3 CFRP pull-out anchor specimens

The prefabricated anchor head was further inserted into a 1200-mm-long steel tube, simulating a rock mass as shown in Fig. 4.4. Three anchor specimens with two different tube thicknesses were investigated in order to study the influence of the rock stiffness on the load-bearing capacity of the CFRP anchor; an overview of the experimental series is shown in Table 4.1. The inner diameter and thickness of the steel tubes in anchors ST10-1/2 were 132.4 and 10 mm respectively, while 129.7 and 5 mm respectively were selected in ST5; these inner diameters corresponded to the minimum borehole size as mentioned above. Based on the thick-wall cylinder theory, the elastic moduli of the equivalent rock medium in these two cases, assuming a Poisson ratio of 0.25, were 38.0 and 20.7 GPa respectively, which are typical for sedimentary rocks [12]. Furthermore, a 50-mm-long bond break (see Fig. 4.4 (a)) was inserted by wrapping a 0.1-mm-thick Teflon sheet around the CFRP tendon. The 10-mm-thick tube configuration was investigated twice to evaluate the repeatability of the results.

Table 4.1: Summary of experimental results

Specimen	Tube thickness (mm)	First peak		Second peak		K_{exp} (kN/mm)
		Load (kN)	Location of complete rupture	Load (kN)	Location of complete rupture	
ST10-1	10	1344	Small strap: division point	925	Large strap: division point	92.0
ST10-2	10	1419	Small strap: end & large strap: division point	230	Air-side strap: end	92.0
ST5	5	1389	None	1402	Air-side strap: end	86.2

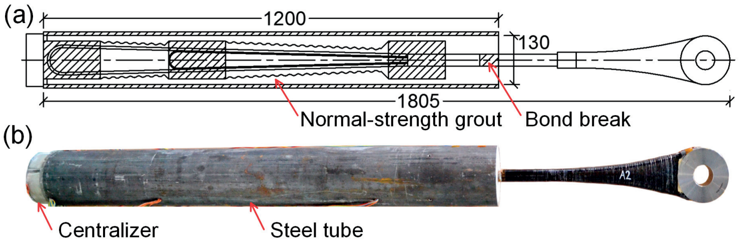

Fig. 4.4: CFRP two-strap anchor specimen: (a) schematic (dimensions in [mm]); (b) photo

A sand/cement grout commonly used for steel ground anchors (Sika normal rock anchor mortar, provided by Sika Schweiz AG, Switzerland) with a maximum aggregate size of 0.8 mm was used as the normal-strength grout; the water/cement ratio was 0.18. A superplasticizer Skiament-212 S with a dosage of 0.8% of the grout-powder weight was added to increase the workability. Three cylinders were fabricated using the normal-strength grout, cured at room temperature and investigated in compression at a rate of 0.05MPa/s, which was close to the equivalent rate in the pull-out experiments; the average compressive strength was 48.0±3.6 MPa. The elastic modulus and yield stress of the steel tube were 210 GPa and 355 MPa respectively.

The fabrication process of the anchor specimens is shown in Fig. 4.5. A polyurethane mold made of SikaBlock M700 was used, as shown in Fig. 4.5 (a). The mold surface was first greased with a demolding agent (Sika Separol), subsequently the CFRP tendon and rings were installed (see Fig. 4.5 (b)) and the high-strength grout was cast. The prefabricated part was demolded after three days (see Fig. 4.5 (c)), inserted into the steel tube and cast with normal-strength grout; the central position was achieved using four temporary screws at 90-degree intervals at the location of the CFRP ring around the division point (removed two hours after casting) and a centralizer located at the bottom of the steel tube (see Fig. 4.4). The pull-out experiments were conducted 21 days (anchor ST10-1) and 28 days (ST10-2 and ST5) after the casting of the normal-strength grout; the specimens were stored at room temperature during the curing period.

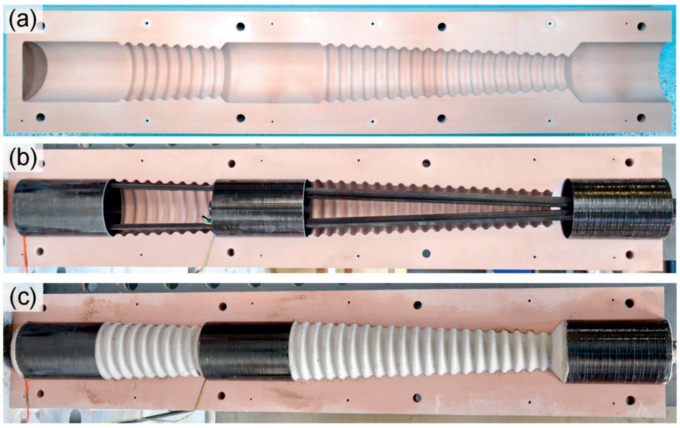

Fig. 4.5: Fabrication of two-strap anchor specimens (only anchor body is shown): (a) mold with corrugated surface; (b) installation of CFRP tendon and rings; (c) anchor head after casting of high-strength mortar

4.2.4 Experimental set-up and instrumentation

The pull-out experiments were conducted on a Trebel 10MN machine. The anchor was suspended at the air side by a steel pin from the top fixed beam of the machine. The loading was applied to the bottom movable beam in displacement-control mode at a rate of 1 mm/min, as shown in Fig. 4.6. The applied load was transferred to the top surface of the anchor body through a loading frame consisting of a bearing plate, two cross-beams, two transverse reinforcements and 18 thread bars; the bars were fixed to the cross-beams on one side and to the bottom movable beam of the machine on the other side. After four load cycles up to 100, 300, 500 and 700 kN respectively, the anchor was loaded up to failure.

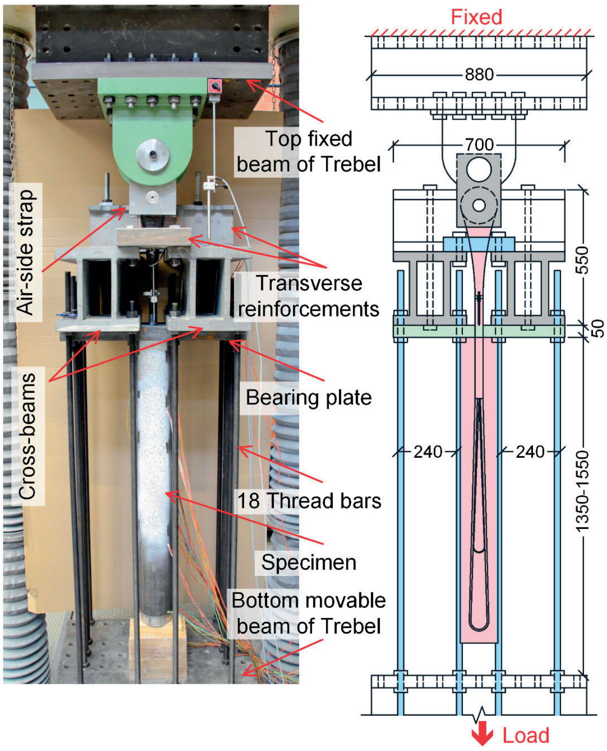
Top fixed beam of Trebel
Air-side strap
Transverse reinforcements
Cross-beams
Bearing plate
18 Thread bars
Specimen
Bottom movable beam of Trebel
Fixed
880
700
550
50
240
240
1350-1550
Load

Fig. 4.6: Experimental set-up (dimensions in [mm], DIC random speckle pattern on tube)

The instrumentation layout is shown in Fig. 4.7. Three methods were used for the deformation and strain measurements: Linear Variable Differential Transformer (LVDT) transducers, strain gages and Digital Image Correlation (DIC). Two LVDTs were symmetrically fixed on the rod at a distance of 115 mm from the top surface of the 50-mm-thick bearing plate to obtain an average pull-out displacement. Strain gages (1-LY61-6/120 from HBM AG, Switzerland) were installed at mid-width of the straps along the tendon to measure the tensile strain in the fiber direction (T1–T14); gages T5 and T13, installed in parallel at a 20-mm center-to-center distance, were both located at the vertex of the semicircle of the small strap due to the limited circular length. The tangential strains of each CFRP confinement ring were measured by four gages (1-LY61-6/120) located at mid-length at 90-degree intervals (CR1–CR12). The strains of the steel tube were measured by two types of strain gages: 1) gages (1-LY61-6/120) only in the longitudinal (SL1–SL8) or tangential (ST1–ST4) directions; 2) Rosetta gages (1-XY31-1.5/120) with measurements in both longitudinal and tangential directions (SB1–SB5). Furthermore, a 1-LY61-6/120 gage was applied in anchor ST10-2 on a 12.7×12.7×35 mm^3 GFRP block (with an Elastic modulus of 34 GPa), in the longitudinal direction (G1, see Fig. 4.7), to measure the compressive deformation of the normal-strength grout at this location. All the strain gages embedded in the grout were protected by a silicon layer of around 2-mm thickness; gage wires were drawn through six holes along the steel tube which were sealed with silicon before casting. Furthermore, DIC was used to measure the strain distribution over a 700-mm-long random speckle pattern area (dashed rectangle in Fig. 4.7) applied on the steel tube surface, on the opposite side to the strain gages SB2/4. Digital images were taken at a frequency of 0.2 Hz. Post-processing was performed using Vic-3D software from Correlated Solutions Inc., USA.

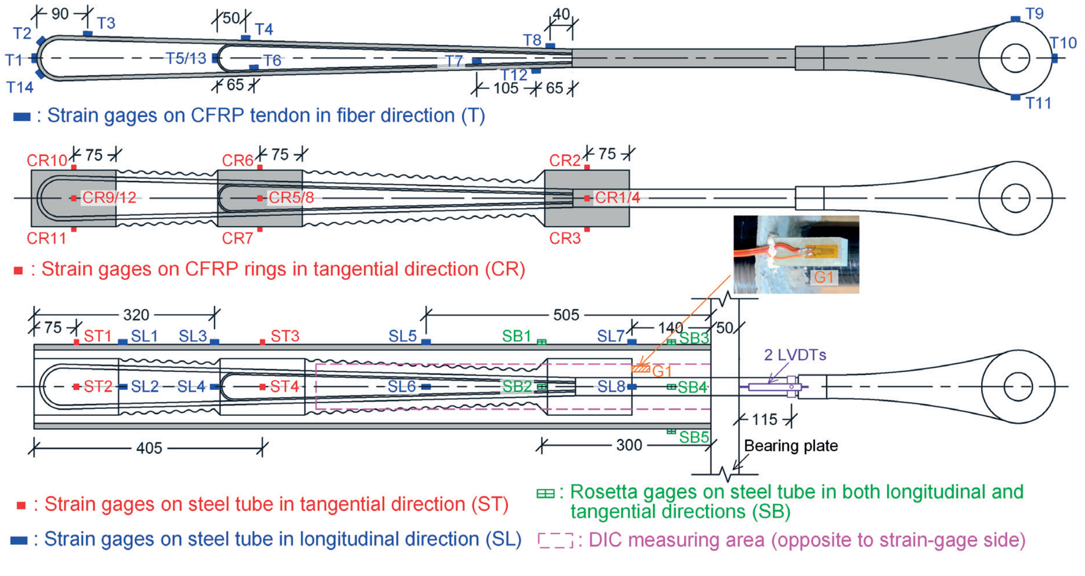
90
T3
T2
T1
T14
50
T4
T5/13
T6
65
T7
40
T8
T12
105
65
T9
T10
T11
▬ : Strain gages on CFRP tendon in fiber direction (T)
CR10
75
CR9/12
CR11
CR6
75
CR5/8
CR7
CR2
75
CR1/4
CR3
G1
▪ : Strain gages on CFRP rings in tangential direction (CR)
320
75
ST1
SL1
SL3
ST3
505
SL5
SB1
SL7
140
50
SB3
ST2
SL2
SL4
ST4
SL6
SB2
SL8
SB4
G1
2 LVDTs
115
SB5
405
300
Bearing plate
▪ : Strain gages on steel tube in tangential direction (ST)
▬ : Strain gages on steel tube in longitudinal direction (SL)
⊞ : Rosetta gages on steel tube in both longitudinal and tangential directions (SB)
⬚ : DIC measuring area (opposite to strain-gage side)

Fig. 4.7: Instrumentation layout (dimensions in [mm])

4.3 Results and discussion

4.3.1 Load vs pull-out displacement responses and failure modes

All specimens exhibited similar load vs pull-out displacement responses in the failure cycle up to a first peak, as shown in Fig. 4.8. An almost linear response was observed, apart from a slight nonlinear behavior at the beginning; the latter was attributed to a progressive debonding at the CFRP/grout interface (see below), which also caused a small residual displacement, i.e. a non-zero starting point of the final-cycle curve, after the four initial load cycles up to 700 kN for all specimens, as shown in Fig. 4.8 for anchor ST5. The stiffness in the linear range, K_{exp}, assumed as being the slope of the linear segment between 500 and 1200 kN, was 90.1±3.4 kN/mm, (see Table 4.1) with anchor ST5 exhibiting a 6.3% lower value as a result of the larger deformation due to the weaker confinement. Repeated audible cracks were noticed above 700 kN up to the first peak load in all the anchors.

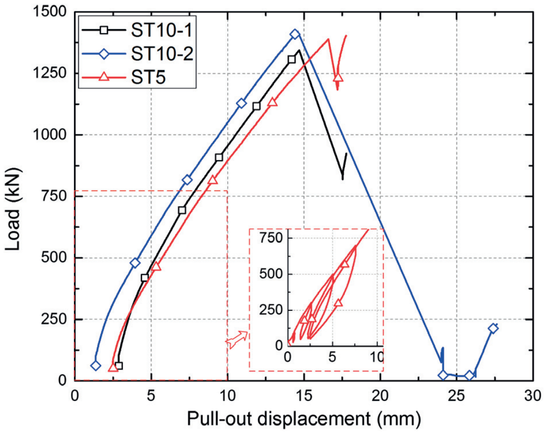

Fig. 4.8: Load vs pull-out displacement responses

The three anchors reached similar loads (1384±38 kN) at the first peak, see Table 4.1, indicating that the confinement level had little influence on the anchors' load-bearing capacity. At this first peak, delamination was observed in the visible air-side straps in anchors ST10-1/2, while no damage was apparent in ST5. After the first peak, the load dropped and then increased again to a second peak in all specimens where partial or complete rupture of the air-side strap occurred in anchors ST10-2 and ST5 respectively, see Fig. 4.9. However, in anchor ST10-2, the load to almost zero after the first peak and the second peak was significantly lower than in the other two specimens. The obtained peak loads are listed in Table 4.1.

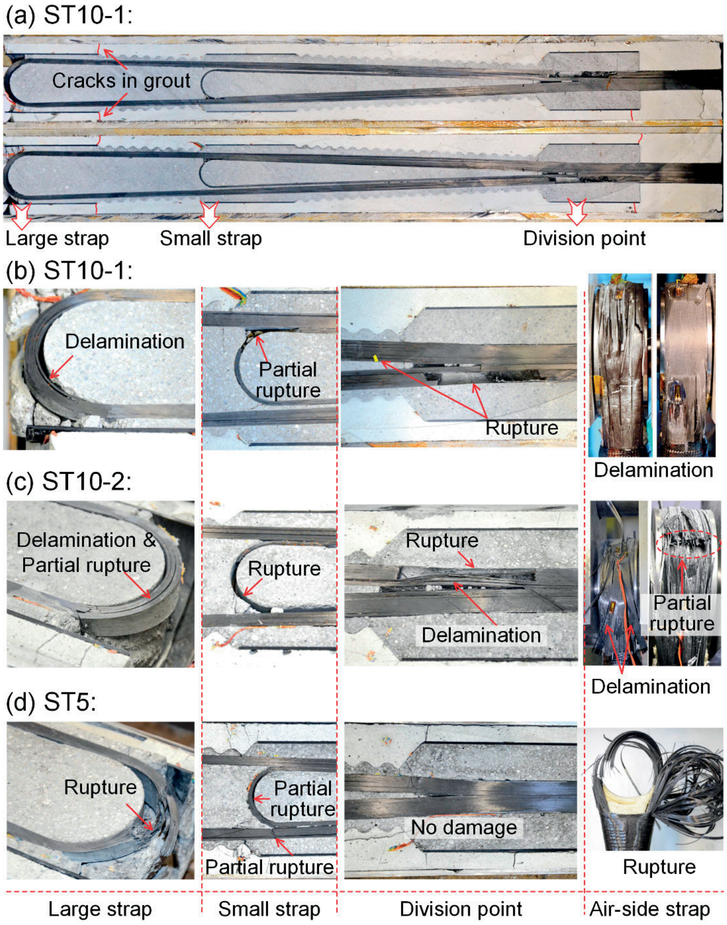
(a) ST10-1:
Cracks in grout
Large strap
Small strap
Division point
(b) ST10-1:
Delamination
Partial rupture
Rupture
Delamination
(c) ST10-2:
Delamination & Partial rupture
Rupture
Rupture
Delamination
Partial rupture
Delamination
(d) ST5:
Rupture
Partial rupture
Partial rupture
No damage
Rupture
Large strap
Small strap
Division point
Air-side strap

Fig. 4.9: Failure modes: (a) cut view of anchor ST10-1; details in (b) ST10-1, (c) ST10-2, (d) ST5

After failure, the specimens were cut into two halves in the strap plane, see Fig. 4.9. All anchors exhibited rupture in the embedded CFRP tendons; no compression failure in the grout parts was observed, except small cracks located in the normal-strength grout at the end of the CFRP rings, see Fig. 4.9(a). In anchor ST10-1, the large and small straps were completely separated from the rod at the division point on one side, while partial rupture or delamination occurred in the semicircles of the small or the large straps, see Fig. 4.9(b). In anchor ST10-2, complete rupture was visible at the division point of the large strap and in the semicircle of the small strap. Furthermore, partial rupture or delamination occurred in the semicircle of the large strap and the division point of the small strap, see Fig. 4.9(c). In anchor ST5, complete rupture occurred in the semicircle of the large strap and partial rupture in one straight part of the large strap and at the end of the small strap; no damage was visible at the division point, see Fig. 4.9(d).

4.3.2 Load vs tensile strains in CFRP tendons

The load vs tangential tensile strains (in the fiber direction), measured on the air-side straps of anchors ST10-2 and ST5, are shown in Fig. 4.10 (a) and (b) respectively. The straps exhibited an almost linear behavior up to around 700 kN; no stiffness losses were observed during the preceding cycles, see anchor ST5 in Fig. 4.10 (b) (position T10). The maximum strain location at 700 kN was at position T10 in both anchors; the strains at positions T9/11 were 10.0/12.7% and 18.1/20.4% lower in anchors ST10-2 and ST5 respectively. It must be noted however, that these strains were measured on the surface and were not uniformly distributed through the thickness due to local bending at these locations [13].

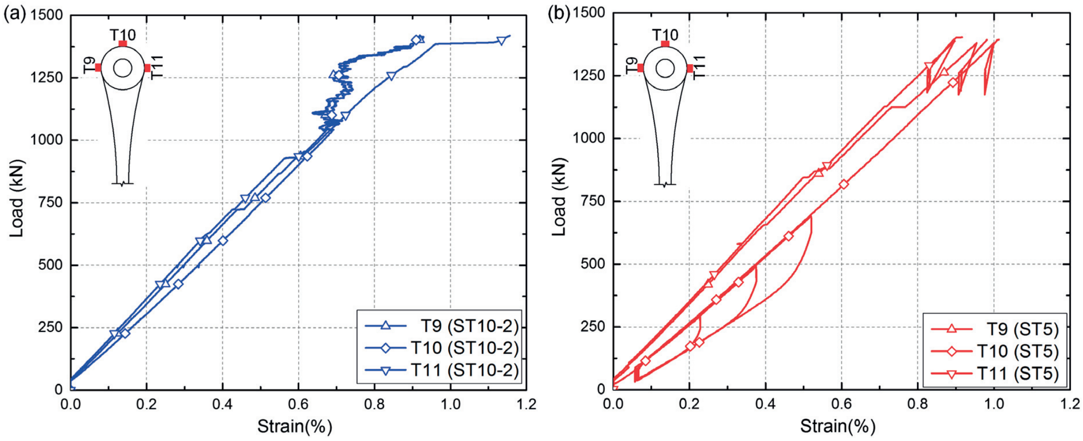

Fig. 4.10: Load vs tensile strain responses of air-side strap: (a) anchor ST10-2; (b) anchor ST5

Sudden small strain increases could be observed above 700 kN, at around 730, 935 and 1100 kN in anchor ST10-2, and at 650, 870 and 1140 kN in ST5, when audible cracks were heard as mentioned before. These strain jumps and audible cracks indicated that partial ruptures were occurring in the CFRP tendon, leading to strain redistributions in the cross section and may also have caused the markedly nonlinear response of anchor ST10-2 at positions T9/10 above around 1140 kN. In anchor ST10-2, subsequent to a sudden strain increase to 1.16% at position T11 at 1419 kN, delamination was observed on the outer surface of the strap (as mentioned above) and the measurements at positions T9-11 therefore stopped. In anchor ST5, the strains followed the two-peak load-displacement response shown in Fig. 4.8, and exhibited slightly higher values at the second peak.

The load vs tensile strain responses in the fiber direction of the embedded (ground-side) large and small straps are shown in Figs. 4.11 and 4.12 respectively. In all the anchors, the straps were activated progressively from the division point to the small and then to the large strap end due to the progressive loss of bond and subsequent friction at the CFRP/grout interface. The gages close to the division point (T7/8) thus started responding first, at lower loads (below 150 kN), while the gages around the large strap (T1/2/14) were activated last, at much higher loads (above 350 kN).

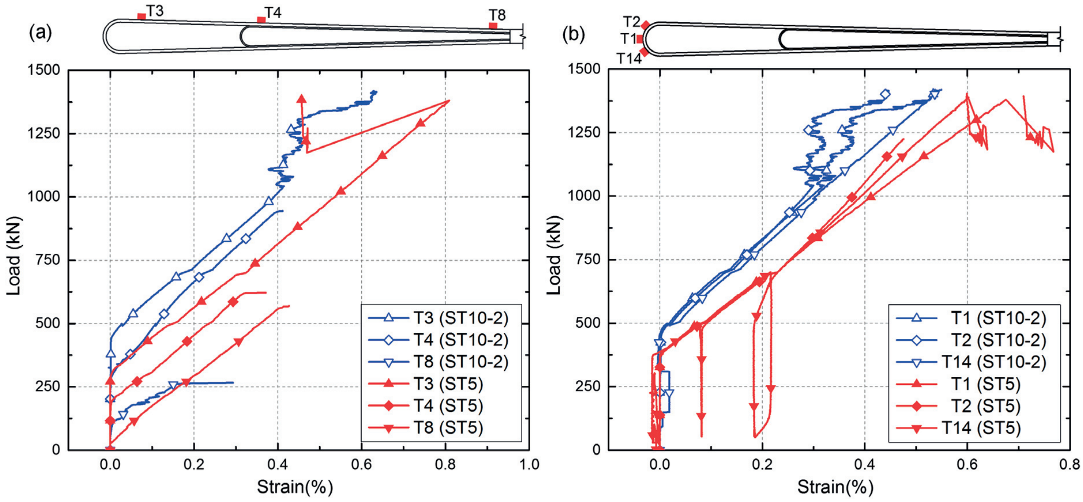

Fig. 4.11: Load vs tensile strain responses of ground-side large strap: (a) along straight segment; (b) at strap end

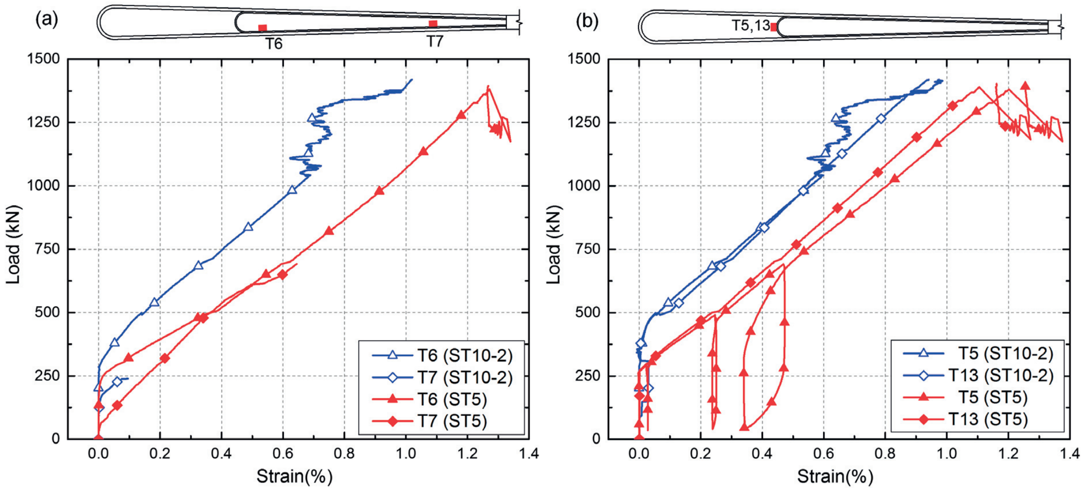

Fig. 4.12: Load vs strain responses of ground-side small strap: (a) along straight segment; (b) at strap end

The strap activation sequence also depended on the confinement level, i.e. at the higher confinement the strap was activated later due to the higher friction at the CFRP/grout interface. Accordingly, the semicircular parts of the large straps (positions T1/2/14) and small straps (T5/13) in anchor ST10-2 were activated later (at around 450 and 350 kN respectively) compared to ST5 (at around 380 and 270 kN respectively). After activation, the strain rates in ST10-2 were also slightly lower than in ST5 due to the higher friction.

Due to the early activation, positions T7/8 generally exhibited the maximum strains. However, gages T4/7/8 stopped measuring after certain loads due to the propagating slippage at the CFRP/grout interface. The maximum strains were measured in the small strap of anchor ST5 due to the earlier activation compared to the large strap and lower confinement level; they approached the ultimate strain of the CFRP material. The strains in the large straps, however, remained far below the ultimate strain.

Furthermore, complete recovery of the strap deformation during unloading was prevented by the friction behavior as well, which also led to the residual displacements after unloading during the first four cycles, shown in Fig. 4.8. The amount of strain recovery also depended on the strap location, i.e. more strain recovery was observed closer to the division point due to the lower friction, see Fig. 4.11 (b) and 12 (b).

4.3.3 CFRP tendons – grout load transfer

The load transfer from the embedded CFRP tendon components to the high-strength grout of anchor ST5, at 500 kN (pre-damage phase) and 1389 kN (first peak), is shown in Fig. 4.13. The load values at the different positions were calculated based on the measured tensile strains (see Figs. 4.11 and 4.12) and strap stiffness ($E{\cdot}A$). The load drops at the large and small straps are based on the strains measured at positions T3 and T6. A further drop occurred at the division point due to the wedge shape of the strap; the load transfer between the drops, derived from the strain differences between the latter, were caused by the bond and friction at the CFRP/grout interface. At 500 kN, strain measurements at all positions were available; the load transfer between the free length and division point was assumed to be equal to the average activation load of T7/8 (30 kN, see Figs. 4.11 and 4.12). In contrast, at 1389 kN only measurements at positions T1/3/5/6 were available, i.e. the drops at the large and small straps could be calculated. To derive the whole transfer curve, the slopes between the drops and the drop at the division point were assumed as being the same as at 500 kN; the resulting applied load at the free length was 1370 kN, which was close to the real applied load (1389 kN).

At 500 kN, the large and small straps transferred only 109 kN (21.7% of 500 kN) each to the grout while 196 kN (39.2%, =72+94+30 kN) were transmitted at the CFRP/grout interface, and the remaining 86 kN (17.2%) were transferred at the division point. In contrast, the load transfer by the large and small straps at 1389 kN was much higher: 650 kN (46.8%) and 438 kN (31.5%) respectively (78.3% in total), corresponding to a load-distribution ratio of 0.6:0.4 as assumed in the design.

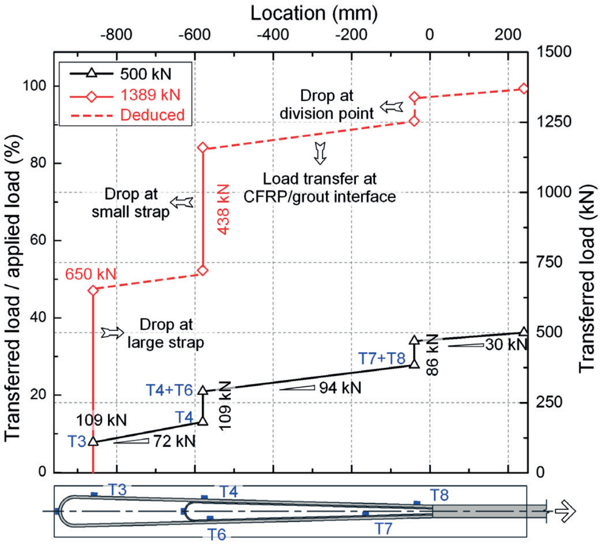

Fig. 4.13: Load transfer along embedded straps at 500 and 1389 kN in anchor ST5

In anchor ST10-2, 500 kN (35.9%) and 344 kN (24.7%) were transferred by the large and small straps at 1389 kN (in total 60.6%), exhibiting a load-distribution ratio of 0.6:0.4 identical to ST5. The transferred loads were 23.1 and 21.5% respectively lower than in anchor ST5, indicating that more load was transferred by friction and at the division point, which also corresponded to the later strap activation due to the higher confinement.

4.3.4 Tangential tensile strains in CFRP rings

The tangential strains in the CFRP confinement rings at the division point and the small and large strap ends of all anchors are shown in Fig. 4.14; two measurements at 90° positions in each ring were selected due to similar strains at the opposite positions. The activation sequence of the CFRP rings was similar to that of the CFRP straps, i.e. the ring at the division point was activated first, followed by those at the small and large strap ends. Anchor ST5 exhibited higher strains in all the rings than ST10-1/2 up to the first peak load. A sudden strain increase was observed after the first peak in some of the rings; the maximum strain, 0.146% at position CR2 in anchor ST10-2, was still low however compared to the material ultimate strain.

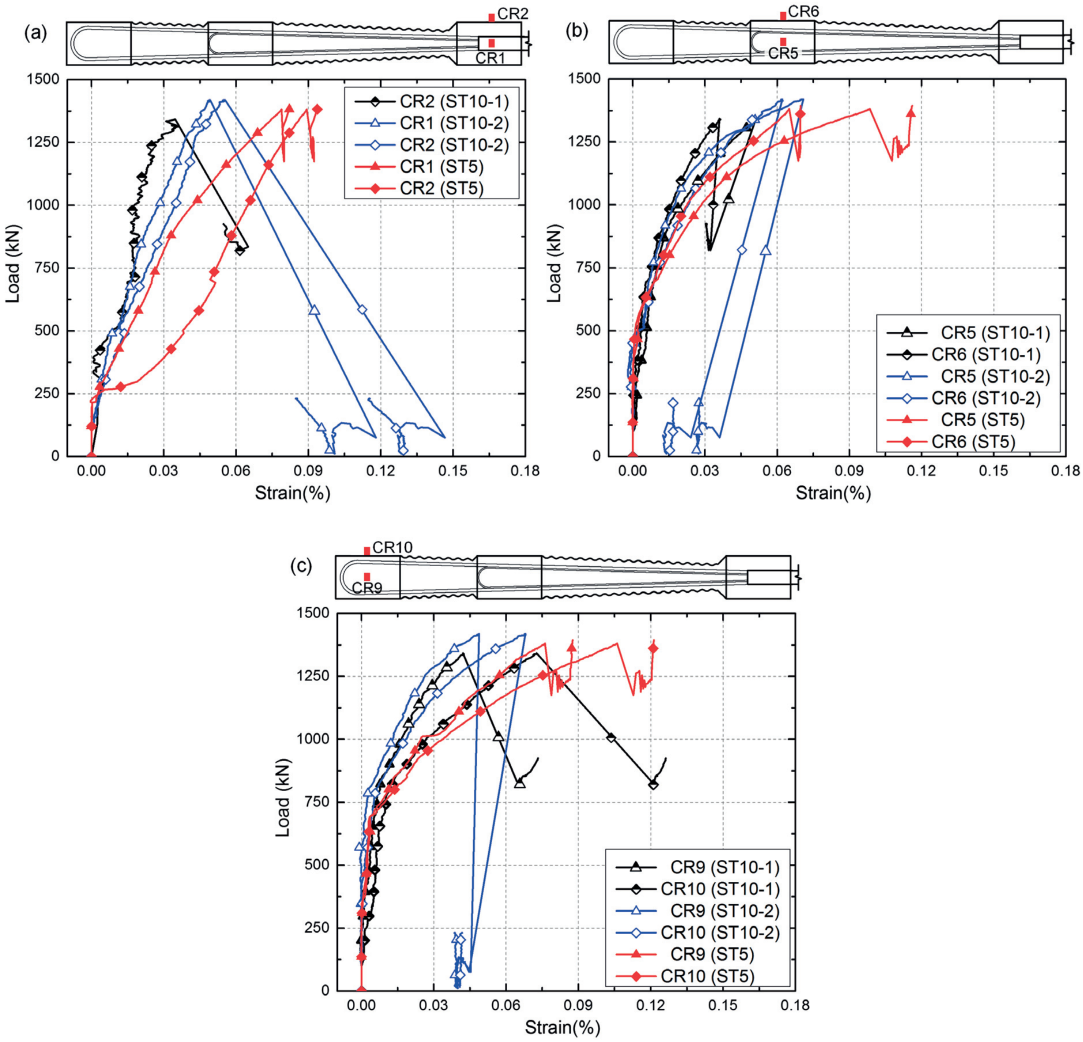

Fig. 4.14: Load vs tangential strain responses in CFRP rings at: (a) division point; (b) small strap location; (c) large strap location

In the CFRP ring located at the large strap end, position CR10 exhibited higher strains than CR9 in all the anchors, although the opposite would have been expected, since the spreading forces mainly occurred perpendicular to the strap plane and activated CR9. It seems that much smaller forces in the strap plane caused locally higher strains in CR10 due to the vicinity of the strap and the ring at this location (5–8 mm distance) and the low ring stiffness transverse to the fibers. In the CFRP ring located at the small strap end, the strains at position CR5 were higher than at CR6 as expected (in ST10-2 above 1300 kN), no local effect occurred due to the larger distance of the small strap from the ring. At the division point, spreading forces were mainly produced in the strap plane by the small kink in this plane at the transition from the rod to the straps, which was confirmed by the slightly higher strains at position CR2 compared to CR1.

4.3.5 Strain distributions in steel tubes

The longitudinal strain distributions along the steel tube are shown in Fig. 4.15; only the measurements from the gages located in the plane perpendicular to the strap plane in anchor ST5 are presented due to similar distributions in both planes and in all the specimens; however, the strains in anchor ST5 were generally twice those of ST10-1/2 due to the halved thickness of the steel tube. The strains were insignificant at low load levels, i.e. 100 kN. During the subsequent load increase, strain maxima formed towards the bearing plate due to the accumulation of the load transferred from the normal-strength grout to the steel tube via friction at the grout/steel interface. The almost linear distribution along the tube length was also confirmed by the DIC measurements from the opposite tube side, as shown in Fig. 4.16. A slight strain decrease was observed at position SB4, which could be attributed to local bending in the tube due to the constraint at the tube end by the bearing plate. The strains at positions SB4, SL8 and SB2 just reached the yield strain (0.17%) in ST5 (not in ST10-1/2), however, no local deformation was observed in the experiments. In real applications, these strain maxima are reduced since the rock-grout anchorage zone is much longer.

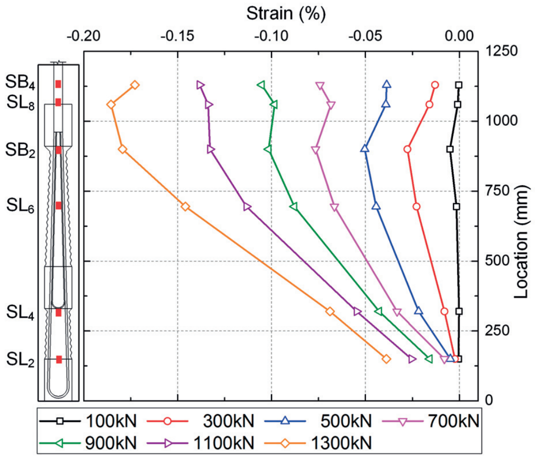

Fig. 4.15: Longitudinal strain distributions along steel tube in plane perpendicular to strap plane, in anchor ST5 at different load levels

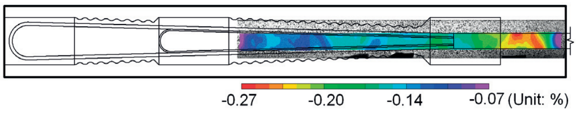

Fig. 4.16: Longitudinal strain distribution along 700-mm-long upper part of steel tube at 1300 kN measured by DIC in anchor ST5

Assuming that the bond stress at the steel/grout interface, τ, is distributed uniformly between two adjacent strain gages, it can be calculated as:

$$\tau_{(i+1)-i} = \frac{E_s(D_o^2 - D_{in}^2)(\varepsilon_{i+1} - \varepsilon_i)}{4D_{in}(L_{i+1} - L_i)} \tag{4.1}$$

where E_s is the steel elastic modulus, D_o and D_{in} are the outer and inner diameters of the steel tube, L_i is the distance between the gages at position i and SL1/2, and ε_i is the measured strain at position i. The tube exhibited an almost linear longitudinal strain distribution in the segment between positions SL2 and SB2 (also between SL1 and SB1), indicating that the bond stress was similar along this segment. The calculated average bond stresses in the strap plane (SL1–SB1) and in the plane perpendicular to the strap plane (SL2–SB2) were 1.70 and 2.17 MPa in anchor ST10-2, and 1.98 and 2.62 MPa in ST5; the bond stresses in the former plane were thus 21.9–24.2% lower than in the latter, which is in accordance with the spreading force directions discussed above. The stress levels (1.70–2.62 MPa) were in the range of the rock-grout bond strengths of rock types such as basalt and granite (1.72–3.10 MPa) [14]. However, these values could also be reduced in real applications, since the rock-grout anchoring length normally ranges from 3 to 10 m [15].

The distributions of the tangential tensile strains along the steel tube, perpendicular and parallel to the strap planes (as in the CFRP rings), are shown in Fig. 4.17; again only the results of anchor ST5 are presented. The strains in two planes exhibited similar distributions in the upper segment close to the bearing end (positions SB1/3 and SB2/4). However, different behaviors were observed at the strap-end locations (positions SR1/3 and SR2/4). Positions SR2/4 exhibited obviously higher strains than SR1/3, confirming once more that more spreading forces were transferred in the plane perpendicular to the strap plane.

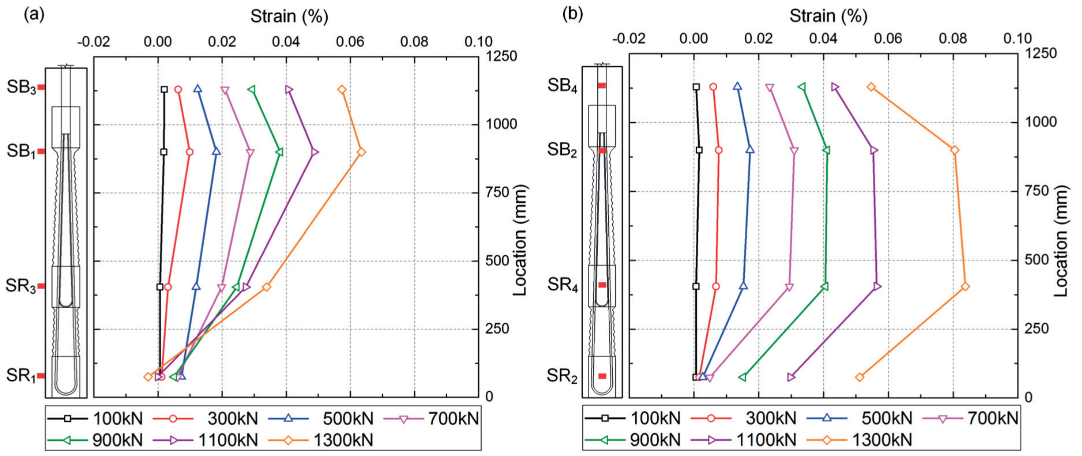

Fig. 4.17: Tangential strain distributions along steel tube in ST5 at different load levels: (a) perpendicular to strap plane; (b) parallel to strap plane

4.3.6 Failure sequence in embedded straps

The failure sequence in the embedded straps could be derived based on the observations made during the experiments, the strain measurements on the CFRP tendon and CFRP rings, and the post-failure pattern in Fig. 4.9; a summary of this failure sequence is shown in Table 4.1. Concerning anchor ST10-1, the relevant results were: 1) in the CFRP rings at the division point and small strap locations, a strain decrease during loading up to the second peak, see Figs. 4.14 (a) and (b); 2) at the large strap ring, a strain increase up to the second peak (see Fig. 4.14 (c)); 3) strain gages installed at the small strap end stopped measuring at the first peak. Based on failure patterns furthermore shown in Fig. 4.9 (b), it could be concluded that the large strap rupture at the division point occurred at the second peak. Since the small strap exhibited partial rupture at the end and complete rupture on one side at the division point, the latter must have occurred earlier or both at the same time, and thus at the first peak.

In anchor ST10-2, the following measurements were significant: 1) a large load drop to almost zero after the first peak; 2) in all CFRP rings, a strain decrease during loading up to the second peak, see Fig. 4.14; 3) strain gages installed on both straps stopped measuring at the first peak (Figs. 4.11 and 4.12). The rupture of the large strap at the division point and small strap at the end, see Fig. 4.9 (c), must thus have occurred at the first peak.

Concerning anchor ST5, the relevant measurements were: 1) the slightly higher second peak than the first peak; 2) in all CFRP rings, a strain increase during loading up to the second peak, see Fig. 4.14; 3) in all straps, a slight strain decrease during loading up to the second peak, see Figs. 4.11 and 4.12 (more pronounced in T3); 4) strains in the large strap far below the ultimate strain at the second peak; 5) strains in the small strap approaching the ultimate strain at the second peak. Based on these results only the partial ruptures shown in Fig. 4.9 (d) could have occurred at the first peak. The rupture in the large strap must have been caused after the strap rupture on the air side at the second peak by the subsequent sudden dropping down of the specimen.

4.3.7 Confined grout behavior

According to the multi-strap anchor concept (see Fig. 4.1), the main purpose of the CFRP rings is to deviate the spreading forces at the strap ends and the division point in the axial direction and not to improve the grout strength. A high grout strength is mainly required in the semicircular regions of the two straps, which is the reason for selecting a high-strength grout for the anchor body; the CFRP strap ends provide further confinement for the grout inside the straps. Nevertheless, the CFRP rings also confine the anchor body and in the following it is thus analyzed to what extent the high-strength grout was confined by the strap ends and CFRP rings. Only anchor ST5, which exhibited the highest strains in the straps and rings, is analyzed and only the large strap, which was much more loaded than the small strap, is considered.

Based on the tangential strains in the semicircle of the straps and CFRP rings, ε_t, the radial confining pressure, f_r, at the inner surface of these elements (assuming a uniform pressure distribution) can be calculated as:

$$f_r = \frac{2 \cdot t \cdot \sigma_t}{d_{in}} = \frac{2 \cdot t \cdot E \cdot \varepsilon_t}{d_{in}} \tag{4.2}$$

where E, d_{in} and t are the elastic modulus, inner diameter and thickness of the confinement elements, and σ_t is the tangential stress. Based on the average measurements at positions T1/14 of the large strap (T2 stopped working at around 1200 kN in ST5), T5/T13 of the small strap, and CR1–4 and CR9–12 of the CFRP rings in anchor ST5, f_r was calculated, as shown in Table 4.2. A high confining pressure of 194.1–225.5 MPa resulted at the inner surface of the strap, while the values in the CFRP ring were small. Under these confining pressures, the confined compressive strength of the high-strength grout, $f'_{cc,H}$, assuming that the grout exhibited a confined behavior comparable to concrete, could be estimated as [16]:

$$f'_{cc,H} = (1 + k_1 \frac{f_r}{f'_{c0,H}}) f'_{c0,H} \tag{4.3}$$

where k_1 is the confinement effectiveness coefficient, which can be obtained from formulations derived from experiments with FRP confinements (see Table 4.2) [16, 17] [18], and $f'_{c0,H}$ is the unconfined compressive strength of the high-strength grout (62.2 MPa). The resulting $f'_{cc,H}$ values, shown in Table 4.3, indicated that the compressive strength improvement was significant in the grout inside the strap ends (4.9–8.2 times $f'_{c0,H}$). The confined compressive strength (>302.9 MPa) was higher than the compressive stresses on the grout inside the large and small strap ends, 205.3 and 235.0 MPa respectively, estimated by dividing the load transferred to the large and small strap ends (650 and 438 kN, see Fig. 4.13) by the inner diameter (66 and 44 mm) and width (40 mm) of the semicircles. This result was also confirmed by the observation that no failure occurred in the high-strength grout (see Fig. 4.9). In contrast, the compressive strength improvement caused by the CFRP rings was low (1.2–1.3 times $f'_{c0,H}$) and thus confirmed their intended main purpose, to deviate the spreading forces.

Table 4.2: Calculation of confinement effectiveness coefficient k_1 at 1389 kN in anchor ST5

	f_r (MPa)	$k_1 = 6.0 f_r^{-0.3}$ [17]	$k_1 = 2.2(f_r / f'_{c0})^{-0.16}$ [18]	k_1 [16]
$\varepsilon_{T1/T14}$ =0.638%	194.1	1.24	1.83	2
$\varepsilon_{T5/T13}$ =1.153%	225.5	1.18	1.79	2
ε_{CR1-4} =0.090%	6.1	3.53	3.21	2
ε_{CR9-12} =0.086%	5.9	3.48	3.19	2

Table 4.3: Estimation of confined compressive strength of grout in anchor ST5

Location	k_1	$f'_{cc,H}$ (MPa)	$f'_{cc,H} / f'_{c0,H}$
T1/T14	[1.24, 2]	[302.9, 450.4]	[4.9, 7.2]
T5/T13	[1.18, 2]	[328.3, 513.2]	[5.3, 8.2]
CR1–4	[2, 3.53]	[74.5, 83.6]	[1.2, 1.3]
CR9–12	[2, 3.48]	[73.9, 82.9]	[1.2, 1.3]

A further element of the multi-strap anchor concept is that the anchor body can be embedded and anchored in normal grout as used in steel anchor applications, i.e. the normal grout strength is not exceeded at the interface transverse to the borehole between high-strength and normal grout. Ideally the uniaxial grout strength (48.0 MPa) should not be exceeded in order to not depend on any confinement effect by the surrounding ground. Based on the yield strain of the steel tube in anchor ST5 (where the tube already reached the yield point in the longitudinal direction) and the longitudinal strains measured at positions SL7/8 in ST10-2 (where no local bending existed), the loads borne by the steel tubes at 1389 kN in ST5 and ST10-2 were estimated as being 751 and 1057 kN respectively. Thus, the loads borne by the normal-strength grout were 638 and 332 kN, corresponding to 49.2 and 25.6 MPa compressive stresses respectively. The former (49.9 MPa) was only 2.5% higher than the uniaxial grout strength (48.0 MPa). This latter value for ST10-2 was also confirmed by the strain measurement at position G1 (see Fig. 4.7); the measured compressive strain was 0.082% at 1389 kN, corresponding to a stress of 27.9 MPa in the grout. These results thus validated the assumptions of the anchor concept.

4.4 Conclusions

Pull-out experiments were performed on three CFRP ground anchors with two-strap ends embedded in a prefabricated high-strength grout anchor body on the ground side. The anchor body was embedded in normal-strength grout confined with steel tubes of different thicknesses to simulate the confinement of different rock masses. The following conclusions were drawn:

1. The targeted 1000-kN anchor capacity was reached. Failure occurred in the CFRP tendons at different positions on the air and ground sides, which proved an almost uniform use of the capacities of the different strap components.
2. The conceptual elements to prevent grout failure, i.e. selection of high-strength grout in the anchor body, CFRP confinement rings to balance and deviate spreading forces and the complex conical anchor body shape to introduce the forces into the normal grout, proved to be effective and well-tailored.
3. The confinement provided by the surrounding media influenced the load-bearing behavior of the anchor body. A higher confinement level led to a delay in the activation of the CFRP components more distant from the free length due to an increase of friction at the CFRP/grout interface; the large strap was thus less loaded and the region of the deviation point more loaded compared to an anchor subjected to lower confinement.

References

[1] Benmokrane B, Zhang B, Chennouf A, Masmoudi R. Evaluation of aramid and carbon fibre reinforced polymer composite tendons for prestressed ground anchors. Can J Civ Eng 2000;27:1031-45.

[2] Tokyo Rope Co. Ltd. Summary of application projects. <https://isabou.net/sponsor/nm-anchor/sekou.asp> (May 02, 2016).

[3] Benmokrane B, Xu H, Nishizaki I. Aramid and carbon fibre-reinforced plastic prestressed ground anchors and their field applications. Can J Civ Eng 1997;24:968-85.

[4] Wang X, Xu P, Wu Z, Shi J. A novel anchor method for multitendon FRP cable: manufacturing and experimental study. J Compos Constr 2015;19:04015010.

[5] Zhang K, Fang Z, Nanni A, Hu J, Chen G. Experimental Study of a Large-Scale Ground Anchor System with FRP Tendon and RPC Grout Medium. J Compos Constr 2014;19:04014073.

[6] Schmidt JW, Bennitz A, Täljsten B, Goltermann P, Pedersen H. Mechanical anchorage of FRP tendons–A literature review. Constr Build Mater 2012;32:110-21.

[7] Winistoerfer AU. Development of non-laminated advanced composite straps for civil engineering applications. Coventry, UK: University of Warwick, 1999.

[8] Keller T, Kenel A, Koppitz R. Carbon Fiber-Reinforced Polymer Punching Reinforcement and Strengthening of Concrete Flat Slabs. ACI Struct J 2013;110.

[9] Huster U, Broennimann R, Winistörfer A. Strengthening of a historical roof structure with CFRP-straps. In: Proceedings of the fourth international conference on FRP composites in civil engineering (CICE2008), Zurich, 22-24 July 2008. B.6.

[10] Lees J, Winistörfer A. Nonlaminated FRP Strap Elements for Reinforced Concrete, Timber, and Masonry Applications. J Compos Constr 2010;15:146-55.

[11] Fan H, Vassilopoulos AP, Keller T. Pull-out behavior of CFRP single-strap ground anchors. In: Proceedings of the 17th European Conference on Composite Materials (ECCM17), Munich, 26-30 June 2016.

[12] Heuze FE. Scale effects in the determination of rock mass strength and deformability. Rock Mech 1980;12:167-92.

[13] Fan H, Vassilopoulos AP, Keller T. Experimental and numerical investigation of tensile behavior of non-laminated CFRP straps. Compos B Eng 2016;91:327-36.

[14] Xanthakos PP. Ground anchors and anchored structures. Washington, U.S.A.: John Wiley & Sons, 1991.

[15] Sabatini P, Pass D, Bachus RC. Geotechnical engineering circular no. 4: Ground anchors and anchored systems. US DOT Federal Highway Administration, 1999.

[16] Lam L, Teng J. Strength models for fiber-reinforced plastic-confined concrete. J Struct Eng 2002;128:612-23.

[17] Samaan M, Mirmiran A, Shahawy M. Model of concrete confined by fiber composites. J Struct Eng 1998;124:1025-31.

[18] Saafi M, Toutanji H, Li Z. Behavior of concrete columns confined with fiber reinforced polymer tubes. ACI Mater J 1999;96:500-9.

5.

Load-transfer mechanisms in CFRP ground anchors with multi-strap ends

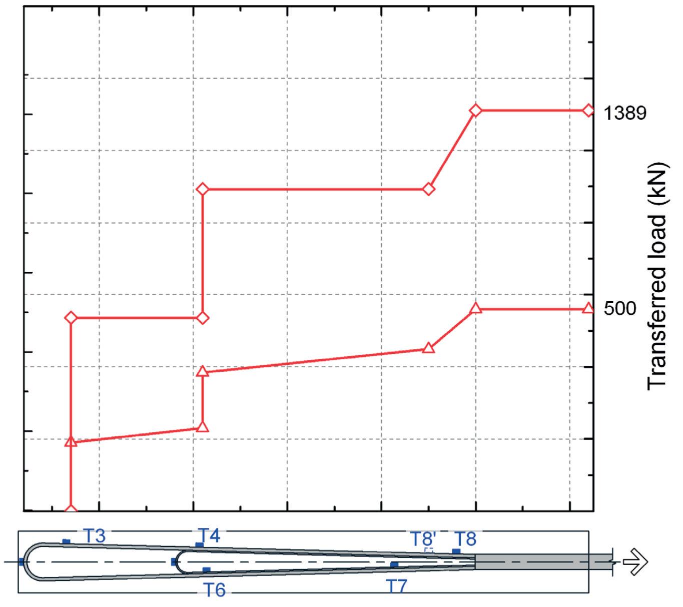

Reference detail:

Fan H, Vassilopoulos AP, Keller T. Load-transfer mechanisms in CFRP ground anchors with multi-strap ends. Submitted to Compos Struct, 2017.

5.1 Introduction

Ground anchors can be divided into tension- and compression-type anchors depending on the load-transfer behavior from the tendon to the surrounding grout. In the widely used tension ground anchors, the load transfer is concentrated at the beginning of the bond length, where a bond stress peak is usually observed, and with increasing loading it progresses towards the anchor end [1]. The three typical failure modes of this anchor type are (1) tendon rupture, (2) bond failure at the grout/ground interface and (3) bond failure at the tendon/grout interface. The failure at the tendon/grout interface has frequently been reported in both steel [2, 3] and fiber-reinforced polymer (FRP) [4, 5] tension anchors in laboratory studies and field applications. Therefore a considerable amount of experimental work has been carried out to investigate the load-transfer mechanism at the tendon/grout interface. By assuming progressive bond failure at the tendon/grout interface, various analytical models have been developed for both steel [6, 7] and FRP [5, 8] anchors to estimate their load-bearing capacity and also bond-stress and tendon-load distributions along the anchor, both of which are essential for anchor designs.

In the compression anchor however, the load is transferred directly to the anchor end, where an end bearing element is usually installed. Apart from failure modes identical to modes (1) and (2) in tension anchors, compression failure of the grout occurs in the compression anchors instead of the bond failure at the tendon/grout interface [1, 9]. Research has been conducted to investigate the load-transfer mechanisms of compression anchors [9, 10]; in the case of bond failure at the grout/ground interface, the ultimate anchor load was estimated using similar models to those used for tension anchors, while the estimation was based on the grout strength in the grout-failure case [9]. Furthermore, by installing multiple compression anchors in the same borehole, a distributive compression anchor can be created, in which the load is better distributed along the bond length and the load concentration at the anchor end is thus reduced [11, 12]. Some field experiments and associated applications concerning distributive compression anchors were reported in [11, 12].

Compared to tension anchors, compression anchors (1) avoid the possible load transfer into the “no-load zone”, i.e. the region between the anchor head and the potential failure surface in the ground [1], (2) reduce creep and relaxation [9], and (3) change the loading of the grout from brittle tension to ductile compression [10].

Conceptually similar to the distributive compression anchors, a permanent post-tensioned CFRP ground anchor based on the strap anchorage concept, which has already been used in different strengthening applications [13, 14], was developed for ground anchors [15, 16]. The CFRP tendon comprises a multi-strap anchor head on the ground side, embedded in a high-strength grout cylinder confined with CFRP rings. The prefabricated anchor head is then inserted into the borehole on the construction site, anchored by injecting fresh standard (normal-strength) grout and finally post-tensioned to 60% of the design load. The strap ends can (1) prevent premature failure in the anchoring head caused by the anisotropic properties of CFRP materials, (2) provide mechanical interlocking between the CFRP tendon and grout and (3) prevent bond failure at the tendon/grout interface. In the strap anchor design, the interface between the normal-strength grout and surrounding ground can be analyzed using identical methods as for the above-mentioned anchors. However, the load-transfer mechanisms from the tendon to the high-strength grout, as well as from high- to normal-strength grouts, need to be investigated.

Pull-out experiments have been conducted on the CFRP anchors with one- and two-strap ends to investigate the load-transfer mechanism inside the strap anchors from the straps to the high-strength grout [15, 16]. Based on experiments conducted on four one-strap anchor specimens with different confinement levels, a general discussion of the load transfer from the strap to the high-strength grout cylinder was presented in [15]. For one two-strap anchor, which had a different strap geometry, a first load-transfer diagram derived along the embedded straps was obtained in [16], based on strain measurements taken along the straps. However, the measurements stopped at around 50% of the ultimate load due to slippage at the tendon/grout interface. The complete load-transfer mechanism in strap anchors is thus not yet clearly understood and no model is available for CFRP multi-strap anchor designs as is the case for grouted steel and FRP bar or strand anchors.

In this chapter, existing and new experimental results concerning the pull-out behavior of one- and two-strap anchors were further analyzed to systematically investigate the load-transfer mechanism in CFRP strap anchors with different strap geometries and strap numbers. The load-transfer behavior in one-strap anchors in relation to the different strap geometries was first studied based on experimental and finite element (FE) results. One- and two-strap anchors with similar strap geometries but different strap numbers were then compared, and an empirical model for obtaining a complete load-transfer diagram along the embedded straps was derived. The model was then applied to develop a new three-strap anchor with a targeted capacity of 2500 kN for rock applications.

5.2 CFRP strap anchor description

In the pull-out experiments, the investigated CFRP strap anchor specimens consisted of an air-side one-strap anchor head, a middle unbonded tendon segment (free length) and an embedded tendon segment with strap ends inside the high-strength grout. Two types of anchor configurations were designed depending on the ground-side strap number (one or two); in the one-strap case, two different strap geometries were investigated. To simulate the confinement provided by the surrounding ground, a steel tube with corresponding stiffness was used in the experiments. Within the scope of developing a three-strap anchor of a 2500-kN capacity, thus applicable mainly in rock masses, only the experiments simulating rock applications from [15, 16] were used for the following analyses. Four anchor specimens were investigated, as shown in Table 5.1; their denominations comprised strap number, curved (C) or straight (S) strap geometry and steel tube thickness (5, 7 and 10 mm); subscripts n were further used as specimen number (n=1–5). The experimental results for anchor specimen 1S7 (one-strap with straight strap geometry and 7-mm tube thickness) have not yet been published. Anchor 3S was newly developed in this work.

Table 5.1: Overview of denominations and experimental matrix

n	Anchor	Strap number	Strap Transition	$t_{tube,n}$ (mm)	$D_{tube,n}$ (mm)	$E_{rock,n}$ (GPa)	$L_{s,n}$ of straps (mm)			$t_{s,n}$ of straps (mm)			w_n (mm)	$D_{rod,n}$ (mm)	$E_{t,n}$ (GPa)	$F_{ult,n}$ (kN)
							1st	2nd	3rd	1st	2nd	3rd				
1	1C7	1	Curved	7	100	35.6	252	-	-	4.0	-	-	40	20	143	497
2	1S7	1	Straight	7	100	35.6	445	-	-	5.3	-	-	30	20	128	523
3	2S5	2	Straight	5	130	20.7	630	950	-	3.0	7.0	-	40	32	143	1402
4	2S10	2	Straight	10	130	38.0	630	950	-	3.0	7.0	-	40	32	143	1419
5	3S	3	Straight	-	164	37.0	630	950	1270	3.0	7.0	9.4	50	50	143	2843*

* *Estimated value*

5.2.1 One-strap anchor with curved strap geometry (1C7)

A 1.38-m-long CFRP one-straptendon with a curved transition between deviation point and strap end was used in the first anchor specimen, as shown in Fig. 5.1 (a). The length of the strap end on the ground side, $L_{s,1}$, was 252 mm (see Table 5.1), while the middle rod segment – with a diameter, $D_{rod,1}$, of 20 mm – was 780 mm long. The thickness, $t_{s,1}$, width, w_1, and outer radius of the semicircular part of the strap were 40, 4.0 and 42 mm respectively, fitting in boreholes of 100-mm (or larger) diameter. The tendon was produced by Carbo-Link, Fehraltorf, Switzerland.

The ground-side strap end was anchored in the high-strength grout cylinder which was confined by a 605-mm-long steel tube to simulate a direct application in rock, as shown in Fig. 5.2 (a). The steel tube was 7 mm thick with an inner diameter of 100 mm, i.e. $t_{tube,1}$=7 mm and $D_{tube,1}$=100 mm. Based on the thick-wall cylinder theory, the elastic modulus of the equivalent rock medium, E_{rock}, with a Poisson's ratio of 0.25, was $E_{rock,1}$=35.6 GPa. More details concerning anchor 1C7 are presented in [15], where less confined strap anchors for soil applications were also investigated; however, in this work, only the rock application case, i.e. the anchor fully confined with a steel tube (designated S605 anchor in [15]), was used, as mentioned above.

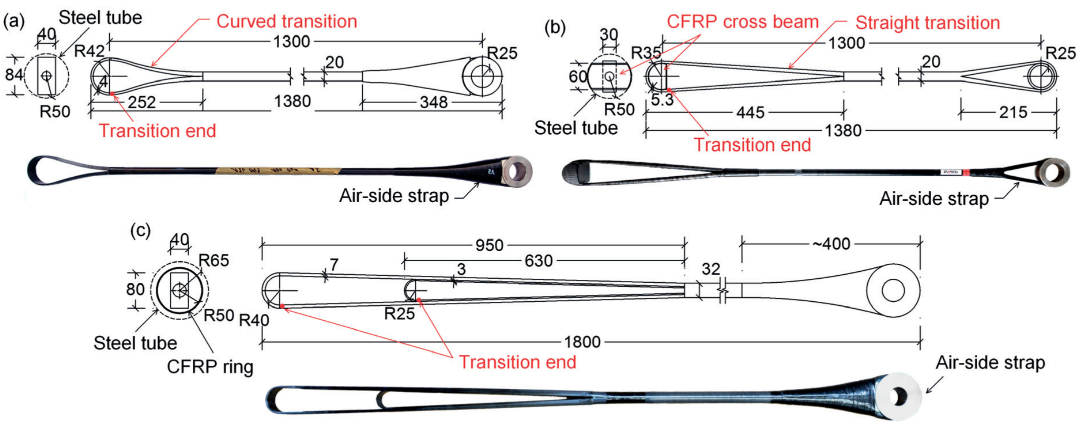
(a)
Steel tube
40
R42
84
R50
4
Curved transition
1300
20
R25
252
1380
348
Transition end
Air-side strap
(b)
30
R35
60
R50
5.3
Steel tube
CFRP cross beam
Straight transition
1300
20
R25
445
1380
215
Transition end
Air-side strap
(c)
40
R65
80
R50
R40
Steel tube
CFRP ring
950
7
630
3
R25
32
~400
1800
Transition end
Air-side strap

Fig. 5.1: CFRP tendons: (a) 1C7 (b) 1S7, (c) 2S5/10 (dimensions in [mm])

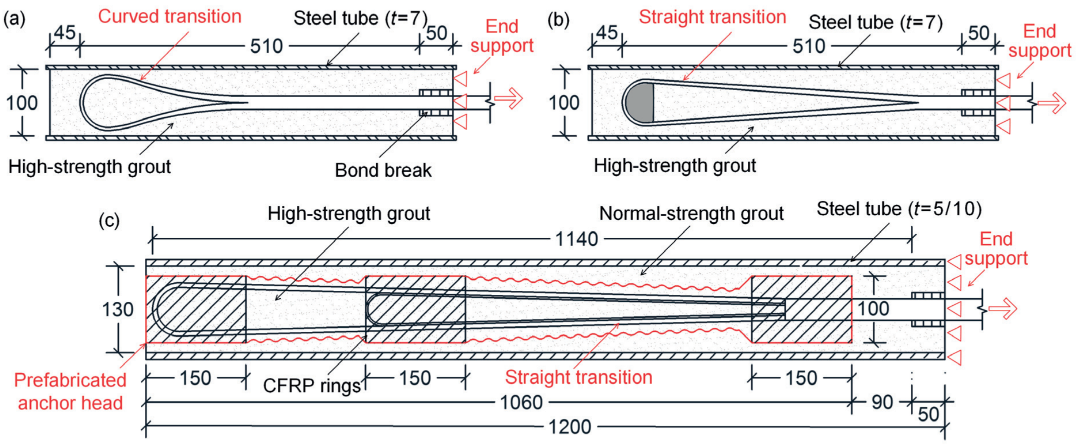
(a)
45
Curved transition
510
Steel tube (t=7)
50
End support
100
High-strength grout
Bond break
(b)
45
Straight transition
510
Steel tube (t=7)
50
End support
100
High-strength grout
(c)
High-strength grout
Normal-strength grout
Steel tube (t=5/10)
1140
End support
130
100
Prefabricated anchor head
150
CFRP rings
150
Straight transition
150
1060
90
50
1200

Fig. 5.2: CFRP anchor specimens: (a) 1C7 (b) 1S7, (c) 2S5/10 (dimensions in [mm])

5.2.2 One-strap anchor with straight strap geometry (1S7)

A 1.38-m-long one-strap tendon with a straight transition and a bonded cross-beam was used as second anchor type, as shown in Fig. 5.1 (b). The strap length was $L_{s,2}$=445 mm and for the semicircular part, $t_{s,2}$=5.3 mm, w_2=30 mm (see Table 5.1) and the outer radius was 35 mm; the anchor was also designed to fit in boreholes of 100 mm in diameter. The rod segment length was decreased to 720 mm, while the diameter remained at $D_{rod,2}$=20 mm. The cross-beam with a semicircular cross section was bonded to the inner surface of the semicircle to reduce the pressure on the grout; the cross-beam was 100 mm long and shaped to fit in 100-mm-diameter boreholes. The tendon was produced by Riostra, London, United Kingdom.

As in anchor 1C7, the ground-side strap end and cross-beam were also directly anchored in a high-strength grout cylinder which was further confined by a steel tube with identical dimensions as in 1C7, as shown in Fig. 5.2 (b).

5.2.3 Two-strap anchors with straight strap geometry (2S5/10)

Two identical 1.80-m-long two-strap tendons with straight transitions (and without cross-beams) were used in anchor specimens 2S5 and 2S10 (n=3 and 4), as shown in Fig. 5.1 (c). On the ground side, a second strap was added, while remaining one strap on the air side. The strap width was identical to that of the 1C7 and 1S7 anchors, i.e. w_3=w_4=40 mm, while the other dimensions were different: the lengths of the first and second straps were $L_{s,3/4}$=630 and 950 mm respectively (see Table 5.1); the semicircles' thicknesses were $t_{s,3/4}$=3.0/7.0 mm, and the outer radii 66 and 44 mm respectively. The middle rod segment was 450 mm long with diameter $D_{rod,3}$=$D_{rod,4}$=32 mm. The CFRP tendons were also produced by Carbo-Link, Fehraltorf, Switzerland.

The CFRP tendons with two-strap ends on the ground side were first embedded in 1060-mm-long high-strength grout cylinders with inclined and corrugated surfaces, forming anchor heads, as shown in Fig. 5.2 (c). Three 150-mm-long and 2-mm-thick identical CFRP confinement rings were installed around the two strap ends and the division point of each specimen; identical high-strength grout to that used in the one-strap anchors was used. The anchor heads were further anchored with normal-strength grout in steel tubes of $t_{tube,3}$=5 and $t_{tube,4}$=10-mm thickness, 1200-mm length, with an inner diameter of 130 mm, i.e. $D_{tube,3}$=$D_{tube,4}$=100 mm. Correspondingly, $E_{rock,3}$ and $E_{rock,4}$ were 20.7 and 38.0 GPa respectively. More details concerning anchors 2S5 and 2S10 were presented in the previous work (see [16], ST5 and ST10-2 anchors).

5.2.4 CFRP and grout material properties

The tendons were all produced by winding continuous unidirectional carbon fibers around steel pins located at the strap ends and then transversely wrapping the middle part to form a rod shape. In the 2S5/10 tendons, Teflon sheets were added at the outer surface of the small strap during the winding of the large one to separate the straps and achieve independent load-bearing behavior. The 1C7 and 2S5/10 tendons were composed of identical materials, i.e. unidirectional UTS50 F24 24k 1600tex D carbon fibers impregnated with XB 3515 AD1571 ACC1573 epoxy resin; the fiber volume fraction was 60±2% and the elastic moduli were $E_{t,1}=E_{t,3}=E_{t,4}=143$ GPa (see Table 5.1). Further details concerning fabrication and materials are presented in [15, 16]. The 1S7 tendon was composed of 12k T700 carbon fibers impregnated with RCX0111 epoxy resin, while 12k IM2C carbon fibers and TR1111 epoxy resin were used for the cross-beam. The elastic modulus in the fiber direction was $E_{t,2}=128$ GPa for the tendon, obtained from experiments as in [15] and 200 GPa for the cross-beam (manufacturer data). Furthermore, the compressive strengths of the high- and normal-strength grouts were 62.2 and 48.0 MPa respectively [16].

5.3 Pull-out experiments and FE modeling

5.3.1 Pull-out experiments on one- and two-strap anchors

Different experimental set-ups were used for the pull-out experiments on the one- and two-strap anchors [15, 16], but the loading concept was similar, i.e. the anchor body was supported at the air-side end while the pull-out loading was applied on the air-side strap via a steel pin, as shown in Fig. 5.2. However, in the 1C7 and 1S7 anchors, only the top surface of the high-strength grout was supported (i.e. not the steel tube), while in 2S5/10 the whole cross section was supported.

The pull-out displacement of the CFRP tendons was measured by LVDTs located at 200- and 165-mm distances from the support surface in the one- and two-strap anchors respectively. The strains of the embedded CFRP straps, CFRP confinement rings and steel tubes were measured by strain gages. Details concerning the experimental set-up and instrumentation of the 1C7 and 2S5/10 anchors are presented in [15, 16].

The one-strap anchors reached similar ultimate loads, i.e. $F_{ult,1}=497$ kN and $F_{ult,2}=523$ kN for 1C7 and 1S7 respectively (see Table 5.1). In anchor 1C7, approximately 50% of the load was transferred to the strap end [15]; however, a detailed analysis of the load transfer along the embedded strap could not be conducted due to the lack of measurements. The

2S5/10 anchors both exhibited ultimate loads higher than 1400 kN, i.e. $F_{ult,3}$=1402 kN and $F_{ult,4}$=1419 kN (see Table 5.1) [16]. In anchor 2S5, the tensile strain measurements along the straps allowed a complete load-transfer diagram to be derived, from the strap to the high-strength grout, at 500 kN. However, the gages installed on the straight transition stopped working at this load level due to interface slippage. Therefore, a load-transfer diagram at 1389 kN (first load peak of anchor 2S5 [16]) could only be derived based on several assumptions. In 2S10, since the strain gages had already stopped working at around 300 kN, no such diagram could be derived.

5.3.2 FE modeling of pull-out experiments on one-strap anchors

Using the commercial FE analysis software ABAQUS 6.11, FE models for simulating the pull-out behavior of one-strap anchors using identical CFRP tendons to those used in 1C7 were already developed and validated in [17]. However, the models were established not with steel tube confinement but with 200/380-mm-long and 2-mm-thick CFRP confinement rings (C200 and C380 anchors in [17]). In this work, similar models were developed for the 1C7 and 1S7 anchors by (1) replacing the CFRP ring with a steel tube in 1C7 and (2) modifying the strap geometry from curved to straight for 1S7 (and including a steel tube), as shown in Fig. 5.3. As in [17], only one quarter of the model was built with symmetric boundary conditions on the x-y and x-z planes. The grout, CFRP tendon and steel tube were modeled using C3D8R solid elements (C3D8R, eight-node linear brick elements with reduced integration); the cross-beam in anchor 1S7 was modeled in an identical way to that of the CFRP tendon using C3D8R solid elements. The total element numbers were 32896 and 24193 in the 1C7 and 1S7 anchors respectively.

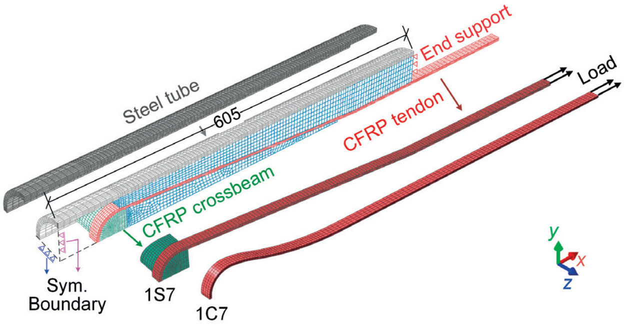

Fig. 5.3: FE models of 1S7 and 1C7 anchors

In both 1S7 and 1C7 anchors, the grout was simulated using the Concrete Damaged Plasticity (CDP) model as in [17], where a parametric study was conducted to investigate the influence of the strain-softening behavior of the grout on the pull-out behavior of the strap anchors. In this work, the grout did not enter the softening stage and the softening slope of the FE input uniaxial compressive stress-strain curve thus had no influence on the results. Considering the fully constrained status of the grout by the steel tubes, the stress-strain curve with the lowest softening slope from [17] was therefore selected. With regard to the CFRP material properties, the input values for anchor 1C7 remained the same as in [17], while in 1S7 the above-mentioned elastic moduli of the CFRP tendon and cross-beam were implemented.

The tendon/grout (T/G) and strap/cross-beam (S/CB) interfaces were simulated using a combination of surface-based cohesive and contact models as in [17]. The full confinement improves the interface behavior and consequently increases the maximum bond stress [18, 19] and friction [20, 21]. Therefore, the parameters of the cohesive model and the coefficient of friction, μ, in the contact model were recalibrated using the load vs tangential tensile strain responses of the embedded strap in the 1C7 and 1S7 anchor experiments, as shown in Fig. 5.4. The new calibrated models simulated the load vs tensile strain behavior of the embedded straps well, including the activation loads (at which positions C4/13 started to bear loads) and the subsequent strain development.

The selected cohesive laws are shown in Fig. 5.5. For the T/G interface, an identical tangential stiffness, i.e. K=1×10^{11} Pa/m, was used in both anchors; the maximum bond stresses, τ_{max}, were 4.4 and 2.2 MPa in 1C7 and 1S7 respectively. For the epoxy-bonded S/CB interface in anchor 1S7, a higher tangential stiffness of 1×10^{13} Pa/m and τ_{max} of 47 MPa (based on the shear strength of the CFRP epoxy matrix) were applied. In both anchors, an exponential softening of the bond stress and a maximum slip, δ_{max}, of 4.1 mm were applied. Furthermore, for the contact models, μ were 0.4 and 0.2 for below and above 300 kN respectively in anchor 1C7, while they were 0.8 and 0.3 for below and above 200 kN respectively in 1S7. Compared to the input values of the cohesive and contact models in [17] (see Fig. 5.5), most values applied in this work were higher due to the increased confinement provided by the steel tube (rock).

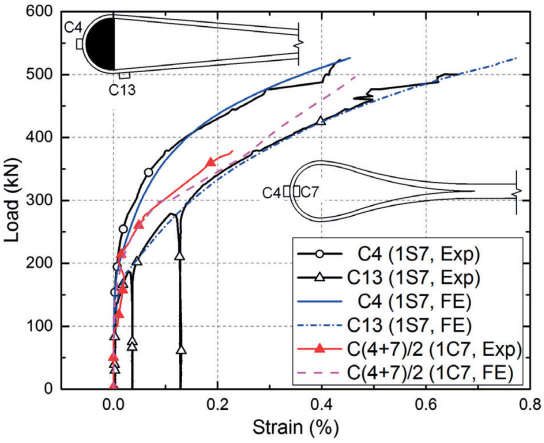

Fig. 5.4: Experimental and numerical load vs tangential tensile strain responses of embedded strap end (C4/13) in 1S7 and 1C7 anchors

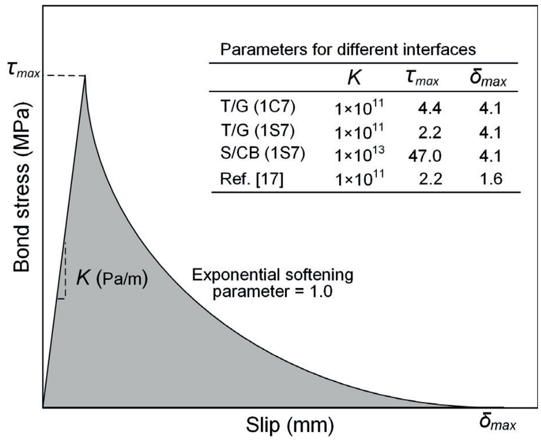

Parameters for different interfaces

	K	τ_{max}	δ_{max}
T/G (1C7)	1×10^{11}	4.4	4.1
T/G (1S7)	1×10^{11}	2.2	4.1
S/CB (1S7)	1×10^{13}	47.0	4.1
Ref. [17]	1×10^{11}	2.2	1.6

Fig. 5.5: Calibrated cohesive laws for tendon/grout and strap/cross-beam interfaces in FE models of 1S7 and 1C7 anchors

5.3.3 FE model validation

The FE models were validated by comparing the experimental and numerical load vs pull-out displacement responses and tangential strain distribution along the length of the steel tubes, as shown in Figs. 5.6 and 5.7 respectively. Good agreement between the numerical and experimental results was generally achieved. In the load vs pull-out displacement responses of anchor 1C7 (see Fig. 5.6), the displacement increase between 100 and 200 kN in the experiments compared to the FE model resulted from the extra deformation of the low Elastic modulus protection layer of the strain gages installed at the inner strap/grout interface (not used in other anchor specimens); the comparably lower strains at the corresponding position in the steel tube (R2, R5) could be attributed to the same effect.

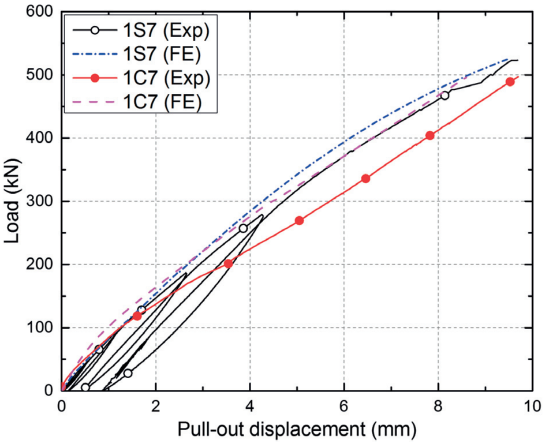

Fig. 5.6: Experimental and numerical load vs pull-out displacement responses of 1S7 and 1C7 anchors

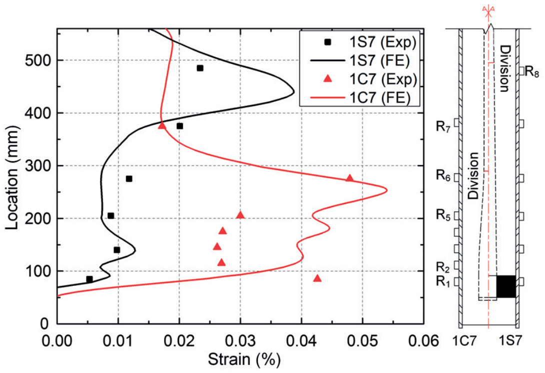

Fig. 5.7: Tangential strain distribution along length of steel tube at 500 kN in 1S7 and 1C7 anchors

The CFRP rupture failure observed at the strap division point and the detachment between the strap and cross-beam at $F_{ult,2}$= 523 kN in the experiment (see Fig. 5.8 (a)) were also well simulated by the FE model (see Fig. 5.8 (b)). A longitudinal tensile strain (LE11) concentration with a maximum value of 1.64%, which was 7% higher than the ultimate tensile strain of the CFRP strap tendons (1.5%, [16]), was obtained at the failure location in the experiment. Most of the strap/cross-beam interface already debonded at $F_{ult,2}$, i.e. CSDMG=1.0 (cohesive surface damage index [22], varying between 0.0 and 1.0), resulting in the final detachment at this interface when a sudden energy release from the ruptured strap occurred at $F_{ult,2}$. The FE models were subsequently used for the following analyses.

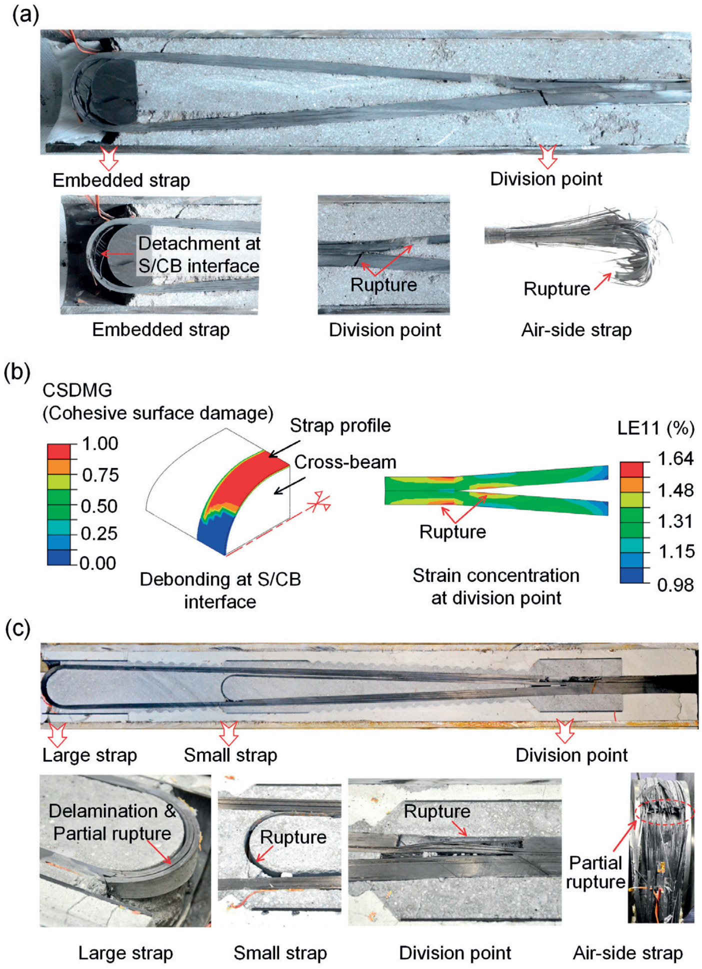
(a)
Embedded strap
Division point
Detachment at S/CB interface
Rupture
Rupture
Embedded strap
Division point
Air-side strap
(b)
CSDMG (Cohesive surface damage)
1.00
0.75
0.50
0.25
0.00
Strap profile
Cross-beam
Debonding at S/CB interface
Rupture
Strain concentration at division point
LE11 (%)
1.64
1.48
1.31
1.15
0.98
(c)
Large strap
Small strap
Division point
Delamination & Partial rupture
Rupture
Rupture
Partial rupture
Large strap
Small strap
Division point
Air-side strap

Fig. 5.8: Failure modes: (a) 1S7 (experiment); (b) 1S7 (FE model results at $F_{ult,2}$); (c) 2S10 (experiment)

5.4 Influence of strap geometry on load-transfer mechanism

The results of the 1C7 and 1S7 anchors were compared in order to investigate the influence of the strap geometry, i.e. curved or straight transition between the division point and strap end and the use of a cross-beam, on the global pull-out and local load-transfer behavior of the one-strap anchors.

Disregarding the displacement increase at 100–200 kN as mentioned above, the 1C7 and 1S7 anchors exhibited similar load vs pull-out displacement responses (see Fig. 5.6), demonstrating that the difference in the local strap geometry did not influence the global pull-out behavior. The two anchors also showed similar load vs tensile strain responses at positions C1/2 in the air-side strap, as shown in Fig. 5.9.

However, the local tangential strain peaks in the steel tube were observed at different locations, where high strap curvatures and corresponding spreading forces existed, i.e. between the semicircle and division point in 1C7 and at the division point in 1S7, as shown in Fig. 5.7.

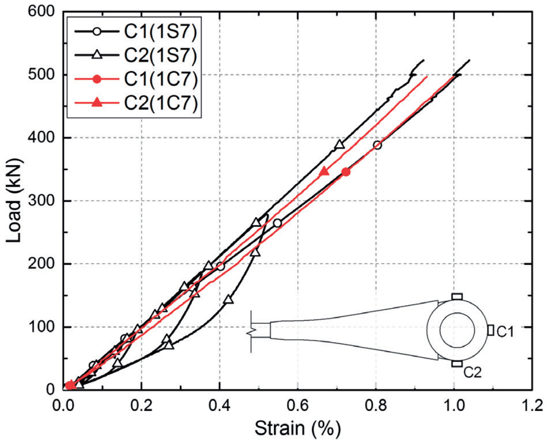

Fig. 5.9: Load vs tensile strain responses of air-side strap of 1S7 and 1C7 anchors

Based on the FE models, the load transfer along the embedded strap from the strap to the grout was analyzed and compared at 497 kN ($F_{ult,1}$), as shown in Fig. 5.10; the transferred load was calculated by multiplying the tensile strain, extracted from the inner and outer surfaces of the strap, by the elastic modulus and cross section. The load-transfer diagrams exhibited a decreasing trend from the air to the ground sides as follows:

(1) At the rod segment, no load transfer was observed due to the detachment at the tendon/grout interface at this load level caused by the Poisson's effect.

(2) At the strap division, an oscillating strain response occurred in both anchors, which was inversed on the inner surface compared to the outer one and thus could be attributed to local bending due to the change from the rod to the strap geometry. Since this change was smoother and the deviation angle was smaller in 1C7, the oscillation was smaller than in ST7.

(3) In the transition segment, located between the division and semicircle, the load transfer depended on the strap geometry, i.e. curvature and wedge-shaped widening of the cross section from the rod to the strap segment, which resulted in different levels of friction and mechanical interlocking. In anchor 1S7, approximately 40% of the load was transferred over a short distance after the division point due to these mechanisms, which was confirmed by the high frictional shear stress obtained from FE (Fig. 5.10, bottom). Subsequently, in the

straight segment, the load transfer was small. In contrast, the continuous curvature in anchor 1C7 also led to a continuous load transfer, which was much higher than in the straight segment of 1S7. However, the transferred load up to the semicircle was similar in both anchors, i.e. around 250 kN (50% of applied load).

(4) In the semicircular segment, again strain oscillation indicated local bending in both cases. The remaining load was transferred earlier in 1S7 than in 1C7 due to the cross-beam.

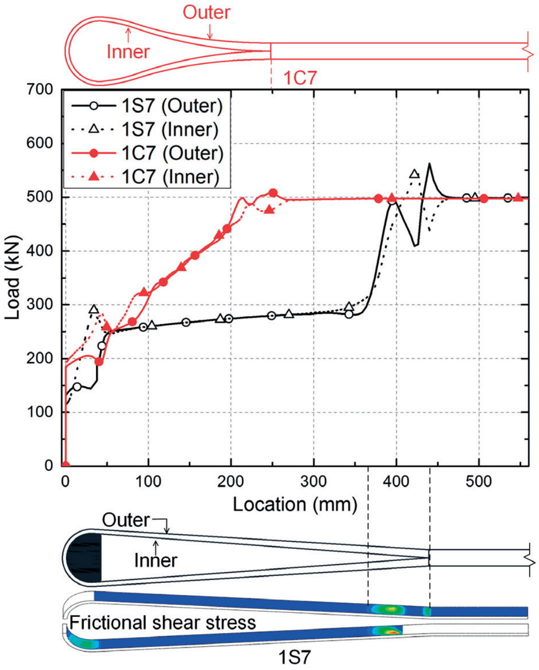

Fig. 5.10: Comparison of load-transfer diagrams along embedded strap at 497 kN obtained from FE models of 1S7 and 1C7 anchors

The effect of the load level on the load-transfer diagrams derived along the embedded strap in anchor 1S7 with straight transition, i.e. the diagrams at 50, 100, 300 and 500 kN, again obtained from the FE model, are shown in Fig. 5.11. At low load levels, e.g. 50 kN, where the progressive debonding along the strap occurred, a continuous load transfer was observed. The oscillating behavior at the division point, as well as the associated local load drop, started at 100 kN and their intensity increased with increasing loading. Correspondingly, the slope of the frictional load transfer along the straight segment diminished with increasing load. The load-transfer diagram, derived at high load levels, could therefore be simplified into three constituent segments, see dashed curve in Fig. 5.11: (1) segment I, the load drop at the division point, (2) segment II, the frictional load transfer and (3) segment III, the load drop at the strap end.

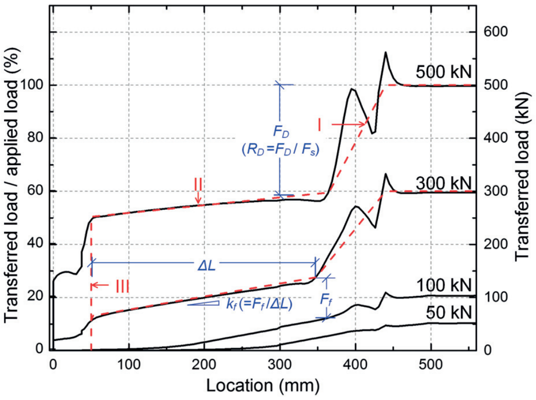

Fig. 5.11: Load transfer along embedded strap in anchor 1S7 at different load levels

5.5 Load-transfer mechanism in multi-strap anchors

5.5.1 Influence of strap configuration on global pull-out behavior

The 1S7 and 2S5/10 anchors with straight strap geometry were compared in order to investigate the influence of the strap configuration, i.e. the strap number, on the load vs pull-out displacement responses, see Fig. 5.12. The load was normalized by the elastic modulus ($E_{t,n}$, see Table 5.1) and cross-section area ($A_{rod,n} = \pi \cdot D_{rod,n}^{2}/4$) of the tendon and the pull-out displacement was normalized by the distance between the installed LVDT and ground-side tendon end, i.e. 760 and 1365 mm for 1S7 and 2S5/10 respectively.

All the curves exhibited similar behavior, i.e. an initial nonlinear segment with steeper slope followed by a linear one, indicating that the difference in the strap configuration did not affect the global pull-out behavior of the anchors. Similar failure modes were also observed in the 1S7 and 2S10 anchors, see Fig. 5.8, i.e. strap rupture occurred at the strap division point due to local bending at this location as mentioned above, demonstrating that the failure mechanism also remained the same. Furthermore, the normalized load vs tensile strain responses of the air-side straps of the 1S7 and 2S10 anchors also exhibited similar behavior, as shown in Fig. 5.13. The 1S7 and 2S5/10 anchors thus exhibited similar behavior despite the different strap configurations.

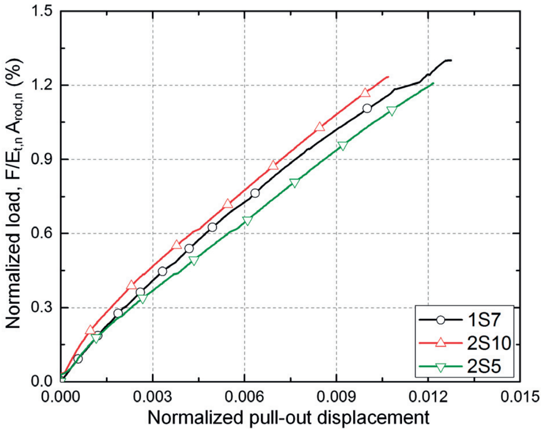

Fig. 5.12: Normalized load vs normalized pull-out displacement responses of 1S7 and 2S5/10 anchors

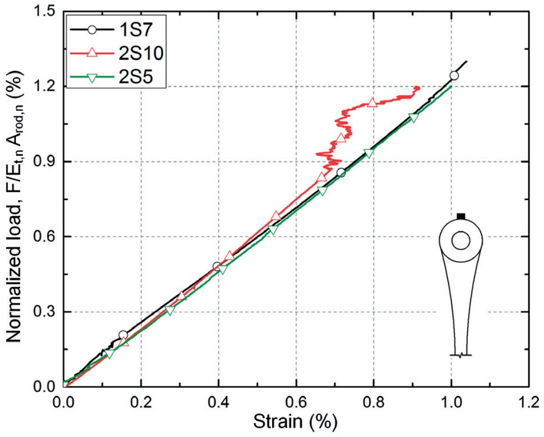

Fig. 5.13: Normalized load vs tensile strains of air-side strap of 1S7 and 2S5/10 anchors

5.5.2 Empirical model of load-transfer diagram for multi-strap anchors

A complete load transfer diagram, as shown in Fig. 5.11 for a one-strap anchor at 300 and 500 kN, is composed of three parameters: (1) load drop at the strap division, F_D, (2) frictional load transfers along each strap, F_f, and (3) load drops at each strap end, F_E. Based on the results obtained for the 1S7 and 2S5/10 anchors, an empirical load-transfer model was developed for multi-strap anchors at load levels where the debonding along the embedded straps was complete, i.e. above 200 and 500 kN in the 1S7 and 2S5/10 anchors respectively [16]. With regard to the 2S5/10 anchors, the total applied load, F (F>500 kN), was assumed to be distributed between the inner (smaller) and outer (larger) straps according to their stiffness, i.e. the applied strap loads, F_s, were F_s=0.4·F and 0.6·F for the inner and outer straps respectively. This assumption is validated in the following.

(1) Frictional load transfer along each strap

In the FE model of anchor 1S7, the frictional load transfer occurred uniformly along the straight segment II (see Fig. 5.11), i.e. the frictional transfer rate, $k_f=\Delta F/\Delta L$, was constant, where ΔF and ΔL are the frictional load decrease and distance between two positions on this segment; therefore, k_f was assumed to also be constant along each strap in the multi-strap anchors. The obtained k_f vs applied strap loads, F_s, in the outer straps of the 2S5/10 anchors is shown in Fig. 5.14; ΔF was calculated as the load difference between positions T3–T4 (ΔL=280 mm) where the strains were measured. A straight line with a correlation of coefficient of 0.92 was fitted to model the relationship between k_f and F_s (i.e. $0.6 \cdot F$) and the frictional load decrease (F_f) in the outer strap can thus be calculated as:

$$F_f = k_f \cdot \Delta L = (-4.68 \times 10^{-4} \cdot F_s + 0.37) \cdot \Delta L \tag{5.1}$$

In contrast, positions T6/7 on the inner straps (see Fig. 5.14) exhibited similar strain measurements above F_s=200 kN (corresponding to F=500 kN) [16]. The inner straps thus did not transfer any load through friction and F_f of Eq. (5.1), i.e. of the outermost strap, can therefore be considered as the total load transferred by friction in multi-strap systems.

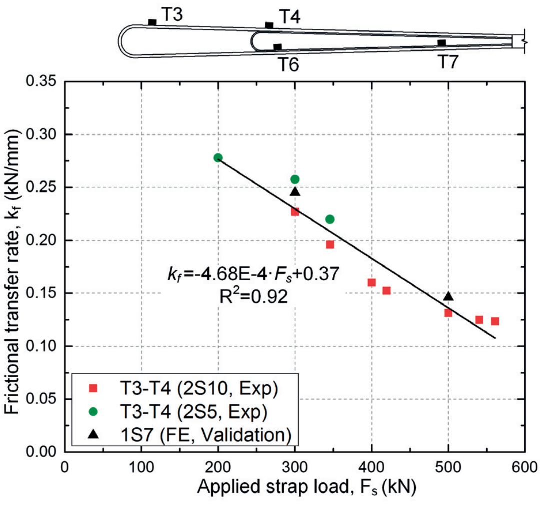

Fig. 5.14: Frictional transfer rate vs applied strap load in 1S7 and 2S5/10 anchors

Eq.(5.1) was further validated by the FE results for anchor 1S7 at F_s=300 and 500 kN ($F_s=F$ in this case). Using Eq. (5.1), the calculated F_f were 43 and 68 kN at 300 and 500 kN respectively, and were thus only 6.9 and 6.3% lower than the FE results (46 and 73 kN), which were added in Fig. 5.14.

Comparing the 1S7 and 2S5/10 anchors at the same load levels, k_f did not exhibit a clear dependence on the confinement level, i.e. E_{rock}, which could result from (1) a low sensitivity of k_f to the investigated E_{rock} range and (2) the low frictional load transfer compared to the total applied load. Eq. (5.1) was thus considered applicable to estimate the frictional load transfer, F_f, in multi-strap anchors under rock confinement, i.e. rock stiffnesses of 20–40 GPa.

(2) Load drop at strap division

In the FE model of anchor 1S7, the load drop at the strap division (F_D), i.e. the load decrease in segment I (see Fig. 5.11), increased with increasing loading; however, the load drop ratio of F_D to F_s, i.e. R_D=F_D/F_s, decreased (comparing R_D at 300 and 500 kN in Fig. 5.11). The obtained R_D vs F_s in the inner straps of the 2S5/10 anchors is shown in Fig. 5.15; F_D was calculated as the difference between the applied strap load ($0.4\cdot F$) and the transferred load at position T6 or T7 (T7 stopped measuring at F_s=200 kN) because no frictional load transfer existed between T6/7 as mentioned before. The calculated R_D in anchor 2S10 was approximately 1.9 times higher than in 2S5 at the same load levels. This value corresponded approximately to the rock stiffness ratio $E_{rock,4}$ /$E_{rock,3}$, i.e. unlike the transfer in the straight segment, the transfer at the division point was confinement-dependent since the friction at this location was high. The R_D of 2S5 was thus magnified by the rock stiffness ratio (1.84) in order to analyze R_D at the same confinement level. An exponential curve with a correlation coefficient of 0.94 was fitted to model the relationship between R_D and F_s at the confinement level of $E_{rock,4}$, as shown in Fig. 5.15.

In the outer strap of the 2S5/10 anchors, no such analysis could be conducted because the strain gage position T8 (see Fig. 5.15) was located inside the load drop region (75–95 mm long in 1S7, see Fig. 5.11) and could thus not be used for calculating F_D. Considering the identical wedge-shaped division geometry of the inner and outer straps, the R_D of the outer strap, and thus also the R_D of the inner plus outer straps, were assumed to be identical to the R_D in the inner strap. By further taking into account the influence of E_{rock} for different rock stiffness cases, R_D in multi-strap systems can thus be calculated as:

$$R_D = (E_{rock,n}/38)\cdot(2.39\cdot e^{(-F/107.69)} + 0.36) \tag{5.2}$$

Eq. (5.2) was first validated by the FE results obtained for anchor 1S7 for the one-strap case. The R_D obtained from the FE results were 0.54 and 0.40 at F=300 and 500 kN respectively, as shown in Fig. 5.15 (where the R_D of 1S7 has been multiplied by $E_{rock,4}$

$/E_{rock,2}$). The R_D calculated using Eq. (5.2) were 0.48 and 0.36 and thus only 11 and 10% lower than the FE results. Furthermore, the assumption of the identical R_D in the two straps was validated by the measurements at positions T6/3 in the 2S5/10 anchors at F=1389 kN, at which load F_f already decreased to zero. The difference between F and the sum of the transferred load at T6/3 (T6+T3=1089 and 844 kN in 2S5/10 respectively) was thus equal to F_D; i.e. F_D=300 and 545 kN; correspondingly, the R_D were 0.22 and 0.39 in 2S5/10 respectively, as shown in Fig. 5.15 (where the R_D of 2S5 has been multiplied by $E_{rock,4}/E_{rock,3}$ and the two data points of 2S5/10 overlap each other). The R_D calculated using Eq.(5.2) were 0.20 and 0.36 in 2S5/10 respectively, i.e. 9 and 8% lower than those obtained from the experimental results. Eq. (5.2) and the associated assumptions were thus considered applicable for estimating F_D as follows:

$$F_D = (E_{rock,n}/38)\cdot(2.39\cdot e^{(-F/107.69)}+0.36)\cdot F \tag{5.3}$$

In order to construct the load-transfer diagram, the length of segment I is also required. This length varied from 92 to 75 mm in anchor 1S7 depending on the load. In the 2S5/10 anchors the length was thus assumed as being constantly 100 mm, corresponding to the length between the division point and the newly added position T8' in Fig. 5.15.

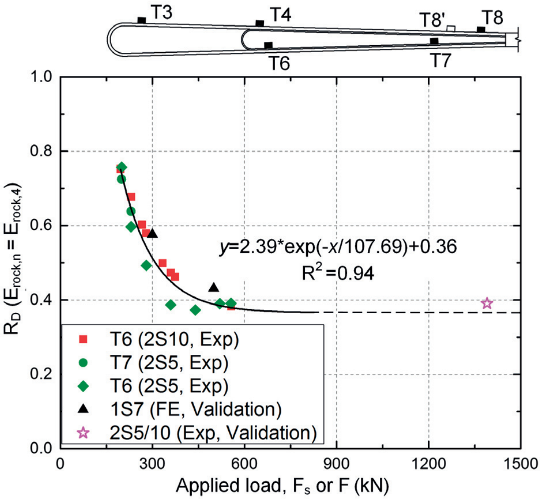

Fig. 5.15: Division load drop ratio vs strap load in 1S7 and 2S5/10 anchors at confinement level of $E_{rock,4}$

(3) Load drops at strap ends

The load drop at each strap end (F_E), i.e. behind positions T6/3 in the inner and outer straps in 2S5/10 anchors, was deduced based on F, F_D and F_f. The total transferred load at the

T4/6 positions was calculated as $F'=F-F_D-F_{f,T4-T8'}$. 40% of F' was borne by the inner strap, i.e. $F_{E,in}=0.4\cdot F'$. For the outer strap, F_E was calculated as $F_{E,out}=0.6\cdot F'-F_{f,T3-T4}$.

(4) Derivation of empirical load-transfer diagram for 2S5/10

Based on the obtained F_D, F_f and F_E, the complete load-transfer diagram can be derived. The load-transfer diagrams for the 2S5/10 anchors at F=700 (50% of F_{ult}) and 1389 kN were obtained as follows, see Fig. 5.16:

(1) Calculate F_D by substituting $E_{rock,n}$ and F into Eq.(5.3). The calculated F_D of the inner plus outer straps for the 2S5/10 anchors, as shown in Table 5.2, corresponded to segment I in Fig. 5.16 (distributed over 100 mm).

(2) Calculate F_f between positions T4-T8' and T3-T4 using Eq. (5.1), as shown in Table 5.2, corresponding to segments II and IV respectively in Fig. 5.16.

(3) Calculate F_E at positions T6/3 based on F, F_D and F_f, as shown in Table 5.2, corresponding to segments III and V respectively in Fig. 5.16.

The deduced F_E was in good agreement with the experimental results in both 2S5/10 anchors, as shown in Table 5.2. Taking into account also the strain measurements at positions T4/6, the assumption of the 60/40% load distribution ratio was thus considered validated. The derived load-transfer diagram showed that the frictional load transfer decreased from 19% of the total applied load at 700 kN to zero at 1389 kN, i.e. the principal load transfer occurred at the division and strap ends.

Table 5.2: Calculated parameters for load-transfer diagrams for 2S5/10 anchors

Anchors	F (kN)	F_D (kN) (In.+out.)	F_f (kN)		$F_{E,in}$ (kN)			$F_{E,out}$ (kN)		
			T4-T8'	T3-T4	Cal.	Exp.	Cal./Exp.	Cal.	Exp.	Cal./Exp.
2S5	700	139	81	51	192	204	0.94	237	240	0.99
	1389	273	0	0	447	438	1.02	670	650	1.03
2S10	700	255	81	51	146	128	1.14	168	157	1.07
	1389	500	0	0	355	344	1.03	532	500	1.06

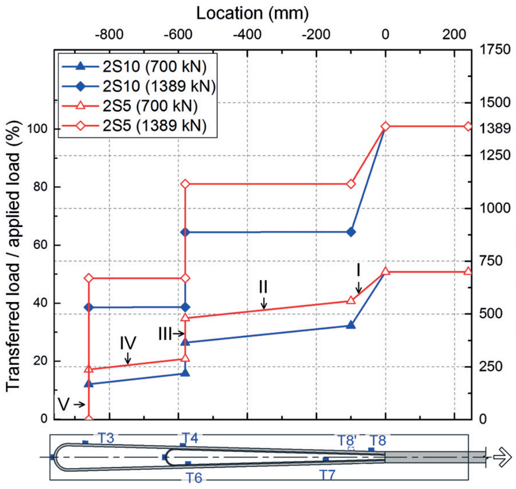

Fig. 5.16: *Derived load-transfer diagrams for 2S5/10 anchors*

5.5.3 Design of three-strap anchor

Maintaining the design of the two-strap tendon, a third strap was added on the ground side in the three-strap anchor to achieve a targeted load-bearing capacity of at least 2500 kN. The outer (third) strap was located at 320 mm from the middle (second) strap, i.e. at an identical distance to that between the other two straps, resulting in an outer strap length of 1270 mm (see Table 5.1). Based on the identical strap opening angle to that in the 2S5/10 anchors, the inner diameters of the CFRP confinement rings and steel tube, $D_{tube,5}$, were 134 and 164 mm; the width of the straps, w_5, could thus be increased to 50 mm (see Table 5.1) due to the increased borehole diameter (i.e. $D_{tube,5}$). Furthermore, the newly added outer strap was designed to bear at least the same load as the middle one.

The load distribution ratio is directly proportional to the strap stiffness as mentioned above. Based on the dimensions of the inner and middle straps and by assigning an identical load distribution ratio to the middle and outer straps, the inner, middle and outer straps bore 24, 38 and 38% of the total applied load respectively. Based on the required stiffness of the outer strap, its thickness was calculated as 9.4 mm. The resulting dimensions of the CFRP tendon are shown in Fig. 5.17 (a) and Table 5.1, and the anchor head is shown in Fig. 5.17 (b). Furthermore, based on the average F_{ult} of the 2S5/10 anchors of 1410 kN and considering the larger width of the three-strap anchor, its load-bearing capacity, $F_{ult,5}$, was estimated as $F_{ult,5}$=1410×(50/40)/(0.24+0.38)=2843 kN.

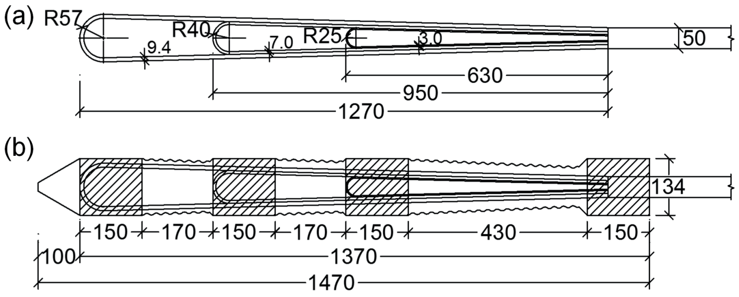

Fig. 5.17: Anchor 3S: (a) CFRP tendon; (b) anchor head

The critical compressive stress at $F_{ult,5}$=2843 kN in the normal-strength grout located at the end support, $\sigma_{G,5}$, was also estimated based on the results obtained for 2S5/10; at 1389 kN, where the grout stresses were $\sigma_{G,3}$=49.2 and $\sigma_{G,4}$=25.6 MPa in 2S5/10 respectively [16]. Considering the increased cross section of the three-strap anchor ($D_{tube,5}$=164 mm vs $D_{tube,3/4}$=130 mm), $\sigma_{G,5}$ at $F_{ult,5}$ was estimated as $\sigma_{G,5}=\sigma_{G,3/4}\cdot(F_{ult,5}/1389)/(D_{tube,5}/D_{tube,3/4})^2$ =63.3 and 32.9 MPa in rocks with low ($E_{rock,3}$=20.7 GPa) and medium ($E_{rock,4}$=38.0 GPa) stiffnesses respectively. Compared to the uniaxial compressive strength of 48.0 MPa of the normal-strength grout [16], the three-strap anchor is thus applicable in medium- or high-stiffness rocks to prevent potential failure in the normal-strength grout. Furthermore, the weight of the prefabricated high-strength anchor head (Fig. 5.17 (b)) with a density of 1.7 kg/L was approximately 28 kg, which can still be manually handled by two workers. The three-strap anchor design was thus considered viable from both the mechanical and construction/installation points of view.

To further validate the design, the load-transfer diagrams at 1250 (50% of the targeted load capacity) and 2500 kN were derived by following the identical procedure as that used for 2S5/10. A rock stiffness of $E_{rock,5}$=37.0 GPa was assumed, which is applicable to many rocks such as Gneiss, Granite and Quartzite [23]. The calculated parameters are listed in Table 5.3 and the derived load-transfer diagrams are shown in Fig. 5.18; positions T1–T4 correspond to the locations of the strap end and division point, based on which the lengths for calculating the frictional load transfer were obtained. In anchor 3S, compared to the load drops at the division and strap ends, the frictional load transfer was low and it decreased from 13% of the total applied load at 1250 kN to zero at 2500 kN. At 2500 kN, 390, 617 and 617 kN were finally transferred at the inner, middle and outer strap ends respectively, corresponding to 16, 25 and 25% of the total applied load, i.e. 66% was transferred at the strap ends and 34% at the division point. The inner strap bore 63% of the middle and outer strap loads, indicating that the anchor would fail due to the rupture of the inner strap as in 2S5/10 [16], considering that its thickness was only 43 and 32% of the middle and outer straps.

Table 5.3: Calculated parameters for load-transfer diagrams for anchor 3S

F (kN)	F_D (kN) (3 straps)	F_f (kN)			$F_{E,in}$ (kN)	$F_{E,mid}$ (kN)	$F_{E,out}$ (kN)
		T3-T4	T2-T3	T1-T2			
1250	438	75	45	45	177	257	213
2500	876	0	0	0	390	617	617

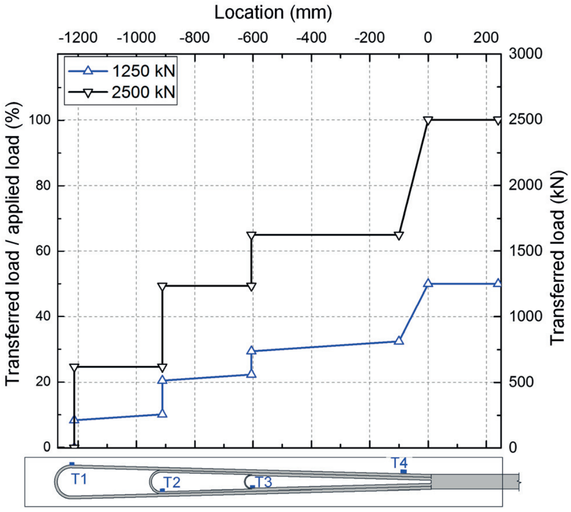

Fig. 5.18: Calculated load-transfer diagrams at 1250 and 2500 kN for anchor 3S

5.6 Conclusions

The experimental and numerical results obtained for one- and two-strap CFRP ground anchors were analyzed to investigate the influence of the strap geometry and configuration on the global pull-out and local load-transfer behavior of the anchors. Based on these analyses, an empirical model for the prediction of the load-transfer from a CFRP multi-strap tendon to the surrounding grout was derived and further applied to a new design for a three-strap anchor. The following conclusions were drawn:

1. The difference in the strap geometry, i.e. different curvature distributions from the division point up to the strap end and different transitions from the rod to the strap cross section, resulted in different load-transfer diagrams, but did not influence the global pull-out behavior of the anchors. High strap curvatures and localized cross-section changes led to high local stress concentrations in the surrounding rock (i.e. steel tube) and thus require a corresponding local confinement capacity.

2. One- and two-strap anchors with similar strap geometries exhibited similar global pull-out behavior and analogous load-transfer diagrams, despite the different strap numbers.
3. The load-transfer in multi-strap anchors consists of (1) load transfer at the strap division, (2) frictional load transfer along each strap and (3) load transfer at the strap ends. An empirical model was developed to predict these components in multi-strap anchors and thus derive corresponding load-transfer diagrams.
4. At higher loads, frictional load transfer occurred only in the outer strap in multi-strap anchors; the friction was not sensitive to variations in the confinement provided by different rock types. However, the load transfer at the strap division was proportional to the confinement level.
5. Based on the developed load-transfer model, a three-strap anchor was designed by adding a third strap to the two-strap anchor. It was demonstrated that the targeted load-bearing capacity of at least 2500 kN can be achieved.

References

[1] Sabatini P, Pass D, Bachus RC. Geotechnical engineering circular no. 4: Ground anchors and anchored systems. US DOT Federal Highway Administration, 1999.

[2] Kaiser P, Diederichs M, Yazici S. Cable bolt performance during mining induced stress change – three case examples. Rock Support, Kaiser & McCreath, Rotterdam, 1992:377-384.

[3] Kılıc A, Yasar E, Celik AG. Effect of grout properties on the pull-out load capacity of fully grouted rock bolt. Tunn Undergr Space Technol 2002;17:355–362.

[4] Benmokrane B, Zhang B, Chennouf A, Masmoudi R. Evaluation of aramid and carbon fibre reinforced polymer composite tendons for prestressed ground anchors. Can J Civ Eng 2000;27:1031-45.

[5] Zhang B, Benmokrane B, Chennouf A. Prediction of tensile capacity of bond anchorages for FRP tendons. J Compos Constr 2000;4:39-47.

[6] Benmokrane B, Chekired M, Xu H. Monitoring behavior of grouted anchors using vibrating-wire gauges. J Geotech Eng 1995;121:466-75.

[7] Chen J, Saydam S, Hagan PC. An analytical model of the load transfer behavior of fully grouted cable bolts. Constr Build Mater 2015;101:1006-15.

[8] Wu Z, Yang S, Zheng J, Hu X. Analytical solution for the pull-out response of FRP rods embedded in steel tubes filled with cement grout. Mater Struct 2010;43:597-609.

[9] Kim N-K. Performance of tension and compression anchors in weathered soil. J Geotech Geoenviron 2003;129:1138-50.

[10] Tian J, Hu L. Review on the Anchoring Mechanism and Application Research of Compression-Type Anchor. Eng 2016;8:777.

[11] Englert CM, Gómez JE, Wilkinson C, Godet V. Development of Removable Load Distributive Compressive Anchor Technology. In: IFCEE 2015:748-62.

[12] Hertz JS, Moormann G, Paquette M, Shapiro SS, Gallagher MJ. Removable Compressive Load Distributive Strand Anchors: Case History and Lessons Learned. In: IFCEE 2015:1597-607.

[13] Keller T, Kenel A, Koppitz R. Carbon Fiber-Reinforced Polymer Punching Reinforcement and Strengthening of Concrete Flat Slabs. ACI Struct J 2013;110.

[14] Huster U, Broennimann R, Winistörfer A. Strengthening of a historical roof structure with CFRP-straps. In: Proceedings of the fourth international conference on FRP composites in civil engineering (CICE2008), Zurich, 22-24 July 2008. B.6.

[15] Fan H, Vassilopoulos AP, Keller T. Pull-out behavior of CFRP single-strap ground anchors. J Compos Constr 10.1061/(ASCE)CC.1943-5614.0000760 , 04016102.

[16] Fan H, Vassilopoulos AP, Keller T. Pull-out behavior of CFRP ground anchors with two-strap ends. Compos Struct 2017;160:1258–1267.

[17] Fan H, Vassilopoulos AP, Keller T. Evaluation of grout materials for CFRP ground anchors with strap ends. Constr Build Mater 2017;145:196-206.

[18] Fédération Internationale du Béton (FIB). Fib model code for concrete structures 2010. Lusanne, Switzerland, 2012.

[19] Japanese Society of Civil Engineers (JSCE). Recommendation for design and construction of concrete structures using continuous fiber reinforcing materials. Japan Soc. of Civil Engineers, 1997.

[20] Biscaia HC, Chastre C, Silva MA. Double shear tests to evaluate the bond strength between GFRP/concrete elements. Compos Struct 2012;94:681-94.

[21] Bakis C, Uppuluri V, Nanni A, Boothby T. Analysis of bonding mechanisms of smooth and lugged FRP rods embedded in concrete. Compos Sci Technol 1998;58:1307-19.

[22] Abaqus Inc. Abaqus analysis user's manual, version 6.11. Providence, RI, USA; 2011.

[23] Heuze FE. Scale effects in the determination of rock mass strength and deformability. Rock Mech 1980;12:167-92.

6.

Experimental and numerical investigation of tensile behavior of non-laminated CFRP straps

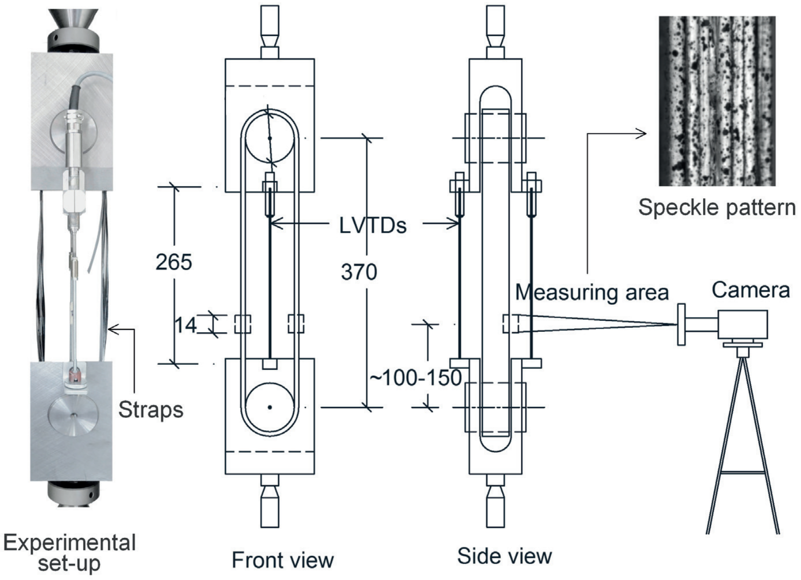
Speckle pattern
LVTDs
265
370
Measuring area
Camera
14
~100-150
Straps
Experimental set-up
Front view
Side view

Reference detail:

Fan H, Vassilopoulos AP, Keller T. Experimental and numerical investigation of tensile behavior of non-laminated CFRP straps. Compos B Eng 2016;91:327-36.

6.1 Introduction

Carbon fibers offer excellent mechanical properties such as a high strength-to-weight ratio and excellent corrosion resistance, which makes them attractive in the civil engineering domain, i.e. in bridge and building construction, for new or the strengthening of existing load-bearing structures. However, mainly due to their high cost, their possible application is, in most cases, limited to linear components with unidirectional (UD) fiber arrangement, such as cables or strips, in order to fully benefit from their excellent mechanical properties [1, 2]. Carbon fibers, however, are strongly anisotropic, exhibiting properties with much lower values in the transverse fiber direction, which makes the anchoring of the fibers at the ends of the linear components difficult. Conceptually similar to steel cables, mechanical or bonded anchors are currently used [3-5]. However, in most cases, the anchor strength is significantly lower than the nominal strength of the CFRP material and the excellent fiber properties thus cannot be fully exploited.

An alternative anchoring method, which does not mimic the steel anchorage technique, are carbon fiber-reinforced polymer (CFRP) straps, in which continuous CFRP tapes are wound around two steel end-pins, as shown in Fig. 6.1. Two different strap concepts exist, laminated straps [6] and non-laminated straps [7, 8]. In the former, the tape layers are fully laminated together while in the latter relative displacements between the non-laminated layers can occur. The outermost and innermost layers are anchored by fusion bonding (of the thermoplastic matrix) and by friction at the steel/CFRP interfaces respectively.

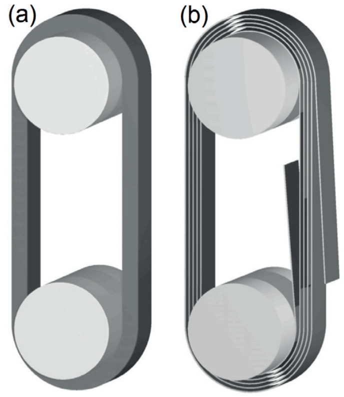

Fig. 6.1: Schematic of: (a) laminated strap; (b) non-laminated strap [7]

Research work has been conducted on non-laminated CFRP straps for the shear strengthening of concrete beams [9] and box girders [10], and as the flexural reinforcing elements in stressed ribbon bridges [11]. Their applications, mainly in pilot projects, were also reported for example for the strengthening of timber roof structures [12] and masonry structures [13], and as the bowstrings of arch bridges [14]. A recent commercial product is used to strengthen existing reinforced concrete flat slabs against punching shear, as shown in Fig. 6.2 [15]. Due to their flexibility, straps can be easily threaded from the top into predrilled holes and anchored and prestressed from the underside.

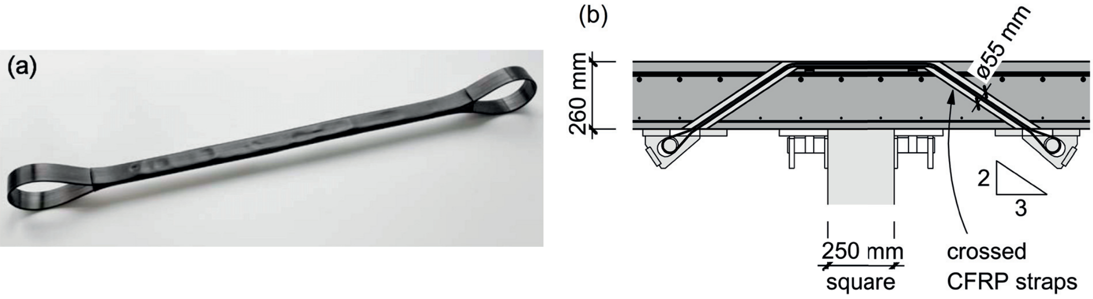

Fig. 6.2: Application of non-laminated CFRP straps for punching shear strengthening of concrete slabs: a) flexible strap component; b) installed and prestressed strap [15]

The possible relative displacements between the layers of non-laminated straps may significantly reduce stress concentrations at the transition from the straight to the curved strap segments and thus increase the strap strength compared to laminated straps [7]. Parameters that influence the strength of non-laminated straps are, according to [8], the ratio of the outer to the inner strap radius, the number of tape layers, the frictional properties at the steel/CFRP and CFRP/CFRP interfaces, the fiber/matrix combinations (AS4/PEEK, T700S/PPS and T700S/PA12 were used) and the anchorage method used for the outermost tape (epoxy bonded, clamped and fusion bonded). To experimentally investigate the strap performance, axial strains were measured by strain gages on the tapes, while relative displacements between individual layers were observed by comparing the locations of edge markings on images captured by a camera at different load levels [8]. However, the results were not always consistent and no complete datasets were obtained. Furthermore, numerical analyses of the structural behavior of multilayer non-laminated straps have not yet been conducted; only the winding procedure for a single-layer tape was studied [16].

In this chapter, the load-bearing behavior of seven-layer non-laminated CFRP straps was experimentally and numerically investigated. Axial tensile experiments were performed to investigate the displacement and strain distributions in the individual layers, as well as the strain field in the fusion-bonded anchorage zone. A corresponding finite element (FE) model was developed and validated by the experimental results. The strain distributions across the curved segments were then obtained and parametric FE analyses were conducted to study the effect of the friction at the CFRP/CFRP and steel/CFRP interfaces on the strap behavior. Based on the experimental and numerical results, the load-bearing and failure mechanisms of the strap could be analyzed.

6.2 Experimental program

6.2.1 Specimen description

The seven-layer non-laminated CFRP straps were fabricated by Carbo-Link, Fehraltorf (Switzerland). The lengths between the pin centers varied slightly and were approximately 370 mm; the width was 30 mm. The tape thickness across the width also slightly varied and was 0.135±0.003 mm. The tapes were composed of unidirectional Toray T700SC fibers impregnated with a thermoplastic polyamide matrix PA12; the fiber volume fraction was approximately 60%. The elastic modulus, characteristic (5%-fractile) tensile strength and mean tensile strength of one tape layer were 132, 2.10 and 2.46 GPa, respectively (manufacturer data).

The outermost layer was fusion bonded along a length of about 100 mm in the straight strap segments, i.e. an eighth layer (L_8) was wound around one of the two pins, as shown in Fig. 6.3(a). The inner tape end (designated free end) remained non-laminated and was anchored by friction. In order to prevent galvanic corrosion between steel and CFRP materials and unwinding before loading, the straps are normally covered by a glass fiber fabric in the pin regions, see Fig. 6.3(b); this glass cover was not removed in the experiments. Six identical straps (designated S1 to S6) were investigated.

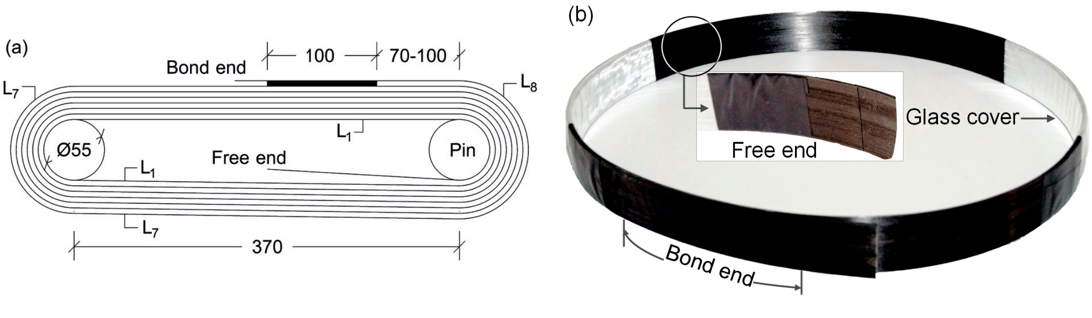

Fig. 6.3: Non-laminated strap: (a) schematic (dimensions in [mm]); (b) slack strap

6.2.2 Experimental set-up and instrumentation

The tensile experiments were performed on an Instron 8801 machine of 100-kN capacity at a temperature of 23±2°C and relative humidity of 50±5%. The experimental set-up and instrumentation layout are shown in Fig. 6.4. Two pins of 55-mm diameter were initially placed at a 350-mm center-to-center distance in order to install the slack strap. The bottom pin was then moved downwards by approximately 20 mm until the specimen was in a taut state under small load. Subsequently, the loading was applied on the bottom pin in displacement-control mode at a rate of 0.5 mm/min.

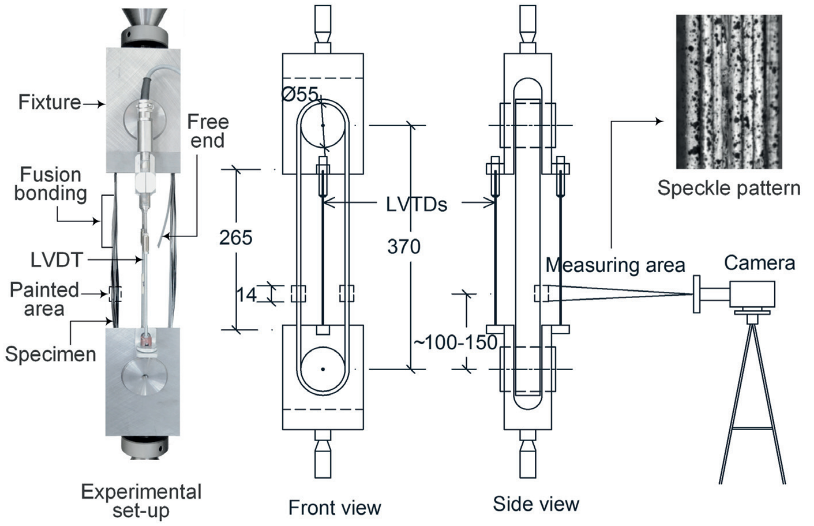

Fig. 6.4: Experimental set-up and instrumentation layout (dimensions in [mm])

In the strap S1 to S3 experiments, only the strap elongation and applied loads were measured using two Linear Variable Differential Transformers (LVDTs) and the machine load cell respectively. The LVDTs were installed between the two pin fixtures, the gage length was 265 mm, see Fig. 6.4. In each experiment, two load cycles up to 40 kN were first applied before the specimens were loaded to failure.

In experiments S4 to S6, the displacements of the individual layers were also measured and the strains calculated. To avoid damaging the fragile tape by gluing strain gages, non-contact Digital Image Correlation (DIC) was used. A random speckle pattern was applied on the strap edges using black and white spray paints, as shown in Fig. 6.4. A 14-mm-long DIC measuring area was selected depending on the pattern quality; the center of this area was located at a distance of 100–150 mm from the bottom pin center in different experiments.

Two-dimensional DIC was used since the measuring area mainly exhibited in-plane motions. Digital images were taken at a frequency of 0.1 Hz. Post-processing was performed using Vic-2D software from Correlated Solutions Inc., USA. Displacements at each point of the measuring area were computed by comparing the location of each subset (a collection of pixels around the point) in images of the un-deformed state (reference) and deformed state [17]. Different strain tensors – Engineering, Lagrange, Logarithmic and Euler-Almansi – could be calculated by the software [18]. However, in the case of low strains, the difference between these tensors is insignificant and the Lagrange strain was selected in this study.

Since the bond and free ends were located on opposite sides of the strap, see Fig. 6.4(a), the camera view (14×14 mm^2) could not capture both sides at the same time. DIC measurements were thus applied on the free-end side first, in an experiment loaded up to 50kN. The strap was then removed and reinstalled with the speckle pattern on the bond-end side and, in a second experiment, also loaded up to 50 kN. The DIC measurements were analyzed after each experiment and, if necessary, an improved speckle pattern was applied and the experiment repeated. This procedure caused minor damage to some tape edges in certain cases. In the second experiment, after the 50-kN cycle, the strap was unloaded and reloaded up to failure.

Due to the initially large lateral motions of the straps, DIC measurements could not be analyzed at the beginning of the experiments, as shown in Fig. 6.5; the DIC images of a 2.8mm-long segment of strap S4, captured at 0.0, 2.5, 6.4 and 29.2 kN, are shown. The segment exhibited an approximately 2.6-mm lateral displacement from 0.0 to 2.5 kN, during which the slack strap was tautened. The software could only compute displacements after the diminishing of these motions, which occurred between 5 and 10 kN. In the following DIC results, measured deformations thus start at loads of between 5 and 10 kN, depending on the experiment.

To exclude any potential motions of the set-up, apart from the strap, the displacements of the upper and lower fixtures, as well as the rotations of the pins, were separately measured using a video extensometer. Only the upper fixture exhibited a small, linearly increasing vertical displacement (of 0.256 mm at 39 kN), resulting from the deformation of the screw connection between the upper fixture and the machine. As a result, the vertical DIC displacement measurements were corrected by subtracting this deformation of the upper fixture.

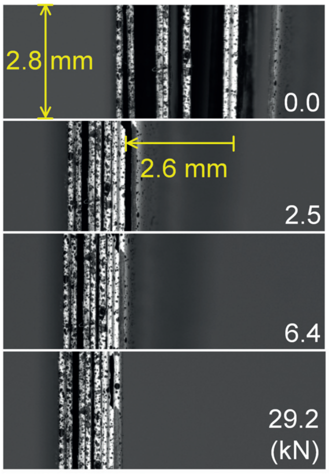

Fig. 6.5: Lateral strap movement in DIC images taken at 0.0, 2.5, 6.4 and 29.2 kN on strap S4

6.3 Experimental Results

6.3.1 Load vs strap elongation responses and failure modes

All straps exhibited similar load vs strap elongation responses (elongations of the 265-mm LVDT gage length), as shown in Fig. 6.6(a). Subsequent to a nonlinear response during tautening, the behavior was linear, followed by a short nonlinear response as the ultimate load F_u was approached. Straps S3 and S4 exhibited a two-peak behavior, however, the second peak being lower than the first one. Although the initial nonlinear behavior varied from case to case, the stiffness in the linear range, K_{exp}, assumed as the slope of the linear segment between 40 and 60 kN, was similar, as shown in Table 6.1. Furthermore, no stiffness losses were observed between the cycles.

Table 6.1: Summary of experimental results

Specimen	F_u (kN)	K_{exp} (kN/mm)	Failure mode
S1	98.3	16.0	Tape rupture
S2	98.8	16.0	Tape rupture
S3	72.4	16.1	Fusion-bond
S4	85.4	16.4	Tape rupture
S5	74.6	16.0	Fusion-bond
S6	87.8	15.8	Tape rupture
S1,S2,S4,S6	92.6 ± 7.0	16.1 ± 0.3	Tape rupture
S3,S5	73.5 ± 1.6	16.1 ± 0.1	Fusion-bond

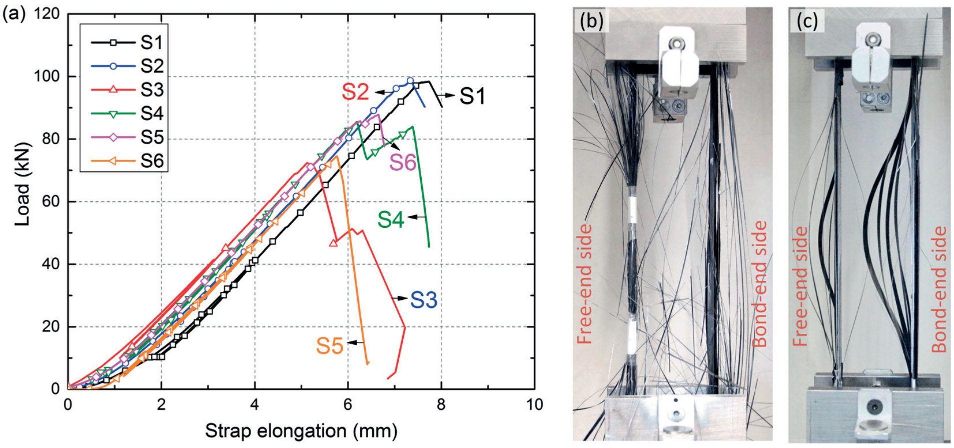

Fig. 6.6: Load vs strap elongation responses (a) and failure modes: (b) tape rupture (S6); (c) fusion-bond (S5)

The obtained ultimate loads, F_u, and observed failure modes are listed in Table 6.1. Straps S1, S2, S4 and S6 exhibited tape rupture failure, see Fig. 6.6(b), while delamination between layers L_7 and L_8 occurred in the fusion bond of straps S3 and S5, as shown in Fig. 6.6(c). The straps exhibiting tape rupture failure had 26.0% higher average ultimate loads than those failing in the fusion bond.

In the tape rupture case, fractured slivers could be seen at the tape edges when the ultimate load was approached; the location of failure initiation, however, could not be identified due to the sudden and brittle failure. At the ultimate load, the straps exhibited extensive splitting in the length direction and fracturing into slivers in the width direction, see Fig. 6.6(b). In strap S4, however, this fracturing occurred at the second peak, i.e. at 83.9 kN, which was 1.8% lower than the first one. The reason for the load drop after the first peak and reincrease to the second one was not visually observable. Straps S4 and S6 exhibited slightly lower ultimate loads than straps S1 and S2. This may have been caused by slight damage resulting from the removal and reinstallation of these straps, as mentioned above.

In the fusion-bond failure case, longitudinal splitting at ultimate load was much less pronounced than in the tape rupture case and transverse fracturing was not observed because of the unwinding of the tape, see Fig. 6.6(c). The fusion-bond failure of strap S3 occurred in two steps, partially at the first peak and completely at the second much lower peak.

6.3.2 DIC displacements and longitudinal strains of individual layers

The measured DIC displacements of the individual layers of straps S4 to S6 were similar and coherent before failure and therefore only the results for strap S5 are presented in the following, see Fig. 6.7. The center points of the DIC measuring areas on the free- and bond-end sides were located at distances of 110 mm and 100 mm from the bottom pin center. The vertical displacement varied significantly along the 14-mm-long measuring areas. Thus, only average displacements of 1.3-mm-long segments, located at the center points of the measuring areas, were used for the following analyses.

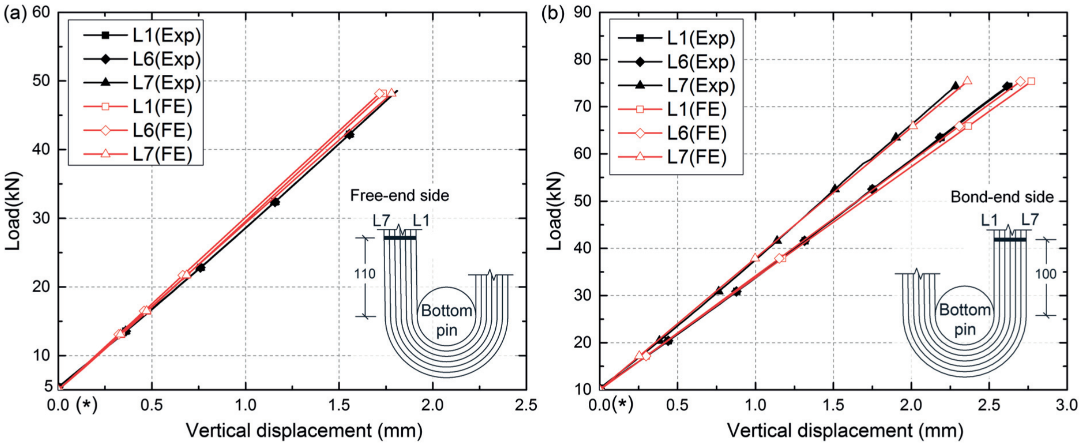

Fig. 6.7: Load vs DIC displacement responses of strap S5 layers on (a) free-end side (loaded to 50 kN) and (b) bond-end side (loaded to failure), experimental and numerical results

The DIC results showed that the displacements of all layers L_1 to L_7 were identical on the free-end side, see Fig. 6.7(a) (only L_1, L_6 and L_7 are shown due to overlapping curves), while on the bond-end side only the displacements of layers L_1 to L_6 were identical and 14.8±0.3% higher than that in layer L_7 at 74 kN, see Fig. 6.7(b). This result is confirmed in Fig. 6.8, which shows the relative displacements between the layers on both strap sides between two load levels. No significant relative displacements were observed between any of the layers, with the exception of layer L_7 on the bond-end side, which exhibited a 0.29-mm relative displacement compared to the other layers.

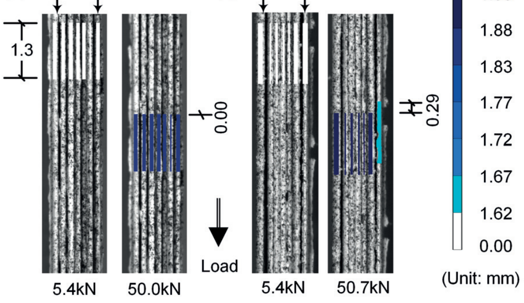

Fig. 6.8: Relative displacements between strap S5 layers on (a) free-end side and (b) bond-end side

The longitudinal strains in the individual layers were also obtained from the 1.3-mm-long segments of the measuring areas. On the free-end side, layer L_1 exhibited 6.3% higher strain than L_7 at 49 kN, see Fig. 6.9(a). On the bond-end side, however, the strains in layers L_1 to L_6 were 27.0±1.0% lower than that in L_7 at 74 kN, as shown in Fig. 6.9(b).

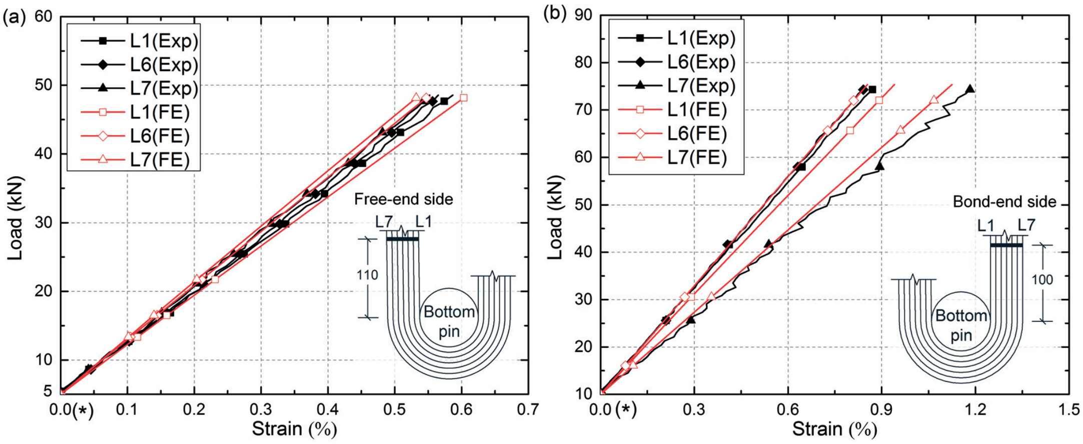

Fig. 6.9: Load vs longitudinal strain responses of strap S5 layers on (a) free-end side (loaded to 50kN) and (b) bond-end side (loaded to failure), experimental and numerical results

6.3.3 Longitudinal strain distribution in fusion-bonding part

The strain field in the fusion-bonding area of layer L_8 was measured up to 40 kN by DIC in strap S6, see Fig. 6.10. To achieve the desired accuracy of the DIC measurement, the measurement area was limited to 90 mm (the upper 90-mm-long part of the 100-mm bonding length). Two small areas of indentation were visible in layer L_8 before the experiment, between lines P4-P6 and P10-P11 shown in Fig. 6.10; the latter area was larger than the former one. These can be resulted from a non-uniform transverse pressure during the fusion bonding.

At each transverse line P1-P11 along the bonding length, the average strains in areas of 20×1.5 mm^2 (green areas in Fig. 6.10) were computed at two load levels (20 and 38 kN); the results are shown in Fig. 6.11. The resulting strains exhibited significant peaks at the two locations were the indentations were observed. The maximum strain at P10 was around three times higher than the average strain and thus may have led to the premature strap failure in the fusion-bonding area. However, the peak strain at P5 was less pronounced due to the smaller indentation area.

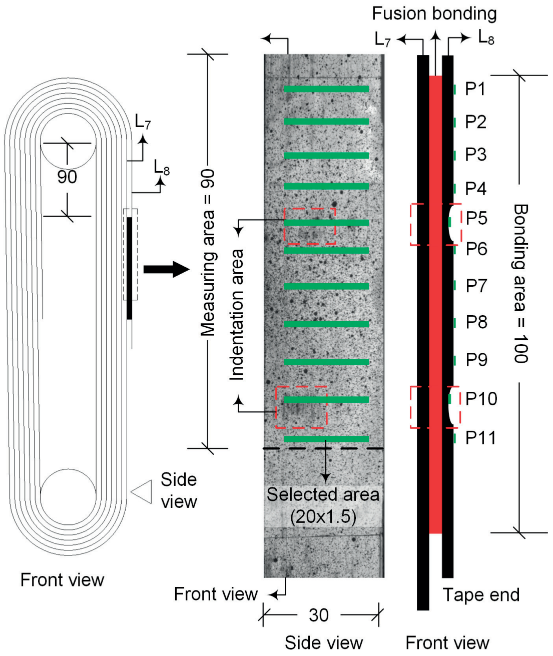
Fusion bonding
L7
L8
90
Measuring area = 90
Indentation area
Selected area (20x1.5)
P1
P2
P3
P4
P5
P6
P7
P8
P9
P10
P11
Bonding area = 100
Side view
Front view
Front view
30
Side view
Tape end
Front view

Fig. 6.10: Experimental set-up and instrumentation layout of fusion-bonding area of strap S6 (dimensions in [mm])

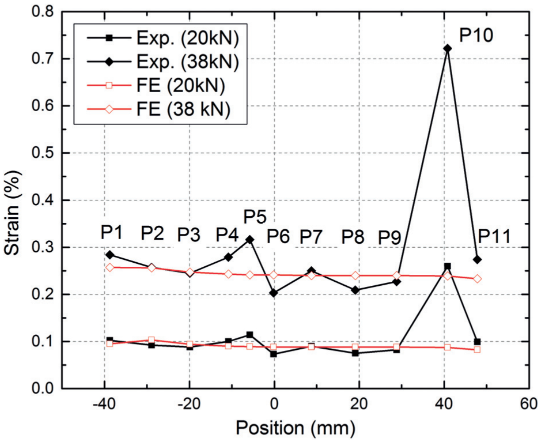

Fig. 6.11: Strain distribution along fusion-bonding length of strap S6 (P1-P11 refer to Fig. 6.10)

6.4 Finite element modeling and validation

6.4.1 FE model description

An FE model was developed to simulate the mechanical behavior of the strap using the commercial Finite Element Analysis (FEA) software, ABAQUS 6.11. Taking advantage of symmetry in the width direction, only half of the model was built with a symmetric boundary condition being applied on the x-y plane; see Fig. 6.12. The steel pins were modeled using solid elements (C3D8R, an 8-node linear brick element with reduced integration) and the tape of the CFRP strap using shell elements (S4R, a 4-node quadrilateral element with reduced integration). An element size of 2.5 mm was selected for the straight segments and 1.8 mm for the pin and the curved strap segments; this selection was based on mesh size sensitivity checks. The aforementioned material properties of the strap were used. The elastic modulus and yield stress of the steel pins were 210 GPa and 355 MPa respectively. In order to avoid convergence difficulties caused by an unstable rigid body motion of the free end, its end points were connected to layer L_1 using two transverse springs with a low stiffness of 100 N/m, see Fig. 6.12.

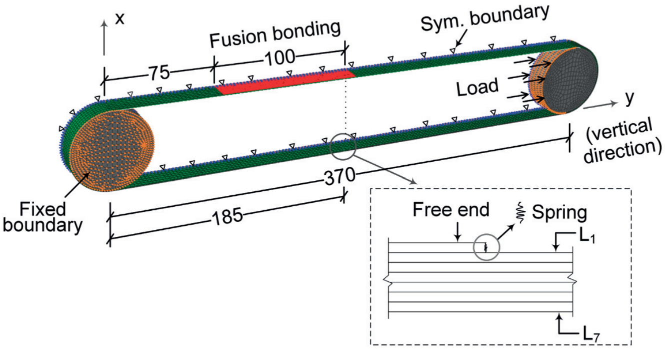

Fig. 6.12: FE model of tensile experiments (dimensions in [mm])

The contact conditions at the CFRP/CFRP and steel/CFRP interfaces were defined in two directions. In the normal (out-of-plane) direction, the "hard contact" model with the augmented Lagrange method was applied. This approach makes the contact solutions easier and avoids problems with overconstraints, while keeping penetrations between contact elements small [19]. In the tangential (in-plane) direction, the isotropic Coulomb friction model with the "penalty method" was applied. In this method, the coefficient of friction, μ, and elastic slip, γ_i, are the two main parameters. The "penalty method" allows the consideration of elastic microslip between the contact surfaces upon the application of loads [19]. To simulate the fusion-bonding behavior, "rough friction" with an infinite value of μ was used; separation and relative sliding motions between the contact layers were thus prevented [19].

The FE model simulated the strap loaded directly from the ideal taut geometry, i.e. the tautening of the slack strap was not modeled. The loading was applied in two steps: 1) a low pressure of 100 Pa was applied on the entire outer surface of the strap to establish the contact constraints at all interfaces while constraining all the displacements; 2) the displacement constraints from the first step were removed, the left-hand pin (in Fig. 6.12) was fixed, and a displacement loading in the y direction was applied on the right-hand pin.

6.4.2 Influence of friction on vertical displacements and longitudinal strains

Parametric FE analyses were conducted by varying the μ and γ_i parameters. The coefficient of friction at the steel/CFRP interface, $\mu_{steel/CFRP}$, was varied between 0.05 and 0.4, and at the CFRP/CFRP interface, $\mu_{\mathrm{CFRP/CFRP}}$, between 0.15 and 0.4. The elastic slip, γ_i, was selected between 0.5% (ABAQUS default value) and 30.0% of the characteristic contact surface length (calculated by scanning all the facets of all the slave surfaces), corresponding to values of between 0.01 and 0.75 mm.

In a first analysis, the same varying coefficient of friction was applied to both interfaces ($\mu_{steel/CFRP}=\mu_{CFRP/CFRP}$), while the elastic slip was maintained constant, γ_i=0.25 mm. The obtained strap stiffness, K_{FE}, again assumed as the slope of the load vs strap elongation responses between 40 and 60 kN, increased only insignificantly from 16.5 to 16.8 kN/mm (by 1.8%) with μ increasing from 0.15 to 0.40. K_{FE} was only 2.5 to 4.3% higher than the average K_{exp} values, see Table 6.1. The corresponding layer displacements and longitudinal strains on both sides of the straight strap segments, from 5.2 to 48.8 kN (two available load steps in the FE models corresponding to the DIC measurements shown in Fig. 6.8), are compared in Figs. 6.13 and 6.14. The results were extracted from the elements at the same locations as the DIC measuring areas. The effect of the varying μ on both the layer displacements and longitudinal strains was very small and thus insignificant.

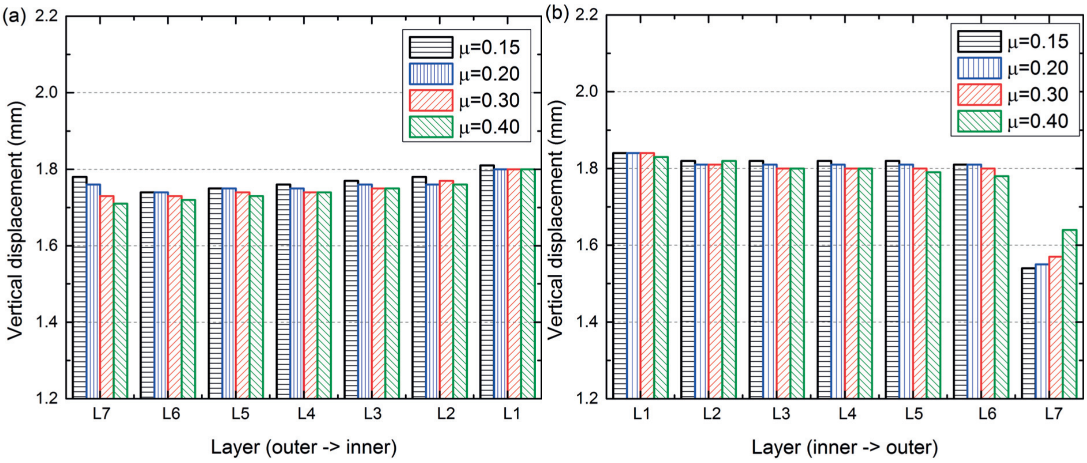

Fig. 6.13: Influence of μ on vertical layer displacements of straight strap segments from 5.2 to 48.8 kN (a) on free-end side, (b) on bond-end side ($\mu=\mu_{steel/CFRP}=\mu_{CFRP/CFRP}$, γ_i=0.25 mm)

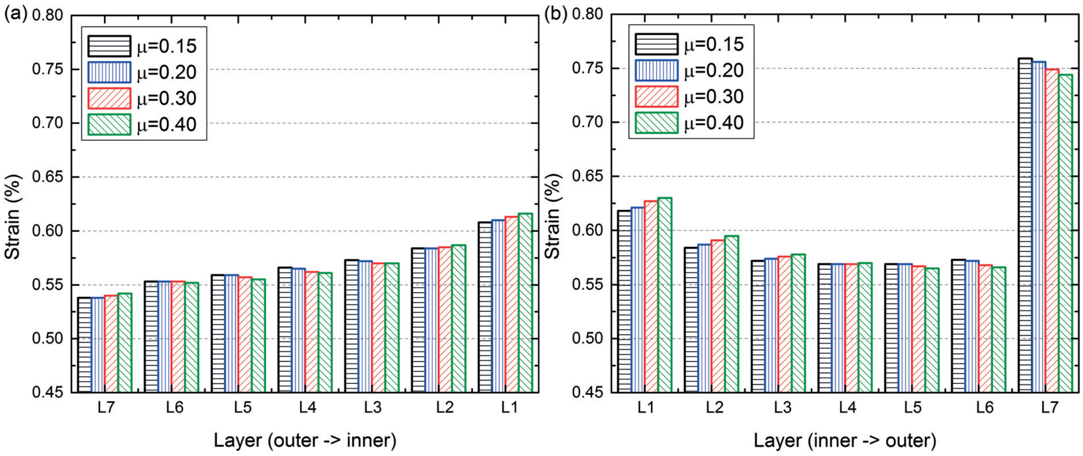

Fig. 6.14: Influence of μ on layer longitudinal strains of straight strap segments from 5.2 to 48.8kN, (a) on free-end side, (b) on bond-end side ($\mu=\mu_{steel/CFRP}=\mu_{CFRP/CFRP}$, $\gamma_i=0.25mm$)

In a second analysis, only $\mu_{steel/CFRP}$ was varied between 0.05 and 0.2 while the remaining parameters were kept constant at $\mu_{CFRP/CFRP}$=0.2 and γ_i=0.25 mm. In a third analysis, γ_i was varied between 0.01 and 0.75 mm with constant $\mu_{steel/CFRP}=\mu_{CFRP/CFRP}$=0.2. The results were similar in both cases - the strap stiffnesses, layer displacements and longitudinal strains of the straight strap segments were not significantly influenced by the varying parameters.

Based on the three parametric analyses and comparison with experimental results, $\mu_{CFRP/CFRP}=\mu_{steel/CFRP}$=0.2 and γ_i=0.25 mm were selected for the model validation and further analyses. This selection of μ was also in agreement with values measured on similar materials in accordance with standard DIN 53375; $\mu_{steel/CFRP}$=0.18 and $\mu_{CFRP/CFRP}$=0.25 were obtained in [8] for a CFRP tape composed of Grafil 34-700 carbon fibers and thermoplastic polyamide PA12 with a fiber volume fraction of 38%. The influence of μ and γ_i on the strain and stress distributions in the curved strap segments will be discussed later.

6.4.3 FE model validation

The numerical results for the layer displacements and longitudinal strains of the straight strap segments are compared with the experimental ones of strap S5 in Figs. 6.7 and 6.9 respectively; a good agreement was obtained. A comparison of these results for all the layers at 48.8 kN, shown in Fig. 6.15, confirms this good agreement; the maximum deviation of the FE results (deviation of points from the 45° line in the figure) was only 6.0%. The smaller displacement of layer L_7 on the bond-end side was also well computed, compare Fig. 6.13(b) (for μ=0.2) with Fig. 6.8(b). Similar good agreements were obtained for straps S4 and S6. Furthermore, the strain distribution calculated by the FE model was in good agreement with the experimental results outside the indentation area, as shown in Fig. 6.11. The validated FE model was used to further analyze the strap behavior.

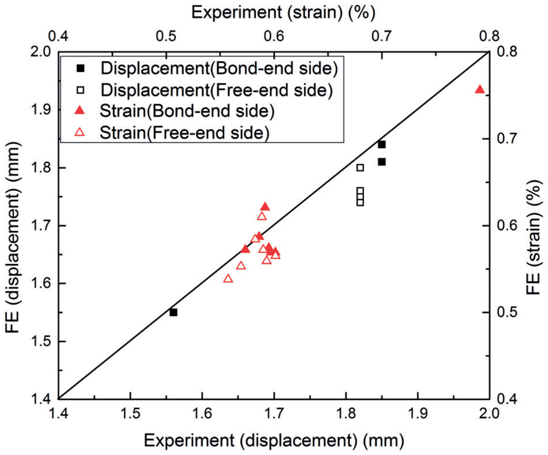

Fig. 6.15: Comparison of layer displacements and longitudinal strains of strap S5 at 48.8 kN, experimental and numerical results

6.5 Discussion

6.5.1 Longitudinal strains and stresses in curved strap segments

The longitudinal strain distribution in layer L_1 around the bottom pin at 20.2, 48.8, 69.8, 80.4 and 99.3 kN is shown in Fig. 6.16; the 99.3-kN load was the load step in the FE model closest to the ultimate loads of straps S1 and S2. The strains of the straight segments were continuously reduced by the frictional shear stresses at the steel/CFRP interface towards the bottom point of the pin. This reduction increased nonlinearly with increasing load; a 28.3% decrease of strain from 0 to 90° was observed at 20.2 kN, while the reduction was 57.9% at 99.3 kN. Small strain peaks arose at the transition from the straight to the curved segments, caused by local bending and the discontinuities of frictional conditions and geometry. Similar peaks were also obtained in the numerical analyses of the winding procedure for a single-layer tape in [16]. The difference between the peak value and its adjacent point increased nonlinearly with the load, while the ratio of this difference to the peak value decreased from 8.5 and 9.2% at 20.2 kN to 3.7 and 3.3% at 99.3 kN on the free- and bond-end sides respectively.

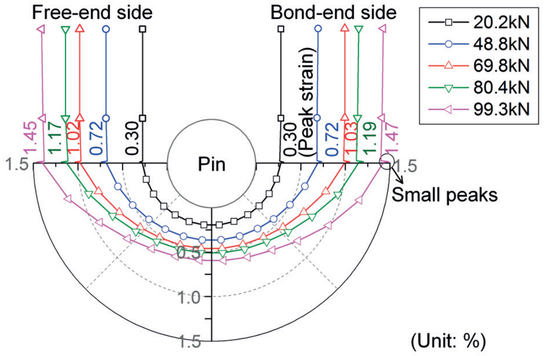

Fig. 6.16: Longitudinal strain distribution in layer L_1 around bottom pin at different loads ($\mu_{CFRP/CFRP}$=$\mu_{steel/CFRP}$=0.2 and γ_i=0.25)

The influence of the μ or γ_i parameters on the strain distribution in the curved strap segment is shown in Fig. 6.17. By increasing μ from 0.2 to 0.4 (at γ_i=0.25 mm), the strain at the bottom point at 99.3 kN decreased by 28.3% (from 0.60 to 0.43%), while it increased by 43.3% (from 0.60 to 0.86%) when γ_i was varied from 0.25 to 0.75 mm (at μ=0.2). However, these parameters had insignificant influence on the strain distribution in the straight strap segments as discussed before.

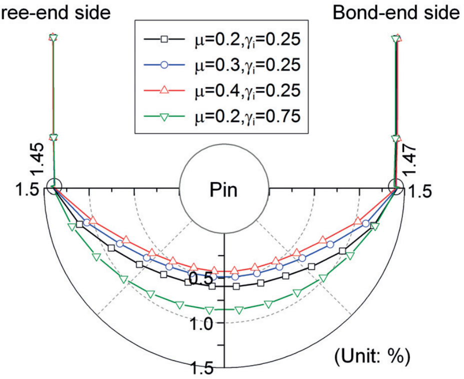

Fig. 6.17: Longitudinal strain distribution in layer L_1 around bottom pin at 99.3 kN obtained from FE models using different μ and γ_i values

The longitudinal stresses in all layers around the top and bottom pins, at five different positions (0, 45, 90, 135 and 180°) below 99.3 kN, obtained from different FE models, are shown in Fig. 6.18. On the bond-end side, the two outermost layers around the top pin exhibited lower stresses (0.98 to 1.11GPa in layer L_7 and 1.20 to1.29 GPa in L_8 at 0°, depending on the friction conditions) than the inner layers, while the maximum stress, 2.32 to

2.51 GPa, developed at 0° in layer L_7 at the bottom pin. Obviously, the stresses of the two layers L_7 and L_8 above the fusion-bonding area (where L_8 stopped) were transferred to the remaining layer L_7 below the fusion-bonding area. However, the higher stress in layer L_7 on the bond-end side was not transferred to the free-end side but absorbed by friction around the bottom pin. The stress in the innermost layer L_0 around the top pin decreased from the maximum value at 0° to almost zero at 180° due to friction.

The tensile stresses of all layers generally decreased with increasing friction (higher μ or lower γ_i values) in the curved segments, as shown in Fig. 6.18. This decrease was more significant in the inner layers, leading to a more linear stress distribution through the layers with higher friction. Layer L_1 at 90° around the bottom pin, for instance, exhibited the maximum stress decrease of 50.4% (from 1.13 to 0.56 GPa), when the friction condition was varied from μ=0.2 and γ_i=0.75 mm to μ=0.4 and γ_i=0.25 mm. In the former, the outer layers exhibited similar stress levels, while the stress in the innermost layer sharply decreased due to the high frictional shear stresses. In the latter, however, a much more continuous stress reduction from the outer to inner layers could be observed. The peak stresses at 0/180° only varied insignificantly with different friction conditions. The maximum variance was located at 0° around the bottom pin, with a 7.6% decrease from 2.51 to 2.32 GPa.

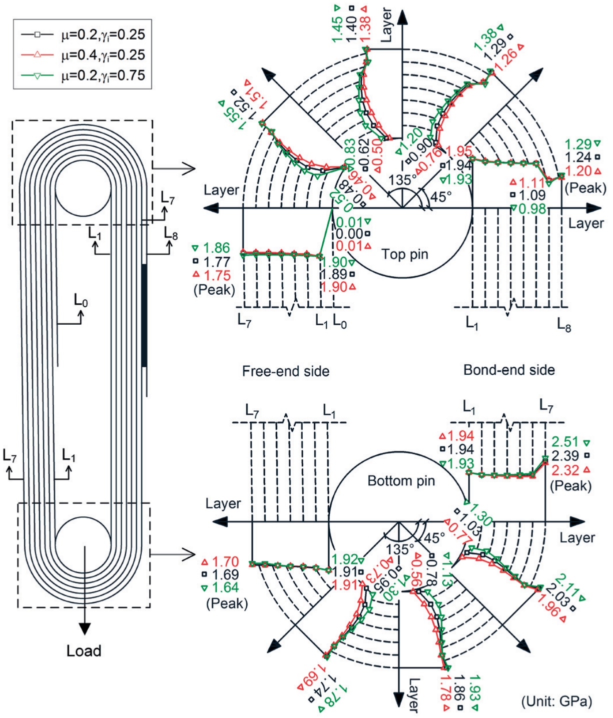

Fig. 6.18: Longitudinal stress distribution in two curved segments at 99.3 kN obtained from FE models using different μ and γ_i values

6.5.2 Vertical displacements and longitudinal strains in straight strap segments

The lower stresses in the two outermost layers (L_7 and L_8) on the top of the bond-end side, as mentioned above, resulted in smaller longitudinal deformations and therefore led to the lower vertical displacement of layer L_7 of the DIC measuring area (see Fig. 6.7(b)). Furthermore, since below the fusion-bonding area the cross section was halved (from $L_7 + L_8$ to L_7), the strain in layer L_7 below the fusion-bonding area was much larger than in the inner layers (see Fig. 6.9(b)).

The elongation of the curved segments decreased from layers L_7 to L_1 due to the reduction of the tensile stresses (see Fig. 6.18) and geometric length. Thus, the elongation of the straight segment under the same pin-to-pin displacement loading increased from layers L_7 to L_1, leading to the increasing strain as shown in Fig. 6.9(a).

6.5.3 Failure mechanism

The maximum calculated stress in the strap at 99.3 kN, 2.32–2.51 GPa (depending on the friction conditions, see Fig. 6.18), was close to the mean tensile strength (2.46 GPa). This could have triggered the ultimate failure in layer L_7 of straps S1 and S2. As mentioned above, the location of the very sudden and brittle failure could not be detected by visual observation. Furthermore, since significant stress concentrations were observed in the fusion-bonding area in strap S6 as shown in Fig. 6.11, bond failure of S3 and S5 can be resulted from larger peak stresses or poor bonding.

Close to the ultimate load, fractured slivers could be observed at the tape edges of all straps. Similar slivers were captured much earlier by the DIC camera in the measuring area of strap S4. The first audible crack was heard at approximately 60.0 kN, but the location could not be visually tracked. However, a sudden increase of the strain in the measuring area of layer L_2 was observed at 59.1 kN, as shown in Fig. 6.19. The longitudinal strain increased rapidly from 0.70 to 1.23% (corresponding to 1.63GPa of stress) during loading from 59.1 to 66.0 kN, at which point the DIC measurements stopped due to a sudden increase in the displacement of layer L_2. This displacement could be traced back on the DIC camera photos to a longitudinal splitting of layer L_2, as shown in Fig. 6.20. Corresponding DIC analyses of the transversal strain, started at 56.7 kN, showed obvious strain concentrations in the middle along the length at 60.2 kN, see Fig. 6.21, which thus caused this splitting. The longitudinal splitting of layer L_2 was followed by the formation of a fractured sliver in this layer at 69.4 kN, as shown in Fig. 6.20. Although layer L_7 on the bond-end side theoretically exhibited the maximum strain, local tape fracturing, caused by minor damage on the tape edges during manufacturing or handling or initial flaws in the tape, could have led to local stress concentrations in other layers. Premature failure could thus occur, which could reduce the ultimate load, as observed in straps S4 and S6 compared to S1 and S2. The local fracturing observed by the DIC camera at 69.4 kN, however, had no effect on the strap stiffness, see Fig. 6.6(a). Stiffness degradation started only at approximately 80kN, close to the first peak load, with an increasing number of fractured slivers. A similar strap behavior was observed in [9] where the fracture of slivers also occurred at high loads while the strap could continue to sustain the load.

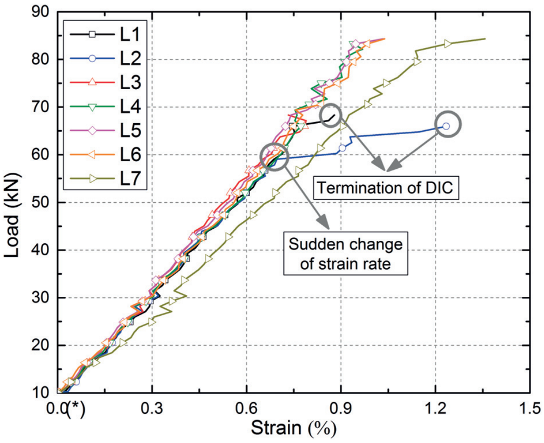

Fig. 6.19: Load vs longitudinal strain responses of strap S4 on bond-end side

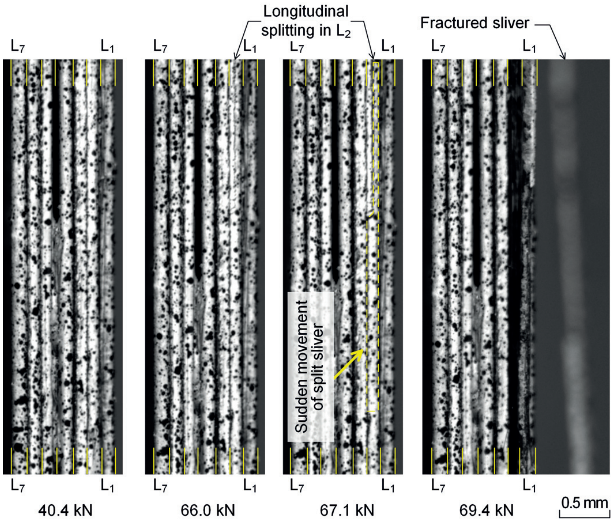
Longitudinal splitting in L₂
Fractured sliver
L₇
L₁
Sudden movement of split sliver
40.4 kN
66.0 kN
67.1 kN
69.4 kN
0.5 mm

Fig. 6.20: Status of DIC measuring areas at different load levels in strap S4

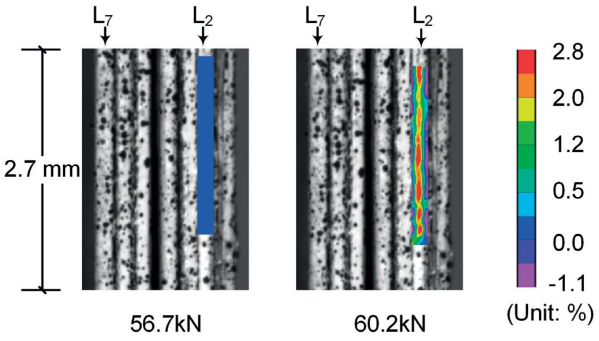

Fig. 6.21: Transversal strain concentrations in middle along tape length at 60.2 kN

6.6 Conclusions

Tensile experiments were performed on seven-layer non-laminated CFRP straps. A corresponding FE model was developed in order to simulate the exhibited behaviors. The model parameters were calibrated and the model validated by the comparison between the numerical and experimental results. Based on the experimental and numerical results, the load-bearing and failure mechanisms of the strap were analyzed. The following conclusions were drawn:

1. A good agreement between the FE model and experimental results was achieved. A parametric study concerning the coefficients of friction and elastic slip showed small effects of the frictional conditions on strap stiffness, vertical displacements and longitudinal strains in the straight strap segments. However, significant effects on the strain and stress distributions in the curved segments around the pins were observed.
2. The anchoring of the outermost tape layer (L_8) by fusion bonding to the adjacent inner layer (L_7) influences the load distribution among the layers significantly. The load borne by two layers (L_7+L_8) on one side of the fusion-bonding area is transferred to only one remaining layer (L_7) on the other side, which increases stresses and strains in this layer (L_7) considerably.
3. Stress concentrations occur at the transition points from the curved to the straight tape segments, which however are small and negligible compared to the above-mentioned effect of the fusion bonding on the stress level in layer L_7.
4. The ultimate load of the strap is thus limited by the strength of layer L_7 on the bond-end side. However, the ultimate load is very sensitive to minor initial damage at the tape edges or flaws as well as to stress concentrations in the fusion-bonding area. The

latter may lead to a premature failure in the anchoring zone. All these effects can reduce the ultimate load significantly.

5. The innermost layer L_0 remained fully anchored only by friction up to strap failure.

References

[1] Keller T. Strengthening of concrete bridges with carbon cables and strips. In: 6th International Symposium on FRP Reinforcement for Concrete Structures (FRPRCS-6), Singapore, July 1331-40; 2003.

[2] Benmokrane B, Xu H, Nishizaki I. Aramid and carbon fibre-reinforced plastic prestressed ground anchors and their field applications. Can J Civ Eng 1997;24(6):968-85.

[3] Schmidt JW, Bennitz A, Täljsten B, Goltermann P, Pedersen H. Mechanical anchorage of FRP tendons–A literature review. Constr Build Mater 2012;32:110-21.

[4] Zhang B, Benmokrane B, Chennouf A. Prediction of tensile capacity of bond anchorages for FRP tendons. J Compos Constr 2000;4(2):39-47.

[5] Reda Taha MM, Shrive NG. New Concrete Anchors for Carbon Fiber-Reinforced Polymer Post-Tensioning Tendons–Part 1: State-of-the-Art Review/Design. ACI Struct J 2003;100(1):86-95.

[6] Bauersfeld DW. Composite graphite/epoxy tensile element. Report 2404. United States Army, Belvoir Research & Development Center, Fort Belvoir, Virginia; 1984.p.1-62.

[7] Winistöerfer A, Meier U. CARBOSTRAP-An advanced composite tendon system. In: 6th International Symposium on FRP Reinforcement for Concrete Structures (FRPRCS-5), Cambridge, UK, July 231-8; 2001.

[8] Winistöerfer AU. Development of non-laminated advanced composite straps for civil engineering applications. Coventry, UK: Department of Engineering, University of Warwick; 1999.

[9] Lees J, Winistörfer A. Nonlaminated FRP Strap Elements for Reinforced Concrete, Timber, and Masonry Applications. J Compos Constr 2010;15(2):146-55.

[10] Czaderski C, Motavalli M, Winistörfer A, Motavalli M. Prestressed shear strengthening of a box girder bridge with non-laminated CFRP straps. In: Proceedings of the 4th International Conference on FRP Composites in Civil Engineering (CICE2008), Zurich, Switzerland, July 7.B.6; 2008.

[11] Schlaich M, Bleicher A. Spannbandbrecke mit Kohlenstofffaser-Lamellen. Bautechnik. 2007;84(5):311-9.

[12] Huster U, Broennimann R, Winistörfer A. Strengthening of a historical roof structure with CFRP-straps. In: Proceedings of the 4th International Conference on FRP Composites in Civil Engineering (CICE2008), Zurich, Switzerland, July 8.B.4; 2008.

[13] Triantafillou TC, Fardis MN. Strengthening of historic masonry structures with composite materials. Mater Struct 1997;30(8):486-96.

[14] Meier U, Brönnimann R, Widmann R, WINISTÖRFER A, Irniger P. Bowstring-arch bridge made of CFRP, GFRP and glulam. In: Proceedings of the 2nd Official International Conference of International Institute for FRP in Construction for Asia-Pacific Region, Seoul, South Korea, December 557–562; 2009.

[15] Keller T, Kenel A, Koppitz R. Carbon Fiber-Reinforced Polymer Punching Reinforcement and Strengthening of Concrete Flat Slabs. ACI Struct J 2013;110(06).

[16] Winistörfer A, Mottram J. Finite element analysis of non-laminated composite pin-loaded straps for civil engineering. J Compos Mater 2001;35(7):577-602.

[17] Sutton MA, Orteu JJ, Schreier H. Image correlation for shape, motion and deformation measurements: basic concepts, theory and applications: Springer Science & Business Media; 2009.

[18] Correlated Solutions Inc. Vic 2D reference manual. Providence, Correlated Solutions, Columbia, USA; 2009.

[19] Abaqus Inc. Abaqus analysis user's manual, version 6.11. Providence, RI, USA; 2011.

7.

Numerical and analytical investigation of tensile behavior of non-laminated and laminated CFRP straps

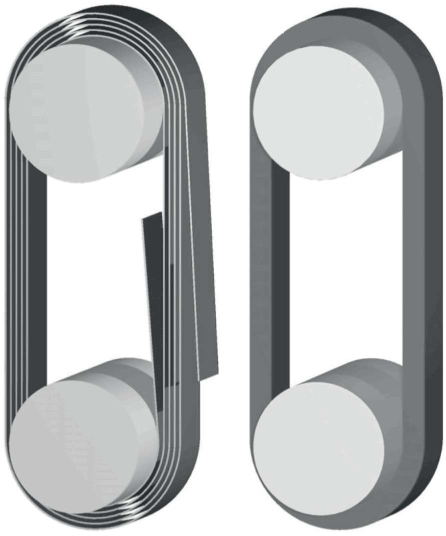

Reference detail:

Fan H, Vassilopoulos AP, Keller T. Numerical and analytical investigation of tensile behavior of non-laminated and laminated CFRP straps. Submitted to Compos B Eng, 2017.

7.1 Introduction

Strap anchorage methods have been developed to overcome the difficulties of anchoring fiber-reinforced polymer (FRP) tension members, in particular in the case of carbon fiber-reinforced polymers (CFRPs) since carbon fibers are strongly anisotropic, i.e. exhibit much lower mechanical properties in the transverse fiber direction than in the fiber direction [1]. Non-laminated [1, 2] and laminated [3] straps are differentiated. In the former, relative displacements between the layers can occur while in the latter the layers are laminated together preventing relative displacements. Non-laminated CFRP straps have already been successfully used in strengthening applications for different structures such as concrete flat slabs [4], box girders [5], timber roofs [6] and masonry walls [7]. Laminated CFRP straps have been used for ground anchors [8, 9] and rigging systems in sailing yachts [10].

The tensile behavior of the straps was investigated in both non-laminated [1, 2, 11] and laminated [1, 12] cases. For the non-laminated case, tensile experiments on the CFRP straps with 10–70 layers were presented in [2]. A decrease of the load-bearing efficiency of the straps, R_u, – i.e. the ratio of the obtained ultimate load to the predicted one based on the material strength – was observed with the increasing outer to inner radius ratio, r_0/r_i, achieved by increasing the layer number or decreasing r_i. However, no detailed analysis of the reasons for this decrease was conducted. Furthermore, tensile experiments on seven-layer CFRP straps were presented in [11], where a corresponding finite element (FE) model was also developed. Based on the experimental and numerical results, the strain distributions among the layers at different locations of the straps and the failure mechanisms were investigated. However, the analysis was limited to a small number of layers. For straps with a large layer number, e.g. 70, no detailed analytical or numerical models exist that would explain their load-bearing behavior.

For laminated straps, analytical models for high r_0/r_i values (1.8–3.0) were first developed by Conen [13] based on the thick wall cylinder theory; the models were validated by tensile experiments on glass fiber-reinforced polymer (GFRP) straps. In [1], tensile experiments on 45 CFRP straps composed of 5-15 layers were presented, based on which several analytical models including the Conen model were used for predicting R_u in relationship to different r_0/r_i values; however, the predicted results overestimated the experimental ones. Other numerical and analytical investigations were also conducted to analyze the stress distribution in the semicircular parts of the laminated straps [12, 14];

however, no analytical model for predicting the load-bearing efficiency (R_u) has been established.

In this chapter, the tensile behavior of both non-laminated and laminated straps with layer numbers of up to 100, corresponding to $0<r_0/r_i<1.5$, which covered the r_0/r_i range of all the CFRP straps reported in the literature [1, 2, 4-6, 8, 9, 15-17], was systematically investigated. For both cases, FE models with integrated failure criteria were developed, while for the laminated straps, an analytical model, taking into account the orthotropic material properties and friction at the pin/CFRP interface, was also derived. All the models were first validated by existing experimental data and then applied to investigate the strain distributions among the layers and the relationship between the load-bearing efficiency and strap radius ratio.

7.2 FE modeling of non-laminated straps

In [11], tensile experiments and corresponding 3D FE models developed using the commercial Finite Element Analysis (FEA) software ABAQUS 6.11 were presented for seven-layer non-laminated strap specimens. In the following, 2D FE models were developed based on this previous work by extending the layer number, n, up to 70, i.e. eight FE models in total were built with n=1, 7, 20, 30, 40, 50, 60 and 70 (designated N1–N70), while maintaining the same dimensions and material properties of the tape layer. The validation of the developed 2D modeling method was conducted on strap N7 by comparing the new results with the experimental and numerical results obtained in [2, 11]. Detailed analyses including failure mechanism, strain distribution among the layers and load-bearing efficiency were carried out based on the validated model.

7.2.1 Description of 2D FE model

(1) Model geometry

To avoid convergence difficulties caused by the large contact surface and element number if using 3D models for the straps with a large layer number, the model was simplified into a 2D one, as shown in Fig. 7.1. The experimentally observed longitudinal splitting in the width direction could thus not be taken into account; however, considering that the final failure of the straps was caused by a tensile rupture of individual tape layers [11], this simplification seemed acceptable. The input material properties and model dimensions remained the same as in the 3D model [11], except the layer number, i.e. the pin-to-pin distance was 370 mm, the width, *w*, and thickness, *t*, of the tape layer were 30 and 0.135 mm respectively and the inner diameter of the strap, identical to the pin diameter, was 55 mm (see Fig. 7.1). Furthermore, the anchoring of the innermost layer by friction and the outermost layer by fusion bonding was also simulated using identical methods, i.e. the "rough contact" method, as in the 3D model [11]; the fusion bonding resulted in double and single layers above and below the bond end [11].

In the 3D model, the loop-forming tape was simulated continuously, using 3D shell elements in the mid-plane of each layer. However, in the 2D model, the non-laminated (separated) individual layers could not be simulated if the strap was modeled as in the 3D case, because the edges between two adjacent layers overlapped each other. Therefore, the strap with n layers was cut at positions C_1–C_n located at the middle of the straight segments on the bond-end side (see Fig. 7.1), resulting in n+1 loops (L_0–L_n) with two connecting points C_n/C_n' at each cut location; the location was vertically shifted by 0.1 mm between two adjacent layers to create an open loop (e.g. L_1 in Fig. 7.1), thus avoiding the overlapping edges. This connection area was therefore 7-mm long in strap N70, as shown in Fig. 7.1. The connection at C_n/C_n' points, e.g. C_1/C_1' for L_0/L_1 loops (see Fig. 7.1), was simulated using the "tie constraint" method, i.e. the two connected loop ends were constrained to have the same displacements in all directions during the analysis.

Both the steel pin and CFRP strap were simulated using plane strain elements (CPE4R, four-node quadrilateral element with reduced integration and hourglass control). A normal mesh size of 2.0 mm in the length (fiber) direction and one-element mesh size in the thickness direction were selected for the whole strap, while a refined mesh was used in the 2-mm-long tape segments located at the four flanks (see Fig. 7.1), i.e. the transition points between the straight to semicircular segments, in order to accurately simulate the local bending behavior at this location. Based on sensitivity checks, a biased mesh with varying size of 0.08–0.13 mm was used in the length (fiber) direction, while in the thickness direction three elements were created. Furthermore, in the adjacent segments connected with these four refined regions, located in both semicircular and straight parts, a biased mesh with varying sizes of 0.1–1.8 mm was created in the length direction to create a continuous variation of mesh size between the refined and normal mesh regions, but only one element was meshed in the thickness direction. The total element number was 8,459 to 73,619 in N7–N70 straps.

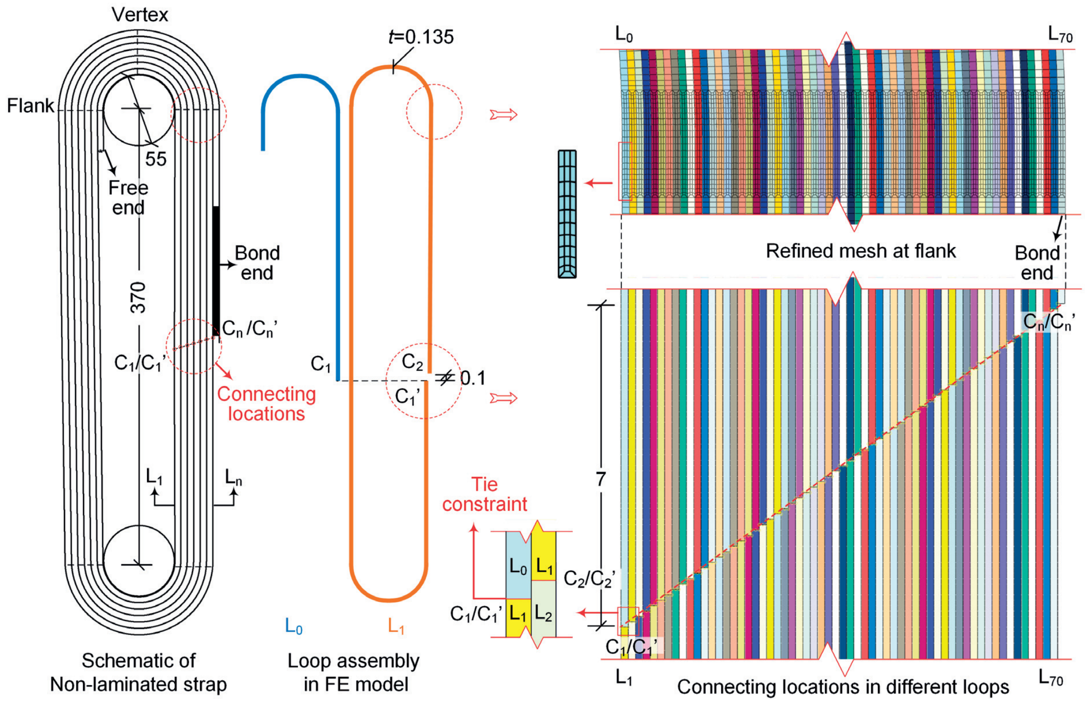
Vertex
Flank
55
Free end
370
Bond end
C_n/C_n'
C_1/C_1'
Connecting locations
L_1
L_n
Schematic of Non-laminated strap
t=0.135
C_1
C_2
C_1'
0.1
L_0
L_1
Loop assembly in FE model
Tie constraint
L_0
L_1
L_1
L_2
C_2/C_2'
C_1/C_1'
L_0
L_{70}
Refined mesh at flank
Bond end
C_n/C_n'
7
C_1/C_1'
L_1
Connecting locations in different loops
L_{70}

Fig. 7.1: FE model of non-laminated straps (dimensions in [mm])

(2) Simulation of interface behavior

In the 3D model of strap N7 [11], the CFRP/CFRP and steel/CFRP interfaces were simulated using the contact method with "hard contact" and "penalty" models in the normal (out-of-plane) and tangential (in-plane) directions respectively. Based on previous parametric analyses [11], the coefficient of friction, μ, and elastic slip, γ_i, were selected as μ=0.2 and γ_i=0.25 mm respectively for both CFRP/CFRP and steel/CFRP interfaces.

Using the same contact constraint for all the interfaces in the straps with a larger layer number as in the 3D model, a significant increase of the number of the contact pairs, located in both the semicircular and straight segments, occurred (e.g. 280 pairs in strap N70) and caused convergence difficulties, despite the reduced number of elements in the 2D models. These difficulties mainly resulted from the significant contact status changes, i.e. closed/open and stick/slip, throughout the analyses due to the relative slippage between layers, particularly in the straight segments where almost no contact pressure existed. Since according to the 3D model, the frictional stress in the straight segments was negligible due to the small contact pressure and most of the contact constraint disappeared at high load levels, the contact constraint in the straight segments was removed to minimize the contact status changes. To avoid convergence difficulties caused by instability without constraint and also the penetrations between the layers in the straight segments, movement constraint was added in each layer in the normal (thickness) direction. The constraint started at 1-mm distance from the flank (see Fig. 7.1) to avoid any influence on the local bending at this location, which was also confirmed by parametric studies on the constrained length. In the semicircular parts, identical contact methods, i.e. “hard contact” and “penalty” models with identical μ and γ_i values as mentioned above, were used as in the 3D model; in strap N70, 142 contact pairs were thus created.

(3) Simulation of strap failure

In the 3D model of strap N7 [11], the ultimate load of the strap specimens exhibiting tape rupture failure was well predicted by comparing the maximum tensile stress at the flank in the outermost layer in the FE model to the mean tensile strength, σ_t=2.46 GPa, of the tape layer. This failure criterion was thus also used for the 2D models, i.e. when the element in individual layers reached the tensile strength, the loop was considered as failed and, by decreasing the elastic modulus in the longitudinal (fiber) direction, E_1, to 1% of the value before failure, it ceased to bear load. The reduction of the material property of the failed layer was achieved by using the software’s temperature-dependent material model, i.e. E_1 was 132 GPa at 20°C, while it decreased to 1%, i.e. 1.32 GPa, at 200°C. The remaining elastic moduli in the direction perpendicular to the fiber direction and Poisson’s ratio were kept as temperature-independent.

In the experiments on strap N7, the first tape rupture occurred in the outermost layer (L_7), resulting in brittle failure of the strap due to the unwinding of the strap starting from the failed layer [11]. However, when the layer number increased to a certain level, e.g. 30 layers in the experiments of [2], the first rupture location switched to the innermost layer (L_1) and failure occurred progressively from the inner to the outer layers. In order to model this progressive failure behavior in the straps with more than 30 layers and at the same time avoid convergence difficulties caused by the sudden change of model geometry due to the tape rupture, the following procedure was applied in the 2D model:

1) In step 1, the strap was loaded in displacement-control mode up to the load level at which the maximum tensile stress at the flank of layer L_i (i=1 in the first run up to the first peak) reached the tensile strength;

2) In step 2, the displacement loading was maintained at the same level, while the temperature in the ruptured layer, i.e. L_i, was increased to 200°C, at which point the load borne by this layer was released due to the reduction of E_1 and a load redistribution occurred in the remaining non-ruptured layers;
3) In step 3, the displacement loading continued until the next layer, i.e. L_{i+1}, reached the tensile strength and step 2 was subsequently repeated for this layer;
4) Steps 1–3 were repeated for the following inner layers until one of these two cases occurred: (1) the new layer rupture was located in the outermost layer; (2) the rupture was located in the inner layers, but the load level at which the new layer rupture occurred, F_{Li+1}, was lower than the previous one, F_{Li}, i.e. $F_{Li+1} < F_{Li}$.

7.2.2 Validation of 2D FE model

A comparison of the load vs longitudinal strain responses of three layers on the bond-end side in the N7 strap between the experimental, previous 3D and new 2D FE results is shown in Fig. 7.2. The strain behavior was well simulated by the 2D model, exhibiting slightly better agreement with the experimental one on the inner layers (L_1 and L_6) compared to the 3D one; however, the difference between the 3D and 2D models was minor, e.g. 3% at 70 kN. This good agreement was also confirmed in the layers on the free-end side.

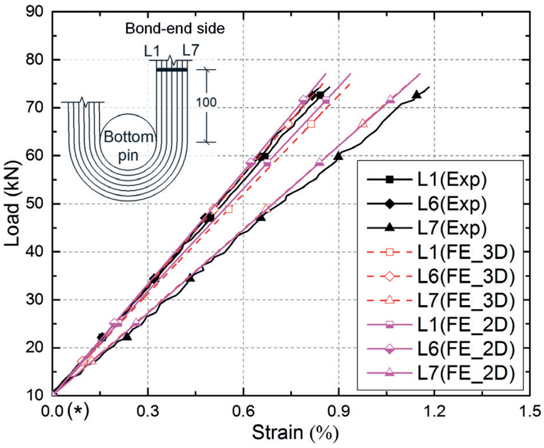

Fig. 7.2: Load vs longitudinal strain responses of three layers on bond-end side in strap N7: experimental, previous 3D and new 2D FE results

To confirm that the replacement of the contact method by the horizontal constraint method in the straight segment did not influence the results, comparisons were conducted between two types of FE models using 1) the contact method for the whole strap and 2) the contact method only in the semicircular parts, while using the horizontal constraint method in the straight segments; the comparisons were made in the N7 and N20 straps where the convergence could still be achieved using the first method. Both straps exhibited similar results with a difference of less than 2%, as shown for N20 in Fig. 7.3 for the comparison of the load vs longitudinal strain responses at the flank of the L_1 and L_{20} layers on the bond-end side. Therefore, the 2D model was considered validated and was used for the following analyses.

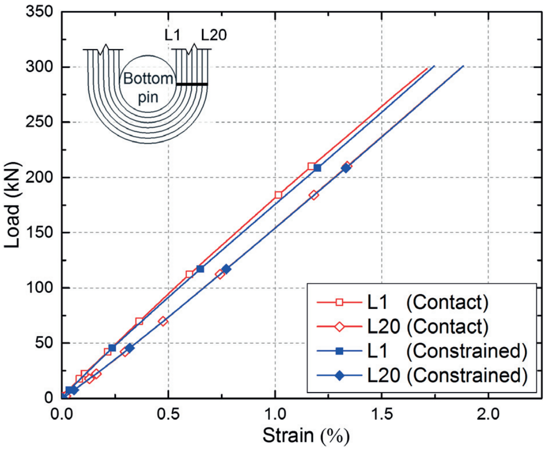

Fig. 7.3: Load vs longitudinal strain responses at flank of L_1 and L_{20} layers on bond-end side in strap N20 using contact and horizontal constraint methods in straight segments

7.2.3 Discussion of modeling results

(1) Load vs strap elongation responses and failure mechanism

The load vs strap elongation responses between the two pin axes in the N1–N70 straps is shown in Fig. 7.4; the load was calculated as the load value extracted from the 2D model (per unit width) multiplied by the strap width (30 mm). The ultimate load, F_{ult}, and stiffness of the strap increased with the increasing layer number. All the curves exhibited linear slopes up to a first load peak, F_{1P}, at which the behavior changed depending on the layer number as follows:

(1) In the N1–N20 straps, strap failure occurred at this load peak due to the rupture of the outermost layer.

(2) In the N30–70 straps, several small load drops followed by load increases were observed after this first peak, caused by a progressive failure starting from the inner towards the outer layers. The load drop/increase sequences resulted from the modeling steps described

above and were observed as continuous curves in experiments [18], see dashed line in the zoom in Fig. 7.4.

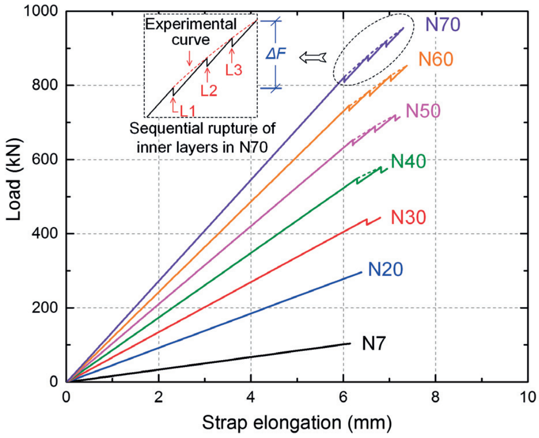

Fig. 7.4: Load vs strap elongation responses between two pins in N7–N70 straps

In the N30–N70 straps, the first peak (F_{1P}) and ultimate (F_{ult}) loads vs layer number are shown in Fig. 7.5; the relationship exhibited a polynomial increasing trend. Furthermore, the difference between first peak and ultimate load, ΔF, increased with increasing layer number and the ratio $\Delta F/F_{1P}$ thus also exhibited a polynomial increase, indicating an increase of the non-linear curve segment up to 16% for N70. Using these two empirical equations, F_{ult} of the straps with more than 70 layers can be calculated as $F_{ult}=\Delta F+F_{1P}$. The layer number was limited to 70 in the FE models due to increasing convergence difficulties. The established empirical model, however, allows the ultimate load of straps to be estimated with n=70–100.

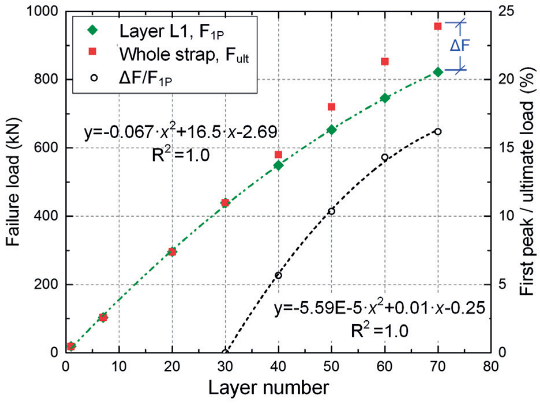

Fig. 7.5: First peak (F_{1P}) and ultimate (F_{ult}) loads and ratio ($\Delta F/F_{1P}$) vs layer number

(2) Load vs tensile stress of layers

In accordance with the load drops in the progressive failure case, the tensile stress dropped in the ruptured layer but increased in the remaining layers due to load redistribution, as shown in Fig. 7.6 for strap N70. The stress in the innermost layer L_1 dropped to almost zero after the element located at the flank reached the tensile strength of 2.46 GPa at the first peak load and a corresponding stress increase was observed in the adjacent layers. The element located at the flank of layer L_5 reached 2.46 GPa at a load level lower than the previous load peak, thus indicating the ultimate load. Furthermore, the different curve slopes indicated a non-uniform load distribution among the layers.

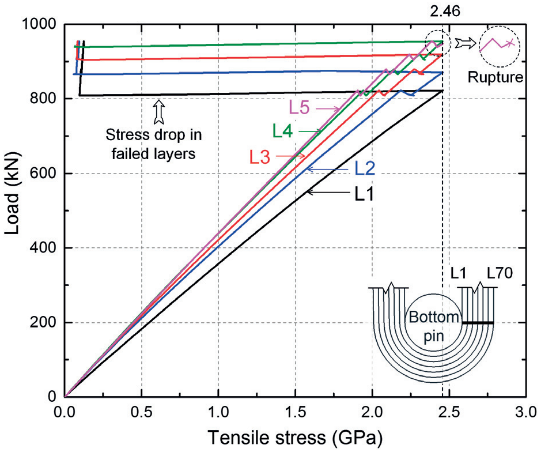

Fig. 7.6: Load vs tensile stress responses at flank in L_1–L_5 layers on bond-end side in strap N70

(3) Tensile strain distribution among layers

The tensile strain distributions among the layers of the N7–N70 straps at the first peak load on both the free- and bond-end sides are shown in Fig. 7.7 (a) and (b) respectively. To exclude bending effects, the values were extracted from elements located at a distance of approximately 30 mm from the flank. The strains, ε, in the individual layers were further normalized by the median strain, $\varepsilon_m=F_{1P}/(2\cdot n\cdot t\cdot w\cdot E_1)$.

The layers on both sides exhibited similar non-linear distributions except the outermost layer, where a significantly higher strain was observed on the bond-end side due to the single cross section below the bonded end compared to the double cross section above (see Fig. 7.1), as also discussed in [11]. On the free-end side, the strains decreased from a peak occurring on the inner L_1 layer to the outer layers. On the bond-end side, however, the peak location switched from the outermost layers L_7–L_{50} of straps N7–N50 (red open symbols in Fig. 7.7) to the inner layer L_1 (black solid symbols) in straps N60/70, corresponding to the two failure modes mentioned above. However, the switching point of the failure mode was shifted from N50 to the above-mentioned N30 due to the additional local bending at the flank. The non-uniformity of the strain distributions also increased with layer number, i.e. strap N70 had the maximum non-uniformity, i.e. the overloaded layers ($\varepsilon/\varepsilon_m$>1) increased from 14% in N7 to 36% in N70. In all cases, the full material strength of the straps could not be exploited over the whole cross section, i.e. the load-bearing efficiency was reduced (R_u < 1.0).

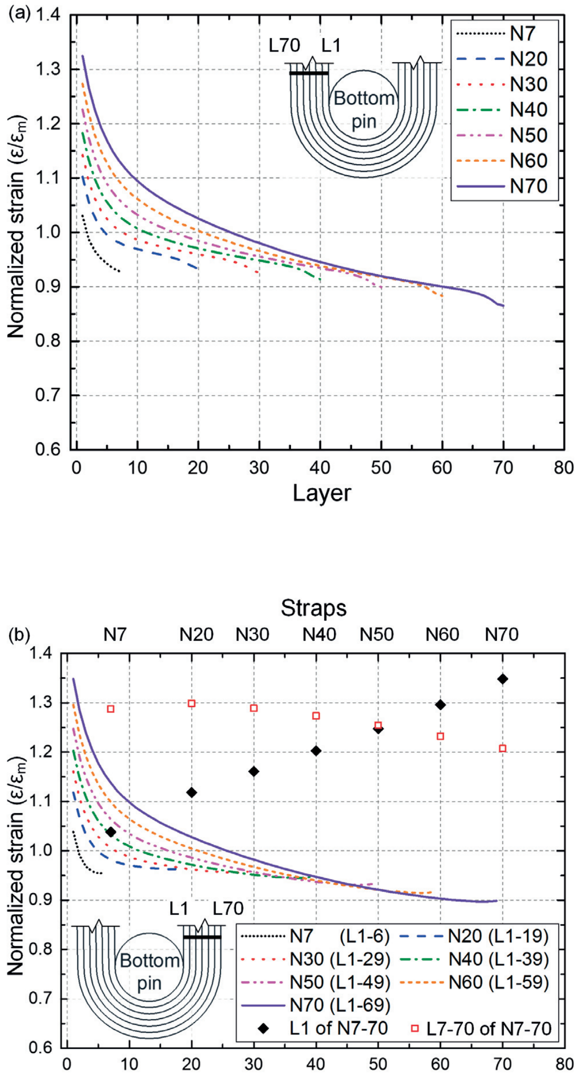

Fig. 7.7: Stress distribution among layers on (a) free-end and (b) bond-end sides at first peak load

(4) Load-bearing efficiency

The relationship between the load-bearing efficiency (R_u) and radius ratio (r_0/r_i) was already experimentally investigated in [2], as shown in Fig. 7.8 (Exp.1/2), for 44 non-laminated straps with n=1–70 layers, tape layer thickness of approximately t=0.13 mm, and pin diameters of D=30 and 50 mm. R_u was calculated by dividing the F_{ult} of the strap specimens by the theoretical capacity, $F_{ult,th}$, estimated as $F_{ult,th}=2 \cdot n \cdot t \cdot w \cdot \sigma_t$ with σ_t=2.25 GPa; r_i was equal to the pin radius and r_0 was calculated as $r_0=r_i+n \cdot t$.

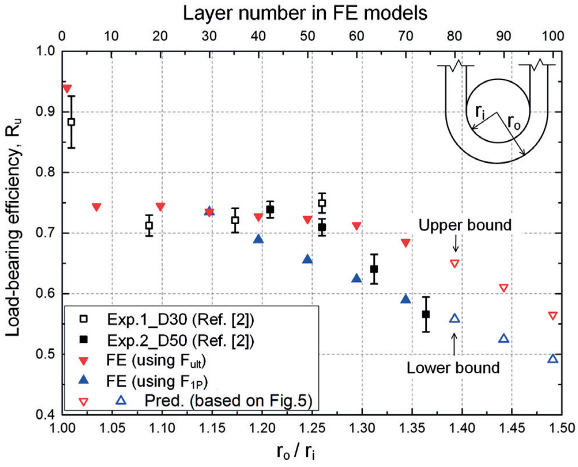

Fig. 7.8: Load-bearing efficiency vs radius ratio in non-laminated straps, experimental and numerical results

Based on the 2D FE models, an identical calculation was also conducted for the N1–N100 straps with r_i=27.5 mm, and the efficiencies based on the first peak (F_{1P}) and ultimate (F_{ult}) loads were also added in Fig. 7.8, whereby the values for N80–N100 were estimated based on the fitted equations in Fig. 7.5. Despite the difference in the strap and pin dimensions, the numerical and experimental results showed similar R_u using F_{ult} up to r_0/r_i of 1.25. However, the FE results overestimated the experimental ones for $r_0/r_i>1.25$, which may be attributed to (1) the disregard of the longitudinal splitting in the width direction in the 2D FE models as mentioned above and (2) underestimated r_0/r_i due to the underestimation of the not precisely measured thickness in [2]. Nevertheless, the R_u values based on the first peak load (F_{1P}) gave a lower bound. For a strap with a large layer number and $r_0/r_i>1.25$, the first peak load (F_{1P}) may thus be considered as a conservative estimate of the ultimate load of the strap.

7.3 Analytical and FE modeling of laminated straps

In [1], analytical models for predicting the load-bearing efficiency (R_u) of laminated straps were presented; however, the agreement with experimental results was not satisfactory. In this work, a new analytical model for predicting the R_u of the laminated straps was first developed based on existing models, which however still exhibited differences with the experimental results in [1]. The reason for this difference was then investigated using FE modeling, based on which the new analytical model was modified.

7.3.1 Review of existing studies in literature

By substituting the tangential and radial strains calculated using the isotropic thick wall cylinder theory into Hooke's law for orthotropic materials, Conen [13] developed an analytical model for predicting the non-uniform tangential strain distribution in the thickness direction at the vertex of the semicircle where the maximum non-uniformity was obtained. A perfect fit between the strap and pins and a zero friction at their interfaces were assumed.

Tensile experiments were conducted on 45 laminated CFRP straps with different layer numbers (n=5, 10 and 15) and pin diameters (D=30, 50 and 150 mm, corresponding to the inner radii of the straps r_i=15, 25 and 75 mm) in [1]. The elastic moduli and Poisson's ratios in the strap plane were: E_1=121 GPa, E_2=4.8 GPa, ν_{12}=0.34, ν_{21}=0.013, ν_{22}=0.4 [1, 18], where 1 and 2 represent the tangential and radial directions in the semicircular parts; the properties in the out-of-plane (width) direction were assumed to be identical to those in the radial direction. From the obtained ultimate loads, F_{ult}, of the non-laminated straps, R_u was calculated, see Fig. 7.9.

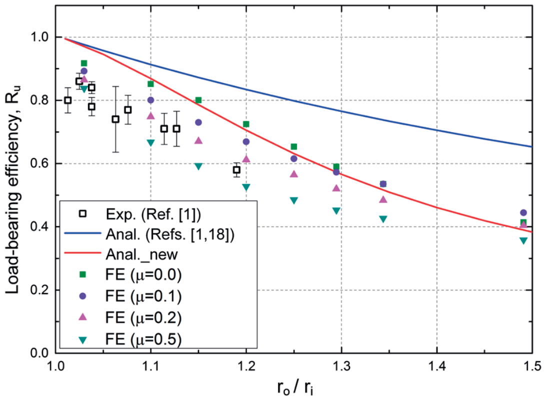

Fig. 7.9: Load-bearing efficiency vs radius ratio in laminated straps: experimental, analytical and numerical results

Since the CFRP straps exhibited more significant anisotropic material properties (E_1/E_2=25.2) than the GFRP straps (E_1/E_2=4.0, [13]), the Conen model showed a significant overestimation in predicting R_u in relationship to r_0/r_i values for the CFRP straps, as presented in [1, 18], see Fig. 7.9. Furthermore, another model for predicting R_u – taking into account the difference between the tangential and radial moduli – was developed by calculating the stress concentration on the inner radius of the strap [19], however, it exhibited overestimated predictions similar to those of the Conen model [1].

7.3.2 Analytical modeling

In the new model, the orthotropic material properties of the CFRP strap were taken into account by using the orthotropic thick wall cylinder theory developed by Jakobi [20]. The tangential and radial stresses calculated using the Jakobi model are as follows [12, 14]:

$$\sigma_r = \frac{-p_i \cdot r_i^{1+E_v}}{r_i^{2\cdot E_v} - r_o^{2\cdot E_v}} r^{E_v - 1} + \frac{-p_i \cdot r_i^{1-E_v}}{r_i^{-2\cdot E_v} - r_o^{-2\cdot E_v}} r^{-E_v - 1} \tag{7.1}$$

$$\sigma_t = \frac{-p_i \cdot E_v \cdot r_i^{1+E_v}}{r_i^{2\cdot E_v} - r_o^{2\cdot E_v}} r^{E_v - 1} - \frac{-p_i \cdot E_v \cdot r_i^{1-E_v}}{r_i^{-2\cdot E_v} - r_o^{-2\cdot E_v}} r^{-E_v - 1} \tag{7.2}$$

where p_i is the pressure on the inner surface of the semicircle, calculated as $p_i = F/2\cdot r_i$, where F is the applied load; E_v is the square root of the ratio of the modified tangential, E_1', to radial, E_2', moduli:

$$E_v = \sqrt{\frac{E_1'}{E_2'}} \tag{7.3}$$

$$E_1' = \frac{E_1}{1 - \nu_{21} \cdot \nu_{12}} \quad \textit{and} \quad E_2' = \frac{E_2}{1 - \nu_{22} \cdot \nu_{22}} \tag{7.4}$$

By substituting Eqs. (7.1) and (7.2) into Hooke's law for orthotropic materials, the non-uniform tangential strain distribution at the vertex of the semicircle for the plane strain case can be calculated as:

$$\frac{\varepsilon}{\varepsilon_m} = (\frac{r_o}{r_i} - 1)[\frac{E_1'}{E_2'} \cdot \nu_{21} \cdot (1 + \nu_{22}) \cdot (A + B) - E_v \cdot (1 - \nu_{21} \cdot \nu_{12}) \cdot (A - B)] \tag{7.5}$$

where

$$A = \frac{(r/r_i)^{E_v - 1}}{1 - (r_o/r_i)^{2E_v}} \quad \textit{and} \quad B = \frac{(r/r_i)^{-E_v - 1}}{1 - (r_o/r_i)^{-2E_v}} \tag{7.6}$$

The strain decreased continuously from the inner to the outer sides; the ultimate load of the laminated straps was thus estimated as the load at which the innermost layer reached the ultimate strain. Substituting r by r_i, R_u can be obtained as a function of r_0/r_i as:

$$R_u = \frac{1-(\frac{r_o}{r_i})^{2E_v}}{(\frac{r_o}{r_i}-1)[\frac{E_1'}{E_2'}\cdot \nu_{21}\cdot (1+\nu_{22})\cdot (1-(\frac{r_o}{r_i})^{2E_v})-E_v\cdot (1-\nu_{21}\cdot \nu_{12})\cdot (1+(\frac{r_o}{r_i})^{2E_v})]} \tag{7.7}$$

By substituting the above-mentioned material properties and r_i/r_0 values of the investigated straps into Eq. (7.7), a new R_u vs r_0/r_i relationship was obtained, as shown in Fig. 7.9. The new model agreed with the experimental results better than the Conen model but still overestimated the values. The assumption of zero friction at the interfaces was thus questioned. To investigate the effect of friction at the pin/CFRP interface, FE modelling was used as described in the following section.

7.3.3 Description of 2D FE model

2D FE models, as shown in Fig. 7.10, were developed to investigate the influence of friction at the pin/CFRP interface on the tensile behavior of the straps, particularly on F_{ult}. The contact method used at the interface was similar to that used for the non-laminated straps described above, except that the coefficient of friction (μ) was varied, i.e. values of 0.0, 0.1, 0.2 and 0.5 were investigated, which covered the range of interfaces between CFRP and different materials including Teflon, steel, CFRP and Wrightlon [1, 17]. The geometry and material properties of the laminated straps remained the same as in the analytical model. Laminated straps with 7–100 layers (designated M7–M100) were simulated, corresponding to r_0/r_i of 1.03–1.49.

The laminated strap was modeled as a solid section, as shown in Fig. 7.10. In the thickness direction, a mesh size of 0.135 mm, i.e. the thickness of the tape layer, was used to create an element number identical to the layer number (see the example of strap M70 in Fig. 7.10). In the longitudinal direction, a general mesh size of 2.0 mm was selected; a refined mesh was used at the flank as in the non-laminated straps, where a biased mesh with varying size of 0.1–0.15 mm was applied based on sensitivity checks. The total element number was 9,028 to 56,641 in the M7–M100 straps.

In the FE results, F_{ult} was calculated using the same method as in the analytical model. The tangential strain distribution in the thickness direction was obtained from the FE models with different μ values, based on which R_u was calculated as $R_u=1/(\varepsilon/\varepsilon_m)_{\max}$, as in the analytical model at the flank and vertex of the semicircular segments (see Fig. 7.10).

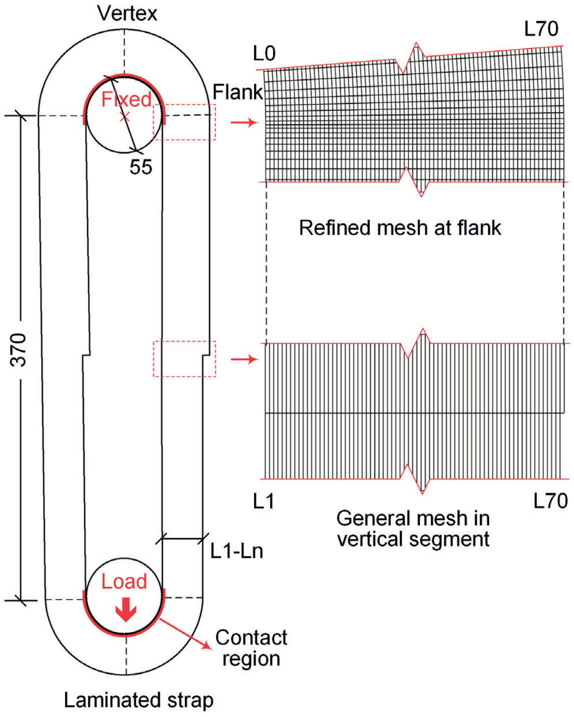

Fig. 7.10: FE model of laminated straps (dimensions in [mm])

7.3.4 Validation of FE and analytical models

In the FE models, $(\varepsilon/\varepsilon_m)_{\max}$ was located at the vertex of the semicircle in the case of μ=0.0, while it was at the flank in the remaining cases; in all cases, $(\varepsilon/\varepsilon_m)_{\max}$ was observed at the innermost layer of the semicircle. The tangential strain distribution at the flank of the semicircle of straps M7–M70 for μ=0.2, at the estimated ultimate loads of the straps, is shown in Fig. 7.11. The strain peak, i.e. the $(\varepsilon/\varepsilon_m)_{\max}$, of each strap was obtained and R_u was subsequently calculated. The resulting R_u vs r_0/r_i relationships based on the FE models for all μ values were compared to the experimental ones, as shown in Fig. 7.9. The FE models with μ=0.2/0.5 well overlapped the scattering band of R_u obtained from the experiments. Since μ=0.2 also corresponded to the measured coefficient of friction at the CFRP/steel interface in [1], the FE model was considered validated. Furthermore, the new analytical model (Eq. (7.7)) was also validated by the good agreement of the results with those of the FE models at μ=0.0, i.e. zero-friction at the pin/CFRP interface. The results also confirmed that the overestimation of the analytical results compared to the experimental results was due to the disregard of the friction at the pin/CFRP interface.

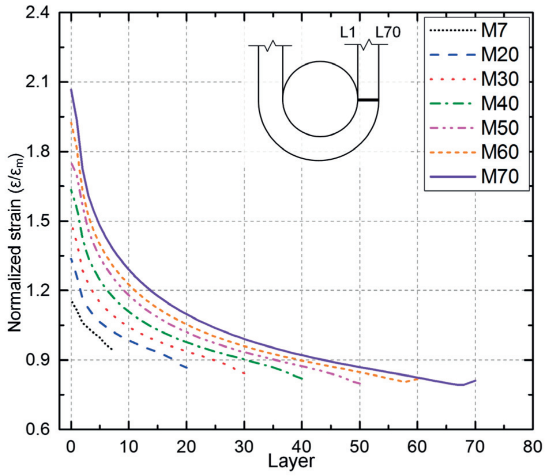

Fig. 7.11: Tangential strain distributions in thickness direction at flank in M7–M70 straps with μ=0.2 at estimated ultimate loads

7.3.5 Modified analytical model

As discussed above, in the case of μ=0.0, the new analytical model can well predict the R_u obtained from the FE models; in contrast, in the cases of μ=0.1–0.5, it showed overestimation compared to the numerical results (Fig. 7.9). The difference between the analytical and FE models with μ=0.1–0.5, at individual r_0/r_i values, was calculated as ΔR_u. A 3D linear surface with a correlation of coefficient of 0.96 was fitted to model the relationship between ΔR_u and μ and r_0/r_i as:

$$\Delta R_u = 0.287 \cdot \mu - 0.387 \cdot (r_o / r_i) + 0.484 \tag{7.8}$$

By combining Eq.(7.8) and Eq.(7.7), $R_{u,mod} = R_u - \Delta R_u$ was calculated for μ=0.1–0.5 and r_0/r_i=1.03–1.50 and compared to the numerical results, as shown in Fig. 7.12. The modified analytical model exhibited good agreement with the numerical results under all friction conditions. Furthermore, the calculated ΔR_u decreased to zero at around r_0/r_i=1.30, 1.40 and 1.60 for μ=0.1, 0.2 and 0.5 respectively. Therefore, the load-bearing efficiency of straps with different μ and r_0/r_i can be calculated as:

$$R_{u,\mathrm{mod}} = \begin{cases} R_u - \Delta R_u, & (0 < r_o / r_i < 1.6) \\ R_u \quad , & (r_o / r_i > 1.6) \end{cases} \tag{7.9}$$

For $0<r_0/r_i<1.2$, Eq. (7.9) was validated by the experimental results in [1], as shown in Fig. 7.12. For the remaining range of r_0/r_i, the experimental results for the GFRP straps presented in [13], based on which the Conen model was derived, were used for the validation. The material properties of the GFRP straps were E_1=37.3 GPa, E_2=9.3 GPa, v_{12}=0.30, v_{21}=0.075, v_{22}=0.50 [13]. By substituting the material properties and r_0/r_i=1.4, 1.8 and 2.4 into Eq. (7.9), $R_{u,mod}$ was obtained; correspondingly, the median stresses at the ultimate load were calculated, i.e. $\sigma_m=E_1\cdot\varepsilon_m=E_1\cdot\varepsilon_{ult}\cdot R_{u,mod}$ with ε_{ult}=0.02 [13]. At r_0/r_i=1.4, the calculated $R_{u,mod}$ were 0.73, 0.70 and 0.61 for μ=0.1, 0.2 and 0.5 respectively (μ was not given in [13]) and the corresponding σ_m were 542, 521 and 456 MPa, which were -12, -8 and 5% different from the experimental value (482 MPa). At r_0/r_i=1.8 and 2.4, the calculated $R_{u,mod}$ were 0.49 and 0.32 and the σ_m were 364 and 239 MPa respectively, which were 4–8% different from the experimental ones (351 and 255 MPa [13]), i.e. the new model performed better compared to the Conen model exhibiting differences of 11–14% from the measured values [13]. Thus, the new model was considered validated.

Furthermore, for isotropic materials, i.e. $E_1=E_2$ and $v_{12}=v_{21}=v_{22}$, the two models (μ=0.0) exhibited identical results. Therefore, the new analytical model comprises the Conen model and performs better in the case of highly anisotropic materials such as CFRP. The new model is applicable for laminated straps composed of different materials (isotropic or orthotropic) and with varying r_0/r_i and μ values. In the case of lack of precise μ values, the calculated minimum and maximum R_u using Eq. (7.9) with μ=0.1–0.5 can be considered as the lower and upper bounds for estimating the ultimate load.

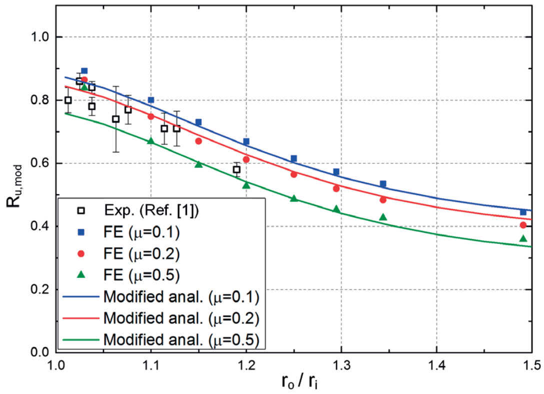

Fig. 7.12: Comparison of modified analytical model with numerical and experimental results

7.4 Comparison of non-laminated and laminated straps

7.4.1 Influence of interface friction and orthotropic material properties

For non-laminated straps, parametric studies on the influence of the interface friction had already been conducted in the previous work presented in [11]; the variation of friction changed the strain distribution in the semicircular parts, but exhibited insignificant influence on the ultimate load of the straps. Further confirmation was obtained by varying the μ of the CFRP/CFRP and pin/CFRP interfaces from 0.2 to 0.5 in strap N70, where only a 3% decrease of the ultimate load was observed. The laminated CFRP straps were sensitive to friction however; strap M70 exhibited an 18% decrease of the ultimate load as a result of increasing μ from 0.2 to 0.5.

The laminated straps were also sensitive to the orthotropic material properties; the ultimate load, back calculated using R_u, decreased with an increasing ratio of modulus between the two directions, i.e. E_v in Eq.(7.7). The significant influence of the orthotropicity on the maximum tangential stress at the inner radius has already been discussed in [12, 19]. In this work, the ultimate load of the strap decreased by 18% by increasing E_1/E_2 from 25.2 to 46.6 (by 85%) in strap M70, while only a decrease of 6% was observed in the non-laminated strap N70. Similarly, the ultimate load of strap M70 increased by 43% when E_1/E_2 was decreased from 25.2 to 4.0, while only an 11% increase was observed in N70.

7.4.2 Strain distribution in thickness direction at flank

The strain distributions at specific locations were different in the non-laminated and laminated cases. Taking the N70 and M70 straps as examples (for μ=0.2), M70 exhibited more uniform strain distribution in the straight segment compared to N70. However, it was inversed at the flank, as shown in Fig. 7.13 at 650 kN (which was close to the F_{ult} of strap M70), the strain peak was more significant in M70 compared to N70, resulting in the lower R_u value in the former than in the latter. This higher strain peak in strap M70 was caused by the local bending of the whole cross section. In N70, however, bending occurred only in the individual layers, which reduced the strains in the inner 20 layers compared to M70.

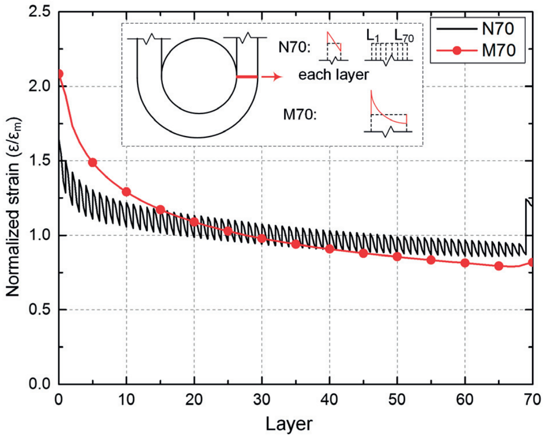

Fig. 7.13: Longitudinal strain distribution at flank in N70 and M70 straps at 650 kN (μ=0.2)

7.4.3 Load-bearing efficiency

The comparison of the R_u of the analyzed non-laminated and laminated straps with E_l=121 GPa is shown in Fig. 7.14, which is based on Figs. 7.8 and 7.9. For the non-laminated straps, linear and exponential curves were fitted to predict R_u based on the first peak (F_{1P}) and ultimate (F_{ult}) loads respectively. The non-laminated straps exhibited lower R_u at around n<20 (i.e. r_0/r_i<1.1) than the laminated ones due to the failure of the outermost layer as mentioned above; however, they showed higher R_u at n>20 (i.e. r_0/r_i>1.1), where even R_u calculated using F_{1P} was higher than R_u of the laminated ones.

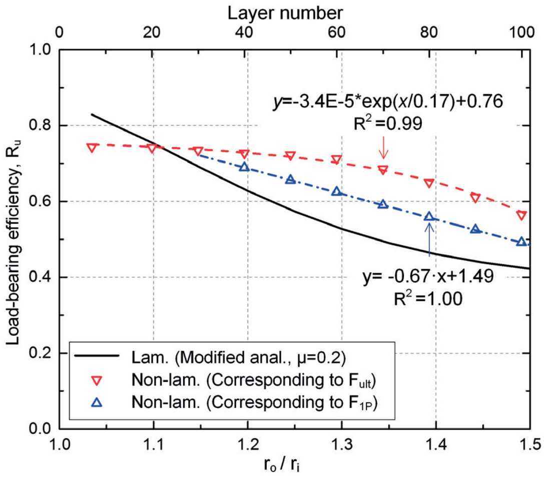

Fig. 7.14: Load-bearing efficiency vs radius ratio for non-laminated and laminated straps (μ=0.2)

7.4.4 Practical application aspects

Despite the better load-bearing performance of the non-laminated straps compared to the laminated ones at r_0/r_i>1.1, factors concerning practical applications also need to be taken into account when comparing these two strap systems. Long non-laminated strap tendons are difficult to coil into small diameters for transportation, particularly in the case of large layer numbers; significant slippage between individual layers and possible local deformation in the inner layers may damage the strap. Long laminated strap tendons however can be coiled into different diameters depending on the tendon stiffness. In applications where strap tendons have to be inserted into a borehole, e.g. in ground anchors, the low transversal stiffness of the non-laminated straps causes difficulties in tendon installation, which is easier in the laminated case. Furthermore, since the tape layers are separated from each other in the non-laminated straps, they are vulnerable to handling [11] and thus a protection layer is usually needed. The bonding of the outermost layer is also essential for the non-laminated straps; bond failure can result in a significant reduction in the ultimate load [11]. Laminated straps are less sensitive to handling and bonding issues however. A summary of the comparison between non-laminated and laminated straps, including mechanical behavior and practical application aspects, is shown in Table 7.1.

Table 7.1: Comparison of non-laminated and laminated straps

Characteristic	Non-laminated	Laminated
1. Mechanical behavior		
Load-bearing efficiency (R_u)	good at > 20 layers (i.e. r_0/r_i>1.1)	good at < 20 layers (i.e. r_0/r_i<1.1)
Strain distribution	near to uniform at flank; near to uniform in straight segment	non-uniform at flank; uniform in straight segment
Sensitivity to orthotropic material properties	low	high
Sensitivity to interface friction	low	high
2. Practical application aspects		
Ease of coiling	low	medium
Ease of insertion into borehole	low	high
Vulnerable to handling	high	low
Sensitivity to bond-end quality	high	low

7.5 Conclusions

The tensile behavior of non-laminated and laminated CFRP straps composed of up to 100 layers was investigated using numerical and analytical methods. The developed numerical and analytical models were validated by experimental results, and the detailed load-bearing behavior of the straps was then analyzed. The following conclusions were drawn:

1. Non-laminated straps exhibited different failure modes, which depended on the layer number. For fewer than 20-30 layers, brittle and sudden strap rupture occurred due to the failure of the outermost layer, while for more than 20-30 layers, strap rupture started in the innermost layer and progressed through the adjacent outer layers, accompanied by a loss of stiffness, up to the ultimate load. This behavior could be attributed to a non-uniform strain distribution and layer number-dependent change of the strain peaks from the outermost to innermost layers. An empirical model was developed to estimate the ultimate load of straps composed of up to 100 layers.
2. Laminated straps exhibited the strain peaks at the flank of the innermost layer. An analytical model was developed to predict the load-bearing efficiency, which takes into account the strap anisotropy and friction at the strap-pin interfaces.
3. Laminated straps exhibited higher strain peaks at the inner flank than non-laminated straps for the same layer number and load.
4. Non-laminated straps showed significantly higher load-bearing efficiency than laminated straps for layer numbers higher than 20 or radius ratios >1.1.
5. Non-laminated straps exhibited lower sensitivity to tape anisotropy and friction at the strap/pin interface than laminated straps.

References

[1] Winistöerfer AU. Development of non-laminated advanced composite straps for civil engineering applications. Coventry, UK: Department of Engineering, University of Warwick; 1999.

[2] Winistöerfer A, Meier U. CARBOSTRAP-An advanced composite tendon system. In: 6th International Symposium on FRP Reinforcement for Concrete Structures (FRPRCS-5), Cambridge, UK, July 231-8; 2001.

[3] Bauersfeld DW. Composite graphite/epoxy tensile element. Report 2404. United States Army, Belvoir Research & Development Center, Fort Belvoir, Virginia; 1984.p.1-62.

[4] Keller T, Kenel A, Koppitz R. Carbon Fiber-Reinforced Polymer Punching Reinforcement and Strengthening of Concrete Flat Slabs. ACI Struct J 2013;110(06).

[5] Czaderski C, Motavalli M, Winistörfer A, Motavalli M. Prestressed shear strengthening of a box girder bridge with non-laminated CFRP straps. In: Proceedings of the 4th International Conference on FRP Composites in Civil Engineering (CICE2008), Zurich, Switzerland, July 7.B.6; 2008.

[6] Huster U, Broennimann R, Winistörfer A. Strengthening of a historical roof structure with CFRP-straps. In: Proceedings of the 4th International Conference on FRP Composites in Civil Engineering (CICE2008), Zurich, Switzerland, July 8.B.4; 2008.

[7] Triantafillou TC, Fardis MN. Strengthening of historic masonry structures with composite materials. Mater Struct 1997;30(8):486-96.

[8] Fan H, Vassilopoulos AP, Keller T. Pull-out behavior of CFRP ground anchors with two-strap ends, Compos Struct 2017;160:1258–1267.

[9] Fan H, Vassilopoulos AP, Keller T. Pull-out behavior of CFRP single-strap ground anchors, J Compos Constr, 10.1061/(ASCE)CC.1943-5614.0000760 , 04016102.

[10] Gardner Business Media Inc. CompositesWorld, March 2015. < http://cw.epubxp.com/i/467593-mar-2015> (May 01, 2017).

[11] Fan H, Vassilopoulos AP, Keller T. Experimental and numerical investigation of tensile behavior of non-laminated CFRP straps. Compos B Eng 2016;91:327-36.

[12] Schürmann H. Konstruieren mit Faser-Kunststoff-Verbunden: Springer; 2005.

[13] Conen H. Deformation und versagen von GFK-strangschlaufen. Kunststoffe. 1966;56(9):629-31.

[14] Havar T. Beitrag zur Gestaltung und Auslegung von 3D-verstärkten Faserverbundschlaufen. Stuttgart, Germany: University of Stuttgart; 2007.

[15] Djamaluddin R, Yamaguchi K, Hino S. Mechanical behavior of the U-anchor of super-CFRP rod under tensile loading. J Compos Mater 2014;48(15):1875-85.

[16] Büttemeyer H, Schiebel P, Solbach A, Emmelmann C, Herrmann AS. Performance of various designs of hybrid loop-loaded CFRP-titanium straps. In: 20th International Conference on Composite Materials, Copenhagen, Denmark, July 19; 19-24, 2015.

[17] Baschnagel F, Rohr V, Terrasi GP. Fretting Fatigue Behaviour of Pin-Loaded Thermoset Carbon-Fibre-Reinforced Polymer (CFRP) Straps. Polym 2016;8(4):124.

[18] Lees J, Winistörfer A. Nonlaminated FRP Strap Elements for Reinforced Concrete, Timber, and Masonry Applications. J Compos Constr 2010;15(2):146-55.

[19] Mansfield E. Load transfer from a pin to a wound fibre composite strip. J Compos Mater 1983;17(5):414-9.

[20] Jakobi R. Zur Spannungs-, Verformungs-und Bruchanalyse an dickwandigen, rohrförmigen Bauteilen aus Faser-Kunststoff-Verbunden. Kassel, Germany: University of Kassel; 1987.

8.

Conclusions and future work

8.1 Summary of conclusions

This chapter presents the main conclusions and recommendations for future work. The conclusions are based on the objectives of this thesis explained in Section 1.2.

8.1.1 Evaluation of cement- and resin-based grout materials

The uniaxial compressive stress vs strain behavior of four cement- and resin-based grout materials was investigated in compression experiments. The appropriate experimental methods for obtaining the softening responses of the grouts were determined. The Sargin concrete model was applied to model the investigated grouts and validated in the FE analyses of the CFRP one-strapanchor heads. The following conclusions were drawn:

1. The appropriate experimental methods were determined as a combined axial and circumferential deformation control and two 0.1-mm-thick Teflon sheets with grease in between; the loading-control method influenced the pre-peak compressive stress vs strain curves, while the specimen boundary conditions affected the post-peak softening behavior.
2. The compressive stress vs strain behavior of the investigated cement- and resin-based grouts was successfully modeled by the Sargin concrete model; this applicability was validated by comparing the FE results for the CFRP one-strapanchor heads with the implemented grout models with the experimental results.
3. Parametric FE analyses demonstrated that only limited stress redistribution occurred after the crack initiation in the grout of the one-strap anchor heads in soil applications.

8.1.2 Pull-out behavior of one-strap anchor

Four CFRP one-strap ground anchor heads were investigated in pull-out experiments. One anchor head specimen was confined with a steel tube to simulate the rock application, while no steel tube was applied to the remaining three, i.e. simulating the soil application. In the latter, the embedded strap region was additionally confined by CFRP confinement rings with different positions and lengths. The following conclusions were drawn:

1. The confinement provided by the rock mass (i.e. steel tube) prevented premature grout failure in the strap region, demonstrating that the anchor could be used without additional confinement; in the soil application however, an additional CFRP confinement ring is needed.

2. If the length and position of the CFRP confinement ring are optimized to deviate the spreading forces in the strap region, the anchor capacity only depends on the uniaxial compressive strength of the unconfined grout cylinder located between the CFRP ring and the free anchor length.
3. Only approximately 50% of the applied load is transferred at the semicircle of the embedded strap, while the remaining 50% is borne by the CFRP/grout interface friction and the curved transition located between the semicircle and the rod segment.

8.1.3 Pull-out behavior of two-strap anchor

Three two-strap CFRP ground anchors were investigated in pull-out experiments. The two-strap anchor head was anchored by normal-strength grout in steel tubes of different thicknesses to simulate the confinement of different rock masses. The following conclusions were drawn:

1. The two-strap anchors reached an average ultimate load of 1384 kN, i.e. the targeted capacity of 1000 kN was achieved, and exhibited the desired failure mode via CFRP strap rupture. The grout failure was thus prevented by (1) selecting the appropriate high-strength grout material for the anchor head, (2) optimizing the CFRP confinement rings to balance and deviate the spreading forces and (3) transferring the load from the high- to normal-strength grouts effectively via a complex conical-shaped interface.
2. The load transfer from the embedded CFRP strap to the surrounding grout was influenced by the confinement provided by the surrounding media. A higher confining pressure resulted in a later activation of the embedded CFRP components; a correspondingly higher load transfer occurred at the deviation point and the remaining strap segments were thus less loaded.

8.1.4 Load-transfer mechanism in multi-strap anchor

The load-transfer mechanism in multi-strap anchors was investigated based on the experimental and numerical results obtained for one- and two-strap anchors. The influence of the strap geometry and strap number on the global pull-out and local load-transfer behavior of the anchors was quantified. An empirical model for deriving the load-transfer diagram for multi-strap anchors was developed and subsequently applied to a new three-strap anchor. The following conclusions were drawn:

1. The different strap geometries resulted in different local load-transfer diagrams, but the global pull-out behavior remained similar. However, anchors with similar strap geometries but different strap numbers exhibited similar pull-out and load-transfer behaviors.
2. An empirical model was developed to predict the three components of the load-transfer diagram for multi-strap anchors: (1) load transfer at the strap division, (2) frictional load transfer along each strap and (3) load transfer at strap ends, based on which the diagram can be derived.
3. The frictional load transfer existed only in the outer strap in multi-strap anchors at higher loads and it was not sensitive to the rock stiffness, unlike the load transfer at the strap division, which was proportional to the rock stiffness.
4. A new three-strap anchor was developed by adding a third strap to the two-strap anchor, which achieved the targeted capacity of 2500 kN; the load-transfer diagram for the three-strap anchor corresponding to one rock stiffness was derived using the developed empirical model.

8.1.5 Tensile behavior of non-laminated and laminated straps

Tensile experiments and 3D FE analyses were first conducted on seven-layer non-laminated CFRP straps. The 3D FE model was then changed to 2D and the FE analyses were extended to non-laminated straps with up to 100 layers. Similarly, the tensile behavior of laminated CFRP straps with up to 100 layers was also investigated using numerical and analytical methods. Based on these results, the strain distribution between the constituent tape layers and the load-bearing efficiency of the non-laminated and laminated straps were investigated. The following conclusions were drawn:

1. The interface friction in the non-laminated straps exhibited an insignificant influence on the strap stiffness and strain distributions in the straight segments, but resulted in different strain distributions in the semicircular segments.
2. In the non-laminated straps, the fusion bonding of the outermost layer to the next outermost layer resulted in a significantly high strain in the former on the bond-end side, leading to the layer rupture and associated brittle strap failure. However, the failure mode changed to progressive failure starting from the innermost layer at 20-30 layers. For the progressive failure case, an empirical model was developed to estimate the ultimate load of the straps with up to 100 layers.

3. Strain peaks were observed at the flank of the innermost layer in both non-laminated and laminated straps, the latter however exhibited higher peak values than the former at the same layer number and load level.
4. For laminated straps, an analytical model, considering the strap anisotropy and friction at the strap/pin interface, was developed to predict the relationship between the load-bearing efficiency and strap radius.
5. The non-laminated straps exhibited a significantly higher load-bearing efficiency for layer numbers higher than 20 (radius ratios >1.1) than the laminated straps; the former were also less sensitive to the strap anisotropy and friction at the strap/pin interface.

8.2 Original contributions

The original contributions provided by the thesis with regard to the three constituent parts presented in Section 1.4 are summarized as follows:

(a) Cement- and resin-based grout materials

- The experimental methods to obtain the softening responses of the grout materials have been established.
- The compressive stress vs strain behavior of cement- and resin-based grouts has been modeled using the Sargin concrete model.
- The influence of the grout strain-softening behavior on the pull-out responses of the CFRP one-strap ground anchor heads has been identified.

(b) Pull-out behavior of CFRP ground anchors with strap ends

- CFRP ground anchors with one-, two- and three-strap ends for different applications have been developed.
- New experimental set-ups for CFRP ground anchors with one- and multi-strap ends have been developed.
- The influence of the confinement, strap geometry and strap number on the pull-out behavior of one- and two-strap CFRP ground anchors has been identified and the load transfer from the strap to the surrounding grout has been quantified.
- An empirical model has been developed to derive the load-transfer diagram along the embedded straps for multi-strap anchors.

(c) Tensile behavior of non-laminated and laminated CFRP straps

- The different failure mechanisms in non-laminated straps have been identified.
- The strain distributions between the constituent tape layers at different positions in non-laminated and laminated straps with up to 70 layers have been quantified.
- The influence of tape anisotropy and interface friction on the tensile behavior of non-laminated and laminated straps has been quantified.
- An empirical model has been derived to predict the load-bearing capacity of non-laminated straps with up to 100 layers.
- A new analytical model has been derived to model the relationship between the load-bearing efficiency and the radius ratio for the laminated straps, taking into account the strap anisotropy and friction at the strap/pin interfaces.

8.3 Future work

This section introduces future prospective research topics based on the present work. The first four topics are dedicated to further research work to better understand the structural performance of the developed CFRP strap ground anchors. The last topic deals with future practical applications.

8.3.1 Shear performance of multi-strap CFRP ground anchors

In applications for the stabilization of structures such as retaining walls and slopes, the ground mass comprises constituent blocks which have a relatively high kinematic potential for sliding. High shear deformation exists at these potential sliding interfaces, i.e. the potential failure surface as shown in Fig. 8.1 [1]. Considering the relatively low strength of the CFRP tendon in the transversal direction compared to the longitudinal (fiber) direction, the mechanical behavior of multi-strap CFRP ground anchors under local shear deformation needs to be investigated and appropriate measures applied if necessary.

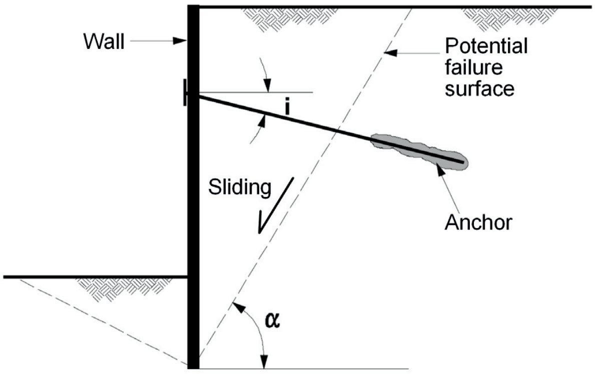

Fig. 8.1: Shear deformation due to unstable block sliding [1]

8.3.2 Creep and relaxation performance of multi-strap CFRP ground anchors

In the CFRP ground anchor, creep deformation may be observed in the CFRP tendon and grout part. Considering that (1) CFRP tendons exhibit excellent creep performance compared to other FRP tendons [2] and (2) cement grouts show better creep behavior than epoxy grouts (see Chapter 2), the creep behavior of the multi-strap CFRP ground anchor would be less critical than in adhesively-bonded CFRP anchors where creep rupture of the adhesive layer and creep deformation at the bond interface occur [3]. Furthermore, CFRP tendons also exhibit better relaxation performance than steel and other FRP tendons [2]. However, since the creep and relaxation characteristics of ground anchors are prescribed in standards such as EN1537:2013 [4], further research work is needed to verify the creep and relaxation performance of multi-strap CFRP ground anchors.

8.3.3 Fatigue performance of multi-strap CFRP ground anchors

Ground anchors may be subjected to fatigues loads when railway lines pass above the strengthened structures such as dams and slopes. The fatigue strength of CFRP tendons well exceeds that of prestressing steel tendons [2]. However, in the anchor system, the influence of other factors such as the grout material and tendon/grout interface on the fatigue life of the system should also be taken into account [3]. Therefore, further research work is needed to verify the fatigue performance of the CFRP ground anchor system.

8.3.4 Durability performance of multi-strap CFRP ground anchors

CFRP materials offered a superior performance to that of prestressing steel in aggressive environments including high temperature and alkali and acid solutions [2]. Considering that long-term durability is essential for permanent ground anchors, further research work is needed to verify the durability performance of multi-strap CFRP ground anchors.

8.3.5 Optimization of tendon design for coil requirement

In ground anchor applications, the CFRP tendon with prefabricated anchor head usually has a length of 20–80 m, which is coiled during transportation to the construction site. The minimum achievable coil diameter depends on the transversal stiffness of the tendon. Therefore, the cross section of the middle tendon segment between the strap ends on the air and ground sides, as well as the constituent materials, the matrix in particular, need to be optimized.

References

[1] Xanthakos PP. Ground anchors and anchored structures. Washington, U.S.A.: John Wiley & Sons, 1991.

[2] Benmokrane B, Xu H, Nishizaki I. Aramid and carbon fibre-reinforced plastic prestressed ground anchors and their field applications. Can J Civ Eng 1997;24:968-85.

[3] Puigvert F, Crocombe AD, Gil L. Fatigue and creep analyses of adhesively bonded anchorages for CFRP tendons. Int J Adhes Adhes 2014;54:143-154.

[4] European Committee for Standardization (CEN). Execution of special geotechnical work–ground anchor. BS EN 1537:2013, Brussels, Belgium.

ANNEX A.

Evaluation of grout materials for CFRP ground anchors with strap ends

A.1 Failure modes in compression experiments

Figs. A.1–A.3 complement the discussion of failure modes in Section 2.3.2 in Chapter 2.

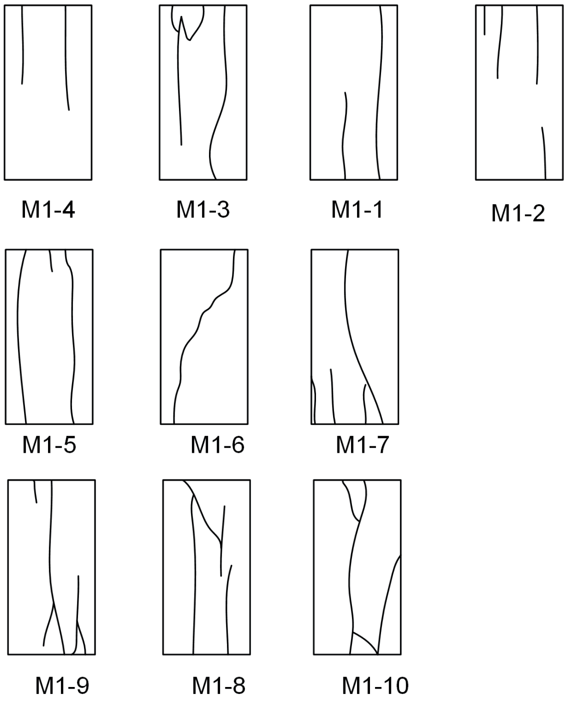
M1-4
M1-3
M1-1
M1-2
M1-5
M1-6
M1-7
M1-9
M1-8
M1-10

Fig. A.1: Failure modes of Sika Rock Mortar (M1)

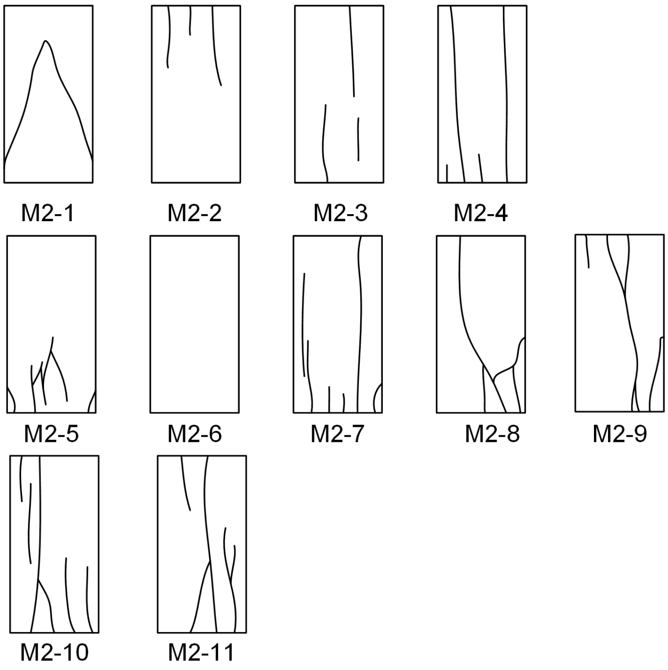
M2-1
M2-2
M2-3
M2-4
M2-5
M2-6
M2-7
M2-8
M2-9
M2-10
M2-11

Fig. A.2: Failure modes of SikaGrout 212 (M2)

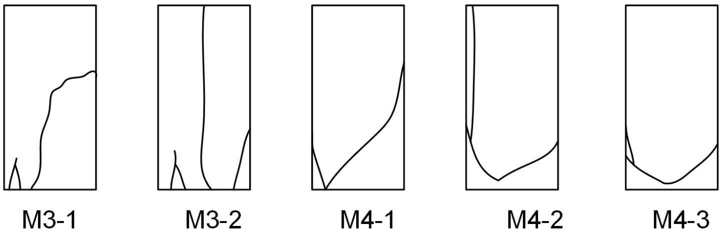

Fig. A.3: Failure modes of Sikadur 42 HE (M3) and Sikadur 42 LE Plus (M4)

Fig. A.4 complements the discussion of the unstable post-peak strain measurements obtained from the surface-mounted omega gages in Section 2.3.2 in Chapter 2.

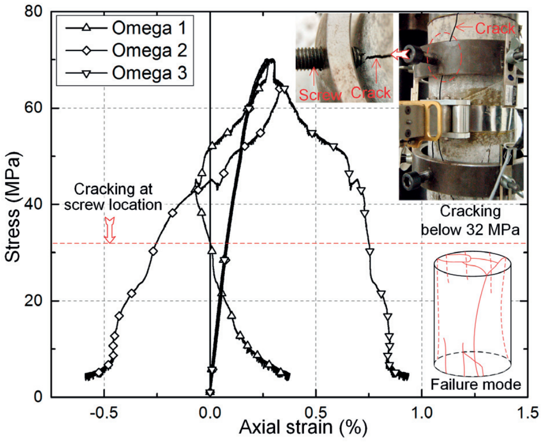

Fig. A.4: Stress-strain responses measured by surface-mounted omega gages in M2-11

A.2 FE model of CFRP ground anchor head

Fig. A.5 complements the discussion of the cracking pattern in anchor head C200 presented in Section 2.4.4 in Chapter 2.

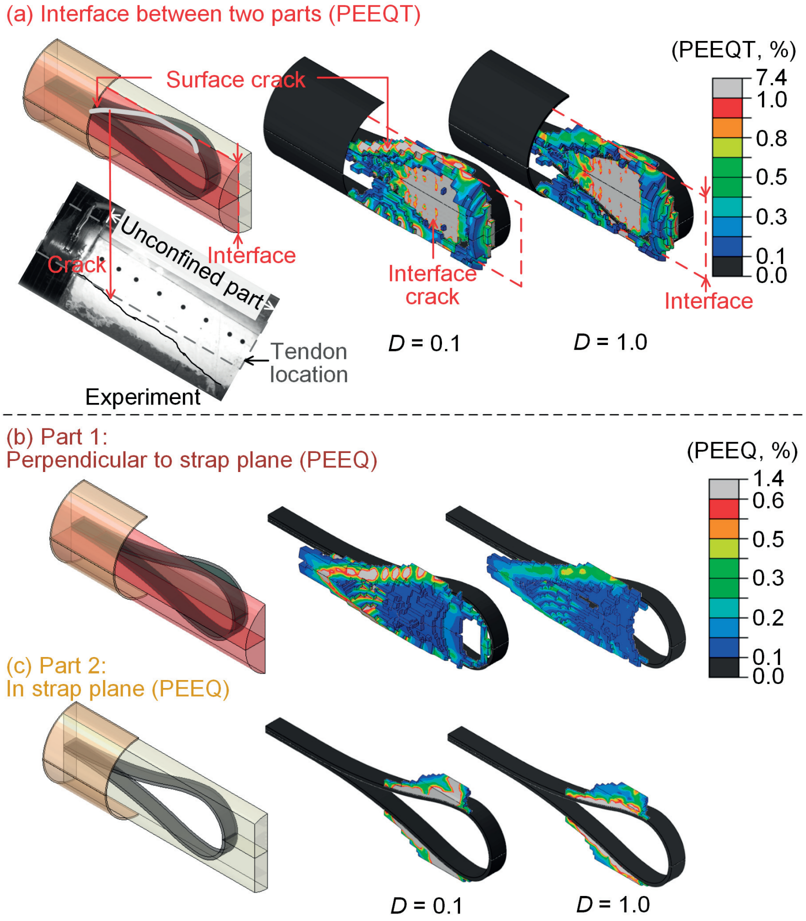
(a) Interface between two parts (PEEQT)
Surface crack
Unconfined part
Interface
Crack
Tendon location
Experiment
Interface crack
Interface
D = 0.1
D = 1.0
(PEEQT, %)
7.4
1.0
0.8
0.5
0.3
0.1
0.0
(b) Part 1:
Perpendicular to strap plane (PEEQ)
(PEEQ, %)
1.4
0.6
0.5
0.3
0.2
0.1
0.0
(c) Part 2:
In strap plane (PEEQ)
D = 0.1
D = 1.0

Fig. A.5: Plasticized zone with equivalent plastic strains higher than 0.1% at 250 kN in FE models of anchor C200 with D = 0.1/1.0: (a) in tension (PEEQT) and (b)/(c) in compression (PEEQ)

ANNEX B.

Pull-out behavior of CFRP single-strap ground anchors

B.1 Parametric studies on CFRP confinement rings

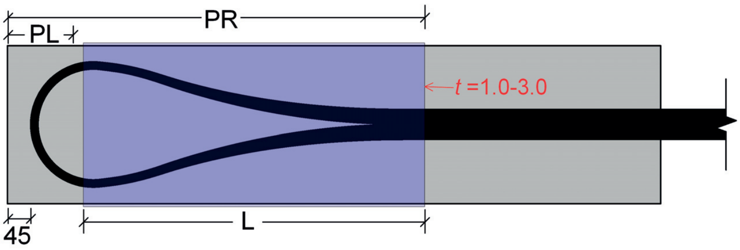

Fig. B.1: Schematic of three parameters (thickness, length and position of CFRP ring)

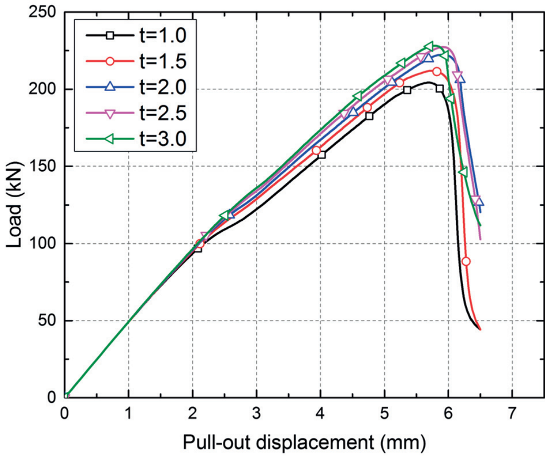

Fig. B.2: Parametric studies on thickness of CFRP ring

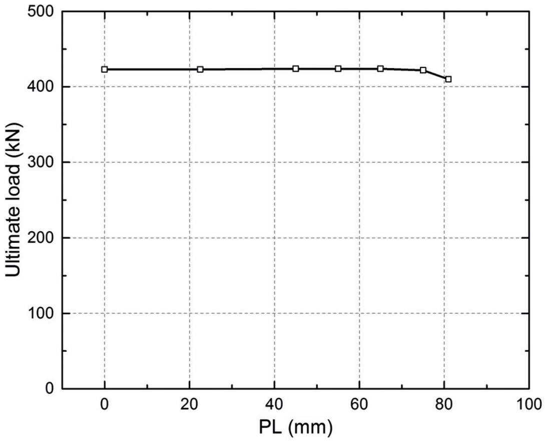

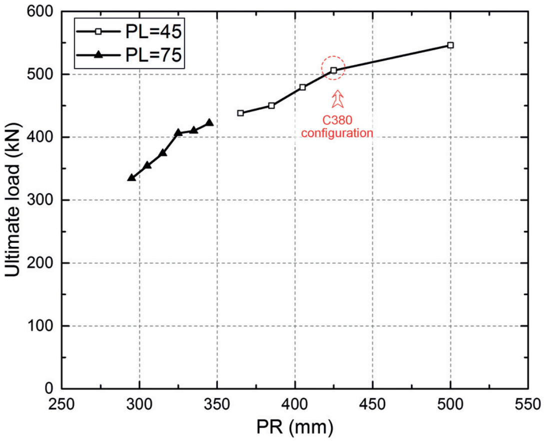

Fig. B.3: Parametric studies on PL of CFRP ring *Fig. B.4: Parametric studies on PR of CFRP ring*

B.2 Pull-out experiments

This section complements the experimental set-up and results presented in Chapter 3.

B.2.1 Experimental set-up

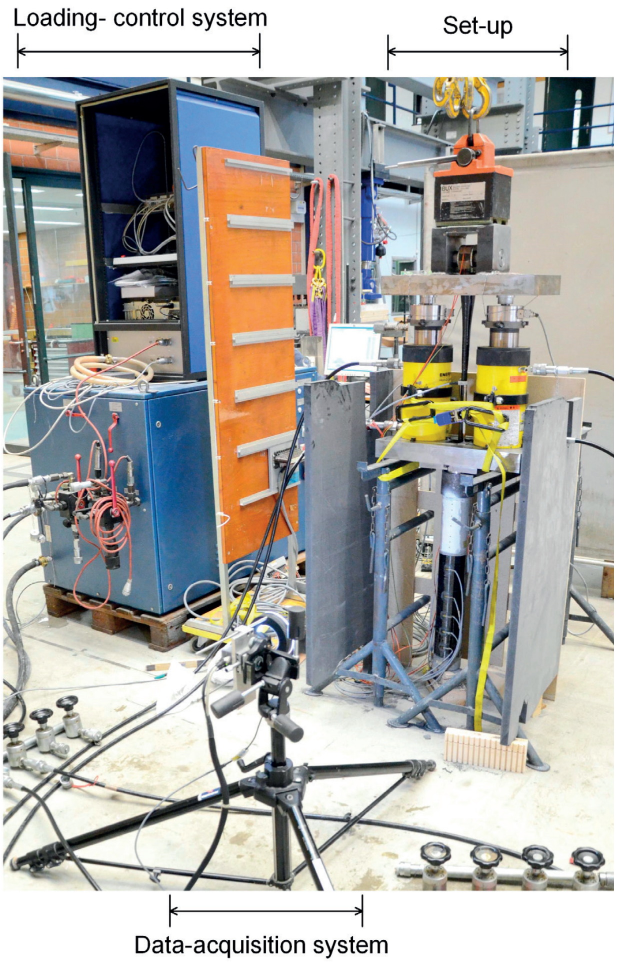
Loading- control system
Set-up
Data-acquisition system

Fig. B.5: Complete experimental set-up

B.2.2 Experimental results

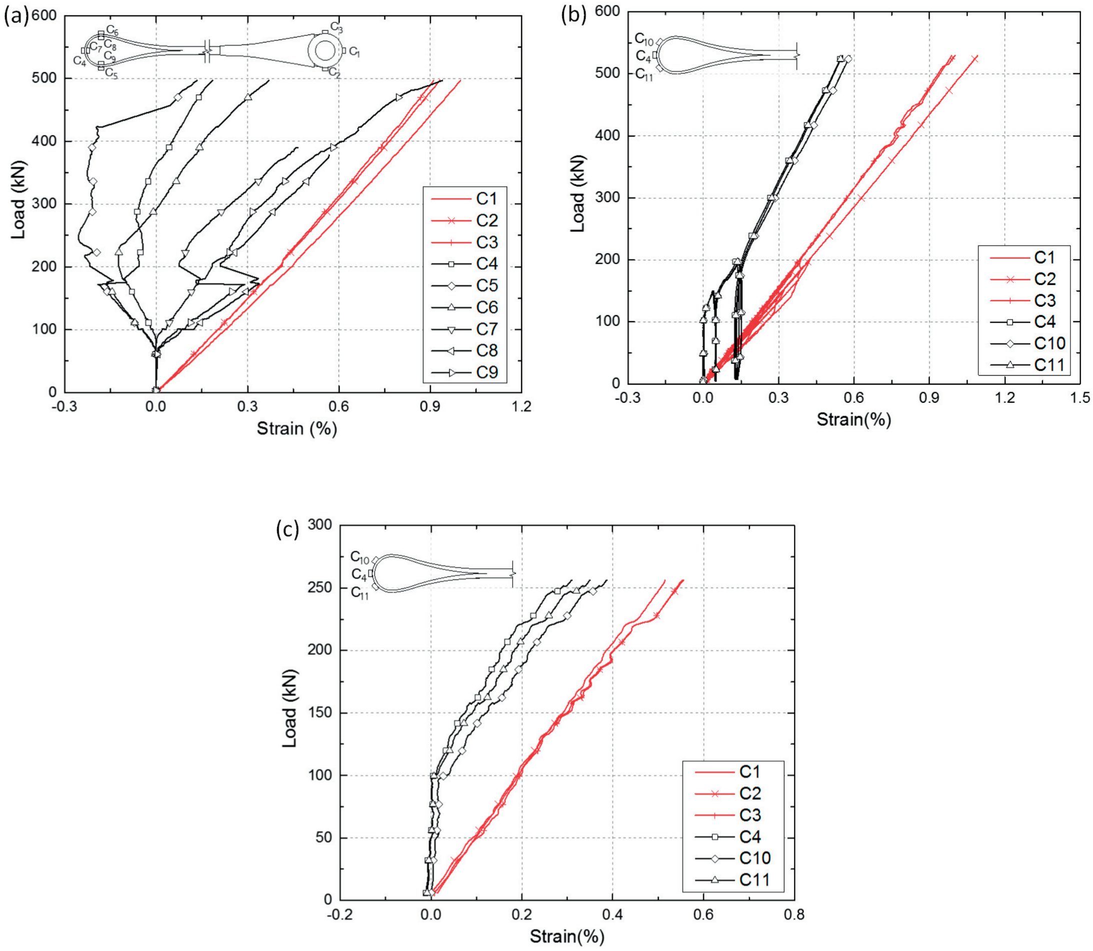

Fig. B.6: Load vs tangential strain of air-side strap: (a) S605; (b) C380; (c) C200

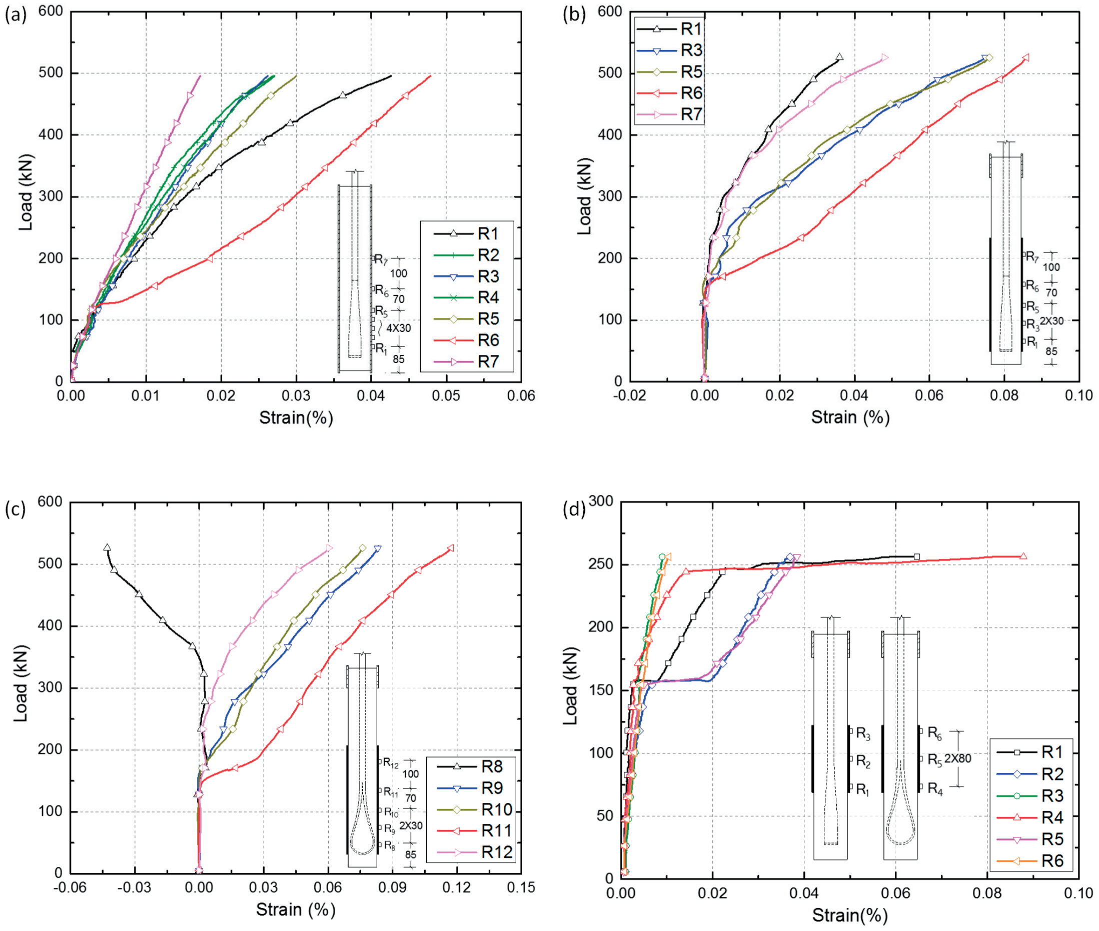

Fig. B.7: Load vs tangential strain of steel and CFRP confinement: (a) S605; (b)/(c) C380; (d) C200

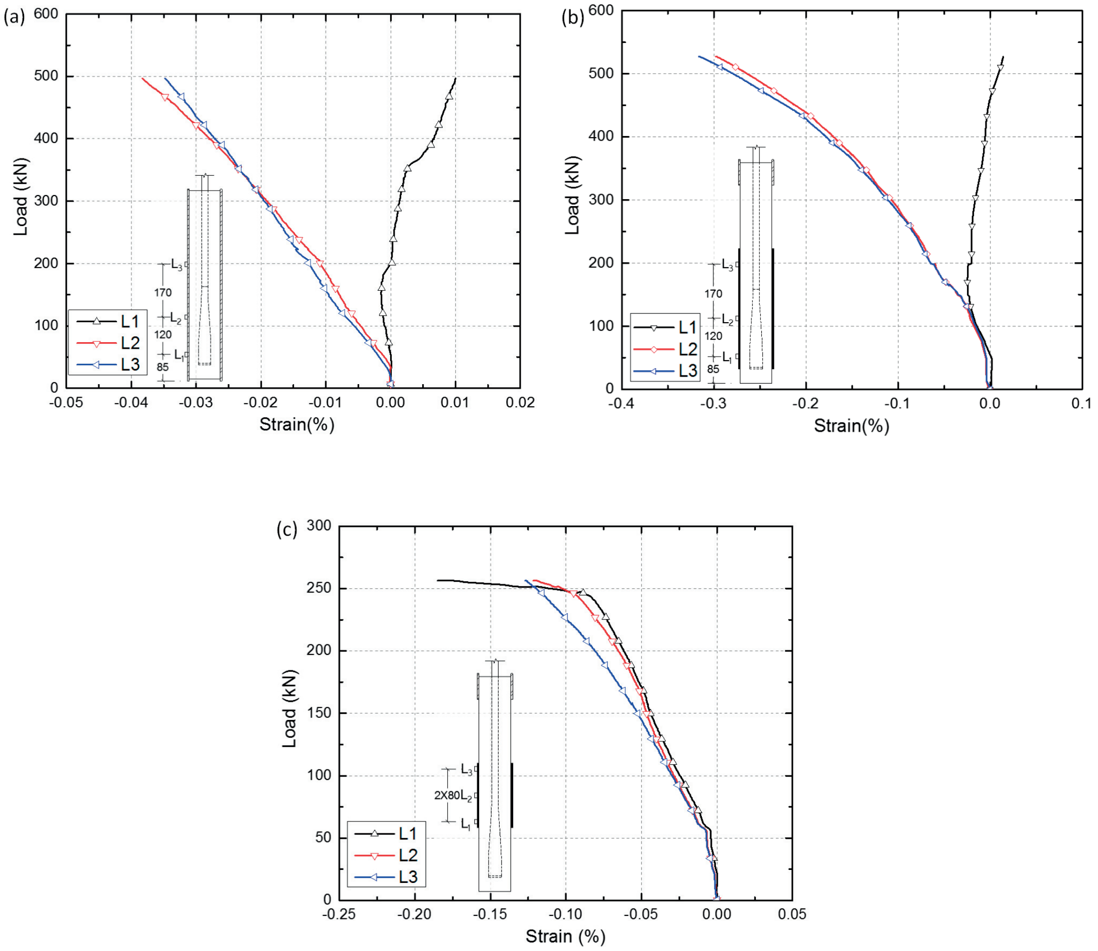

Fig. B.8: Load vs longitudinal strain of steel and CFRP confinement:

(a) S605; (b) C380; (c) C200

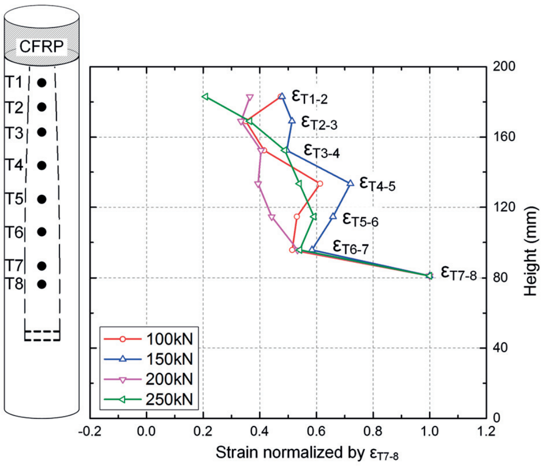

Fig. B.9: Compressive strain distribution in anchor C200

ANNEX C.

Pull-out behavior of CFRP ground anchors with two-strap ends

C.1 Fabrication procedure for anchor specimens

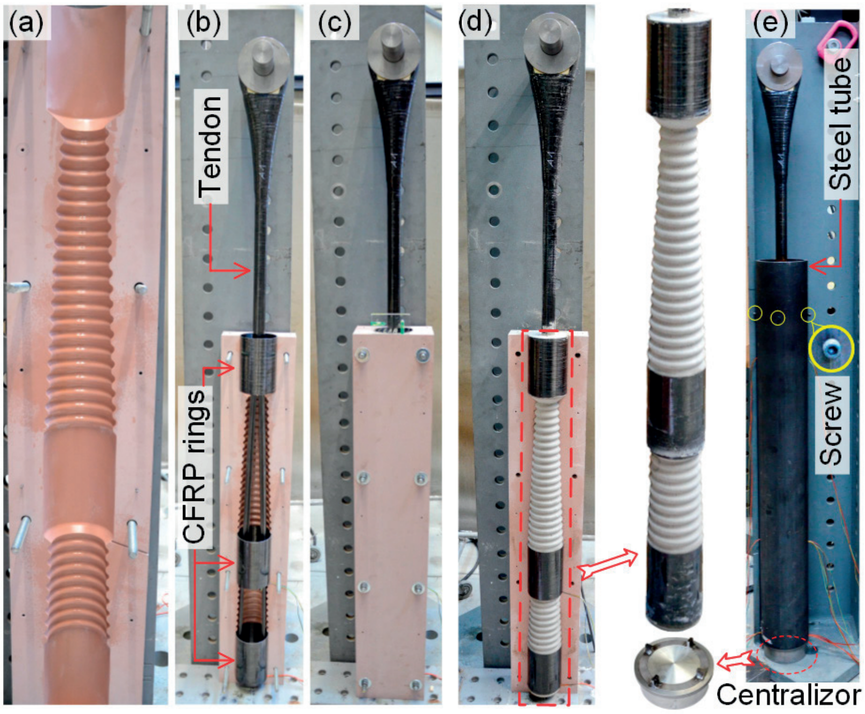
(a)
(b)
(c)
(d)
(e)
Tendon
CFRP rings
Steel tube
Screw
Centralizor

Fig. C.1: Fabrication procedure for two-strap anchors: (a) mold with corrugated surface; (b) installation of CFRP tendon and rings; (c) casting of high-strength grout; (d) demolding of prefabricated part; (e) casting of normal-strength grout

C.2 Experimental set-up

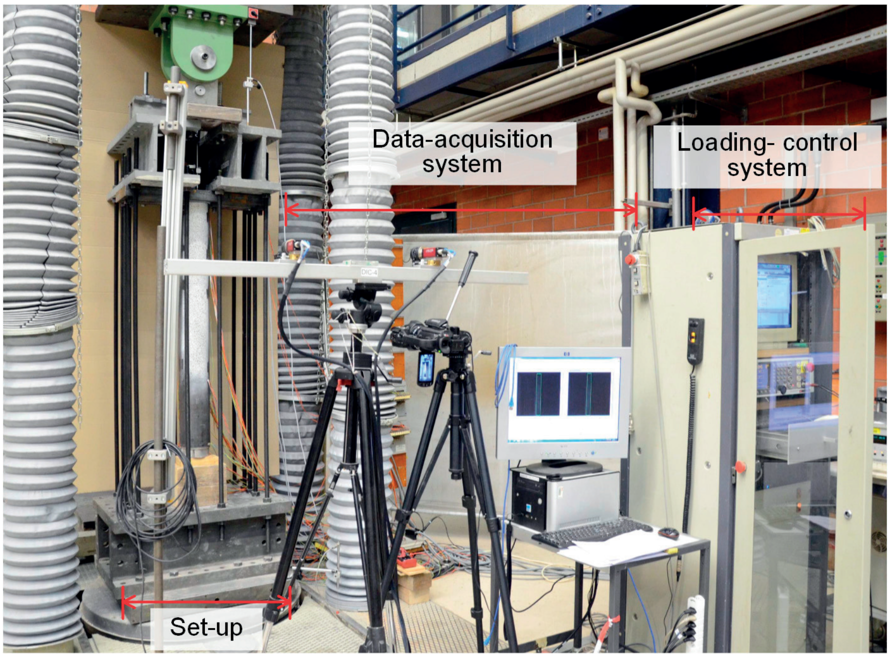
Data-acquisition system
Loading- control system
Set-up

Fig. C.2: Complete experimental set-up

C.3 Experimental results

This section complements the experimental results presented in Section 4.3 in Chapter 4.

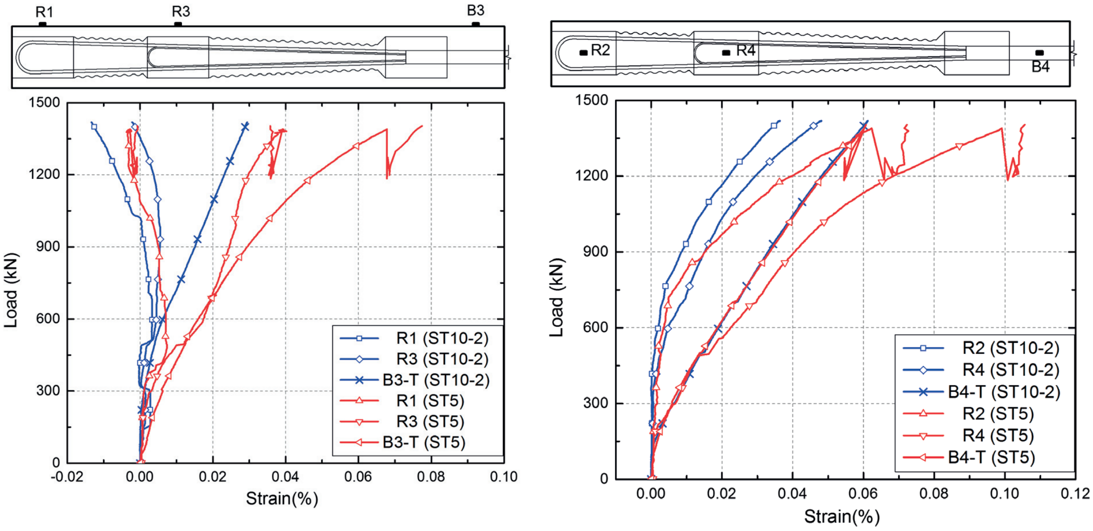

Fig. C.3: Load vs tangential strain of steel tube: (a) perpendicular to strap plane; (b) parallel to strap plane

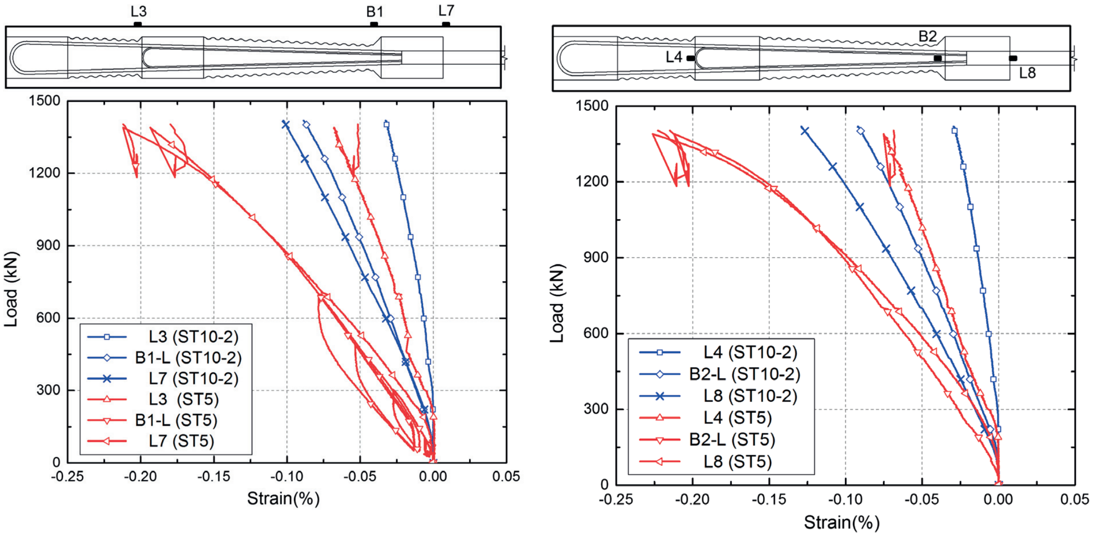

Fig. C.4: Load vs longitudinal strain of steel tube: (a) perpendicular to strap plane; (b) parallel to strap plane

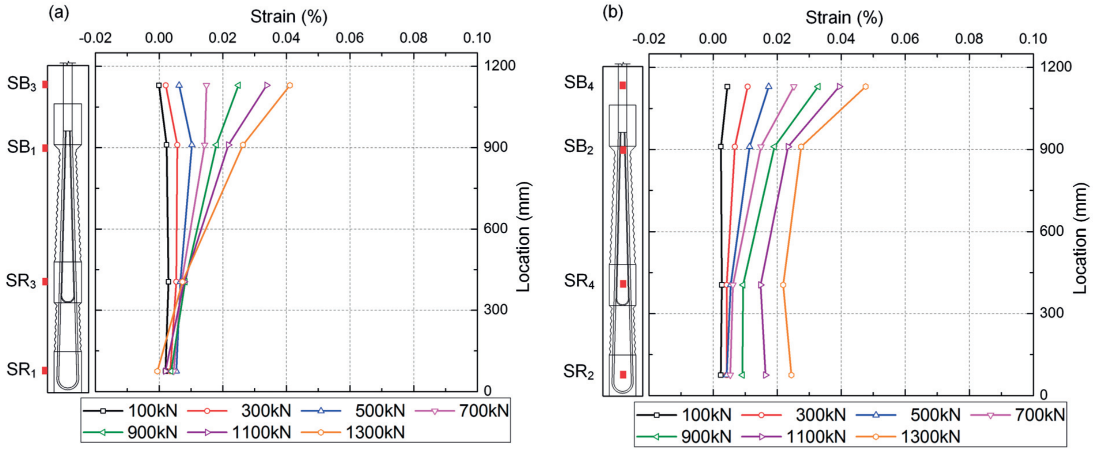

Fig. C.5: Tangential strain distributions along steel tube in ST10-1 at different load levels: (a) perpendicular to strap plane; (b) parallel to strap plane

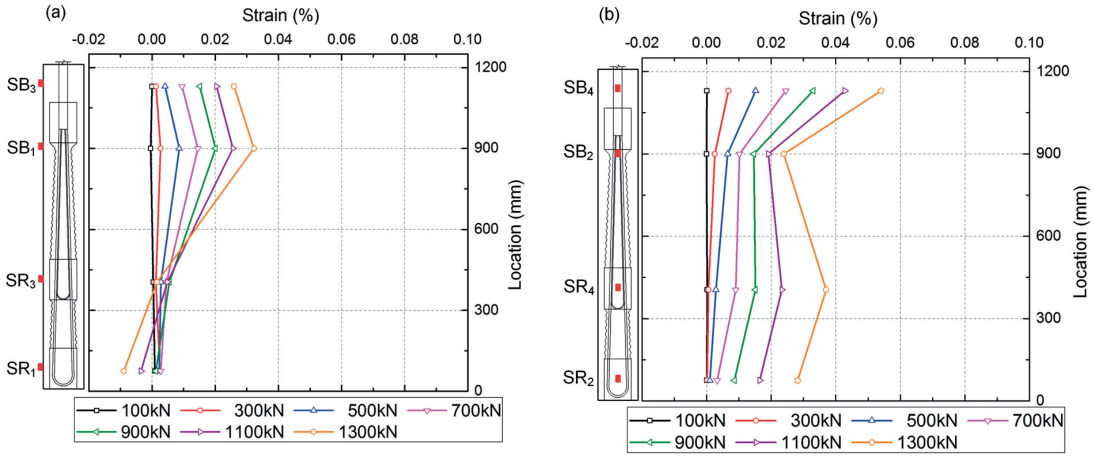

Fig. C.6: Tangential strain distributions along steel tube in ST10-2 at different load levels: (a) perpendicular to strap plane; (b) parallel to strap plane

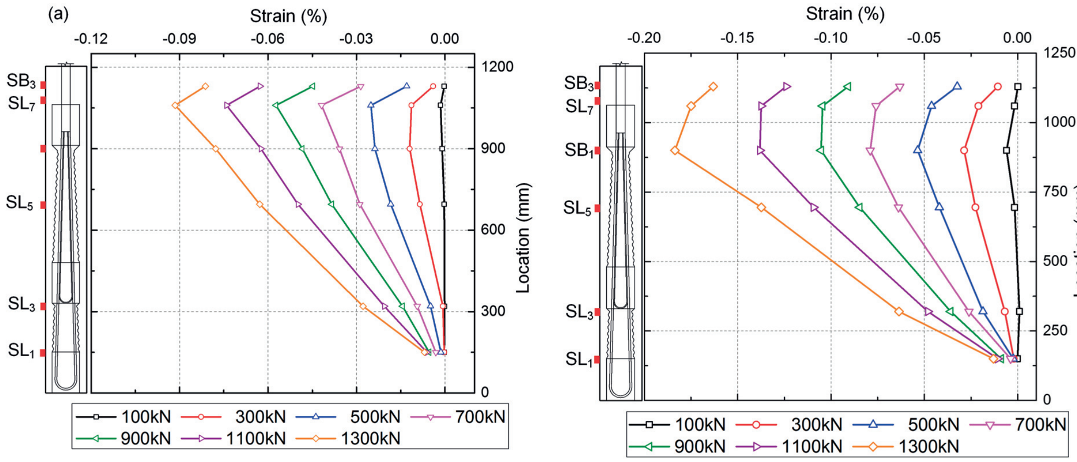

Fig. C.7: Longitudinal strain distributions along steel tube in ST10-2 at different load levels: (a) perpendicular to strap plane; (b) parallel to strap plane

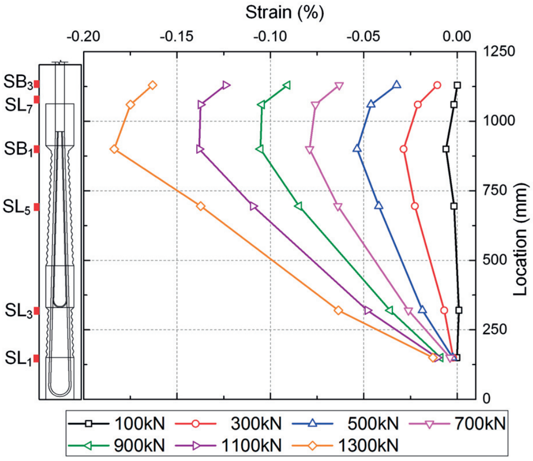

Fig. C.8: Longitudinal strain distributions along steel tube in ST5 at different load levels perpendicular to strap plane (parallel to strap plane shown in Chapter 4)

C.4 Simplified FE model

Two different configurations of two-strap CFRP ground anchors were investigated using FE methods: (1) with conical-shaped interface between the high- and normal-strength grout parts, as shown in Fig. C.9, and (2) with cylindrical-shaped interface between the two parts, as shown in Fig. C.10. In the FE models, as shown in Fig. C.11 for configuration (1), the grout parts were modeled using solid elements (C3D8R, eight-node linear brick elements with reduced integration) and the steel tube using shell elements (S4R, four-node quadrilateral elements with reduced integration). The rod segment of the CFRP tendon and the two embedded straps were simulated using three spring elements; the stiffness of the spring elements was equal to the strap stiffness, which determined the load distribution. Therefore, the progressive load transfer along the embedded strap was not simulated and the resulting stresses in the grout were more conservative than the experimental results.

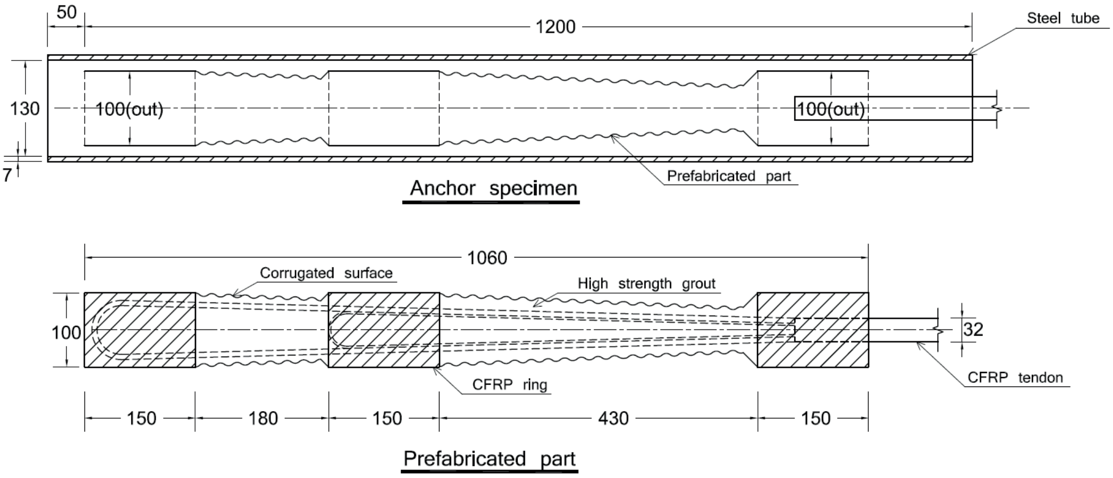
50
1200
Steel tube
130
100(out)
100(out)
7
Prefabricated part
Anchor specimen
1060
Corrugated surface
High strength grout
100
32
CFRP ring
CFRP tendon
150
180
150
430
150
Prefabricated part

Fig. C.9: Two-strap CFRP ground anchors – configuration (1)

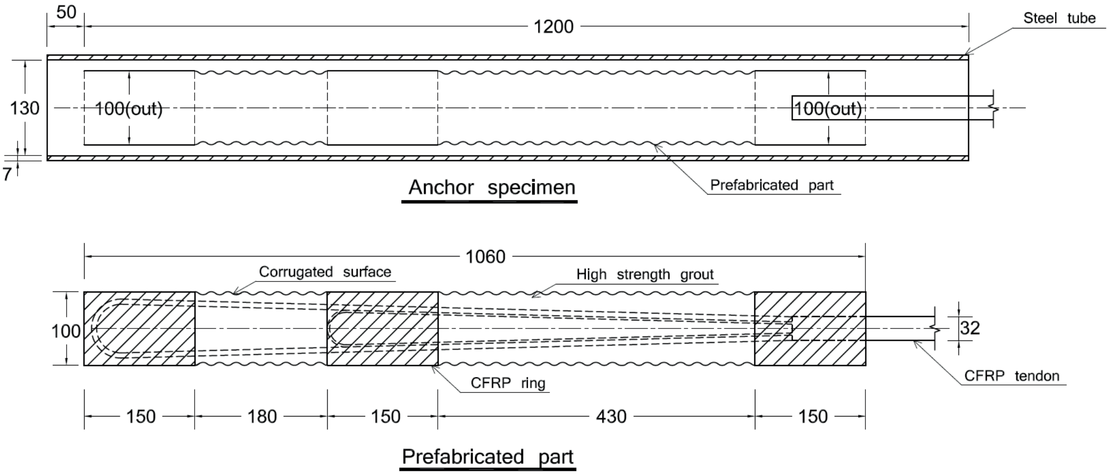
50
1200
Steel tube
130
100(out)
100(out)
7
Prefabricated part
Anchor specimen
1060
Corrugated surface
High strength grout
100
32
CFRP ring
CFRP tendon
150
180
150
430
150
Prefabricated part

Fig. C.10: Two-strap CFRP ground anchors – configuration (2)

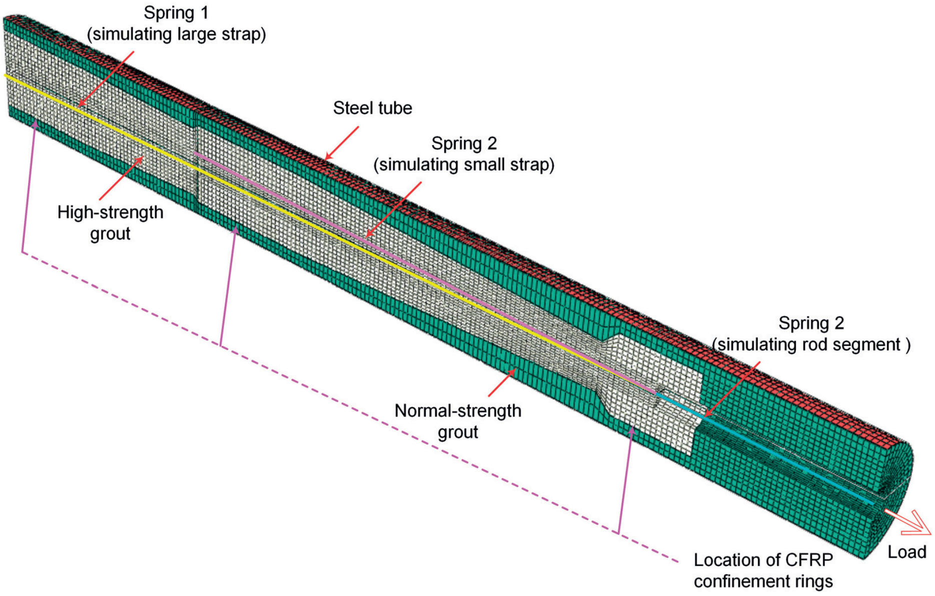
Spring 1
(simulating large strap)
Steel tube
Spring 2
(simulating small strap)
High-strength
grout
Spring 2
(simulating rod segment)
Normal-strength
grout
Location of CFRP
confinement rings
Load

Fig. C.11: Simplified FE model of two-strap CFRP ground anchor (configuration (1))

C.4.1 Anchor configuration (1)

The compressive stress distribution in the normal- and high-strength grout parts at 1000 kN is shown in Fig. C.12 and the status of the steel tube, i.e. the maximum principal stress and frictional shear stress on the inner surface, at 1000 kN is shown in Fig. C.13.

(a) Normal-strength grout

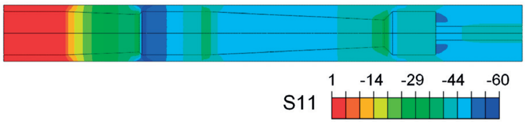

(b) High-strength grout

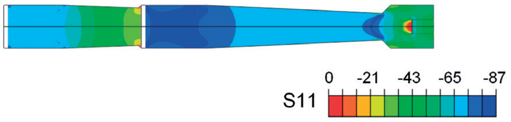

Fig. C.12: Compressive stress in grout at 1000 kN (Unit: MPa)

(a) Tube

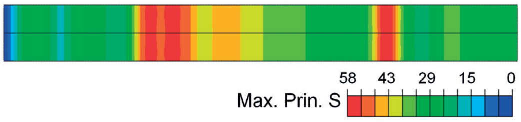

(b) Tube/grout interface

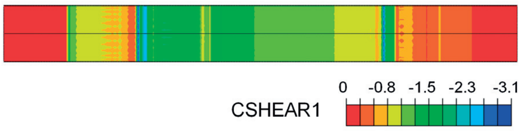

Fig. C.13: Status of steel tube at 1000 kN (Unit: MPa)

C.4.2 Anchor configuration (2)

The compressive stress distribution in the normal- and high-strength grout parts at 1000 kN is shown in Fig. C.14 and the status of the steel tube at 1000 kN is shown in Fig. C.15.

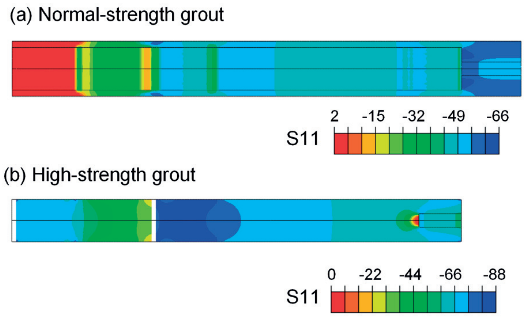
(a) Normal-strength grout
2 -15 -32 -49 -66
S11
(b) High-strength grout
0 -22 -44 -66 -88
S11

Fig. C.14: Compressive stress in grout at 1000 kN (Unit: MPa)

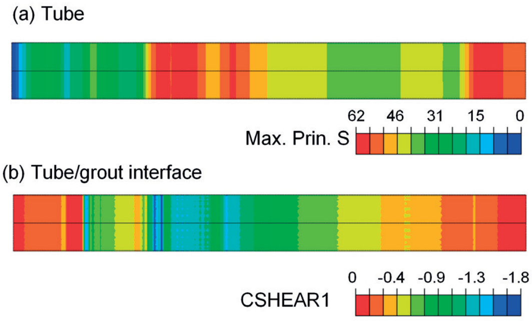
(a) Tube
62 46 31 15 0
Max. Prin. S
(b) Tube/grout interface
0 -0.4 -0.9 -1.3 -1.8
CSHEAR1

Fig. C.15: Status of steel tube at 1000 kN (Unit: MPa)

C.4.3 Comparison between two configurations

The compressive stress in the normal-strength grout part and the maximum principal stress in the steel tube in anchor configuration (2) were higher than that in configuration (1), indicating that the risk of grout and confinement (rock) failure was higher in the former. The frictional shear stress at the tube/grout interface in configuration (1) was higher than in configuration (2); however, the higher shear stress in the former can be reduced by increasing the bond length of the anchor. Therefore, configuration (1) was finally selected to reduce the risk of failure in the normal-strength grout and rock.

ANNEX D.

Design of CFRP tendons with three-strap ends

D.1 Parameter description

In order to design a three-strap anchor, as shown in Fig. D.1, 12 parameters have to be determined, where t_1, t_2 and t_3 are the thicknesses of the outer, middle and inner straps, R_{o1}, R_{o2} and R_{o3} are the outer radii of the semicircles of the straps, L_1, L_2 and L_3 are the strap lengths, θ is the inclination angle of the strap, R is the radius of the rod segment and D is the diameter of the borehole.

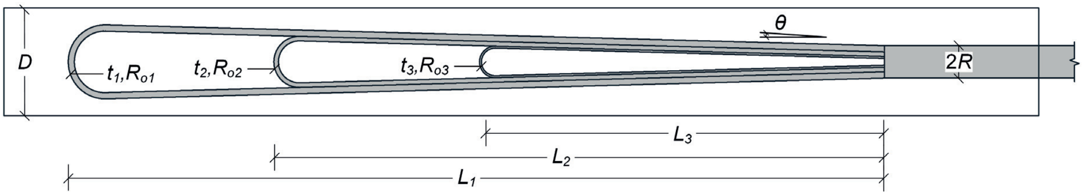

Fig. D.1: Schematic of three-strap anchor and geometrical parameters

The geometrical relationships between the parameters are as follows:

$$R = \sqrt{\frac{80 \times (tr_1 + tr_2 + 1) \times t_3}{\pi}} \tag{D.1}$$

$$R_{o1} = \frac{R + L_1 \times \tan\theta}{1 + \tan\theta} \tag{D.2}$$

$$R_{o2} = \frac{R - tr_1 \times t_3 + L_2 \times \tan\theta}{1 + \tan\theta} \tag{D.3}$$

$$R_{o3} = \frac{R - (tr_1 + tr_2) \times t_3 + L_3 \times \tan\theta}{1 + \tan\theta} \tag{D.4}$$

where tr_1 and tr_2 are the thickness ratios, i.e. $tr_1=t_1/t_3$ and $tr_2=t_2/t_3$. The load-bearing ratios of the outer to inner straps, F_{r1}, and of the middle to inner straps, F_{r2}, are determined by the strap stiffness ratios, i.e. $Fr_1=tr_1/Lr_1$ and $Fr_2=tr_2/Lr_2$, where Lr_1 and Lr_2 are the length ratios, i.e. $Lr_1=L_1/L_3$ and $Lr_2=L_2/L_3$. In the design of laminated CFRP straps, the outer to inner radius ratios, i.e. r_1, r_2, r_3 for the outer, middle and inner straps respectively, should be limited to prevent a large reduction of the load-bearing capacity as explained in Chapter 7. The geometrical relationship between the radius ratios and strap dimensions are as follows:

$$r_i = \frac{R_{oi}}{R_{oi} - tr_{1i} \times t_3}, \qquad (i = 1,\ 2) \tag{D.5}$$

$$r_3 = \frac{R_{o3}}{R_{o3} - t_3} \tag{D.6}$$

Furthermore,

$$Lr_i = \frac{L_i}{L_3}, \quad (i = 1,\ 2) \tag{D.7}$$

$$\frac{L_i}{L_3} = \frac{tr_i}{F_{1i}}, \quad (i = 1,\ 2) \tag{D.8}$$

The following constraint criteria were selected:

$$\begin{cases} L_1 \le 1270\,mm \\ L_1 - L_2 \ge 330\ mm \\ L_2 - L_3 \ge 330\ mm \\ 1.20 \le r_1 \le 1.30 \\ 1.20 \le r_2 \le 1.25 \\ 1.10 \le r_3 \le 1.20 \\ t_3 \ge 3\,mm \\ D \le 170\,mm \end{cases} \tag{D.9}$$

D.2 Design of three-strap CFRP tendon

In the three-strap anchor, the middle and outer straps have not yet reached the tensile strength as the inner strap does when the anchor fails at the ultimate load, i.e. the material utilization efficiencies, $R_{eff,i} = Fr_i/tr_i$, of the middle and outer straps cannot achieve 1.0 as the inner strap does. For the whole anchor, $R_{eff}=(1+Fr_1+Fr_2)/(1+tr_1+tr_2)$. A higher anchor capacity can be achieved by selecting a higher Fr_i value, i.e. increasing the loads borne by the middle and outer straps. For each targeted anchor capacity (corresponding to an Fr_i value), an optimized R_{eff} value can be obtained within the above-mentioned constraints using the optimization function in Matlab, as shown in Fig. D.2; the Matlab code is shown in Section D.4. The R_{eff} decreased with increasing Fr_1. Since the estimated load capacity already reached the targeted capacity of 2500 kN with $Fr_1=Fr_2=1.55$, these values were selected for the three-strap design presented in Chapter 5. Similarly, in comparing the one-, two- and three-strap anchors, a decrease of R_{eff} from 1.0 to 0.63 was also observed, as shown in Fig. D.3, where a polynomial decreasing trend was observed.

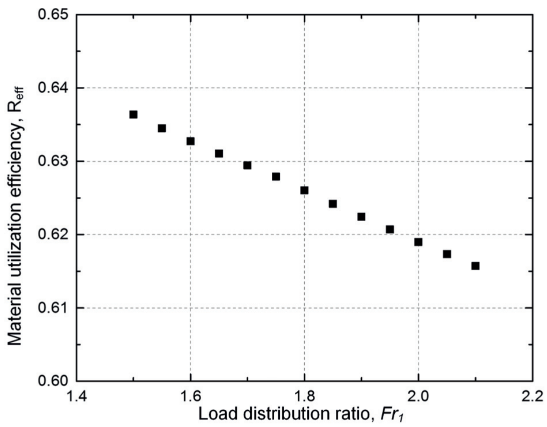

Fig. D.2: R_{eff} *vs* Fr_1 *responses*

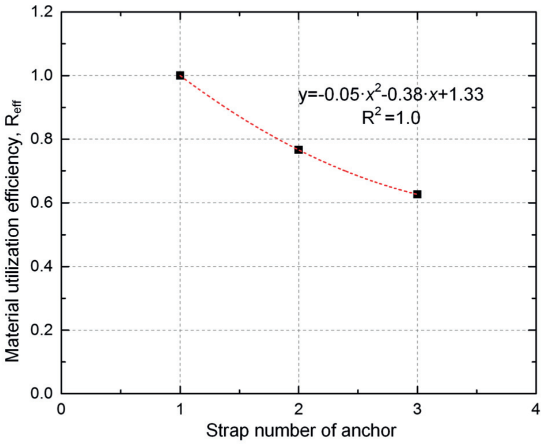

Fig. D.3: R_{eff} *vs strap number of anchors*

D.3 Design of air-side strap end

D.3.1 Validation of design method in two-strap anchors

Based on the analytical model for predicting the load-bearing efficiency of laminated straps presented in Chapter 7, the ultimate load of the CFRP ground anchors can be estimated when the final failure occurs in the semicircle of the strap ends. In anchor ST5 presented in Chapter 4, strap rupture occurred at 1402 kN at the semicircle of the air-side strap, resulting in the final anchor failure. Therefore, a comparison between the measured and predicted ultimate loads was made to validate the applicability of the developed analytical model for the strap end design.

The inner and outer radii of the air-side strap were 55 and 65 mm respectively, corresponding to a radius ratio of 1.18. The elastic modulus, E_m, and Poisson's ratio, v_m, of the epoxy resin used were E_m=3.1 GPa and v_m=0.4 respectively. The elastic modulus, E_f, of the carbon fiber used was 245 GPa and the fiber volume fraction, V_f, was 60%. The elastic moduli in the fiber, E_1, and perpendicular to the fiber, E_2, directions of the strap can be calculated as [1]:

$$E_1 = E_f V_f + E_m(1-V_f) \tag{D.10}$$

$$E_2 = \frac{\frac{E_m}{1-v_m^2}(1+V_f^3)}{(1-V_f)^{0.75} + 6V_f \frac{E_m}{E_f(1-v_m^2)}} \tag{D.11}$$

The calculated E_1 and E_2 were 148 and 8 GPa respectively. The Poisson's ratios and tensile strength of the strap were assumed to be identical to those of the investigated non-laminated straps presented in Chapters 6 and 7, i.e. v_{12}=0.34, v_{22}=0.4 and σ_t=2.46 GPa. By substituting the material properties into Eq. (7.8) in Chapter 7, the calculated load-bearing efficiency ($R_{u,mod}$) with μ=0.2 was 0.68. Thus, the ultimate load of the air-side strap was estimated as $F_{ult,cal}=R_{u,mod}\cdot\sigma_t\cdot A$, where A is the cross section of the 32-mm-diameter rod segment, i.e. $F_{ult,cal}$=1345 kN, which was only 4% lower than the experimental result (1402 kN).

Furthermore, the ratio of the tangential to the median strains, i.e. $\varepsilon_o/\varepsilon_m$, at the flank of the outermost layer can also be estimated by substituting $r=r_o$ into Eq. (7.7) in Chapter 7, i.e. $\varepsilon_o/\varepsilon_m$ =0.86. Based on the ultimate load of 1402 kN, ε_m was calculated as 1.22%; ε_o was thus estimated as 1.05%, which was 7% higher than the measured strain (0.98%). Therefore, the applicability of the analytical model for the strap-end design was considered validated and subsequently used for the design of the air-side strap of the three-strap tendon.

D.3.2 Design of air-side strap of three-strap tendon

The dimensions of the three-strap anchor are presented in Chapter 5, where the diameter of the rod segment was $D_{rod,5}$=50 mm and the thickness of the air-side strap was t=19.4 mm. Assuming that the material properties and tensile strength of the three-strap tendon were identical to those of the two-strap tendon, a minimum $R_{u,mod}$ to reach the estimated ultimate load of F_{ult}=2843 kN was calculated as $F_{ult}/\sigma_t\cdot A$, i.e. $R_{u,mod}\geq$0.59; the maximum radius ratio with μ=0.2 was back calculated as 1.29 using Eq. (7.8) in Chapter 7 and the minimum inner radius of the air-side strap, r_i, was calculated as 67 mm.

D.4 Matlab code

The code consists of three parts as follows:

- Part 1:

```
clear
clc
L1_low=200;
L1_up=1270;
L2_low=200;
L2_up=1270;
L3_low=200;
L3_up=1270;
```

```
t3_low=3;
t3_up=5;
tRatio1_low=1.1;
tRatio1_up=5;
tRatio2_low=1;
tRatio2_up=5;
FRatio1_up=2.1;
FRatio2_low=1.5;
FRatio2_up=2.1;
i=1;
for a0=1.5:0.05:2.1
   FRatio1_low=a0;
   %[L1 L2 L3 t3 tRatio1 tRatio2 FRatio1 FRatio2]
   x0=[ 1270.0, 950.0, 630.0, 3.0, 2.2, 1.65, 1.55, 1.55]
   A=[-1,1,0,0,0,0,0,0;0,-1,1,0,0,0,0,0];
   b=[-320;-320];%larger L distance
   l=[L1_low L2_low L3_low t3_low tRatio1_low tRatio2_low FRatio1_low FRatio2_low];
   u=[L1_up L2_up L3_up t3_up tRatio1_up tRatio2_up FRatio1_up FRatio2_up];
   [x,f,g,output]=fmincon('max_Eff_NoAng',x0,A,b,[],[],l,u,'RRatio_NoAng')
   %output to excel
   i=i+1
   datas(i,1)=x(1);
   datas(i,2)=x(2);
   datas(i,3)=x(3);
   datas(i,4)=x(4);
   datas(i,5)=x(5);
   datas(i,6)=x(6);
   datas(i,7)=x(7);
   datas(i,8)=x(8);
   xlswrite('C:\Users\....\FRatio_1_Para.xlsx',datas)
end
TitleLine={};
ArrTitle={'L1','L2','L3','t3','tRatio1','tRatio2','FRatio1','FRatio2'};
TitleLine(1,1)=ArrTitle(1);
TitleLine(1,2)=ArrTitle(2);
TitleLine(1,3)=ArrTitle(3);
TitleLine(1,4)=ArrTitle(4);
TitleLine(1,5)=ArrTitle(5);
TitleLine(1,6)=ArrTitle(6);
TitleLine(1,7)=ArrTitle(7);
TitleLine(1,8)=ArrTitle(8);
xlswrite('C:\Users\...\FRatio_1_Para.xlsx',TitleLine);
```

- Part 2:

```
function [c,ceq]=RRatio_NoAng(r)
L1=r(1);
L2=r(2);
L3=r(3);
t3=r(4);
tRatio1=r(5);
tRatio2=r(6);
FRatio1=r(7);
FRatio2=r(8);
angle=1.51;
LRatio2=tRatio2/FRatio2;
sita=angle/180*pi;
ceq(1)=L1/L3-tRatio1/FRatio1;
ceq(2)=L2/L3-LRatio2;
R=sqrt((100*(tRatio1+tRatio2+1))*t3/pi);
R1Out=(R+L1*tan(sita))/(1+tan(sita));
R2Out=(R+L2*tan(sita)-tRatio1*t3)/(1+tan(sita));
R3Out=(R+L3*tan(sita)-tRatio1*t3-tRatio2*t3)/(1+tan(sita));
R1_low=1.2;
R1_up=1.3;
R2_low=1.1;
R2_up=1.25;
R3_low=1.1;
R3_up=1.2;
```

```
c(1)=R1Out/(R1Out-tRatio1*t3)-R1_up;
c(2)=R1_low-(R1Out/(R1Out-tRatio1*t3));
c(3)=R2Out/(R2Out-tRatio2*t3)-R2_up;
c(4)=R2_low-(R2Out/(R2Out-tRatio2*t3));
c(5)=R3Out/(R3Out-t3)-R3_up;
c(6)=R3_low-(R3Out/(R3Out-t3));
c(7)=tRatio2-tRatio1;
c(8)=FRatio2-FRatio1;
c(9)=R1Out+25-170/2;
```

- Part 3:

```
function Eff=max_Eff_NoAng(r)
L1=r(1);
L2=r(2);
L3=r(3);
t3=r(4);
tRatio1=r(5);
tRatio2=r(6);
FRatio1=r(7);
FRatio2=r(8);
Eff=-(1+FRatio1+FRatio2)/(tRatio1+tRatio2+1);
```

References

[1] Meier U. Grundlagen zum Bemessen von Kunststoffbauteilen. Skript ETH-Vorlesung 20-638, ETHz, Zurich Switzerland, 1997: 63.

ANNEX E.

Pull-out behavior of CFRP ground anchors using strand tendons

E.1 CFRP strand tendons and anchor specimens

Two types of CFRP tendons were investigated: (a) a small 3.5-mm-diameter wire tendon, as shown in Fig. E.1 (a); (b) a large strand tendon composed of four strands consisting of seven twisted 3.5-mm-diameter wires each, as shown in Fig. E.1 (b). The design loads of the wire and strand tendons were 14 and 200 kN respectively. The tendons (produced by Riostra, London, United Kingdom) were made of Toray's T700/24k fibers with an elastic modulus of 85.5 GPa in the fiber direction (manufacturer data).

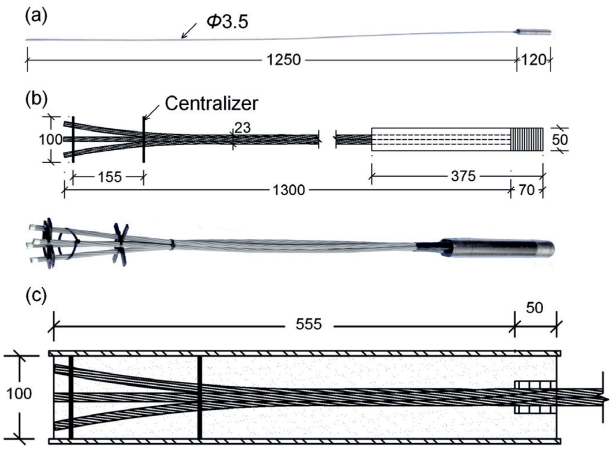

Fig. E.1: CFRP (a) wire and (b) strand tendons and (c) anchor specimen

The CFRP tendons were inserted into a 605-mm-long steel tube with an inner diameter of 100 mm and grouted with normal-strength grout as that used for the two-strap anchors presented in Chapter 4. The anchor specimens had similar configurations as the one-strap anchors presented in Chapter 3, as shown in Fig. E.1 (c).

E.2 Experimental set-up

The experimental set-up is shown in Fig. E.2. Strain gages in the longitudinal and tangential directions were installed along the steel tube and video extensometers were used to measure the displacement of the air-side anchor head due to the difficulty of installing LVDTs. The specimens were loaded in displacement control at a rate of 0.1mm/min.

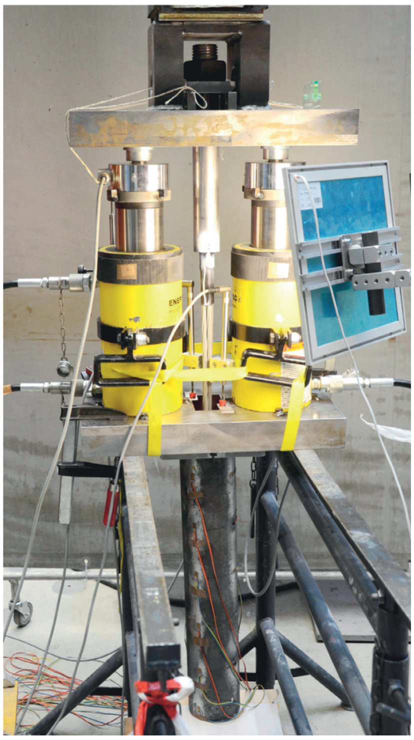

Fig. E.2: Experimental set-up

E.3 Experimental results

The load vs displacement responses of the two anchor specimens are shown in Fig. E.3. Bond failure occurred at 112 kN in the anchor with the large strand tendon and at 9.5 kN in the small tendon case. Therefore, the material strength of the CFRP tendon was not achieved.

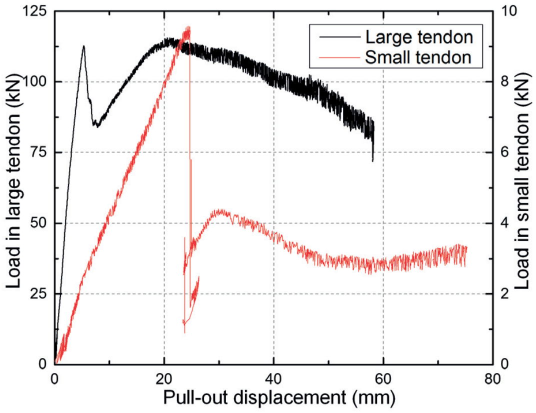

Fig. E.3: Load vs pull-out displacement responses of anchor specimens with small (wire) and large (strand) tendons

The longitudinal strain distributions along the tube length in planes (a) and (b) at 30, 50, 70, 90 and 109 kN are shown in Fig. E.4, based on which the bond stress at the tube/grout interface located was deduced; the bond stress distribution is shown in Fig. E.5. The maximum longitudinal strain was located at 150–250 mm distances from the bearing end. Two bond peaks, i.e. at the bearing and tendon ends, were observed. However, the tube strain and bond stress levels were both low.

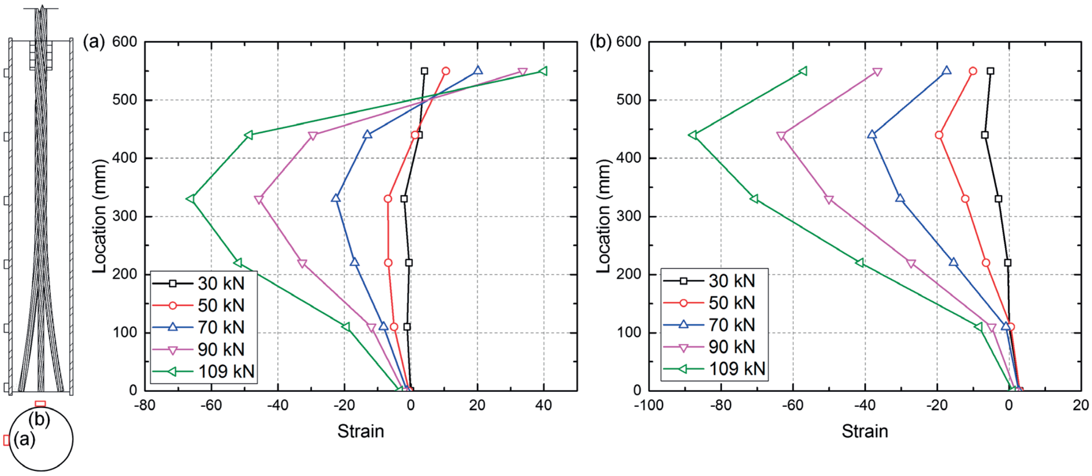

Fig. E.4: Distribution of longitudinal strain along steel tube in planes (a) and (b)

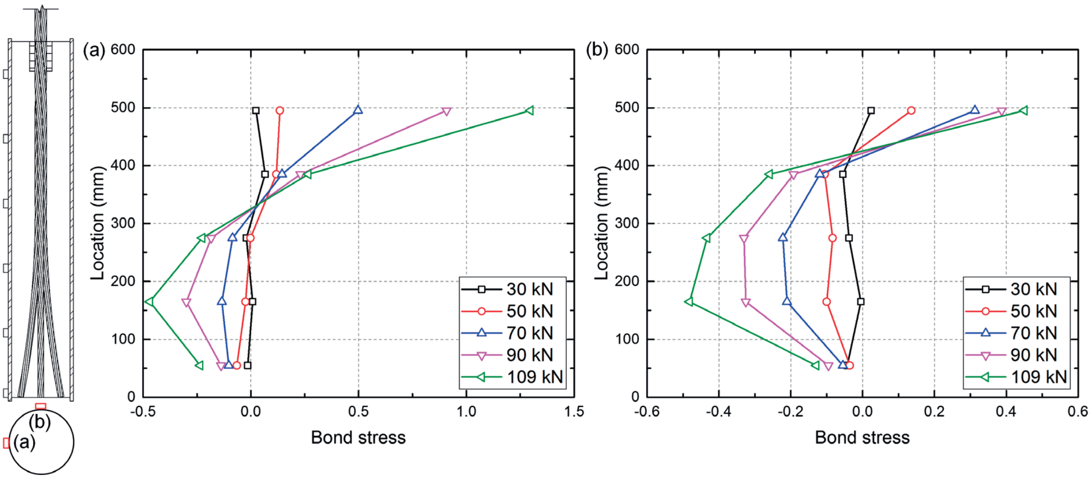

Fig. E.5: Distribution of bond stress at grout/tube interface along steel tube based on measured longitudinal strains in planes (a) and (b)

The load vs tangential strains responses of the steel tubes in planes (a) and (b) are shown in Fig. E.6; again the strains were low.

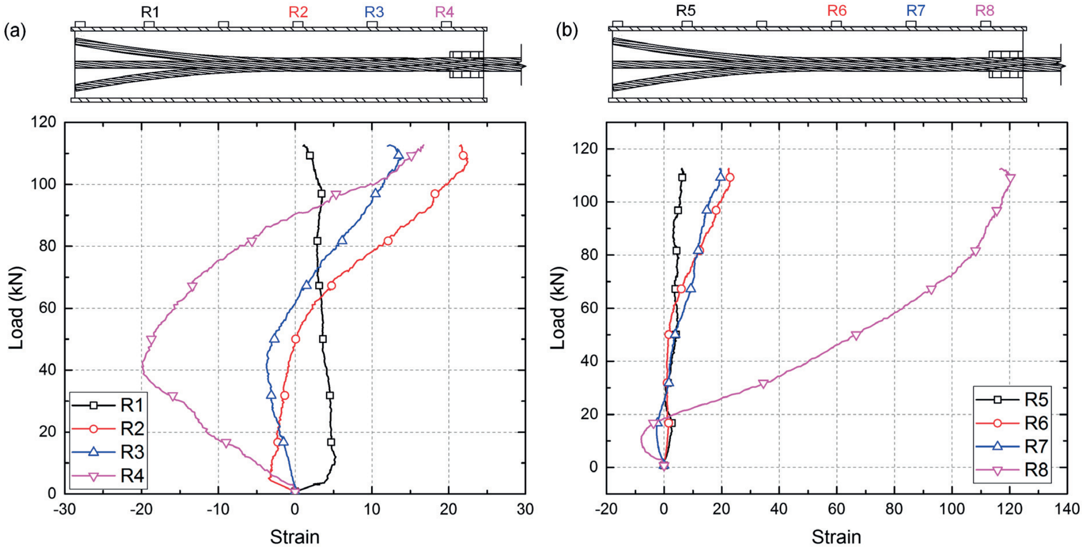

Fig. E.6: Distribution of tangential strain along steel tube in planes (a) and (b)

E.4 Analytical modeling

E.4.1 Analytical model

An analytical model was deduced based on the model presented in Ref. [1] for fully grouted cable bolts by adapting the different end constraint in this work, i.e. only the grout part was supported. The pull-out behavior of the grouted tendons consists of six different stages: (1) elastic, (2) elastic-softening, (3) elastic-softening–debonding, (4) pure softening, (5) softening–debonding and (6) debonding. In this work, only the first three stages that concern the estimation of the ultimate load are presented.

A tri-linear bond-slip model is used for simulating the bond behavior at the tendon/grout interface:

$$\tau = \begin{cases} k\delta & (0 \le \delta \le \delta_1) \\ \dfrac{\tau_p \delta_2 - \tau_f \delta_1}{\delta_2 - \delta_1} - \dfrac{\tau_p - \tau_f}{\delta_2 - \delta_1}\delta & (0 \le \delta \le \delta_1) \\ \tau_f & (\delta \ge \delta_2) \end{cases} \tag{E.1}$$

where δ is the interface shear slippage; k is the stiffness in the elastic stage; τ_p is the interfacial shear strength and τ_f is the residual strength. The relationship between the axial stress and shear stresses can be calculated as:

$$\tau(x)=\frac{D}{4}\frac{d\sigma_b(x)}{dx} \tag{E.2}$$

(1) elastic stage

The shear stress at the tendon/grout interface, τ, can be calculated as:

$$\frac{d\tau}{x}=a_0(\frac{\sigma_b}{E_b}-\frac{\sigma_m}{E_m}) \tag{E.3}$$

where σ_b and σ_m are the stresses of the tendon and steel tube, E_b and E_m are the elastic moduli of the tendon and steel tube, and a_0 can be calculated as:

$$a_0=\frac{kE_G}{E_G+Dk(1+v_G)\ln\frac{D+2t}{D}} \tag{E.4}$$

where v_G and E_G are the Poisson's ratio and elastic modulus of the grout, D is the diameter of the tendon, t is the thickness of the grout. In the case of only end support on the grout, the stress of the steel tube is assumed to be identical as that in the grout:

$$\sigma_m=\frac{\pi D^2}{4A_1}\sigma_b \tag{E.5}$$

where A_1 is the equivalent cross section of the grout plus tube:

$$A_1=\frac{\pi}{4}[(D+2t+2b\frac{E_m}{E_G})^2-D^2] \tag{E.6}$$

By substituting Eqs. (E.2) and (E.5) into (E.3):

$$\frac{d^2\sigma_b}{dx^2}-\alpha^2\sigma_b=0 \tag{E.7}$$

where:

$$\alpha^2=\frac{kE_G}{E_G+Dk(1+v_G)\ln\frac{D+2t}{D}}[\frac{1}{E_b}+\frac{\pi D^2}{4A_1E_G}] \tag{E.8}$$

The tendon stress and shear stress at the tendon/grout interface can be calculated as:

$$\sigma_b(x)=\frac{4F}{\pi D^2}\frac{e^{\alpha x}-e^{-\alpha x}}{e^{\alpha L}-e^{-\alpha L}} \tag{E.9}$$

$$\tau(x)=\frac{F\alpha}{\pi D}\frac{e^{\alpha x}+e^{-\alpha x}}{e^{\alpha L}-e^{-\alpha L}} \tag{E.10}$$

where L is the bond length. The initial cracking load can be calculated as:

$$F_{ini}=\frac{\tau_p\pi D}{\alpha}\frac{e^{\alpha L}-e^{-\alpha L}}{e^{\alpha L}+e^{-\alpha L}} \tag{E.11}$$

In the elastic stage, the pull-out load F is always lower than F_{ini}.

(2) Elastic-softening stage

In this stage, the region with a length of a_s at the bearing end already enters the softening stage of the tri-linear model, i.e. $\tau(x=L-a_s)=\tau_P$. For the remaining bond region of $L-a_s<x<L$, the tendon stress can be calculated by solving:

$$\frac{d^2\sigma_b}{dx^2}+\omega^2\sigma_b=0 \tag{E.12}$$

where:

$$\omega^2=\frac{4E_G(\tau_p-\tau_f)}{DE_G(\delta_2-\delta_1)+D^2(\tau_p-\tau_f)(1+\nu_G)\ln\frac{D+2t}{D}}[\frac{1}{E_b}+\frac{\pi D^2}{4A_1E_G}] \tag{E.13}$$

F can be calculated as:

$$F=\frac{\tau_p\pi D}{\alpha}\tanh(\alpha(L-a_s))\cos(\omega a_s)+\frac{\tau_p\pi D}{\omega}\sin(\omega a_s) \tag{E.14}$$

By solving $dF/da_s=0$, the critical softening length a_{sc} can be obtained. The ultimate pull-out load, F_{ult}, can be calculated by substituting a_{sc} into Eq. (E.14). Furthermore, τ_L can be calculated as:

$$\tau_L=\tau_p\cos(\omega a_{sc})-\frac{\tau_p\omega}{\alpha}\tanh(\alpha(L-a_{sc}))\sin(\omega a_{sc}) \tag{E.15}$$

(3) elastic-softening–debonding stage

In this stage, the pull-out load F can be calculated as:

$$F=\tau_p\pi Da_f+\frac{\tau_p\pi D}{\alpha}\tanh(\alpha(L-a_s-a_f))\cos(\omega a_s)+\frac{\tau_p\pi D}{\omega}\sin(\omega a_s) \tag{E.16}$$

where the frictional length a_f can be calculated from:

$$\cos(\omega a_{sc})-\frac{\omega}{\alpha}\tanh(\alpha(L-a_s-a_f))\sin(\omega a_s)-\frac{\tau_f}{\tau_p} \tag{E.17}$$

F_{ult} can be finally estimated by following two steps:

a) Calculate α, ω and τ_L using Eqs. (E.8), (E.13) and (E.15) respectively.
b) If $\tau_L>\tau_f$, calculate F_{ult} using Eq. (E.14), otherwise, Eq. (E.16) is used.

E.4.2 Results of analytical modeling

By substituting the dimensions and material properties of the anchor using the large cable tendon (see Table D.1) into the analytical model established in Matlab (see code in Section E.4.3), F_{ult} of the CFRP anchor with the large strand tendon was estimated as 108.7 kN, which matched well with the experimental result (112 kN). Furthermore, the predicted longitudinal strain distribution along the steel tube at 90 kN was also in good agreement with the experimental results in plane (b), as shown in Fig. E.7. The difference at location of 550 mm resulted from the disregard of the slippage at the tube/grout interface close to the bearing end.

Table D.1: Input parameters in analytical model

D (mm)	t (mm)	b (mm)	L (mm)	E_G (MPa)	v_G	E_b (MPa)	E_m (MPa)	τ_p (MPa)	τ_f (MPa)	δ_1 (mm)	δ_2 (mm)
20	90	7	555	25900	0.15	85480	210000	3.25	3.00	4.0	4.5

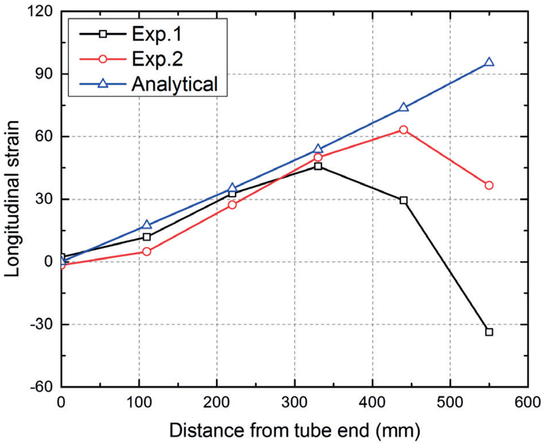

Fig. E.7: Comparison of experimental and analytical longitudinal strain distribution along steel tube

E.4.3 Matlab code

```
%Cable tendon, calculate Fult
%Improved Chen's model by adapting end constraint
clear
clc
syms F a1 alfa L x w b1 tp tf D F1 re k Eg Eb Es b t vg delta1 delta2 x2 x3 sigmab sigmas;
Eg=25900;
Eb=85480;
D=20;
Es=210000;
b=7.1;
t=40;
vg=0.15;
```

```
tp=3.25;
tf=3;
delta1=4;
delta2=4.5;
k=tp/delta1;
L=555;
A1=pi/4*((D+2*t+2*Es/Eg*b)^2-D^2);
% only different part with Chen's model
alfa=sqrt(4*k/D*(1/Eb+pi*D^2/4/A1/Eg));
b0=(tp-tf)/(delta2-delta1);
w=sqrt(4*b0/D*(1/Eb+pi*D^2/4/A1/Eg))
%
% Eq.( E.11)
Fini=tp*pi*D/alfa*(exp(alfa*L)-exp(-alfa*L))/(exp(alfa*L)+exp(-alfa*L))
a1=tp*pi*D/alfa;
b1=tp*pi*D/w;
%Eq. (E.14)
F=a1*tanh(alfa*L-alfa*x)*cos(w*x)+b1*sin(w*x);
%Eq. (E.15)
tl=tp*cos(w*x)-tp*w/alfa*tanh(alfa*(L-x))*sin(w*x);
%differentiate F with respect to the variable x
F1=diff(F,x,1);
%solve the new equation F1
as=subs(solve(eval(F1),'x'))
%solve equations (31) to calculate as and tl, if tl<tf, enter the
%elastic-softening-debonding stage
F=subs(F,{x},{as});
tl=subs(tl,{x},{as})
if tl>=tf
  subs(F)
else
  F=tf*pi*D*x2+a1*tanh(alfa*L-alfa*x-alfa*x2)*cos(w*x)+b1*sin(w*x);
  F1=diff(F,x,1);
  F2=cos(w*x)-w/alfa*tanh(alfa*L-alfa*x-alfa*x2)*sin(w*x)-tf/tp;
```

```
    %Equ (16, 17)
    [x x2]=solve(eval(F1),eval(F2))
    % x=as; x2=af
    vpa(subs(F),5)
end
%strain distribution at 90 kN
F0=90000;
for x3=0:110:550
    subs(x3)
    sigmab=(4*F0/(pi*D^2))*(exp(alfa*x3)-exp(-alfa*x3))/(exp(alfa*L)-exp(-alfa*L));
    ss=vpa((sigmab*pi*D^2/4/A1/Eg*1000000),5)
    %vpa(subs(sigmas),5)
    %average stress of grout -> strain -> compare to exp, assuming steel
    %has the same strain as the grout
end
```

References

[1] Chen J, Saydam S, Hagan PC. An analytical model of the load transfer behavior of fully grouted cable bolts. Constr Build Mater 2015;101:1006-15

Haifeng FAN

Av. de florissant 18
1020 Lausanne
haifeng.fan.ch@gmail.com
+41 78 639 23 17

EDUCATION

2012-present **Swiss Federal Institute of Technology Lausanne(EPFL), Lausanne, Switzerland**
Ph.D. in Civil Engineering

2008-2011 **Tongji University, Shanghai, China**
Master in Bridge and Tunnel Engineering

2004-2008 **Nanjing University of Aeronautics and Astronautics, Nanjing, China**
Bachelor in Civil Engineering

CORE EXPERIENCE

2012-present **Swiss Federal Institute of Technology Lausanne(EPFL), Lausanne, Switzerland**
Research and teaching assistant

- Developed an innovative post-tensioned anchor product using Carbon Fibre Reinforced Plastic (CFRP) for applications in dams, tunnels, etc.
- Conducted more than 30 material tests and 10 full-scale pull-out tests on anchor specimens with up to 1400 kN of capacity
- Developed an analytical model for used grouts based on fib code, built 5 finite element models corresponding to the pull-out tests and conducted optimization of the anchor design using Matlab
- Compiled 3 technical reports and 6 scientific papers and gave presentations in international conferences
- Assisted a class of 150 bachelors for the course of *Structure and Material* on their exercises in French

2011-2012 **Shanghai Tonghao Civil Engineering Consulting Co., Ltd, Shanghai, China**
Bridge engineer

- Participated in developing a new software program for analysis and design of different types of prestressed bridges
- Conducted structural analyses using engineering software and designed two prestressed bridges: one 30-m-span continuous bridge and one 130-m-span rigid frame bridge

2008-2011 **Tongji University, Shanghai, China**
Research & teaching assistant

- Developed a new GFRP (glass FRP) and concrete composite bridge deck
- Conducted static and fatigue experiments on 6 deck specimens and developed corresponding finite element models
- Analyzed millions of data, wrote technical reports and published 7 journal and conference papers

SELECTED PUBLICATIONS

Journal papers:

1. Fan H, Vassilopoulos AP, Keller T. Numerical and analytical investigation of tensile behavior of non-laminated and laminated CFRP straps. Submitted to Compos B Eng, 2017.
2. Fan H, Vassilopoulos AP, Keller T. Load transfer mechanisms in CFRP ground anchors with multi-strap ends. Submitted to Compos Struct, 2017.
3. Fan H, Vassilopoulos AP, Keller T. Evaluation of grout materials for CFRP ground anchors with strap ends, Constr Build Mater 2017;145:196-206.
4. Fan H, Vassilopoulos AP, Keller T. Pull-out behavior of CFRP single-strap ground anchors, J Compos Constr, 10.1061/(ASCE)CC.1943-5614.0000760 , 04016102.
5. Fan H, Vassilopoulos AP, Keller T. Pull-out behavior of CFRP ground anchors with two-strap ends, Compos Struct 2017;160:1258–1267.
6. Fan H, Vassilopoulos AP, Keller T. Experimental and numerical investigation of tensile behavior of non-laminated CFRP straps. Compos B Eng 2016;91:327-36.
7. Xin H, Liu Y, He J, Fan H, Zhang Y. Fatigue behavior of hybrid GFRP-concrete bridge decks under sagging moment. Steel Compos Struct 2015;18: 925-946.
8. Liu Y, Fan H, Dai L. Construction process simulation of corrugated GFRP formwork with ribs. J Fiber Reinf Plast/Compos, 2010.

Conference papers:

1. Fan H, Vassilopoulos AP, Keller T. Pull-out behavior of CFRP ground anchors with two-strap ends. In: the 8th International Conference on FRP Composites in Civil Engineering (CICE 2016), Hong Kong China, 2016.
2. Fan H, Vassilopoulos AP, Keller T. Pull-out behavior of CFRP single-strap ground anchors. In: the 17th European Conference on Composite Materials (ECCM17), Munich, Germany, 2016.
3. Liu Y, Fan H, He J. Static and fatigue experimental study on flexural behavior of hybrid GFRP-concrete bridge decks. In: the Third Asia-Pacific Conference on FRP in Structures (APFIS 2012), Hokkaido, Japan, 2012.
4. Liu Y, He J, Fan H, Chen A. Experimental study on flexural behavior of hybrid GFRP/ concrete bridge deck. In: the 5th International Conference on FRP Composites in Civil Engineering (CICE 2010), Beijing, China, 2010.

LANGUAGES

Chinese: mother tongue

English: fluent

French: fluent

German: intermediate

COMPUTER SKILLS

Basic: MS office (Word, Excel, PowerPoint, Visio, Project)

Technic: C++, Midas Civil, AutoCAD, ORIGIN, Matlab, ANSYS, ABAQUS